Outstanding problems in the statistical physics of active matter

Benoît Mahault

To cite this version:

Benoît Mahault. Outstanding problems in the statistical physics of active matter. Soft Condensed Matter [cond-mat.soft]. Université Paris Saclay (COmUE), 2018. English. NNT : 2018SACLS250 . tel-01880315

HAL Id: tel-01880315
https://theses.hal.science/tel-01880315

Submitted on 24 Sep 2018

NNT : 2018SACLS250

Thèse de doctorat

Outstanding Problems in the Statistical Physics of Active Matter

Thèse de doctorat de l'Université Paris-Saclay
préparée à l'Université Paris Sud

Ecole doctorale n°564 Physique de l'Ile de France (PIF)
Spécialité de doctorat : Physique

Thèse présentée et soutenue à Gif sur Yvette, le 30 août 2018, par

BENOÎT MAHAULT

Composition du Jury :

Cécile Appert-Rolland Directrice de recherche, Université Paris Sud	Présidente
Erwin Frey Professeur, Ludwig-Maximilians-Universität München	Rapporteur
Yariv Kafri Professeur, Technion-Israel Institute of Technology	Rapporteur
Raphaël Voituriez Directeur de recherche, Université Pierre et Marie Curie	Examinateur
Hugues Chaté Chercheur CEA, CEA Saclay	Directeur de thèse

Acknowledgements

First, I would like to thank my referees Erwin Frey and Yariv Kafri their careful reading of this manuscript. I would also like to thank the other members of the jury, Cécile Appert-Rolland and Raphaël Voituriez, for their interest in my work and accepting to evaluate it.

Mes remerciements vont ensuite à mon directeur de thèse, Hugues Chaté, pour l'attention qu'il m'a porté durant ces trois années, ses suggestions et commentaires précieux ayant aiguisé mon esprit critique de jeune scientifique. Je souhaite aussi le remercier pour toutes les opportunités qu'il m'a offert, allant bien au delà de la science et qui ont fait de cette thèse une période de découvertes et de rencontres.

Les travaux présentés dans ce manuscript découlent en grande partie d'interactions que j'ai eu le plaisir d'avoir avec Aurelio Patelli qui m'a supervisé habillement à mes débuts, Eric Bertin que je remercie chaleureusement pour la semaine que j'ai pu passer à Grenoble, Xiaqing Shi qui a eu la gentillesse de nous guider durant nos séjours en Chine et de m'avoir introduit au système de santé local, et Cesare Nardini pour son ouverture d'esprit et ses bons conseils quant à ma future carrière.

Durant cette thèse j'ai aussi eu la chance de participer à de nombreux échanges à la fois enrichissants et agréables, je souhaite en particulier remercier Giordano Fausti, Francesco Ginelli, Li-Shi Luo, Ananyo Maitra, Daiki Nishiguchi, Wanming Qi, Sriram Ramaswamy, Masaki Sano, Julien Tailleur, Mathiew Turner, et Hepeng Zhang.

Je veux aussi remercier Bertrand Delamotte et Pascal Viot qui ont eu la gentillesse d'assister à ma répétition et de rendre ma soutenance moins soviétique.

Un grand merci également à tout le service du SPEC du CEA Saclay et son directeur François Daviaud où j'ai apprécié travailler durant ces trois années, en particulier à Nathalie Royer qui m'a permis de ne pas me perdre dans les formalités administratives du CEA, Ivan pour avoir joué son rôle de parrain et nos discussions stimulantes lorsque je me retrouvais seul au bureau, et enfin Alizée pour m'avoir introduit à l'escalade. Je souhaite aussi remercier le LPTMC et son directeur Bertrand Delamotte où j'ai passé une grande partie de mon temps, ainsi que le CSRC et son directeur Hai-Qing Lin pour son accueil et la mise à disposition du supercalculateur TianHe, sans qui certains des travaux exposés dans cette thèse n'auraient pas pu voir le jour.

Je remercie ensuite ma famille pour leur soutient inconditionnel et pour leur aide dans l'organisation de ce moment important de ma vie, bien que je faille parfois à leur expliquer toutes les subtilités de mon travail. Une mention spéciale va bien entendu à ma soeur Marie Noëlle et ma mère Marie Christine sans qui le pot the thèse n'aurait pas été aussi savoureux.

Mes remerciements chaleureux vont aussi à Anne, Benoît, Dimitri, Florent, Loïc, Matthieu, et Marina que j'aurais aimé voir plus souvent.

Ensuite viennent les « vrais », ceux qui ont particulièrement marqué ces trois années : Hugo, mon compagnon de route avec qui j'ai bu l'apéro sur trois continents, gravi des sommets escarpés, élaboré des plats à 32 étoiles, et que j'espère retrouver plus en forme que jamais de l'autre côté du Rhin. Mallory, qui bien qu'aiguisant ses talents de cuisinier en mer du Nord, en est toujours revenu avec le sourire. Lauriane, que je remercie pour ses petits plats que l'on a jamais réussi à égaler. Et Matthieu qui est jamais le dernier. Un grand merci à eux pour les discussions interminables sur le canapi, les cadeau improbables, les vacances au chalet, les films dont je n'ai jamais pu voir la fin, les ferias mémorables et les pistes rouges qui m'ont fait frissonner.

Enfin, je souhaite adresser un merci particulier à 혜린 , qui a su me présenter aussi bien Tokyo que Berlin à sa façon, 너는 너라서 고마워.

Contents

A mes parents

Chapter 1

Modeling of active matter, simple models and continuous theories

1.1 The world of nonequilibrium statistical mechanics

Statistical mechanics is the field of physics that aims at solving problems with a large number of degrees of freedom. Since for many applications this one is typically of the order of the Avogadro number, is not possible to integrate all the microscopic laws of motion for the elementary constituents of a system, and statistical methods are required. Hopefully, isolated systems at equilibrium are fully characterized by a few macroscopic parameters (temperature, pressure, etc…) which can be expressed as ensemble averages of the microscopic ones under the ergodicity postulate. Therefore, statistical mechanics builds the link between the equilibrium thermodynamics, which relies on principles based on empirical studies, and the microscopic details of matter [1].

Equilibrium statistical mechanics is the origin of powerful tools such as the Gibbs measure, the Monte Carlo methods, the Ginzburg-Landau phenomenological theory, or the (Nonperturbative) Renormalization Group formalisms that allow the study of very distinct systems from Bose Einstein condensates to protein folding. These ones instigated important concepts in modern physics such as the notion of *universality* [2], which states that the description of systems near criticality can be done based on symmetry arguments and dimensionality only, and is independent of their microscopic details. However, most systems in nature are subject to fluxes of matter and energy and are thus out of the scope of equilibrium thermodynamics. Formally, thinking in terms of problems composed of elementary processes, this means that transitions between these states do not satisfy the detailed balance condition in their stationary state [3].

In practice, there are various ways to be out of equilibrium. The first one is to remain close to equilibrium by, for example, considering isolated systems that relax to their steady state, or that are subject to small external perturbations. For those small deviations from equilibrium one can apply the linear response theory which provides a unified framework and strong results like the fluctuation dissipation theorem [4].

On the contrary, many nonequilibrium systems cannot be studied from linear theory and are said to be far from equilibrium. This is the case for glasses, made from fast cooled liquids that end up trapped in an energy landscape providing an infinity of metastable states. These materials thus relax to equilibrium on timescales much larger than the ones accessible experimentally [5]. Other examples are found considering large perturbations w.r.t. equilibrium [6]: driven diffusive systems [7], interface growth [8], turbulent flows that spread energy from its injection on large scales to the microscopic Kolmogorov scales [9], or quantum systems coupled to nonequilibrium reservoirs [10]. Finally, the last class of systems are the ones whose microscopic dynamics is already out of equilibrium. This includes systems with absorbing states such as reaction diffusion processes [11] and the subject of this thesis, active matter.

Absence of detailed balance prevents a description of these open systems in terms of a small number of phenomenological variable. This is why their study typically requires a more complicated framework, and the far from equilibrium world is still an active research topic in modern statistical mechanics. Because the equilibrium statistical physics toolkit is not relevant for those cases, several useful techniques have been developed over the years in order to solve them. We can cite for instance the Langevin and master equations, large deviations theory, or kinetic approaches such as the Bolztmann and Fokker-Planck equations from which hydrodynamic theories in terms of slow modes of the dynamics can be derived [12]. Moreover, remarkable progress in computing power in past decades now allow for both extensive numerical studies directly at the microscopic level and numerical solving of the, typically nonlinear, equations that statistical physicists encounter everyday. It should finally be mentioned that a substantial part of nonequilibrium systems exhibit generic scale invariance [13]. Therefore, based on Renormalization Group ideas, the concept of *universality* has also naturally emerged out of equilibrium and several universality classes can be defined in this context [11, 14–17].

1.2 Active matter

1.2.1 Definition and experimental realizations

Are referred as *active matter* all systems composed of microscopic units that are capable of dissipating locally the energy present in their environment into systematic motion. As mentioned earlier, contrary to systems that are driven out of equilibrium by external forces, it is nonequilibrium in its bulk. This peculiar feature yields new physics such as the generic properties of ensembles of coherently moving agents, known as *collective motion*. Active matter has therefore attracted a lot of interest from soft matter and statistical mechanics communities in the past decades [18–23].

Nature provides many examples of active matter systems, at the macroscopic scale we find human crowds [24, 25], or animal groups that can move collectively without leader [20]. Among them we can cite starling flocks, for which 3 dimensional reconstructions of individual trajectories within *in vivo* experiments have allowed the measure of scale free velocity correlations and the characterization of pairwise interactions [26–28]. In 2 dimensions, we find studies of fish trajectories in groups ranging from a few individuals in order to infer interaction rules [29, 30], to schools of few hundreds of animals that exhibit collective motion [31]. Swarms of midges, on the contrary, do not show any obvious collective behavior although interactions between insects play a crucial role. Indeed, Attanasi, Cavagna *el al.* have shown that these assemblies display strong correlations and even obey dynamic scaling laws, suggesting that they are driven close to a critical point [32–34].

At microscopic scales, it has been reported that dense colonies of certain bacteria self organize into large scale collective oscillatory motion [35], which is well reproduced by a simple model considering short range interactions. At lower densities and in quasi-2-dimensional geometry, elongated mutants of *Escherichia coli* show collective motion with long range correlations and strong density fluctuations [36]. For bacteria with lower aspect ratio, such as *Bacillus subtilis*, organization into swarming clusters [37] and chaotic phases [38, 39] are observed. One more topic related to biology is cell migration, which is involved in various phenomena such as morphogenesis, wound healing, or cancer development [40].

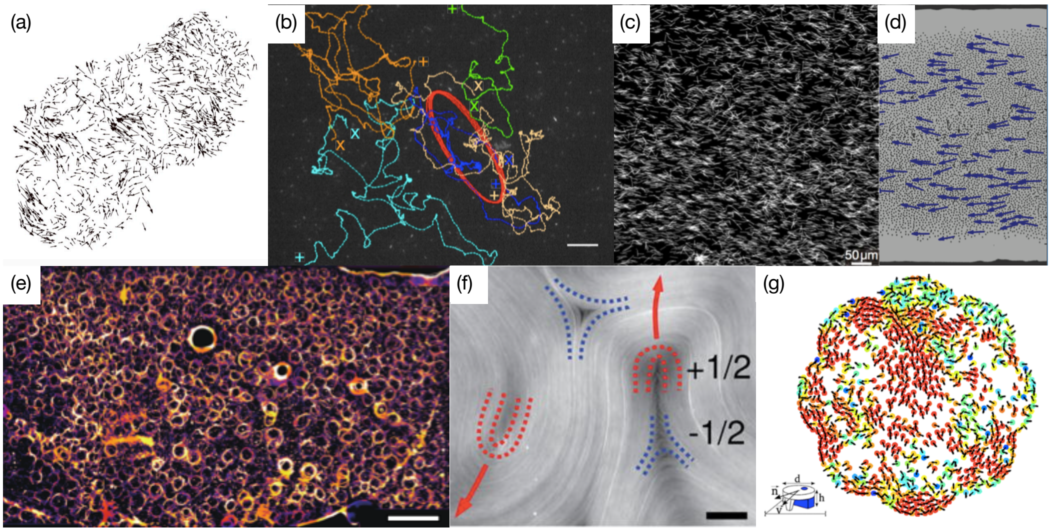

FIGURE 1.1 – Selection of active matter experiments. (a): Reconstruction of the 3 dimensional velocity field of a starling flock in [27]. (b): From [35], the red curve shows the trajectory of a passive tracer that highlights collective oscillation of bacteria. Other curves represent single bacteria trajectories, scale bar: 20μm. (c): *E. coli* mutants forming an ordered nematic phase, taken from [36]. (d): Self-propelled colloids from [44] organized into a flocking phase. (e): Vortex array of microtubules from [41], scale bar: 2mm. (f): Microtubules from [42] forming an active nematics phase with half integer charged topological defects, scale bar: 50μm. (g): Flocking dynamics of polar disks from [45].

Collective behavior also occurs at the sub-cellular scale. *In vitro* collections of 15μm long microtubules propelled by a carpet of molecular motors whose non motile head is attached to a substrate, known as motility assays, constitute interesting active matter examples. Indeed, the self organization of these filaments into millimeter large vortex structures, themselves organized in hexagonal arrays, was observed in these systems [41]. Experiments where the microtubules are confined between two fluid layers and propelled when bound together by the same molecular motor constitute a realization of the so called active nematics phase, in which topological defects exhibit genuine nonequilibrium behavior [42]. Another constituent of the cytoskeleton, the actin filaments, show patterns that possess a different symmetry. Namely, motility assays experiments have shown the emergence of polar waves and vortices [43].

Moreover, numerous man-made active matter systems have been designed, which often offer better experimental control. Although there exist realizations of swimmers in 3 dimensions [46], most of artificial systems evolve in 2 dimensions. The first example are spherical colloids whose hemispheres are covered with two different materials, plastic and platinum for instance. When immersed in hydrogen-peroxyde, chemical reactions occur only on one side and the particle self-propels [47–51]. In the same spirit, similar particles can also be put into moton because of thermophoresis when exposed to a laser beam [52], or from and electroosmotic flow induced by surface charges if in presence of an external electric field [53]. Other self propulsion mechanisms do not rely on asymmetry of particles such as the water droplets of [54, 55] that, in an oil and surfactant environment, spontaneously break the rotational symmetry and move thanks to Marangoni effect. Motile colloids studied by Bricard *et al.* self-propel because, when subject to a large enough electric field in the third direction, an instability mediated by the electric charge distribution on their surface occurs, resulting in a rotating motion [44, 56]. We note that an interesting property of this system is that, because of hydrodynamics, colloids interact in the form of velocity alignement and can thus move collectively. Collective motion are also observed in assemblies of elongated particles endowed with polar symmetry that are shaken vertically [45, 57, 58], contrary to symmetric rods [59] that nevertheless show genuine nonequilibrium behavior.

We see from this (non extensive) list of examples that active matter covers a wide range of scales with systems whose self-propulsion mechanisms are disparate. However most of them, despite their differences, exhibit similar collective properties due to the interplay of activity and interactions among agents, their description is thus routinely done with simple models.

1.2.2 Active matter from the physicist viewpoint: minimal models and universality

Even though minimal models of active matter do not seek quantitative agreement with experiments, they have been decisive for the deep understanding of active matter generic features. Indeed, in addition to the fact that they usually depend on a few independent control parameters, their simplicity makes them numerically efficient. Therefore, they allow for simulations of large systems in situations that are often subject to strong finite size effects, in addition to extensive studies of parameter spaces. Moreover, their simple dynamics can often be coarse-grained in field theories, building the link between microscopic dynamics and phenomenological equations.

All active particles are immersed in a fluid, which introduces long range hydrodynamic interactions between them. However, in many situations this effect is negligible. This is the case for instance in 2 dimensional systems where particles are in contact, and exchange momentum, with a substrate. More generally the fluid can be neglected, or taken into account effectively (friction forces), in any situation where the dynamics is dominated by local interactions. Models that follow this path, which are typically simpler, are referred as *dry*.

The simplest model of dry active matter consists of self-propelled particles which move at constant speed v_0 and experience angular noise. Denoting by $\vec{r}$ and θ the position and velocity orientation of one of these *Active Brownian Particle* (ABP), its 2 dimensional dynamics is thus governed by

$$\frac{d\vec{r}}{dt} = v_0 \hat{e}(\theta) \quad ; \quad \frac{d\theta}{dt} = \sqrt{2D_r}\xi(t)\,, \tag{1.1}$$

where $\hat{e}$ is a unit vector, ξ a Gaussian white noise with unit variance, and D_r the rotational diffusion coefficient. Most active particles are subject to a constant active force and thus experience and overdamped dynamics. Therefore, this model faithfully accounts for the dynamics of single animals like birds or fishes, non tumbling bacteria, or Janus colloids and shaken polar grains as in [45, 58]. Despite their minimalistic dynamics, ABPs that interact though for example, hard sphere repulsion, can form clusters in absence of attractive forces [60, 61] (see Figure 1.2(a)). This *Motility Induced Phase Separation* (MIPS), due to introduction of activity in the form of persistence in the individual motion, has no equivalent at equilibrium. On the theoretical side it can be explained by the fact that such particles move effectively slower in dense areas, and in return tend to accumulate in regions where their velocity is small, creating a positive feedback loop for clusterization. Moreover the MIPS phenomenology is common to any system whose constituents have a velocity that decreases with their density [62, 63]. The genericity of this behavior thus defines a universality class in which other models like run and tumbles and quorum sensing particles fall [64].

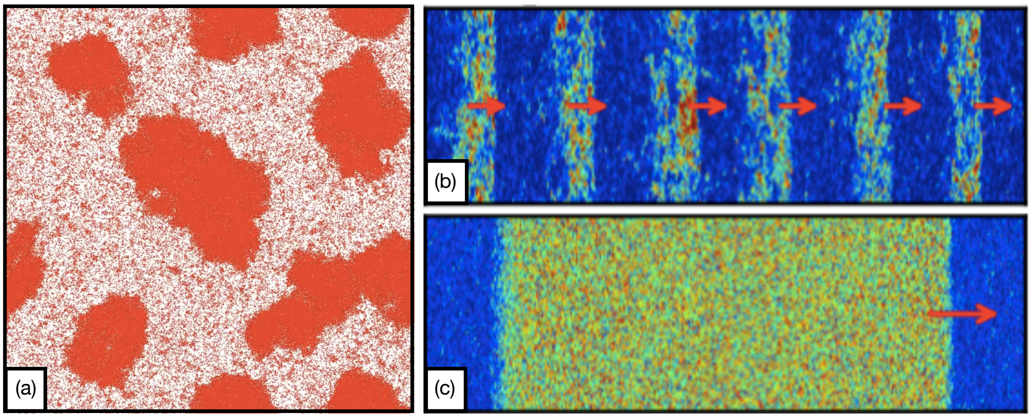

Figure 1.2 – Phase separation occurring in simple active matter models. (a): MIPS observed in a numerical simulation of ABPs with hard sphere potential, from [61]. (b) and (c): Snapshots of respectively Vicsek and Active Ising bands taken from [67]. Red arrows indicate the direction of the global magnetization.

The study of collective motion requires addition of other ingredients in the models. Indeed, in most of situations where agents move coherently, the global dynamics is dominated by their interactions [20]. In real systems these can take the form of "social forces" that encourage animals to move together, synchronization of bacterial motion due to exchange of chemicals or coupling with a fluid, or more simply hard core repulsion between elongated objects. All these effects can of course be taken into account explicitly in sophisticated models. However, it is simpler and often sufficient to come up with models where they appear *implicitly* through velocity alignment interactions.

One of such models considers particles whose velocities are modeled by ±1 Ising spins in 2 dimensions, hopping stochastically on a lattice [65, 66]. The dynamical rules are such that the transition rates from one site to another are biased (in the direction given by the spins, the other one being symmetric) according to the current spin orientation. In that situation the temperature T competes with spin-spin interactions: when T is large the system is globally disordered, however decreasing it leads to a spontaneous symmetry breaking and macroscopic alignment of the spins, which in turn generates collective motion. This *Active Ising Model* (AIM) therefore defines a universality class of collective motion with discrete symmetries.

In fact, natural systems possess a continuous symmetry of orientations, which imposes to study off-lattice models. This problem, namely the self-propelled version of the XY model, is addressed in the following Section.

1.3 Dry aligning active matter, the Vicsek model

1.3.1 The transition to collective motion

In their celebrated paper from 1995 [68], Vicsek and collaborators introduced what has probably become the most popular model for collective motion. This one consists of a simple discrete time dynamics in which N point-like particles, that move at constant speed v_0 in a periodic 2 dimensional domain, interact by local alignment of their directions of motion in presence of angular noise[1]. This is summarized in

---

[1] Vectorial version of the noise has also been studied [69, 70], but its precise form do not affect qualitatively the asymptotic properties of the model.

the following evolution equations for a particle i at a position $\vec{r}_i$, that points in the direction θ_i at time t,

$$\vec{r}_i^{\,t+1} = \vec{r}_i^{\,t} + v_0 \hat{e}\left(\theta_i^{t+1}\right) , \tag{1.2a}$$

$$\theta_i^{t+1} = \mathrm{Arg}\left[\left\langle \hat{e}\left(\theta_j^t\right)\right\rangle_i\right] + \eta \xi_i^t , \tag{1.2b}$$

where the ξ_i are independent white noises that draw random numbers uniformly distributed in $(-\pi;\pi]$ and η denotes the noise amplitude. The average over neighbors $\langle \ldots \rangle_i$ is taken in the disk of radius r_0 centered in $\vec{r}_i$ as sketched in Figure 1.3(a), and the function Arg returns the angle parametrizing the direction of this vector. A non metric version of the model is briefly discussed in Section 2.1.2. Rescaling space we set the radius of interaction to 1, the model is therefore defined by three control parameters: the average density of particles ρ_0, their velocity v_0, and the noise η. In practice, v_0 does not change qualitatively the results but only affects the size below which finite size effects occur [70], and can thus be fixed (usually to 0.5). Finally, the phase space of the Vicsek model is limited to two independent parameters: ρ_0 and η which reflect the competition between local alignment, strengthened at high densities, and noise.

The only conservation law for the Vicsek dynamics concerns the total number of particles. Therefore, since momentum is not conserved, the model does not satisfy Galilean invariance. We conclude that it has to be formulated in the reference frame where the momentum sink, *i.e.* the substrate on which particles move, is at rest.

Applying the Vicsek rules (1.2) at large noises and/or low densities results in a disordered phase characterized by exponentially decaying correlations and zero order parameter $M(t) = \frac{1}{N}\left|\sum_{i=1}^{N} \hat{e}(\theta_i)\right|$. Decreasing η (or equivalently increasing ρ_0), the model exhibits a nonequilibrium phase transition to a symmetry broken state with $M > 0$ because the agents globally move collectively in a given direction. In terms of self-propelled XY spins, this phase exhibits true long range polar order, something impossible at equilibrium because of spin wave excitations [71], anomalous fluctuations and superdiffusion [70, 72–74]. Giant density fluctuations can be identified by computing the number of particles in boxes of various sizes, in the flocking phase of the Vicsek model the variance of this number grows faster than its mean as shown in Figure 1.3(b). This has been reported in several experiments [36, 37, 45, 58, 59, 75], and constitute one of the typical feature of collective motion.

The transition to collective motion was initially believed to be continuous [68, 77]. However, both large scale molecular dynamics simulations [69, 70] and hydrodynamic theories derived from microscopic models [78–80] have shown that this was due to finite size effects. It is in fact discontinuous and well understood as a *phase separation scenario* with coexistence of dense ordered liquid patches and a disordered dilute gas. This phenomenology, characteristic of the Vicsek class, is due to the interplay between local density and order that destabilizes the homogeneous system close to the transition: aligned particles are harder to separate and denser regions are more ordered. The dense ordered structures are elongated and the order, such as their direction of propagation, are transversal to their axis. They are usually referred as *bands* and have a well defined size, leading to a typical smectic arrangement as shown in Figure 1.2(b), so called *microphase separation.* Note that contrary to equilibrium liquid-gas transition, the two phases at play possess different symmetries, which prevents the existence of a supercritical regime, the critical point is thus sent to infinite densities. The phase diagram of the Vicsek model therefore shows three distinct phases: disordered gas, ordered liquid and phase coexistence between the two (see Figure 1.3(c)).

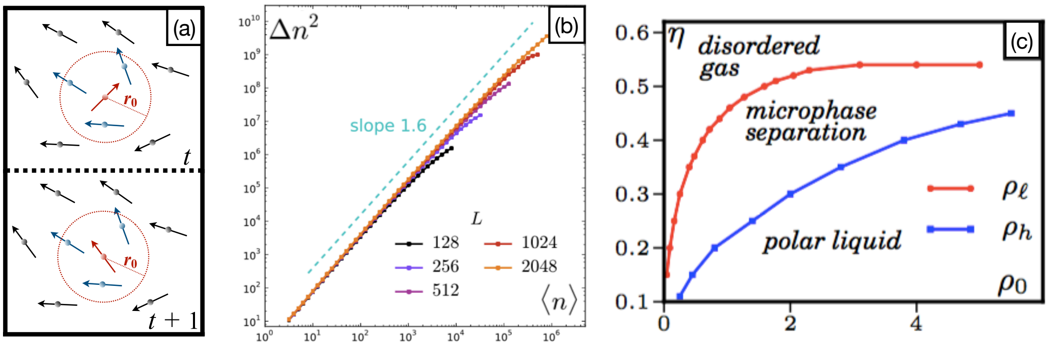

FIGURE 1.3 – (a): Illustration of the Vicsek-style alignment of the red particle's velocity with its neighbors (in blue) within the disk of radius r_0. (b): The variance of the number of particles in boxes of various sizes vs. its mean (see text) showing giant density fluctuations in the polar phase of the Vicsek model for different system sizes L, adapted from [76]. (c): Phase diagram of the Vicsek model in the particle density ρ_0 and noise amplitude η plane, taken from [67]. The lines are the binodals that mark the limit of stability of the coexistence phase.

The AIM introduced in Section 1.2.2, exhibits a similar phase diagram with three phases. However the nature of its coexistence phase is different than in the Vicsek model. In this case, bands do not have a characteristic width but adapt to the system size as shown in Figure 1.2(c) [65–67]. This case is referred as *macrophase separation* or simply phase separation.

Many real systems presented in Section 1.2.1 do not belong to the Vicsek class. In fact several universality classes for collective motion, defined from symmetries of the motion and interaction, have been explored both at microscopic and continuous levels [80–95], and will be presented in Section 2.1.1. Moreover, these minimal models have been extended in order to account for additional properties of dry active matter systems such as the presence of chirality [96–100], memory [101], asymmetric interactions [102–105], inertia [106–108], or static obstacles [23, 109–111].

1.3.2 Theoretical description of the flocking phase: the Toner Tu phenomenological approach

Hydrodynamic equations describing the Vicsek class were first written on the basis of symmetry arguments by Toner and Tu [72–74]. In that case the relevant hydrodynamic fields are the coarse grained density $\rho(\vec{r},t)$ and polarity $\vec{p}(\vec{r},t)$, which satisfy

$$\partial_t \rho + \vec{\nabla}\cdot\vec{p} = 0\,, \tag{1.3a}$$

$$\begin{aligned}\partial_t \vec{p} + \lambda_1 \left(\vec{p}\cdot\vec{\nabla}\right)\vec{p} + \lambda_2\left(\vec{\nabla}\cdot\vec{p}\right)\vec{p} + \lambda_3\vec{\nabla}\left(|\vec{p}|^2\right) = \\ \left(\alpha - \beta|\vec{p}|^2\right)\vec{p} - \vec{\nabla}P + D_{\mathrm{I}}\Delta\vec{p} + D_{\mathrm{A}}\vec{\nabla}\left(\vec{\nabla}\cdot\vec{p}\right) + \vec{f}\,,\end{aligned} \tag{1.3b}$$

and where *a priori* all the seven coefficients, plus the pressure, are arbitrary functions of the microscopic parameters, ρ and $|\vec{p}|$. Note that the space and time dependencies of the fields have been omitted in order to lighten the notations. The first equation describes the conservation of the total number of particles, which are advected by their polarity.

In Equation (1.3b), the polar order is advected by itself through the λ terms. If the system was invariant under Galilean transformations:

$$\vec{p} \to \vec{p} + \vec{p}_0 \quad ; \quad \vec{r} \to \vec{r} - \frac{\vec{p}_0}{\rho} t \,, \tag{1.4}$$

the coefficients λ_1 and λ_2 would have been equal to $\frac{1}{\rho}$ together with $\lambda_3 = 0$[2]. The first term on the r.h.s. of Equation (1.3b) is a Ginzburg-Landau potential that models the ordering of polarities. For low enough noise and/or large enough densities we expect α and β to be positive, then Equations (1.3) admit a homogeneous ordered solution

$$\rho = \rho_0 \quad ; \quad \vec{p} = \vec{p}_0 = \sqrt{\frac{\alpha}{\beta}} \hat{e} \,, \tag{1.5}$$

with $\hat{e}$ an arbitrary unit vector. The next term on the r.h.s. is the pressure, that Toner and Tu expressed in terms of an expansion around the average density $P = \sum_n \sigma_n (\rho - \rho_0)^n$ with coefficients $\{\sigma_i\}$. Finally, the system shows both isotropic (D_I) and anisotropic (D_A) spatial diffusion and $\vec{f}$ is an additive Gaussian white noise.

Hydrodynamic Equations (1.3) are the starting point of Toner and Tu “quantitative theory of flocking” in which, using Dynamical Renormalization Group techniques, they characterized the fluctuations of the fields around the solution (1.5). We give a short summary of their results, whose discussion is the subject of Chapter 3.

In [73], Toner and Tu compute an algebraic expression for the velocity and density two-point equal time correlation functions. Since the Vicsek model shows long range order even in two dimensions, for any $d < 4$ the corresponding scaling exponents are different along, and in any direction perpendicular to the order. The algebraic decay of correlations is therefore characterized by two exponents. The roughness exponent, χ, measures how velocity fluctuations decay with system size in the direction(s) orthogonal to the global order. The anisotropy of the scaling is then characterized by the exponent ξ. Note that, even in $d = 2$, χ is negative so that the system shows long range order.

Another important result is the presence of propagating sound modes whose speed depends on the direction w.r.t. the global order. Moreover, for a given direction there are two modes propagating at two different speeds which is shown to be related to the non conservation of momentum. The dynamical exponent z characterizes the damping of the modes, which is also anisotropic.

Toner and Tu firstly claimed an exact computation of the exponents χ, ξ and z in $d = 2$ because of a special symmetry present only in this dimension. However, in a more recent publication [112] Toner argued that possibly relevant terms had not been taken into account previously, and that they could invalidate this statement. Although there is no apparent reason that the exact values of the exponents are the ones computed in [73], their qualitative predictions, namely the true polar order in 2 dimensions, the presence of propagative sound modes and the anomalous fluctuations, remain valid.

Even though the Toner Tu theory succeeds in reproducing the large-scale long time behavior of the flocking phase, it lacks from connexions with microscopic models. As we already mentioned most of the terms in Equations (1.3) have coefficients whose dependencies on the physical fields and particle-level parameters are unknown. Such information may be precious, for instance, to account for the nature of the transition.

---

[2] The formulation is different than in the original papers from Toner and Tu [72, 73] because we wrote equations for the polarization and not velocity fields: $\vec{p} = \rho \vec{v}$.

Indeed, in Section 1.3.1 it was argued that the formation of polar bands is due to the fact that polarity grows with density *locally.* We thus expect the linear coefficient α to depend explicitly on the density field. Moreover Toner and Tu considered an additive noise $\vec{f}$. In fact, as for reaction diffusion processes [113, 114], there must be no fluctuations in regions deprived of particles, therefore the noise has to be multiplicative. We see here that the nature of the noise in coarse-grained Langevin theories relates to relevant physical mechanisms, this point happens to be crucial in nonequilibrium systems showing absorbing states [115]. Although it is not clear whether the precise form of noise correlations affects the long time and large distance behavior of the Toner Tu equations, it may be important if one wants to reach a more quantitative description.

More generally, such equations written on symmetry arguments, or from equilibrium theories adding “active contributions” [116], often possess a large number of free parameters, which makes extensive studies of phase diagrams difficult, if not impossible. One would therefore know the dependencies of the coefficients of these equations as function of the, typically small number of, microscopic parameters in the models. In the next section, we review the different approaches that can be employed to derive continuous theories, such as the Toner Tu hydrodynamic equations, by coarse graining Vicsek-like microscopic models. The different equations, their behavior, and their coefficients as well as their dependencies as function of the particle-level parameters, are discussed.

1.4 Hydrodynamic description of active matter models: derivation from microscopic dynamics

1.4.1 The Boltzmann-Ginzburg-Landau approach

The Boltzmann equation

The first approach we consider is the one proposed by Bertin *et al.* in [78, 79], that we detail because it will be regularly used throughout this manuscript. Its starting point is to write a Boltzmann equation describing the evolution of the single-particle distribution $f(\vec{r},\theta,t)$ that measures the probability of being at a position $\vec{r}$ with an orientation θ at time t. One way to achieve that is to coarse grain a model which belongs to the Vicsek class, but showing a slightly different dynamics. Indeed, a convenient way to model stochastic interactions is to consider particles moving ballistically at constant speed v_0 and experiencing random tumblings with a rate λ. The equation for $f(\vec{r},\theta,t)$ thus reads

$$\partial_t f(\vec{r},\theta,t) + v_0\hat{e}(\theta)\cdot\vec{\nabla} f(\vec{r},\theta,t) = I_{\rm sd}[f] + I_{\rm coll}[f]\,, \tag{1.6}$$

where the integrals of the r.h.s. model tumbling, or “angular self-diffusion” events

$$I_{\rm sd}[f] = -\lambda f(\vec{r},\theta,t) + \lambda\int_0^{2\pi} d\theta' f(\vec{r},\theta',t)P_\eta(\theta-\theta')\,, \tag{1.7a}$$

with P_η the noise distribution of variance η^2, and collisions

$$\begin{aligned} I_{\rm coll}[f] \;=\; & -f(\vec{r},\theta,t)\int_0^{2\pi} d\theta' K(\theta'-\theta)f(\vec{r},\theta',t) + \qquad (1.7b)\\ & + \int_0^{2\pi} d\theta_1 \int_0^{2\pi} d\theta_2 f(\vec{r},\theta_1,t)f(\vec{r},\theta_2,t)K(\theta_2-\theta_1)P_\eta(\theta-\theta_1-H(\theta_2-\theta_1))\,. \end{aligned}$$

In the last equation $K(\theta) = 4r_0v_0 \left|\sin\left(\frac{\theta}{2}\right)\right|$, with r_0 the interaction radius, measures the frequency of collisions and $H(\theta) = \frac{\theta}{2}$ denotes the post-collisionnal alignment rule[3]. Collisions are assumed to be punctual because the model considers particles with no spatial extension.

The Boltzmann equation is therefore written under two assumptions [117]. The first one is that the collisions are essentially binary, meaning that the equation should hold in the dilute limit: $r_0 \ll \frac{1}{\sqrt{\rho_0}}$ where ρ_0 is the average density of particles. Secondly, we used the molecular chaos hypothesis in order to express the two-particle distribution as the product of two single-particle distributions. Physically, it is assumed that the states of a pair of particles are uncorrelated prior to collision, which corresponds to the case where the typical flight distance $v_0\lambda^{-1}$ is much larger than the collision radius r_0. This approximations have been discussed in the context of active systems [118, 119]. Indeed the Boltzmann approach supposes that the timescale of a collision is much smaller than any other timescale of the dynamics. Because of the aligning nature of the interactions, this is probably not verified in most systems, and regular interactions between more than two particles should be likely. However, as we discuss in Section 1.4.3, considering more than two-body collisions leads to a much more complicated framework that is not necessary in order to achieve qualitative agreement with microscopic models.

In the following we will consider a nondimensional version of (1.6), obtained by rescaling time, space, the kernel of interaction K, and f as

$$t \to \lambda^{-1}t \quad ; \quad \vec{r} \to v_0\lambda^{-1}\vec{r} \quad ; \quad K \to 2r_0v_0K \quad ; \quad f \to \rho_0 f\,. \tag{1.8}$$

Then the equation depends on only two parameters that are the noise variance η^2 and the nondimensional density $\tilde{\rho}_0 = 2r_0v_0\lambda^{-1}\rho_0$.

Since θ is a 2π-periodic variable, the next step of the procedure is to expand the distribution f in terms of angular Fourier modes:

$$f(\vec{r},\theta,t) = \frac{1}{2\pi}\sum_{k=-\infty}^{\infty} \hat{f}_k(\vec{r},t)e^{-\imath k\theta}\,, \tag{1.9}$$

where, because of the reality of the distribution, the complex modes satisfy $\hat{f}_{-k}(\vec{r},t) = \hat{f}_k^*(\vec{r},t)$. The resulting Boltzmann hierarchy reads

$$\partial_t\hat{f}_k + \frac{1}{2}\left(\nabla^*\hat{f}_{k+1} + \nabla\hat{f}_{k-1}\right) = \left(\hat{P}_k - 1\right)\hat{f}_k + \sum_{q=-\infty}^{\infty} J_{k,q}\hat{f}_q\hat{f}_{k-q}\,, \tag{1.10}$$

where $\hat{P}_k$ is the k^{th} mode of the distribution P_η, the complex gradient $\nabla = \partial_x + \imath\partial_y$ and the $J_{k,q} = \tilde{\rho}_0\left(\hat{P}_kI_{k,q} - I_{0,q}\right)$ with

$$I_{k,q} = \left\{\begin{array}{cc} \frac{4}{\pi}\frac{1-(k-2q)(-1)^q\sin\left(\frac{k\pi}{2}\right)}{1-(k-2q)^2} & \text{if } |k-2q| \neq 1 \\ \frac{2}{\pi} & \text{otherwise} \end{array}\right. . \tag{1.11}$$

Here the space and time dependencies of the modes have been omitted in order to lighten the notations, for the same reason we drop hats and tildes in the following.

---

[3] The noise distributions in (1.7a) and (1.7b) have been assumed to be the same for simplicity. In general one could consider two different distributions.

Truncation and closure

The first angular modes of the distribution correspond to the complex representation of the density ρ, polarity $\vec{p}$ and nematic $\mathbf{Q}$ fields[4]:

$$\begin{aligned} f_0 &= \int_0^{2\pi} d\theta f(\theta) = \rho\,, && (1.12a)\\ f_1 &= \int_0^{2\pi} d\theta f(\theta) e^{\imath\theta} = p_x + \imath p_y\,, && (1.12b)\\ f_2 &= \int_0^{2\pi} d\theta f(\theta) e^{2\imath\theta} = 2\left(Q_{xx} + \imath Q_{xy}\right)\,. && (1.12c)\end{aligned}$$

In this model with polar symmetry, we expect all the modes with $k > 1$ to have a fast dynamics. Formally, the linear stability of the disordered state, $\rho = 1$ and $f_k = 0\ \forall k > 0$, to homogeneous perturbations is ruled by the linear coefficients $\mu_k = P_k - 1 + (J_{k,0} + J_{k,k})$. Moreover it has been shown [80] that, except for μ_1, these coefficients are all negative for any value of ρ_0 and η, which indicates that the higher modes are slaved to f_1.

When the disordered solution becomes unstable, *i.e.* when μ_1 becomes positive, we assume that $|f_1| \approx \varepsilon$ with $\varepsilon \ll 1$ that measures the distance from the transition. Then the only possible scaling allowed by the hierarchy (1.10) is given by $|\rho - 1| \approx \varepsilon$ and $|f_k| \approx \varepsilon^k$ for $k > 0$. In order to take into account the spatial and temporal variations of the fields, we need to assign a scaling to the ∂_t and ∇ operators. Since the dynamics of particles is propagative, the two scale the same way, therefore and in a Ginzburg-Landau spirit we set $\partial_t \approx \nabla \approx \varepsilon$.

The Boltzmann-Ginzburg-Landau hydrodynamic equations

Truncating (1.10) at the first non trivial order ε^3, we get equations for ρ, f_1 and f_2. Comparing the terms in f_2 equation, $\partial_t f_2$ can be set to 0 so that it is slaved to the density and polar fields and we recover the Toner Tu equations (1.3), here expressed in complex notations:

$$\partial_t \rho + \Re\left(\nabla^* f_1\right) = 0\,, \qquad (1.13a)$$

$$\partial_t f_1 = -\frac{1}{2}\nabla\rho + \left(\mu_1[\rho] - \xi |f_1|^2\right) f_1 + \nu\Delta f_1 - \kappa_1 f_1 \nabla^* f_1 - \kappa_2 f_1^* \nabla f_1\,, \qquad (1.13b)$$

where the Laplacian $\Delta = \nabla\nabla^*$ and all coefficients expressions as functions of the density and the moments of the distribution P_η, in addition to their correspondence with Equations (1.3) are given in Table 1.1.

We first comment on the coefficients of Equations (1.13): the linear coefficient, $\mu_1[\rho]$, depends explicitly on the density as indicated by the brackets. Moreover they admit positive cubic (ξ) and diffusion (ν) coefficients, and are thus expected to be well behaved. We also note that, using Toner and Tu notations, $\lambda_3 = -\frac{\lambda_2}{2}$ which means that Equations (1.13) can be formally derived from a free energy[5] [21]. The pressure is simply linear in density which corresponds to keeping only the first term in the expansion from Toner and Tu, and although authorized by symmetries, there is no anisotropic diffusion. Finally, this approach provides deterministic equations and thus there is no noise term to compare with the one in (1.3). Noise terms could

---

[4] The reference frame has been chosen so that the x direction in tensorial representation corresponds to the real axis in complex notations.

[5] This would of course reintroduce phenomenological parameters in the equations.

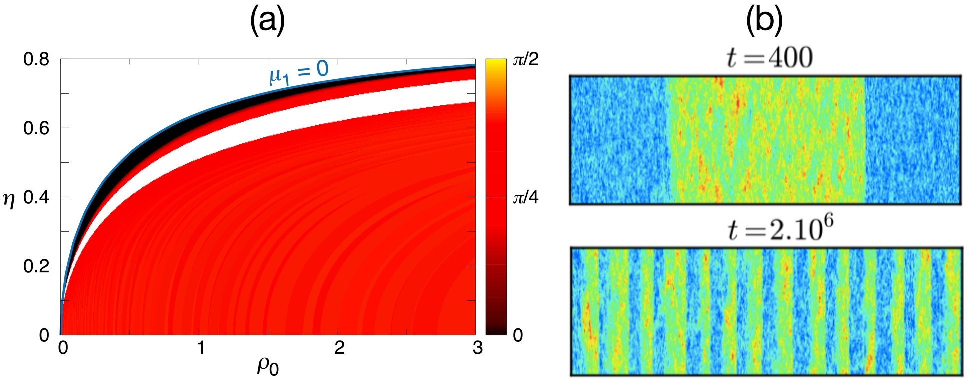

FIGURE 1.4 – (a): Linear stability of the homogeneous ordered solution of the hydrodynamic equations (1.13) derived from the Boltzmann-Ginzburg-Landau approach in the density noise plane (a gaussian noise distribution $P_k = \exp(-k^2\eta^2/2)$ was assumed). The blue line marks the linear stability limit of the disordered solution and the color code indicates the direction of the most unstable wave vector w.r.t. the order (white means that the solution is stable). From top to bottom we thus see the band region, a domain with stable homogeneous order and the spurious instability (see text). (b): Simulation of a stochastic hydrodynamic equation for the Vicsek class with noise on the polar field from [67]. The large band, stable at the *deterministic* level, becomes unstable at the *fluctuating* level and the microscopic picture is recovered (see Figure 1.2(b)).

nevertheless be computed from the Boltzmann equation using perturbative techniques developed in [120].

Equations (1.13) show an homogeneous ordered solution for $\mu_1 > 0$: $\rho = 1$, $|f_1|^2 = \frac{\mu_1}{\xi}$. A linear stability analysis of this solution reveals an instability, whose most unstable wave vector $\vec{q}$ is longitudinal to the global order, close to the transition [79] (see Figure 1.4(a)). A computation in the limit of small $|\vec{q}|$ reveals that this instability is in fact triggered by the explicit density dependence of μ_1, and thus could not be seen by Toner and Tu. Deeper in the ordered phase another instability, no more longitudinal to the order, develops [80]. This one is not observed in microscopic simulations, moreover its spatial extension reduces adding positional diffusion by hand. As we will see in Chapter 3, this instability results from the truncation procedure, whose validity is ensured only close to the transition, and is considered as *spurious* because it is not present at the kinetic level.

At the nonlinear level the longitudinal instability close to the transition leads to the formation of the bands observed in microscopic simulations of the Vicsek model. However Caussin, Solon *et al.* have shown that, at a given phase space point, the band solutions of (1.13) are not unique [121, 122]. In particular the deterministic hydrodynamic level does not make any selection between the phase and microphase separation scenarios that take place respectively in the Active Ising and Vicsek models. This selection nevertheless occurs adding a noise term[6] in Equations (1.13), so that the correct scenario is recovered at the fluctuating level [67] (see Figure 1.4(b)).

As a conclusion to this section, the Boltzmann-Ginzburg-Landau approach provides a systematic procedure to derive well behaved hydrodynamic equations from a Vicsek-like microscopic model. It therefore allows to study the phase diagram of the model at the continuous level. Despite the differences that occur in the deep ordered region and that are due to the truncation procedure, good agreement with molecular

---

[6] Additive or multiplicative.

Toner Tu	Boltzmann	Smoluchowski
α	$\mu_1[\rho] = P_1 - 1 + \frac{4}{\pi}\left(P_1 - \frac{2}{3}\right)\rho_0\rho$	$\mu_1^{\mathrm{S}}[\rho] = \rho\rho_c - 1$
β	$\xi = \frac{16}{\pi}\frac{(5P_1-2)(3P_2+1)\rho_0^2}{15\pi(1-P_2)+8(7+5P_2)\rho_0}\ (>0)$	$\xi^{\mathrm{S}} = \frac{\rho_c^2}{2}$
$P = \sum_n \sigma_n(\rho-\rho_0)^n$	$\frac{1}{2}\rho$	$\frac{1}{2}\rho$
D_{I}	$\nu = \frac{15\pi}{4(15\pi(1-P_2)+8(7+5P_2)\rho_0)}\ (>0)$	$\nu^{\mathrm{S}} = \frac{1}{16}$
D_{A}	0	0
λ_1	$\kappa_1 + \kappa_2 = \frac{2(16+30P_2-15P_1)\rho_0}{15\pi(1-P_2)+8(7+5P_2)\rho_0}$	$\kappa_1^{\mathrm{S}} + \kappa_2^{\mathrm{S}} = \frac{3\rho_c}{8}$
λ_2	$\kappa_1 - \kappa_2 = \frac{2(4+30P_2+15P_1)\rho_0}{15\pi(1-P_2)+8(7+5P_2)\rho_0}$	$\kappa_1^{\mathrm{S}} - \kappa_2^{\mathrm{S}} = \frac{5\rho_c}{8}$
λ_3	$-\frac{\lambda_2}{2}$	$-\frac{\lambda_2}{2}$
$\langle f_i(\vec{r},t)f_j(\vec{r}\,',t')\rangle =$ $\Delta\delta_{ij}\delta(\vec{r}-\vec{r}\,')\delta(t-t')$ (additive)	Deterministic equations	$\langle\, \Xi_i(\vec{r},t)\Xi_j(\vec{r}\,',t')\rangle =$ $\left(\rho\delta_{ij} + \left[\frac{1}{4}\nabla_i p_j - \rho_c p_i p_j\right]_{\mathrm{ST}}\right)$ $\times\delta(\vec{r}-\vec{r}\,')\delta(t-t')$

Table 1.1 – Correspondence between the coefficients of the hydrodynamic equations for the Vicsek class written by Toner and Tu (1.3) and the ones derived from the Boltzmann (1.13) and Smoluchowski (1.17) equations. $[Q_{ij}]_{\mathrm{ST}}$ gives the ij component of the symmetric traceless part of the tensor $\mathbf{Q}$.

dynamics simulations is found and the correct qualitative phase diagram is recovered. This approach has also been generalized to other active matter models with different symmetries [80, 89–91], showing similar success. We therefore apply it in Chapter 2 to derive hydrodynamic equations for a new class of dry active matter and its formalism in 3 dimensions is developed in Chapter 5. A detailed study of the Boltzmann equation itself is done in Chapter 3.

1.4.2 The Smoluchowski approach

Another approach to derive the Toner Tu equations consists to start from a Smoluchowski equation. This one can be derived from an explicit rod model as in [84, 86, 123] assuming binary collisions, or as the equation governing the evolution of the marginal distribution from a Fokker-Planck equation [124–128]. Equations presented in these references globally show additional terms than (1.13) because of the presence of volume exclusion, different interactions, or because a higher truncation order was chosen. In [124, 128], the derivation is based on a Maxwellian approximation for the single-particle distribution. The resulting "Self-Organized Hydrodynamic" equations are unfortunately not able to account for any phase transition in the overdamped limit. However, it is shown below that applying the truncation and closure schemes introduced earlier leads to hydrodynamic equations which are formally the same as (1.3) and (1.13).

Another derivation of the Smoluchowski equation can be done from the approach proposed by Dean in [129] and that was used in [130] to derive hydrodynamic equations from a continuous-time version of the Vicsek model. Considering a particle i at position $\vec{r}_i$ with a velocity along θ_i at time t, the corresponding Langevin equations read

$$\frac{d\vec{r}_i}{dt} = v_0\hat{e}(\theta_i) \quad ; \quad \frac{d\theta_i}{dt} = \frac{\gamma}{\pi r_0^2}\sum_j \sin(\theta_j - \theta_i) + \sqrt{2D_r}\xi(t)\,, \tag{1.14}$$

where we have noted v_0 the speed of particles, γ the strength of the interaction and D_r the angular diffusion coefficient. The interaction is computed over all neighbors inside a disk of radius r_0 and ξ is a Gaussian white noise with unit variance. From these equations and denoting by $f(\vec{r},\theta,t) = \sum_i \delta(\vec{r}-\vec{r}_i(t))\delta(\theta-\theta_i(t))$ the density of particles, the Dean approach allows to derive a stochastic version of the Smoluchowski equation

$$\begin{aligned} \partial_t f(\vec{r},\theta,t) + v_0\hat{e}(\theta)\cdot\vec{\nabla} f(\vec{r},\theta,t) &= D_r\partial^2_{\theta\theta} f(\vec{r},\theta,t) - \partial_\theta\left(\sqrt{2D_r f(\vec{r},\theta,t)}\tilde{\xi}\right) \\ &\quad -\gamma\partial_\theta\left[f(\vec{r},\theta,t)\int_0^{2\pi} d\theta' f(\vec{r},\theta',t)\sin(\theta'-\theta)\right]. \end{aligned} \tag{1.15}$$

The l.h.s. of this equation is the same as in the Boltzmann (1.6) case, *i.e.* usual advection at constant speed v_0. On the contrary, since we have considered angular diffusion and not tumblings, the "self-diffusion" term in the r.h.s. is different. Because the derivation relies on the expression of f in terms of Dirac distribution, this procedure gives an exact mean field form of the interaction. We note however that this approximation is verified only in the high density regime, since in practice we are looking for smooth solutions of the equation. Finally, the Dean approach is particularly interesting because it allows for the derivation of noise terms at the kinetic level. Here $\tilde{\xi}$ is a Gaussian white noise such that the variance of the total noise in the equation scales like $2D_r\partial^2_{\theta\theta} f(\vec{r},\theta,t)$, the latter therefore being multiplicative. As in the Boltzmann case, Equation (1.15) can be de-dimensionalized using

$$t \to D_r^{-1} t \quad ; \quad \vec{r} \to v_0 D_r^{-1}\vec{r} \quad ; \quad f \to \rho_0 f \quad ; \quad \tilde{\xi} \to (D_r\rho_0)^{\frac{1}{2}}\tilde{\xi}\,, \tag{1.16}$$

so that it depends on a single nondimensional parameter: $\Gamma = \gamma\rho_0 D_r^{-1}$ (we note $\rho_c = \frac{\Gamma}{2}$ in the following)[7].

We can now apply the procedure detailed in Section 1.4.1 in order to derive hydrodynamic equations. However, the treatment of the noise term in (1.15) requires some care. Indeed, since all the angular Fourier modes are stochastic processes we cannot set $\partial_t f_2$ to zero for the closure, but need to consider a more sophisticated procedure [131, 132]. In fact, following the scaling approximation of Section 1.4.1, timescales associated to the evolution of f_2 scale like the ones related to the polar field f_1 times a factor ε. Therefore f_2 is ergodic on timescales where f_1 is almost constant and we can safely consider the equation for f_1 averaged over the stationary distribution of f_2. After some algebra, this results in the following hydrodynamic equations

$$\partial_t\rho + \Re\left(\nabla^* f_1\right) = 0\,, \tag{1.17a}$$

$$\partial_t f_1 = -\frac{1}{2}\nabla\rho + \left(\mu_1^{\mathrm{S}}[\rho] - \xi^{\mathrm{S}}|f_1|^2\right) f_1 + \nu^{\mathrm{S}}\Delta f_1 - \kappa_1^{\mathrm{S}} f_1\nabla^* f_1 - \kappa_2^{\mathrm{S}} f_1^*\nabla f_1 + \Xi\,, \tag{1.17b}$$

$$\text{with}\left\{\begin{array}{c} \langle\,\Xi(\vec{r},t)\Xi^*(\vec{r}\,',t')\rangle = 2\rho\delta(\vec{r}-\vec{r}\,')\delta(t-t') \\ \langle\,\Xi(\vec{r},t)\Xi(\vec{r}\,',t')\rangle = \left(\frac{1}{4}\nabla f_1 - \rho_c f_1^2\right)\delta(\vec{r}-\vec{r}\,')\delta(t-t') \end{array}\right.\,, \tag{1.17c}$$

---

[7] Contrary to the Boltzmann case in Section 1.4.1, there is just one independent parameter because rotational diffusion has been considered instead of tumblings.

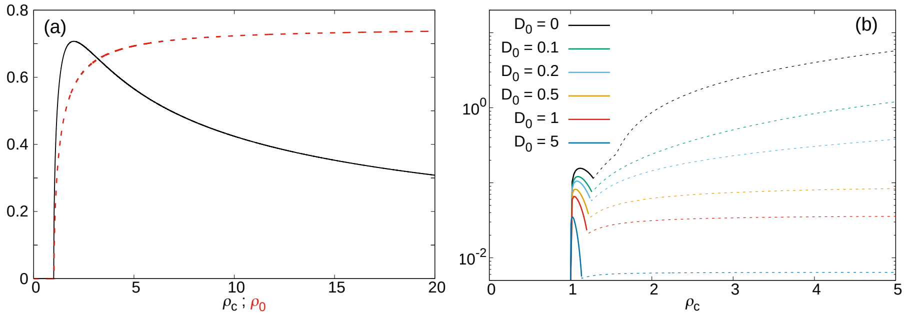

FIGURE 1.5 – (a) Homogeneous ordered solution of the Smoluchowski (full black) and Boltzmann (dashed red) hydrodynamic equations vs. respectively ρ_c and ρ_0. While the solution corresponding to the Boltzmann case is monotonous and saturates at a finite value, the one corresponding to Smoluchowski shows a maximum and tends to 0 when $\rho_c \to \infty$. The Boltzmann curve has been evaluated at constant noise $\eta = 0.645$ using a Gaussian distribution $P_k = \exp(-k^2\eta^2/2)$. (b): Growth rate of the linear instability of the homogeneous ordered solution of the deterministic version of Equations (1.17). With and without additional spatial diffusion (in the form $D_0 \Delta f$ in (1.15)), the solution is unstable in all its existence domain. When the lines are continuous, the instability is longitudinal to the order, it is purely transversal deeper in the ordered phase only in the large D_0 limit.

where all the coefficients are given in Table 1.1 so as their expression as function of ρ_c. Because the interaction is mean field, they are typically simpler than in the Boltzmann case. We note that Equations (1.17) share similarities with (1.13): the linear coefficient depends explicitly on density, the cubic and diffusion coefficients are positive, the pressure is linear in ρ, there is no anisotropic spatial diffusion, and the relation $\lambda_3 = -\frac{\lambda_2}{2}$ still holds. However a Gaussian white noise term, whose variance is linear in ρ and depends non trivially on the order, was derived in the polar field equation. To our knowledge, all the studies until now have focused on the deterministic part of the equations, so that an extensive study of the stochastic hydrodynamic theory for the Vicsek model is still missing. More generally, the effect of the precise form of the noise on the solutions of these equations is completely unexplored.

Restricting ourselves to the deterministic equations, their homogeneous solution for $\rho_c \geq 1$ is given by $\rho = 1$ and $|f_1|^2 = 2\frac{\rho_c - 1}{\rho_c^2}$. We first note that, contrary to solutions of Equations (1.13), the order is not monotonous with ρ_c, and even vanish like $\frac{1}{\sqrt{\rho_c}}$ in the high density limit as shown in Figure 1.5(a). Moreover, a linear stability analysis of this solution shows that it is always unstable, contrary to the Boltzmann case which exhibits an intermediate region of stability (see Figure 1.4(a)). The instability is longitudinal to the order close to the transition, then rotates and gets a transversal component. Contrary to the Boltzmann equation, adding spatial diffusion does not suppress the instability at large ρ_c, even at large values of the diffusion coefficient as shown in Figure 1.5(b).

To conclude this section, hydrodynamic equations derived from the Boltzmann approach at this point are more successful at reproducing the Vicsek phase diagram than the ones obtained from the Smoluchowski equation (1.15), even in dense systems where the later is supposed to be a better description. A comparison of these approaches at the kinetic level is proposed in Chapter 3.

1.4.3 Other approaches

The Ihle approach

In [133, 134] Ihle proposed a direct coarse graining of the discrete time Visek model (1.2). Contrary to the Boltzmann case, this approach considers multi-body interactions and thus, does not assume a dilute system. The kinetic equation is then obtained from the molecular chaos hypothesis that allows the factorization of the N-particle distribution. This one is used for the derivation of a hydrodynamic description of the Vicsek model by mean of a Chapman-Enskog expansion. Because the truncation procedure is different, the resulting equations for the density and polar fields show additional terms than (1.13), using notations of Section 1.4.1, they are of order up to ε^6. While they succeed at reproducing the generic linear instability of the ordered solution close to the threshold, Ihle's hydrodynamic equations are not well behaved and cannot account for the solitary wave solutions.

Simulations of his kinetic equation are typically difficult because they rely on collisional integrals that are not local neither analytic. Practically, additional assumptions are necessary such as restricting the dynamics to two-body collisions. This was done in [135] where Ihle simulated his kinetic equation truncated at the 5^{th} Fourier mode. In a quasi-one dimensional geometry, he was able to reproduce the usual band solutions, although no discussion about selection is proposed.

The Langevin formulation

In [90], Bertin *et al.* show how to derive stochastic hydrodynamic equations by direct coarse graining of a Vicsek-like microscopic model. The Langevin equations are build by defining fluctuating coarse grained density and order fields. However, as opposed to the Dean approach the authors did consider smooth distributions. Because of this, there were able to treat only the collisionless dynamics, dealing with interactions separately using the Boltmann-Ginzburg-Landau formalism. This approach thus provides stochastic equations that show, as expected, multiplicative noise terms. Its limitations mostly lie in the fact that it does not consider fluctuations due to collisions, which are taken into account effectively at the cost of an unknown rescaling phenomenological constant. As we mentioned in Section 1.4.2, extensive studies of Langevin formulations of active matter are still missing and we cannot comment on any result.

Active matter on lattice, exact equations

We finally mention a work that focusses on active matter models on lattices and allows for a derivation of *exact* hydrodynamic equations [136]. The authors study two of these models, respectively in the MIPS and Active Ising universality classes. The principle of their derivation relies on a clever choice of the microscopic transition rates such that diffusion dominates locally, while all process of the dynamics are equivalent macroscopically. This in fact allows to safely neglect two points correlations in the asymptotic limit and leads to exact equations. Although it surely constitutes a powerful tool for the study of active matter systems, which as we mentioned earlier are typically subject to strong finite size effects, this procedure is probably impossible to apply to models with continuous symmetries.

1.5 Organization of the manuscript

This thesis is divided into four main themes.

Chapter 2 first presents the different universality classes of dry active matter, defined from symmetries of the motion and interaction. It then introduces a Vicsek-style model defining a new class, whose phenomenology is characterized by means of both numerical and analytical studies. It is based on a work that is now published [137].

Chapter 3 is devoted to the study of the Boltzmann and Smoluchowski kinetic theories introduced in Sections 1.4.1 and 1.4.2. We discuss the linear stability of the homogeneous ordered solution of these equations and characterize the phase diagram. A discussion about the selection of band solutions at the kinetic level is given.

In Chapter 4 we quantitatively assess the Toner Tu theory, briefly introduced in Section 1.3.2, by mean of large scale molecular dynamics simulations of the Vicsek model. We show measurements of the critical exponents of the flocking phase in 2 and 3 dimensions, and compare them to the Toner Tu theory [72, 73].

Chapter 5 is the reproduction of an article submitted to the *Journal of Statistical Mechanics: Theory and Experiment* that establishes the formalism to apply the Boltzmann-Ginzburg-Landau approach, presented in Section 1.4.1, to three dimensions. 3 dimensional hydrodynamic equations are derived for several classes of active systems and compared to the 2 dimensional case. Solutions of these equations are computed and their linear stability is discussed.

Chapter 2

Active matter class with second-order transition to quasi-long-range polar order

2.1 Classification of dry aligning active matter models

2.1.1 The Vicsek universality classes, a common phase separation scenario

The Vicsek model introducted in Section 1.3.1 constitutes a minimal description of self-propelled particles that align their velocities with a polar symmetry. However, in many situations, the active units do not have distinct head and tail and the symmetries of their walk and/or interaction can be different. For instance, the shaken rods in [59] do not move ballistically but exhibit an apolar walk which is diffusive on large scales, and interact via volume exclusion forces that equate to a nematic alignment. This system therefore possess a full nematic symmetry. On the contrary, while the bacteria of [36], the microtubules in [41, 42], or the rods of [57] show similar alignment, they move persistently and thus form systems with mixed symmetries. To account for this diversity, different active matter universality classes can be built as function of the symmetries of the particles free motion and alignment.

The three classes of dry active matter studied so far all possess a Vicsek-style representative. Polar particles with ferromagnetic alignment have been addressed in Section 1.3.1 and are described by the original Vicsek model. Such particles interacting nematically, *i.e.* which anti-align if their pre-collisional directions form an obtuse angle, are known as self propelled rods [87]. On the contrary, if such particles reverse their velocities at some rate, their free motion has an apolar symmetry and they define the active nematics class [82].

Similarly to the original polar case, these additional classes have been studied intensively both numerically [82, 85, 87, 91, 94] and at the continuous level [80, 81, 84, 86, 88–90, 95, 123]. The Vicsek-style dynamics for such particles moving at constant speed v_0 reads

$$\begin{aligned}
\vec{r}_i^{\,t+1} &= \vec{r}_i^{\,t} + v_0 \hat{e}\left(\theta_i^{t+1}\right) \,, && \text{(2.1a)}\\
\theta_i^{t+1} &= \mathrm{Arg}\left[\left\langle \mathrm{sgn}\left(\hat{e}\left(\theta_i^t\right)\cdot\hat{e}\left(\theta_j^t\right)\right)\hat{e}\left(\theta_j^t\right)\right\rangle_i\right] + \eta\xi_i^t + \epsilon_i^t\pi \,, && \text{(2.1b)}
\end{aligned}$$

where, as usual, we denote by $\vec{r}_i^{\,t}$ and θ_i^t the position and orientation of the particle i at time t. The processes ϵ_i model velocity reversals, at each timestep they take the values 0, with a probability $1-\alpha$, and 1 otherwise. In the propagative rods case, α and ϵ_i are therefore equal to 0. The functions $\mathrm{sgn}(x)$ returns the sign of x so that

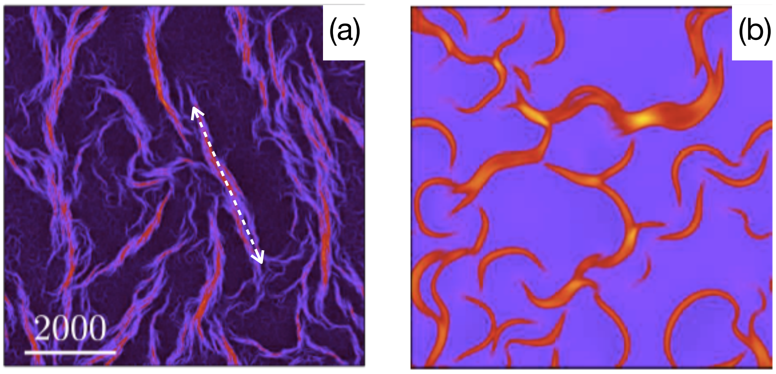

Figure 2.1 – (a) & (b): Snapshots of the spatiotemporal chaos observed in the phase coexistence region of active nematics in simulations of, respectively the microscopic model and the hydrodynamic equations derived from the Boltzmann-Ginzburg-Landau approach. The white dashed arrow in (a) shows the local orientation of the order, directed along the nematic bands. Adapted from [91].

two particles initially pointing in opposite directions will anti-align. The resulting interaction, taken within the disk of radius r_0, has the nematic symmetry that is found, for instance, in liquid crystals [138]. Finally the angular noise, uniform in $)-\eta\pi;\eta\pi]$, competes with alignment as in the polar case.

We have shown in Section 1.3.1 that r_0 can be set to 1 and that v_0 does not affect qualitatively the results. Moreover in the active nematics case, the reversal probability α has no incidence on the conclusions presented below, as soon as it remains finite. It is thus usually fixed to its maximum value: $\frac{1}{2}$. The phase diagram for these class therefore depends on two parameters: the average density of particles ρ_0 and the amplitude of the noise η. Its structure remains the same as the one shown in Figure 1.3(c) for the Vicsek model, with three distinct phases.

The low noise/large density nematic ordered phase is quasi-long-ranged in the finite velocity reversal case [81, 82, 88, 91], *i.e.* it vanishes in the infinite size limit and there is no symmetry breaking asymptotically. Self-propelled rods are theoretically expected to exhibit the same behavior, however both numerical and experimental studies suggest true long-range order [36, 87]. Shankar *et al.* have discussed the existence of a nonuniversal crossover scale below which no power law decrease of the order vs. system size can be observed [95]. This means that the current observations are probably strongly influenced by finite size effects and larger systems need to be considered to draw any definitive conclusion. Anyhow, in both cases the presence of long-range correlations in the nematic ordered phase gives rise to the generic giant density fluctuations observed in the polar class.

Another common feature with the original Vicsek model is the intermediate coexistence phase separating the disordered and ordered regions. Indeed, the order also emerges from a phase separation mechanism where the liquid structures now take the form of nematic bands oriented along the direction of the order. These ones are unstable to long wavelength longitudinal perturbations, leading to a spatiotemporal chaotic regime pictured in Figure 2.1(a).

The approaches presented in Section 1.4 to derive hydrodynamic equations for the polar class are applicable to the other cases. After writing the kinetic equation with the correct symmetries, the main difference lies in the choice of the scaling ansatz for the truncation and closure. This one indeed needs to be chosen according to the symmetry breaking field and the type of dynamics considered (propagative or diffusive) [80], as presented in Section 2.3. Like in the polar case, the Boltzmann-Ginzburg-Landau approach allows to recover the phase diagram of both active nematics and self-propelled rods models [89–91], and even accounts for the chaotic coexistence phase as shown in Figure 2.1(b).

2.1.2 The several routes to criticality

In the preceding section we have discussed the different classes of dry active matter with local alignment interactions. In particular, we have seen that all of them exhibit the phase separation mechanism that prevents the emergence of a continuous transition to order. As it relies on one of the main characteristic of these simple models, interplay between local density and order, this scenario is in fact very robust. For the same reasons as the ones exposed in Section 1.3.1, criticality thus cannot be observed in these dry active matter systems.

Different paths exist to get rid of phase separation. The first one is to consider systems with birth and death processes, *i.e.* making the density non-hydrodynamic [139]. The second way consists in imposing an incompressibility condition on the ordering field ($\vec{\nabla} \cdot \vec{p} = 0$ in the polar case) that effectively introduces long range interactions and suppresses the density dynamics [140, 141]. The only hydrodynamic field is then the order, and the generic instability driving the apparition of phase coexistence is trivially suppressed. Although these models exhibit nonequilibrium phase transitions and critical behavior, their ordered phase does not show any anomalous density fluctuations, which makes them stand further from real systems.

The third possibility, that allows to keep the density dynamics, is to consider metric free interactions. This can be achieved either by choosing “topological” neighbors from a Voronoi paving of space [142, 143], or by always interacting with the same fixed number of closest particles [144, 145]. This way, the interaction strength does no more depend on the local density, which kills one of the feedback mechanism for phase separation. Such non-metric interaction rules have been shown to be relevant in flocks of birds [26, 28], that always interact with on average six or seven closest neighbors. In addition to showing a nonequilibrium continuous transition, the ordered phase in metric free models have giant density fluctuations, akin to their metric counterparts.

In summary, the different approaches for which phase separation is suppressed so far rely on either the removal of the density field and/or introduction of long range interactions. A natural question is wether criticality can be observed in a system with only local alignment. In this Chapter we show that this can be done defining a new class of dry active matter, namely apolar particles that interact ferromagnetically. Using the Boltzmann-Ginzburg-Landau approach introduced in 1.4.1, we derive kinetic and hydrodynamic equations for this new class. In both cases the linear instability of the ordered solution responsible for the coexistence phase in the other classes is absent. This point is confirmed by simulations of the microscopic model, that show a continuous transition to a quasi-ordered polar phase with continuously varying exponents and giant number fluctuations. Although this new case possesses many of the properties of the (equilibrium) XY model, surprisingly, an extensive numerical study of the transition leads to conclude that it does *not* belong to the Berezinskii-Kosterlitz-Thouless universality class [146–148]. We give strong evidence that it is in fact best described as a standard critical point with algebraic divergence of correlations. Finally, these findings are rationalized by showing that the coupling between density and order deprives defects from their usual role.

2.2 A new class of dry active matter with continuous transition

In the restricted Vicsek framework, this fourth class is a trivial problem because it obviously cannot give rise to any orientational order. Indeed, because of the "Vicsek constraint" that the polarity of particles is given by their velocity, the order is destroyed by stochastic reversals. This difficulty can be overcome considering agents that are conferred a polarity and are able to move along or against it. Thinking the Vicsek model in terms of flying spins, this case therefore corresponds to shaken spins, and we name is the *Vicsek-shake model*. An experimental realization could consist in vertically-shaken granular disks, such as in [45], but endowed with two identical legs and carrying magnets. The symmetric legs would induce apolar motion with reversals. The magnets could dominate the interactions and lead to ferromagnetic alignment.

A mathematical definition of the model reads

$$\vec{r}_i^{\,t+1} = \vec{r}_i^{\,t} + v_0 \epsilon_i^t \hat{e}\left(\theta_i^{t+1}\right) , \tag{2.2a}$$

$$\theta_i^{t+1} = \mathrm{Arg}\left[\left\langle \hat{e}\left(\theta_j^t\right)\right\rangle_i\right] + \eta \xi_i^t , \tag{2.2b}$$

where we have kept the notations of Sections 1.3.1 and 2.1.1. Contrary to (2.1), the reversals now take place in the dynamics for positions rather than the one for orientations, which allows to preserve local ordering of the system. The processes ϵ_i are therefore equal to ± 1 and change sign with a probability α. We checked that the results presented below are not sensitive to the value of α, provided that it remains finite. It is thus fixed in the following to the numerically-convenient value $\frac{1}{2}$. Following the literature on the other classes [70], we also don't expect to see any qualitative change varying the speed v_0, which is set to $\frac{1}{2}$. With α and v_0 fixed, the main parameters remain those of classic Vicsek-style models, the mean density of particles ρ_0, and the noise amplitude η.

We first determined numerically the phase diagram of our model in the (ρ_0,η) plane (see Figure 2.2(a)). We find a single transition line from the disordered gas observed at strong noise and/or low densities to a phase with global ordering of polarities, characterized, at finite size, by a finite average value of the magnetization $M(t) = \left|\sum_{i=1}^{N} \hat{e}(\theta_i^t)\right|$. Contrary to the other known classes mentioned in Section 1.3.1 and 2.1.1, we do not see any sign of phase separation. The transition seems continuous, with only quasi-long-range order: the time averaged magnetization decreases algebraically with system size: $\langle M \rangle \sim L^{-\kappa(\eta)}$, with κ increasing continuously with the noise η as shown in Figure 2.2(c). At strong-enough noise, the correlation length of the system remains finite. Therefore, at large-enough sizes, the systems is composed of uncorrelated parts and, from the central limit theorem, a crossover to a fully disordered phase with $\langle M \rangle \sim N^{-\frac{1}{2}} \sim L^{-1}$ is observed (see Figure 2.2(d)). Here the brackets $\langle \ldots \rangle$ stand for an ensemble average, that we equate to a time average in the following.

Like in all known orientationally-ordered dry active matter phases, Figure 2.2(b) shows that giant number fluctuations are present: the variance $\langle \Delta N^2 \rangle$ of the number of particles in a sub-system containing on average $\langle N \rangle$ particles grows faster than $\langle N \rangle$. We find that $\langle \Delta N^2 \rangle \sim \langle N \rangle^{\zeta}$ with $\zeta = 1.73(3)$, a value similar to those reported for the other classes [70, 72, 73, 87, 91].

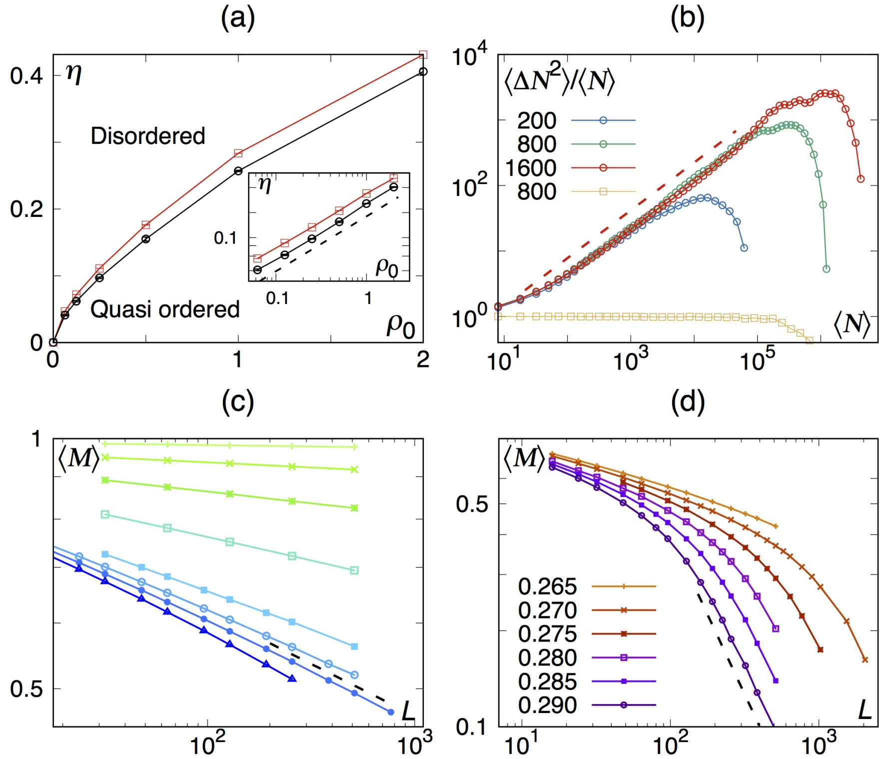

FIGURE 2.2 – (a): Phase diagram of the Vicsek-shake model in the (ρ_0, η) plane. The asymptotic order-disorder transition line is shown in black. The red curve reports the location of the susceptibility peak η_χ measured for $L = 256$ (error bars are smaller than symbols). Inset: same data in logarithmic scales, with the dashed line marking slope 0.66. (b): Variance $\langle \Delta N^2 \rangle$ over mean $\langle N \rangle$ of the number of particles present in sub-systems in the quasi-ordered (circles, $\eta = 0.2$) and disordered (squares, $\eta = 0.5$) phases for various system sizes L ($\rho_0 = 2$). The dashed line corresponds to $\zeta = 1.73$. (c) and (d): Averaged magnetization as a function of system size for several noise values in the quasi-ordered and disordered phases ($\rho_0 = 1$). In the quasi-ordered state, $\langle M \rangle$ decays algebraically, with an η-dependent exponent $\kappa(\eta)$). Curves in (c) correspond to, from top to bottom, $\eta = 0.05$, 0.1, 0.15, 0.2, 0.24, 0.25, 0.255 and 0.26. In (c) (resp. (d)) the dashed black line marks slope $-\frac{1}{8}$ (resp. -1).

2.3 Hydrodynamic description of the Vicsek-shake model

We now turn to the derivation of hydrodynamic equations for the Vicsek-shake class from a microscopic model sharing same symmetries. Encouraged by its overall success in the other cases, we adopt the Boltzmann-Ginzburg-Landau approach presented in Section 1.4.1. These equations are derived in the finite and infinite velocity reversal rate limits in respectively Sections 2.3.1 and 2.3.2. Then Section 2.3.3 connects the two sets of equations. Finally, their homogeneous solutions, as well as their stability, are studied in 2.3.4.

2.3.1 Derivation of hydrodynamic equations with finite reversal

In the finite velocity reversal rate limit, the model considers two sub-populations: the particles which move along and against their polarity that we denote respectively by "+" and "−" in the following. We thus start by writing two coupled Boltzmann equations for the corresponding single-particle distributions $f_\pm(\vec{r},\theta,t)$:

$$\partial_t f_\pm \pm v_0 \vec{e}(\theta)\cdot\vec{\nabla} f_\pm = a\,(f_\mp - f_\pm) + I_{\rm sd}[f_\pm] + I_{\rm coll}[f_\pm, f_\mp]\,, \tag{2.3}$$

where, as before, $\vec{e}(\theta)$ in the material derivative of $f_\pm$ is the unit vector directed along θ and a is the exchange rate between the two sub-populations (akin to the microscopic reversal probability α). Space, time and orientation dependencies of the distributions have been omitted for the sake of clarity. The self-diffusion and collisional integrals read

$$\begin{aligned}
I_{\rm sd}[f_\pm] &= -\lambda f_\pm + \lambda \int_0^{2\pi} d\theta' f_\pm(\theta') P_\eta(\theta-\theta')\,, && \text{(2.4a)}\\
I_{\rm coll}[f_+, f_-] &= -f_+ \int_0^{2\pi} d\theta' \left[f_+(\theta')K^+(\theta'-\theta) + f_-(\theta')K^-(\theta'-\theta)\right] \\
&\quad + \int_0^{2\pi} d\theta_1 \int_0^{2\pi} d\theta_2 f_+(\theta_1) \big(f_+(\theta_2)K^+(\theta_2-\theta_1) + f_-(\theta_2)K^-(\theta_2-\theta_1)\big) \\
&\quad \times P_\eta(\theta-\theta_1-H(\theta_2-\theta_1))\,. && \text{(2.4b)}
\end{aligned}$$

where λ is the tumbling rate and P_η is the noise distribution of variance η^2. $H(\theta) = \frac{\theta}{2}$ models the ferromagnetic alignment of polarities and the kernels of interactions

$$K^+(\theta_2-\theta_1) = 2r_0v_0|\hat{e}(\theta_2)-\hat{e}(\theta_1)| = 4r_0v_0\left|\sin\left(\frac{\theta_2-\theta_1}{2}\right)\right|\,, \tag{2.5a}$$

$$K^-(\theta_2-\theta_1) = 2r_0v_0|\hat{e}(\theta_2)+\hat{e}(\theta_1)| = 4r_0v_0\left|\cos\left(\frac{\theta_2-\theta_1}{2}\right)\right|\,, \tag{2.5b}$$

are different and are used depending on whether the two colliding particles belong to the same population or not. De-dimentionalization of these kinetic equations is done with

$$t \to \lambda^{-1} t \quad , \quad \vec{r} \to v_0\lambda^{-1}\vec{r} \quad , \quad K^\pm \to 2r_0v_0K^\pm \quad , \quad f_\pm \to \rho_0 f_\pm\,, \tag{2.6}$$

except that now, in addition to the noise intensity η, we do not have one but two nondimensional control parameters that are the rescaled density $\tilde{\rho}_0 = 2r_0v_0\lambda^{-1}\rho_0$ and reversal rate $\tilde{a} = \lambda^{-1}a$.

Hydrodynamic equations are then derived from (2.3) by expanding the distributions in terms of their angular Fourier modes

$$f_\pm(\theta) = \sum_{k=-\infty}^{\infty} \hat{f}_k^\pm e^{-\imath k\theta}\,, \tag{2.7}$$

truncating and closing the resulting hierarchies as presented in Section 1.4.1. In the Vicsek polar case the remaining hydrodynamic (or slow) fields correspond to the first two angular modes of the distribution, *i.e.* density and polarity (equal to velocity). Here these fields are the zeroth and first modes of the sum $f = f_+ + f_-$, *i.e.* the density and polarity of the total population, while the velocity field, now distinct from polarity, is the first mode of the difference $g = f_+ - f_-$. Rewriting the Boltzmann equations in terms of the modes of f and g, we obtain

$$\partial_t \hat{f}_k + \frac{1}{2}\left(\nabla^* \hat{g}_{k+1} + \nabla \hat{g}_{k-1}\right) = \left(\hat{P}_k - 1\right)\hat{f}_k + \sum_{q=-\infty}^{\infty} A_{k,q}\hat{f}_q\hat{f}_{k-q} + B_{k,q}\hat{g}_q\hat{g}_{k-q}\,, \tag{2.8a}$$

$$\partial_t \hat{g}_k + \frac{1}{2}\left(\nabla^* \hat{f}_{k+1} + \nabla \hat{f}_{k-1}\right) = \left(\hat{P}_k - 1 - 2\tilde{a}\right)\hat{g}_k + \sum_{q=-\infty}^{\infty} C_{k,q}\hat{f}_q\hat{g}_{k-q}\,, \tag{2.8b}$$

where $\hat{P}_k = \int d\theta P_\eta(\theta)\exp(\imath k\theta)$, the complex gradient $\nabla = \partial_x + \imath\partial_y$, and the coefficients are $A_{k,q} = (J^+_{k,q} + J^-_{k,q})/2$, $B_{k,q} = (J^+_{k,q} - J^-_{k,q})/2$ and $C_{k,q} = A_{k,q} + B_{k,k-q}$ with

$$\begin{aligned}
J^\pm_{k,q} &= \tilde{\rho}_0\left(\hat{P}_k I^\pm_{k,q} - I^\pm_{0,q}\right)\\
I^+_{k,q} &= \begin{cases} \frac{4}{\pi}\frac{1-(k-2q)(-1)^q\sin\left(\frac{k\pi}{2}\right)}{1-(k-2q)^2} \text{ if } |k-2q| \neq 1\\ \frac{2}{\pi} \text{ otherwise}\end{cases}\\
I^-_{k,q} &= \begin{cases} \frac{4}{\pi}\frac{\cos\left(\frac{\pi(k-2q)}{2}\right)}{1-(k-2q)^2} \text{ if } |k-2q| \neq 1\\ 1 \text{ otherwise}\end{cases}
\end{aligned}$$

In the following, we will choose a Gaussian noise distribution $\hat{P}_k = \exp(-k^2\eta^2/2)$ for all numerical applications and drop hats and tildes in order to lighten notations.

Similarly to the polar case, at the onset of order the polar field grows like a small parameter ε. Then the Hierarchies (2.8) impose the following ansatz

$$|\rho - 1| \approx |g_0| \approx \varepsilon\ ,\ |f_k| \approx |g_k| \approx \varepsilon^k\ \ \forall k > 0\,, \tag{2.9}$$

and we keep the propagative scaling $\partial_t \approx \nabla \approx \varepsilon$ for space and time derivatives. The order ε^3 gives equations for ρ, g_0, f_1, g_1, f_2 and g_2. The last two modes are then enslaved to the four remaining ones, yielding

$$\partial_t\rho = -\Re\left(\nabla^* g_1\right)\,, \tag{2.10a}$$

$$\partial_t g_0 = -2ag_0 - \Re\left(\nabla^* f_1\right)\,, \tag{2.10b}$$

$$\begin{aligned}\partial_t f_1 = {} & \left(\mu_1[\rho] - \xi|f_1|^2 - \delta|g_1|^2\right) f_1 + \Gamma\Delta f_1 + \left(\gamma[g_0] - \beta f_1^* g_1\right) g_1\\ & -\frac{1}{2}\nabla g_0 + \eta_1 f_1^*\nabla g_1 + \eta_2 g_1^*\nabla f_1 + \eta_3\nabla^*\left(f_1 g_1\right)\,,\end{aligned} \tag{2.10c}$$

$$\begin{aligned}\partial_t g_1 = {} & \left(\nu_1[\rho] - \tau|g_1|^2 - \omega|f_1|^2\right) g_1 + \lambda\Delta g_1 + \left(\kappa[g_0] - \chi g_1^* f_1\right) f_1\\ & -\frac{1}{2}\nabla\rho + \sigma_1 g_1^*\nabla g_1 + \sigma_2 f_1^*\nabla f_1 + \sigma_3\nabla^* f_1^2 + \sigma_4\nabla^* g_1^2\,,\end{aligned} \tag{2.10d}$$

where the Laplacian $\Delta = \nabla\nabla^*$ and all coefficients, expressed as functions of the microscopic parameters ρ_0, a and the moments of P_η are listed in Table 2.1, while their dependence on local density and g_0 has been made explicit. Equations (2.10) can be seen as two coupled Toner-Tu equations (1.3) (or (1.13) for the same equations in complex notations). Note, however, that here density is *not* advected by the order field f_1, but by g_1, in strong contrast to the classic polar case.

f_1 equation	g_1 equation
$\mu_1[\rho] = P_1 - 1 + \frac{1}{\pi}\left((2+\pi)P_1 - 4\right)\rho_0\rho$	$\nu_1[\rho] = P_1 - 1 - 2a - \frac{2}{3\pi}\left(4 - 3P_1\right)\rho_0\rho\,(< 0)$
$\xi = \frac{8P_2(15P_1-2)\rho_0^2}{\pi(15\pi(1-P_2)+56\rho_0)}\,(> 0)$	$\tau = \frac{8(5P_1-4)\rho_0^2}{\pi(15\pi(1-P_2)+56\rho_0)}$
$\delta = \frac{8(3P1-2)(1+3P2)\rho_0^2}{3\pi(3\pi(1-P_2+2a)+4(3+P_2)\rho_0)}$	$\omega = \frac{8P_1(1+3P_2)\rho_0^2}{\pi(3\pi(1-P_2+2a)+4(3+P_2)\rho_0)}$
$\Gamma = \frac{3\pi}{4(1-P_2+2a)+4(3+P_2)\rho_0)}\,(> 0)$	$\lambda = \frac{15\pi}{4(15\pi(1-P_2)+56\rho_0)}\,(> 0)$
$\gamma[g_0] = \frac{2}{15\pi}(2 - 15P_1)\rho_0 g_0$	$\kappa[g_0] = \frac{2}{\pi}P_1\rho_0 g_0$
$\beta = \frac{8(15P_1-2)\rho_0^2}{3\pi(15\pi(1-P_2)+56\rho_0)}$	$\chi = \frac{24P_2(5P_1-4)\rho_0^2}{\pi(15\pi(1-P_2)+56\rho_0)}$
$\eta_1 = \frac{(15P_1-2)\rho_0}{15\pi(1-P_2)+56\rho_0}$	$\sigma_1 = \frac{3(5P_1-4)\rho_0}{15\pi(1-P_2)+56\rho_0}$
$\eta_2 = \frac{(3P_1-2)\rho_0}{3\pi(1-P_2+2a)+4(3+P_2)\rho_0}$	$\sigma_2 = \frac{3P_1\rho_0}{3\pi(1-P_2+2a)+4(3+P_2)\rho_0}$
$\eta_3 = \frac{2(3P_2+1)\rho_0}{3\pi(1-P_2+2a)+4(3+P_2)\rho_0}$	$\sigma_3 = -\frac{30P_2\rho_0}{15\pi(1-P_2)+56\rho_0}$
	$\sigma_4 = -\frac{10\rho_0}{15\pi(1-P_2)+56\rho_0}$

TABLE 2.1 – Coefficients of the hydrodynamic equations (2.10) for the Vicsek-shake model in the low reversale rate limit.

2.3.2 Derivation of hydrodynamic equations in the large reversal rate limit

In this section we consider that the timescale associated to velocity reversal is smaller than any other timescale of the problem. In this limit the microscopic dynamics is essentially diffusive, as for active nematics. Therefore g is a fast mode by construction and we can write a Boltzmann equation for f only:

$$\partial_t f = D_0 \Delta f + D_1 q_{\alpha\beta}\partial_\alpha\partial_\beta f + I_{\rm sd}[f] + \frac{1}{2}I_{\rm coll}[f,f]\,, \tag{2.11}$$

where summation of repeated indices is assumed and the self-diffusion and collisional integrals have been defined in (2.4). Contrary to Equation (2.3), the free transport term in (2.11) is not trivial and needs to be derived. On the scales resolved by the Boltzmann equation, a given particle will move with a displacement $v_0\Delta t$ along or against its orientation with equal probabilities such that we can write [90]

$$f(\vec{r},\theta,t+\Delta t) = \frac{1}{2}\left[f\left(\vec{r} - v_0\Delta t\hat{e}(\theta),\theta,t\right) + f\left(\vec{r} + v_0\Delta t\hat{e}(\theta),\theta,t\right)\right]\,. \tag{2.12}$$

Expanding the r.h.s. to second order in $v_0\Delta t$, then separating it into isotropic ($\sim \delta_{\alpha\beta}$) and anisotropic ($\sim q_{\alpha\beta} = e_\alpha e_\beta - \delta_{\alpha\beta}/2$) parts gives the free transport term in (2.11) with $D_0 = \frac{v_0^2\Delta t}{4}$ and $D_1 = 2D_0$. As usual, we de-dimentionalize the Boltzmann equation using

$$t \to \lambda^{-1}t \quad , \quad \vec{r} \to \sqrt{2D_0\lambda^{-1}}\vec{r} \quad , \quad K^{\pm} \to 2r_0v_0K^{\pm} \quad , \quad f \to \rho_0 f\,, \tag{2.13}$$

$\mu_1[\rho] = P_1 - 1 + \frac{1}{\pi}\left((2+\pi)P_1 - 4\right)\rho_0\rho$	$\mu_2[\rho] = P_2 - 1 - \frac{56}{15\pi}\rho_0\rho\,(< 0)$
$\zeta = \frac{2(2-15P_1)\rho_0}{15\pi}$	$\Pi = \frac{8P_2(4+15(2+\pi)P_3)\rho_0^2}{225\pi(\pi(1-P_3)+2(2+P_3)\rho_0)}$
$\Omega = \frac{4P_2\rho_0}{\pi}$	$\Xi = \frac{2P_2\rho_0}{15(\pi(1-P_3)+2(2+P_3)\rho_0)}$

TABLE 2.2 – Coefficients of the hydrodynamic equations (2.15) for the Vicsek-shake model in the large reversal rate limit.

so that the only two parameters of the problem are the noise variance η^2 and average (rescaled) density ρ_0.

The hierarchy for the angular Fourier modes of f then reads

$$\partial_t f_k = \frac{1}{2}\Delta f_k + \frac{1}{4}\left(\nabla^{*^2} f_{k+2} + \nabla^2 f_{k-2}\right) + \left(P_k - 1\right) f_k + \sum_{q=-\infty}^{\infty} A_{k,q} f_q f_{k-q}\,, \tag{2.14}$$

with the $A_{k,q}$ coefficients defined in the preceding section. From the symmetry of the interaction, the scaling ansatz for the $k > 0$ modes is still given by (2.9). However, because the diffusive dynamics considered here, space and time are not expected to scale the same way and we choose $\partial_t \approx \nabla^2 \approx \varepsilon^2$. The continuity equation

$$\partial_t \rho = \frac{1}{2}\Delta\rho + \frac{1}{2}\Re\left(\nabla^{*^2} f_2\right)\,, \tag{2.15a}$$

then imposes that density variations $|\rho - 1|$ scale like ε^2. It also suggests that the order of the truncation should be at least ε^4, otherwise the density would be decoupled from the order. From this analysis, we identify f_2 as a relevant field and obtain equations for ρ, f_1, f_2, and f_3. The later is finally enslaved to the other three fields in order to obtain

$$\partial_t f_1 = \mu_1[\rho] f_1 + \zeta f_1^* f_2 + \frac{1}{2}\Delta f_1 + \frac{1}{4}\nabla^2 f_1^*\,, \tag{2.15b}$$

$$\partial_t f_2 = \left(\mu_2[\rho] - \Pi|f_1|^2\right) f_2 + \Omega f_1^2 + \frac{1}{2}\Delta f_2 + \frac{1}{4}\nabla^2\rho - \Xi f_1^* \nabla^2 f_1\,, \tag{2.15c}$$

where the coefficients expressions as functions of ρ_0 and the moments of P_η are listed in Table 2.2.

2.3.3 Connexion between finite and infinite velocity reversal rate limits

In this section, we present how to pass from the finite to the infinite velocity reversal rate limits. Indeed, in the limit $a \to \infty$, we must recover (2.11) from the Boltzmann equation (2.3). Let us consider these equations expressed in Fourier space. When a is sent to infinity, the g_k modes in (2.8) acquire a diverging damping term ($\sim -2a$) and can thus be enslaved to the f_k fields. These ones, previously advected by the g_k modes, get an effective diffusion coefficient scaling like $v_0^2 a^{-1}$. To keep it finite, we therefore need to impose that $v_0^2 \sim a$ when $a \to \infty$. After enslaving the g_k modes and keeping terms up to $\mathcal{O}(v_0^2 a^{-1})$, the hierarchy (2.3) is formally the same as (2.14) with $D_0 = \frac{v_0^2}{4a}$ and $D_1 = 2D_0$.

Therefore, the two hierarchies can be studied from (2.3) setting, for instance, $v_0 = \sqrt{1+a}$ and varying the value of the reversal rate. Unfortunately, this is not true at the hydrodynamic level because we have considered two different truncation orders. In the following section, we will thus study the two sets of equations (2.10) and (2.15).

2.3.4 Homogeneous solutions, linear stability analysis

The linear coefficients $\nu_1[\rho]$ and $\mu_2[\rho]$ of, respectively, g_1 and f_2 are always negative. Moreover $\mu_1[\rho]$ can change sign, so that in both cases the transition to polar oder is given, as expected, by

$$\mu_1 = P_1 - 1 + \frac{1}{\pi}\left((2+\pi)P_1 - 4\right)\rho_0 = 0\,, \tag{2.16}$$

that defines a line in the (ρ_0, η) plane (see Figure 2.3). Expanding $P_1 \approx 1 - P_1'\eta^2$[1], this mean field transition line goes to the origin as $\eta \approx \sqrt{(\pi-2)\rho_0/(\pi P_1')} \sim \sqrt{\rho_0}$. Furthermore, since μ_1 does not depend on a, the location of the transition is insensitive to the reversal rate, in agreement with the microscopic model of Section 2.2. When $\mu_1 < 0$ the disordered solution

$$\rho = 1\,; \left| \begin{array}{c} g_0 = f_1 = g_1 = 0 \quad (a < \infty) \\ \\ f_1 = f_2 = 0 \quad (a \to \infty) \end{array} \right. \,, \tag{2.17}$$

is linearly stable, and becomes unstable when $\mu_1 > 0$. It is then replaced by the homogeneous ordered solution[2]

$$\rho = 1\,; \left| \begin{array}{c} g_0 = g_1 = 0\,;\; f_1 = \sqrt{\frac{\mu_1}{\xi}} \quad (a < \infty) \\ \\ f_1 = \sqrt{\frac{\mu_1 \mu_2}{\zeta\Omega + \Pi\mu_1}}\,;\; f_2 = -\frac{\mu_1}{\zeta} \quad (a \to \infty) \end{array} \right. \,. \tag{2.18}$$

Linearizing the hydrodynamic equations (2.10) and (2.15) around the solutions (2.18), we can study their stability numerically by solving the corresponding eigenvalue problem. For low values of a, the homogeneous ordered solution is unstable to perturbations transversal to the order deep in the ordered phase (see Figure 2.3(a)). In the limit of infinite reversal, Figure 2.3(b) shows that a longitudinal instability is present at low noises. The discrepancy between the two cases is probably due to the fact that the equations are obtained at different orders of ε, which is known to affect the stability of the homogeneous ordered solutions far from the transition [80].

This is a strong indication that both of these instabilities are spurious, which is confirmed by an analysis at the kinetic level, *i.e.* truncating the Fourier hierarchies (2.8) and (2.14) at a given (large) order ε^{N+1} by setting all the modes with an index $k \geq N$ to 0. The homogeneous ordered solutions are then computed numerically, but the global procedure remains the same and is detailed in Section 3.2. For both finite and infinite velocity reversal rates, considering $N \leq 10$ is enough to suppress any spurious instability. The polar order is then stable everywhere below the transition line.

This result can be understood from the analytic structure of the hydrodynamic equations. Contrary to the order classes, here the density is not directly advected by

---

[1] There is no chirality in the system, so P_η has to be symmetric w.r.t. $\eta \to -\eta$.

[2] We can assume that the order is along the x axis without loss of generality.

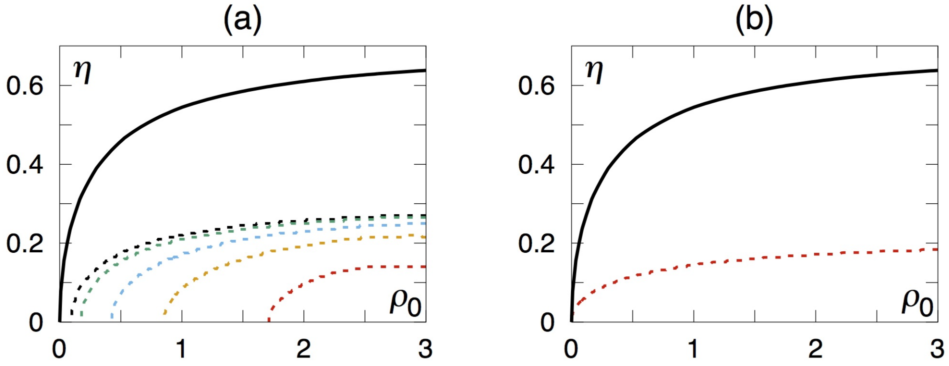

FIGURE 2.3 – (a): Phase diagram determined from Equations (2.10) in the finite reversal limit. The dashed lines mark the upper limit of existence of an instability of the homogeneous solution, transversal to it, for reversal values, from left to right, $a = 5 \cdot 10^{-3}$, 10^{-2}, $2.5 \cdot 10^{-2}$, $5 \cdot 10^{-2}$, and 10^{-1}. (b): Phase diagram determined from Equations (2.15) in the infinite reversal limit. The homogeneous polar order is linearly unstable to longitudinal perturbations below the red dashed line. In (a) and (b) the thick black line represents the mean field transition given by $\mu_1 = 0$.

the ordering field, which breaks the feedback loop responsible for the generic instability leading to the phase separation scenario. Therefore, we have a single transition line separating polar order from the disordered phase. Moreover, the order f_1 either diffuses or is advected by the auxiliary field g_1, thus the mechanism proven by Toner and Tu to generate true long-range order is absent [72, 73]. With fluctuations, polar order is only quasi-long-range, as in equilibrium. Consequently, our problem possesses many of the hallmarks of the XY model. In the next section we investigate whether this extends to the nature of the transition, *i.e.* whether it belongs to the celebrated Berezinskii-Kosterlitz-Thouless (BKT) universality class.

2.4 Characterization of the transition

2.4.1 The Berezinskii-Kosterlitz-Thouless universality class

The BKT transition was firstly described in the context of the two dimensional XY model [146–148]. The low-temperature ordered phase of this model is characterized by absence of global magnetization due to spin waves [71], but algebraic correlations with continuously varying exponents. Above the critical temperature T_{BKT}, topological excitations of the order, or vortices, become energetically favorable. As a consequence, pairs of vortices unbind and long-ranged correlations are destroyed. The BKT theory therefore describes an unusual transition with no symmetry breaking occuring at T_{BKT}, but rather a modification of the behavior of correlations in the system. This transition is not restricted to the only XY model but is general for any system that can be mapped to a Coulomb gas of particles with logarithmic interactions such as superfluids, superconductors, or dislocations in two dimensional crystals [149].

Approaching T_{BKT} from above, a particularity of the BKT transition is the exponential divergence of the correlation length

$$\xi \sim e^{(T-T_{\mathrm{BKT}})^{-\nu}}, \tag{2.19}$$

where the exponent $\nu = \frac{1}{2}$ is universal. Another universal feature of the BKT class is the value of the decay exponent of the correlation functions at the critical point, from which we can deduce the corresponding scaling of the magnetization with system size

$$\langle M \rangle \sim L^{-\kappa(T_{\mathrm{BKT}})} \,, \tag{2.20}$$

with $\kappa(T_{\mathrm{BKT}}) = \frac{1}{8} = \beta/\nu$ using the classic notations for phase transitions. The hyperscaling relation $\gamma + 2\beta = d\nu$ with $d = 2$ then gives the divergence of the susceptibility at the transition

$$\chi = L^2 \left(\langle M^2 \rangle - \langle M \rangle^2 \right) \sim L^{\frac{\gamma}{\nu}} \,, \tag{2.21}$$

with $\gamma/\nu = \frac{7}{4}$. The BKT universality class can therefore be identified measuring the functional form of the divergence of the correlation length ξ, in addition to the two independent exponents ν and γ/ν as it was done at equilibrium [150–152].

2.4.2 Numerical study of the transition

In order to find out the nature of the transition to polar quasi-long-range order in the Vicsek-shake class, we have carried out molecular dynamics simulations of the microscopic model (2.2) for densities ranging from $\frac{1}{16}$ to 2. With system sizes up to 1024^2, the largest runs represent a numerical effort of more than a million particles, collecting statistics on typically 10^8 timesteps in order to get satisfactory averaging. Such large scales cannot be reached with the usual single-core, even optimized, codes in a reasonable amount of time. Therefore a parallelized code, based on the Message Passing Interface library [153] and whose performances scale roughly as the inverse of the number of processors, was designed and run on a supercomputer on which we used of the order of 10^2 cores for the largest sizes.

Susceptibility

At finite size L and fixed density, decreasing the noise η from the disordered phase the susceptibility χ exhibits a maximum $\chi_{\max}(L)$ located at $\eta_\chi(L)$. Assuming BKT scaling and increasing L, $\chi_{\max}$ diverges and from (2.19), η_χ converges to the asymptotic threshold η_c like

$$\begin{aligned} \chi_{\max}(L) &\sim L^{\frac{\gamma}{\nu}} \,, && (2.22a) \\ \eta_\chi(L) - \eta_c &\sim (\log(L) - c)^{-\frac{1}{\nu}} \,, && (2.22b) \end{aligned}$$

with c a nonuniversal constant, $\nu = \frac{1}{2}$ and $\gamma/\nu = \frac{7}{4}$. We have measured the dependence of the magnetization $\langle M \rangle$ and χ on η for various densities and system sizes. However, the susceptibility curves being numerically costly, we focused most of our numerical effort on a single value of the density, thus, otherwise stated $\rho_0 = 1$ in what follows[3]. As shown in Figure 2.4(a), for both $\rho_0 = \frac{1}{4}$ and 1 the susceptibility peak maximum $\chi_{\max}$ does diverge algebraically with an exponent $\gamma/\nu = 1.755(6)$ in full agreement with the BKT/Ising value $\frac{7}{4}$. Moreover, scaling the corresponding curves with $L^{-\frac{7}{4}}$ allows us to identify the (density-dependent) characteristic system size $L^*(\rho_0)$ below which the scaling regime is not attained. We find $L^*\left(\frac{1}{4}\right) \gtrsim 200$ and $L^*(1) \gtrsim 100$, the points for which $L < L^*$ are thus not used in the following analysis. The peak location η_χ at density 1 is reasonably well fitted by Equation (2.22b)

---

[3] We recall that α and v_0 have been fixed to $\frac{1}{2}$ in Section 2.2, the results presented here are insensitive to their values as soon as they remain finite.

with $\nu = \frac{1}{2}$, yielding an estimate of the asymptotic threshold $\eta_c = 0.247(2)$ (see Figure 2.4(b)).

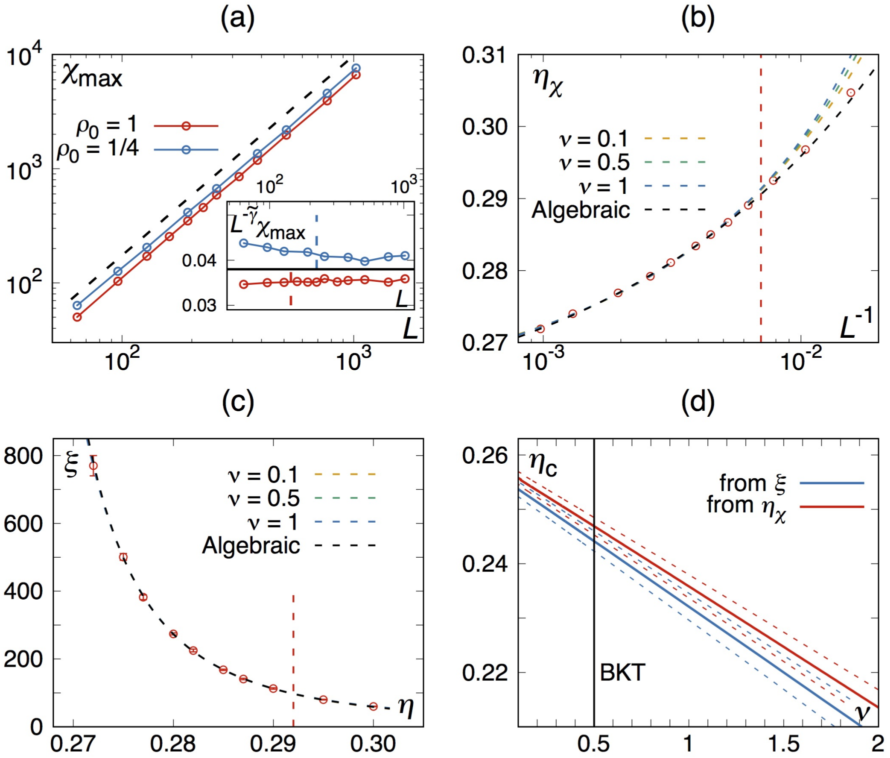

FIGURE 2.4 – (a): Susceptibility peak maximum $\chi_{\max}$ vs. system size L. The dashed line has slope $\frac{7}{4}$. Inset: same data scaled with $L^{-\frac{7}{4}}$. Here and in (b,c) errorbars if not present, are smaller than symbols and the vertical dashed line delimits system sizes below which the scaling regime is not reached (these points are not used for the fits in (b), (c) and (d)). (b): Position of $\chi_{\max}$ vs. L^{-1}. The different lines are fits using (2.22b) (BKT-like scaling) for several values of ν, and (2.26b) (Algebraic scaling). (c): same as (b) but for the divergence of the correlation length with noise. (d): asymptotic threshold η_c obtained from fits of ξ and η_χ with BKT-like scaling (2.24) and (2.22b) varying the exponent ν. The dashed lines represent the confidence intervals on η_c given by the fits.

Correlation length

The correlation length ξ was defined from the decay of the magnetization $\langle M \rangle$ with system size L. As explained in Section 2.2, in the disordered phase where ξ is finite, $\langle M \rangle$ vs. L undergoes a crossover between two power laws (see Figure 2.2(d)): at small L we observe a slow algebraic decay like in the quasi-ordered-phase, but at large L $\langle M \rangle \sim L^{-1}$. Therefore, as L increases, $L^{\alpha}\langle M \rangle$ with $0 < \alpha < 1$ shows a maximum (see Figure 2.5(a)) whose position is directly related to ξ. Acceptable choices for α (that prevent finite size effects) are from 0.4 to 0.6 and we verified that they all lead to similar results. Data presented here corresponds to $\alpha = 0.55$.

To check the validity of this measure, we remark that above the threshold, the decay exponent of the magnetization κ is fixed to its value at the transition: $\frac{1}{8}$. Therefore, $\langle M \rangle$ depends on the noise only through ξ and we can write

$$\langle M \rangle(L, \eta) = L^{-\kappa(\eta_c)} \Gamma \left(\frac{L}{\xi(\eta)} \right) , \tag{2.23}$$

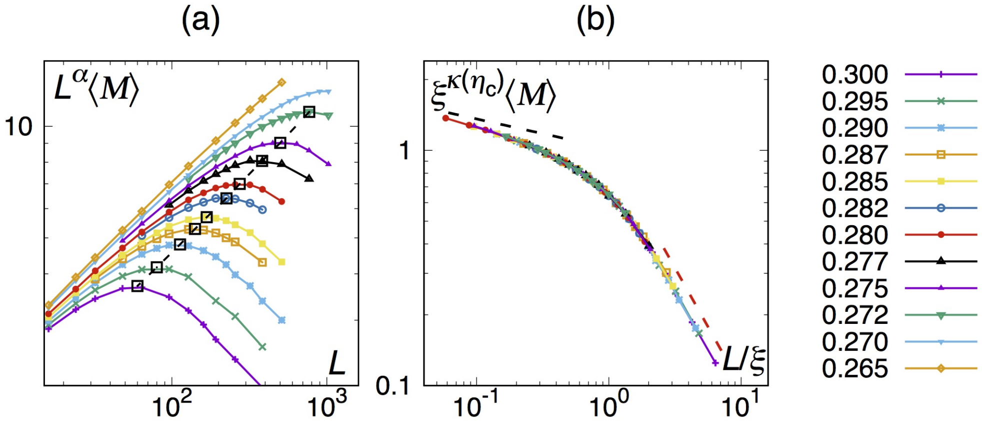

FIGURE 2.5 – (a): The magnetization curves scaled by L^α vs. system size, with $\alpha = 0.55$ for different values of η. (b): Collapse of the magnetization curves from (2.23) and using correlation lengths ξ shown in Figure 2.4(c) with $\kappa(\eta_c) = \frac{1}{8}$. The black (respectively red) dashed line marks the slope $-\frac{1}{8}$ (respectively -1)

with Γ an unspecified nonuniversal function. Consequently, $\xi(\eta)^{\kappa(\eta_c)}\langle M\rangle$ as function of $L/\xi(\eta)$ will collapse on a universal curve independent of the noise amplitude η. This is indeed what is observed in Figure 2.5(b) using $\kappa_c = \frac{1}{8}$.

The divergence of ξ with decreasing η is well fitted by

$$\xi \sim e^{(\eta-\eta_c)^{-\nu}}\,, \tag{2.24}$$

with $\nu = \frac{1}{2}$ (see Figure 2.4(c)). This fit yields and estimate $\eta_c = 0.244(2)$ (barely) compatible with that obtained from the susceptibility. However, for $0.244 \leq \eta \leq 0.247$, $\langle M\rangle$ decreases with an exponent $\kappa \simeq 0.100(5)$ *incompatible* with the BKT value $\frac{1}{8}$ (see Figure 2.2(c)). Repeating the procedure for $\rho_0 = \frac{1}{2}$ and 2 we reach the same conclusion and find *different* values of $\kappa(\eta_c)$, respectively 0.089(6) and 0.117(2).

Algebraic scaling

Allowing ν to vary in a range $[0.1; 2]$, we find fits of the variations of η_χ and ξ as convincing as for the BKT value $\frac{1}{2}$. Interestingly, as shown in Figure 2.4(d) the two independent estimates of η_c become closer to each other as $\nu \to 0$. In this limit, considering A and b real

$$Ae^{b(\eta-\eta_c)^{-\nu}} = Ae^{be^{-\nu\log(\eta-\eta_c)}} \underset{\nu\to 0}{\sim} Ae^{b(1-\nu\log(\eta-\eta_c))} = Ae^{b}(\eta-\eta_c)^{-b\nu}\,. \tag{2.25}$$

This therefore suggests an *algebraic* divergence for ξ at threshold. We consequently redefine the exponent ν as that of a standard second-order phase transition:

$$\xi \sim (\eta-\eta_c)^{-\nu}\,, \tag{2.26a}$$

$$\eta_\chi(L) - \eta_c \sim L^{-\frac{1}{\nu}}\,. \tag{2.26b}$$

Fitting our data accordingly, we obtain better fits for both ξ and η_χ and, importantly, fully-compatible threshold values at which, moreover, $\kappa(\eta_c) \simeq \frac{1}{8}$. Imposing a common value for the asymptotic threshold, both datasets give the same estimate of ν, and we finally conclude that $\eta_c = 0.257(1)$ with $\nu = 2.4(1)$.

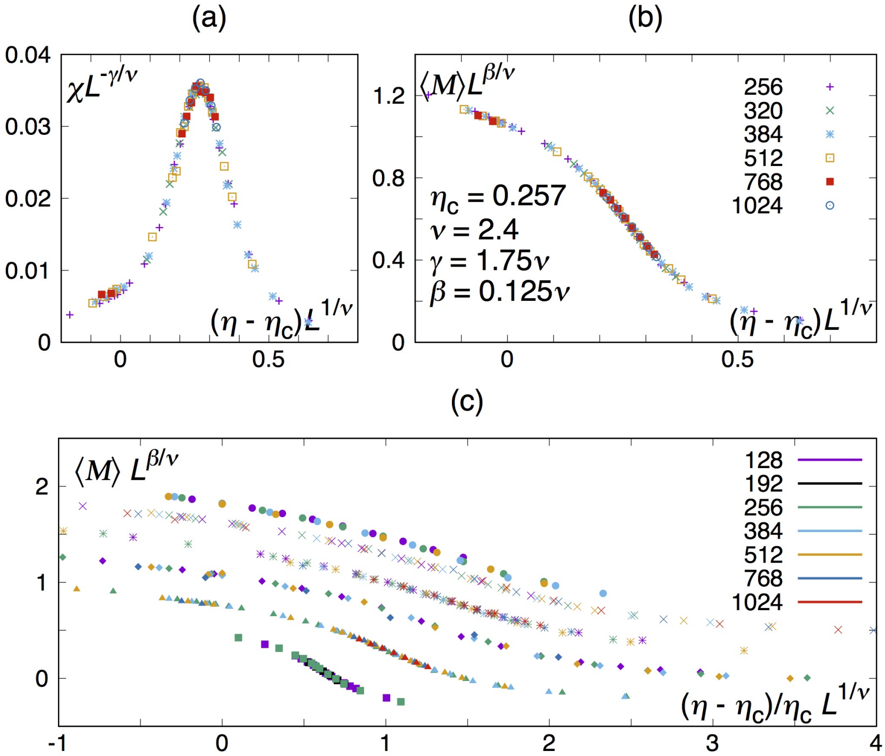

FIGURE 2.6 – (a) and (b): Collapses of the susceptibility and magnetization curves at density $\rho_0 = 1$. (c): Collapses of the magnetization curves with various system size (labeled by the color code in the caption) for densities, from top to bottom, $\frac{1}{16}$, $\frac{1}{8}$, $\frac{1}{4}$, $\frac{1}{2}$, 1 and 2. The curves have been shifted vertically for clarity and normalized by the critical noise η_c horizontally.

From these values and assuming the following scaling forms of the magnetization and susceptibility

$$\langle M\rangle = L^{-\frac{\beta}{\nu}}\tilde{M}\left((\eta-\eta_c)L^{\frac{1}{\nu}}\right) , \tag{2.27a}$$

$$\chi = L^{\frac{\gamma}{\nu}}\tilde{\chi}\left((\eta-\eta_c)L^{\frac{1}{\nu}}\right) , \tag{2.27b}$$

with $\gamma/\nu = \frac{7}{4}$ and $\beta/\nu = \frac{1}{8}$, panels (a) and (b) of Figure 2.6 show that both datasets collapse, confirming the algebraic scaling (2.26). The hyperscaling relation $\gamma+2\beta = d\nu$ with $d = 2$ is thus satisfied. Using data obtained at various global densities, we find the same values for γ/ν and β/ν (see Figures 2.4(a) and 2.6(c)), although our estimate of ν shows some variations due to its sensitivity to the estimated value of the threshold η_c. As shown in Figure 2.2(a), the asymptotic thresholds thus obtained behave as $\eta_c \sim \rho_0^h$ with $h \sim 0.66$, in clear departure from the mean field value $\frac{1}{2}$.

Our numerical analysis leads us to conclude that the transition to polar order exhibited by our system is *not* of the BKT-type. As mentioned in Section 2.4.1, this transition is closely related to the (effective) Coulomb interactions between topological singularities of the ordering field that unbind and proliferate above the critical temperature. The following section is therefore dedicated to the study of such objects in our system. We show that, due to coupling between density and order, they exhibit genuine nonequilibrium behavior, which supports the above conclusion.

2.5 Defects dynamics in dry active matter

2.5.1 Annihilation of a pair of defects

Detecting defects in simulations of our microscopic model is made very difficult, if not impossible, by the presence of strong density fluctuations. Indeed, the very existence of topologically constrained defects requires that order can be defined everywhere. Here, the local order is hard to measure in sparse regions, and even impossible to define if the local density is below the ordering threshold $\rho_0^c(\eta)$, the transitional density found by varying ρ_0 keeping η fixed.

One can nevertheless study the fate of defects from carefully prepared initial configurations containing a ±1 pair[4]. Running the model (2.2) deep in the ordered phase, we observe that the positive defect expels particles from its core and is quickly transformed into a sparse, almost void circular region as shown in Figure 2.7. Meanwhile,

---

[4] We consider integer charged defects because of the polar symmetry of the interaction.

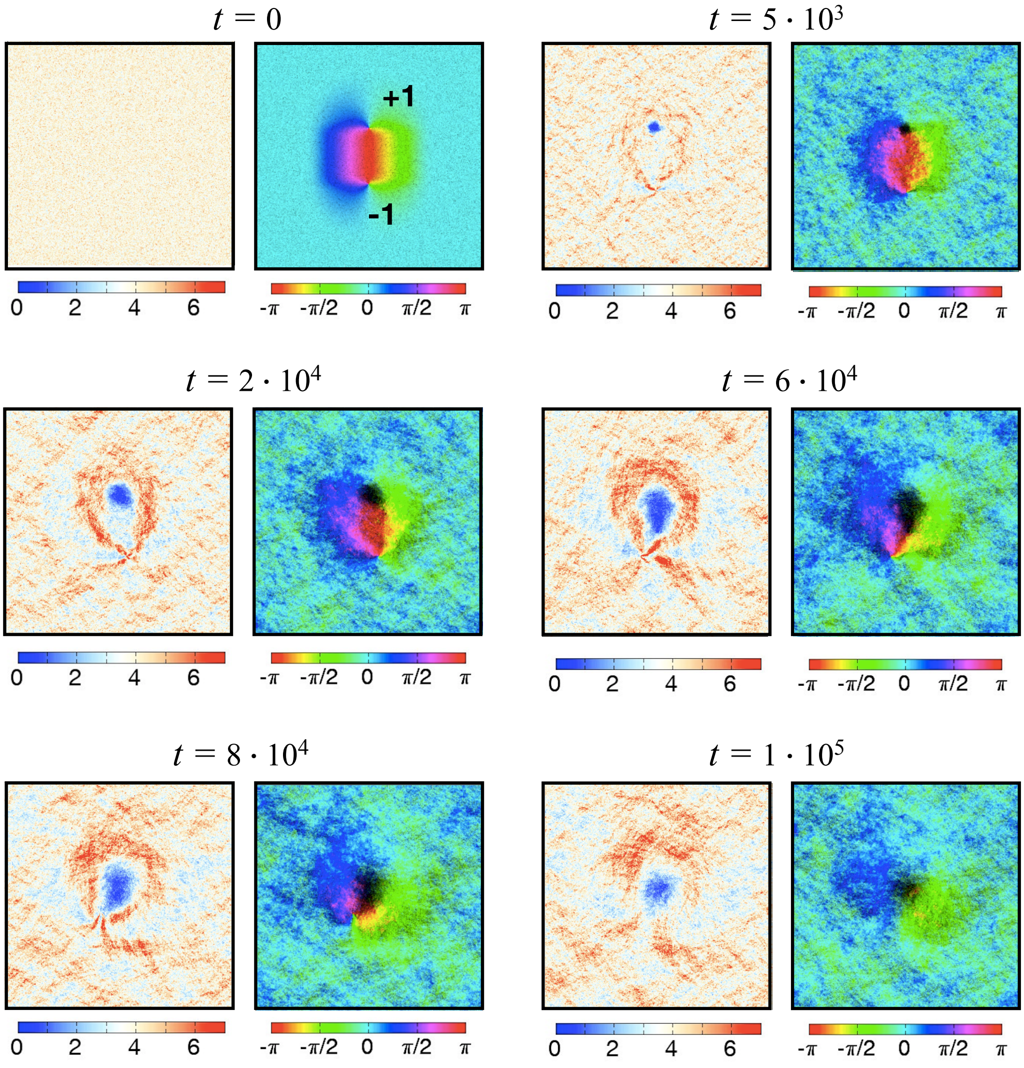

FIGURE 2.7 – Annihilation of an initially prepared ±1 pair of defects deep in the ordered phase. We show snapshots of the density and polarity orientation fields from our microscopic model at different times ($\rho_0 = 4$, $\eta = 0.2$, $L^2 = 1024^2$).

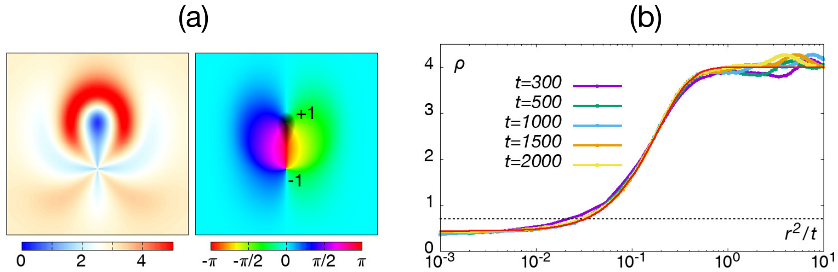

Figure 2.8 – (a): Annihilation of an initially prepared ±1 pair of defects deep in the ordered phase. Snapshot of the density and polarity orientation fields from simulations of the hydrodynamic equations (2.10) ($\rho_0 = 3$, $\eta = 0.4$, $a = 1$, $L^2 = 256^2$, $t = 2500$, $dx = \frac{1}{2}$, $dt = 10^{-2}$). (b): Time-rescaled radial density profiles around the +1 defect in microscopic simulations (same parameters as in Figure 2.7). The dashed black line indicates the transitional density $\rho_0^c(\eta)$ corresponding to $\eta = 0.2$. The continuous red line is a fit of the $t = 2000$ profile with (2.39a).

the negative defect reorganizes the flow in a cross-like shape over length scales comparable to the system size. Since the density is high in its core, its position is more sensitive to fluctuations than the center of the dilute region created by the positive defect, that is almost motionless. After some time, this void domain has become sufficiently large so that it reaches the negative defect and the system eventually repairs itself. This behavior is also reproduced in simulations of the deterministic hydrodynamic equations derived in both finite (2.10) and infinite (2.15) reversal rate limits as shown in Figure 2.8(a).

Time averaging the radial density profiles around the positive defects in the molecular dynamics simulations, we show that the diameter of the circular, near-empty, region grows like $\sqrt{t}$ (see Figure 2.8(b)). Moreover, the averaged density in the vicinity of the center is found to be smaller than the ordering threshold $\rho_0^c(\eta)$, showing that the core of the positive defect is disordered. Considering larger and larger system sizes, we did not find any saturation of the diameter of this disordered region, suggesting that it will not stop growing until it meets an oppositely charged defect. This simple simulation has thus revealed that, contrary to equilibrium, defects are not topologically constrained objects in the context of dry active matter. Closer to the transition, we obviously expect fluctuations to play a major role, but this conclusion should still hold. As we will show in the next section, this phenomenology is intrinsically related to the coupling between density and order. It thus occurs to all the dry active matter classes presented in Sections 1.3.1 and 2.1.1.

2.5.2 Derivation of the positive defect dynamics

In this section we derive the dynamic of the +1 charged defect described previously. In order to get analytical results, we consider our hydrodynamic equations retaining density and polar order only:

$$\partial_t \rho = \frac{1}{2}\Delta\rho - \sigma_3 \Re\left(\nabla^{*^2} f_1^2\right) , \tag{2.28a}$$

$$\partial_t f_1 = \left(\mu_1[\rho] - \xi|f_1|^2\right) f_1 + \frac{1}{2}\Delta f_1 + \frac{1}{4}\nabla^2 f_1^* , \tag{2.28b}$$

where all the coefficients are defined in Table 2.1. These equations can be obtained from (2.10) enslaving g_0 and g_1, but keeping the nonequilibrium advection term in the continuity equation, that is of order ε^4, in order to avoid trivial results. We

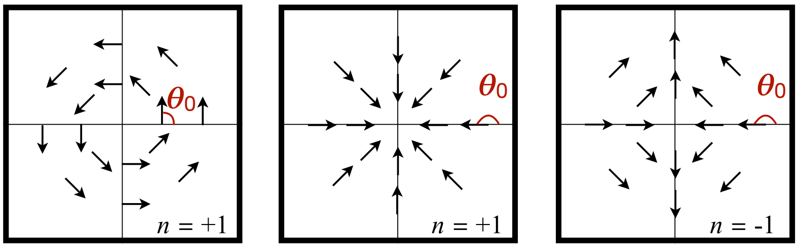

FIGURE 2.9 – Sketches of defects of the polar field. Left and center panels show respectively an anti-clockwise vortex and a sink, defined by a positive charge and a phase shift $\theta_0 = \frac{\pi}{2}$ and π. Right panel represents a saddle that is negatively charged and for which $\theta_0 = \pi$.

place ourselves in the ordered phase, *i.e.* where $\mu_1 > 0$, and recall that from our computation $\xi > 0$ and $\sigma_3 < 0$.

From the symmetries of the problem, we consider polar coordinates (r, φ) and a frame centered on the defect position. The polar field can then be written as $f_1(r, \varphi, t) = U(r, \varphi, t)\exp(\imath\theta(r, \varphi, t))$ and we give the expression of the spatial derivative operators in these coordinates

$$\Delta = \partial^2_{rr} + \frac{1}{r}\partial_r + \frac{1}{r^2}\partial^2_{\varphi\varphi}\,, \tag{2.29a}$$

$$\nabla = e^{\imath\varphi}\left(\partial_r + \frac{\imath}{r}\partial_\varphi\right)\,, \tag{2.29b}$$

$$\nabla^2 = e^{2\imath\varphi}\left(\partial^2_{rr} - \frac{1}{r}\partial_r - \frac{1}{r^2}\partial^2_{\varphi\varphi} + \frac{2\imath}{r}\left(\partial^2_{r\varphi} - \frac{1}{r}\partial_\varphi\right)\right)\,. \tag{2.29c}$$

Replacing this expression for the polar field in (2.28), equations for U and θ read

$$\partial_t U = \left(\mu[\rho] - \xi U^2\right)U + \frac{1}{2}\left(\Delta U - U|\nabla\theta|^2\right) + \frac{1}{4}\Re\left(e^{-\imath\theta}\nabla^2 f_1^*\right)\,, \tag{2.30a}$$

$$\partial_t\theta = \Delta\theta + \frac{1}{U}\Re\left(\nabla U \nabla^*\theta\right) + \frac{1}{4U}\Im\left(e^{-\imath\theta}\nabla^2 f_1^*\right)\,. \tag{2.30b}$$

These equations are essentially the ones derived from a Ginzburg-Landau theory at equilibrium [154] plus the anisotropic diffusion term.

We consider a $n = \pm 1$ charged defect configuration defined by $\theta = n\varphi + \theta_0$, where θ_0 is a global phase shift, defined in Figure 2.9. We note that, because of the anisotropic diffusion terms in Equations (2.30), these ones depend explicitly on θ_0. Therefore, two defects with same charge but different global phase, vortices and sink or sources for instance, are not equivalent, in strong contrast to equilibrium. Replacing this expression in (2.30b), we get

$$\begin{aligned} 0 = & -\frac{n}{r^2}\partial_\varphi U + \frac{\cos(2(1-n)\varphi - 2\theta_0)}{2r}\left(\partial^2_{r\varphi} + \frac{n-1}{r}\partial_\varphi\right)U \\ & + \frac{\sin(2(1-n)\varphi - 2\theta_0)}{4}\left(\partial^2_{rr} + \frac{2n-1}{r}\partial_r + \frac{1-2n}{r^2} - \frac{1}{r^2}\partial^2_{\varphi\varphi}\right)U\,, \end{aligned} \tag{2.31}$$

where the two last terms of the r.h.s. are brought by anisotropic diffusion. Because of the cosine and sine functions dependencies, the positive defect is easier to treat. In the following we will thus set $n = +1$ and leave the other case for future work.

We are interested in solutions of the form $\bar{\theta}_0 = \frac{k\pi}{2}$ with $k \in \mathbb{Z}$. From (2.31), the corresponding polar field norm $\bar{U}$ must then satisfy

$$\left(\frac{(-1)^k}{2}\partial_r - \frac{1}{r}\right)\partial_\varphi \bar{U} = 0\,. \tag{2.32}$$

As we are looking for nontrivial solutions and $\bar{U}$ cannot diverge in both $r = 0$ and $r \to \infty$, the only way to satisfy this condition is to impose that it is isotropic: $\partial_\varphi \bar{U} = 0$. Then the density must have the same symmetry and Equations (2.28) simplify as

$$\begin{aligned} \partial_t \bar{\rho} &= \frac{1}{2}\left(\partial^2_{rr} + \frac{1}{r}\partial_r\right)\bar{\rho} + (-1)^{k+1}\sigma_3\left(\partial^2_{rr} + \frac{3}{r}\partial_r\right)\bar{U}^2\,, && \text{(2.33a)} \\ \partial_t \bar{U} &= \left(\mu_1[\bar{\rho}] - \xi\bar{U}^2\right)\bar{U} + \frac{1}{2}\left(1 + \frac{(-1)^k}{2}\right)\left(\partial^2_{rr} + \frac{1}{r}\partial_r - \frac{1}{r^2}\right)\bar{U}\,. && \text{(2.33b)} \end{aligned}$$

We note that the sign of the advection term in the density equation depends on k, in fact numerical simulations of the hydrodynamic equations (2.10) and (2.15) show that the positive defect configurations with even k are always unstable and converge to the odd k solutions. In the following we will thus consider k odd only.

At equilibrium, the equation for $\bar{U}$ is the same as (2.33b) except for the density dependence of the linear coefficient. With μ constant, this equation admits a stationary solution [154], this is however no more true outside equilibrium. Because its dynamics is not conserved, $\bar{U}$ evolves on smaller timescales than $\bar{\rho}$, we can thus enslave it to the density:

$$\bar{U}^2 = \frac{\mu_1[\bar{\rho}]}{\xi} = \alpha_0 + \alpha_1\bar{\rho}\,, \tag{2.34}$$

with $\alpha_0 < 0$ and $\alpha_1 > 0$. The equation for the density then reads

$$\partial_t \bar{\rho} = \left(\frac{1}{2} + \alpha_1\sigma_3\right)\partial^2_{rr}\bar{\rho} + \frac{1}{r}\left(\frac{1}{2} + 3\alpha_1\sigma_3\right)\partial_r\bar{\rho}\,. \tag{2.35}$$

From the analysis of Section 2.5.1, we know that the solutions to this equation are written in the form $\bar{\rho}(r,t) = \tilde{\rho}(r^2/t) = \tilde{\rho}(x)$, which yields an equation for the density profile

$$x\left(\frac{1}{2} + \alpha_1\sigma_3\right)\tilde{\rho}''(x) + \left[\left(\frac{1}{2} + 2\alpha_1\sigma_3\right) + \frac{x}{4}\right]\tilde{\rho}'(x) = 0\,, \tag{2.36}$$

where $\tilde{\rho}'$ and $\tilde{\rho}''$ are respectively the first and second derivatives of $\tilde{\rho}$ w.r.t. x. The solutions of this equation are given by

$$\tilde{\rho}(x) = C_0 + C_1\Gamma\left[-\frac{2\alpha_1\sigma_3}{1 + 2\alpha_1\sigma_3}, \frac{x}{2(1 + 2\alpha_1\sigma_3)}\right]\,, \tag{2.37}$$

where $\Gamma[s,x]$ is the incomplete Gamma function: $\Gamma[s,x] = \int_x^{+\infty} t^{s-1}\exp(-t)dt$ and C_0 and C_1 two real constants. For $s > 0$, the incomplete Gamma function has the following behaviors in $x = 0$ and $x \to +\infty$:

$$\begin{aligned} \Gamma[s,x] &= \Gamma[s,0] + \frac{x^s}{s} + \mathcal{O}(x^{s+1}) \quad \text{when} \quad x \to 0\,, && \text{(2.38a)} \\ \Gamma[s,x] &= x^{s-1}e^{-x}\left(1 + \mathcal{O}(x^{-1})\right) \quad \text{when} \quad x \to +\infty\,. && \text{(2.38b)} \end{aligned}$$

We thus identify C_0 as the average density 1 that is attained when $r^2 \gg t$. C_1 is computed from Equation (2.34): the solution can be continuous only if the polar field cancels at the center of the defect, hence we have $\tilde{\rho}(0) = -\alpha_0/\alpha_1 = \rho_c$ the mean field transitional density. The positive defect solution finally reads

$$\begin{aligned}
\tilde{\rho}(x) &= 1 - (1-\rho_c)\frac{\Gamma\left[-\frac{2\alpha_1\sigma_3}{1+2\alpha_1\sigma_3}, \frac{x}{2(1+2\alpha_1\sigma_3)}\right]}{\Gamma\left[-\frac{2\alpha_1\sigma_3}{1+2\alpha_1\sigma_3}, 0\right]}\,, &\text{(2.39a)}\\
\tilde{U}^2(x) &= \alpha_1(1-\rho_c)\left(1 - \frac{\Gamma\left[-\frac{2\alpha_1\sigma_3}{1+2\alpha_1\sigma_3}, \frac{x}{2(1+2\alpha_1\sigma_3)}\right]}{\Gamma\left[-\frac{2\alpha_1\sigma_3}{1+2\alpha_1\sigma_3}, 0\right]}\right). &\text{(2.39b)}
\end{aligned}$$

In the range of microscopic parameters we consider, $0 < -\alpha_1\sigma_3 \ll 1$ so that the solution (2.39) is always well defined. As pointed out in microscopic simulations, ρ decreases in the core of the defect until it reaches the (mean-field) transitional density. With fluctuations, we thus expect the region around the center of the positive defect to be disordered, such that it can no more be considered as a singularity of the polar order. Figure 2.8(b) shows that the density profiles are indeed well fitted by the incomplete Gamma function.

Following this computation, we note that a derivation of the interaction force between defects using usual equilibrium techniques [154, 155] will suffer severe difficulties. Firstly, the negative defect is not isotropic, the equation describing the polar field in its vicinity is thus no more the same as the one for the positive defect. Moreover, we were not able to find any analytical solution for this case, which is more complicated. Secondly, we have shown the study of defects in the active matter context requires an additional field that is density. This one indeed triggers nontrivial and significant effects. Thirdly, because of the interplay between polar and density fields, the defects are no more singularities of the order but dynamical objects with a spatial extension, which breaks down the equilibrium picture.

2.6 Conclusion

In this Chapter, we have studied the collective behavior of active particles with velocity reversals that align ferromagnetically their polarities. Using kinetic and hydrodynamic level descriptions derived from the microscopic model, we demonstrated that the analytic structure of this problem is qualitatively different from that of the three other classes of dry, dilute, aligning active matter. In particular, the generic linear instability at the root of the liquid-gas phase separation scenario is absent, and for the first time is prevented “structurally”.

This new class is therefore characterized by a continuous transition to a phase with quasi-long-range polar order and anomalous number fluctuations. Like in the XY model, scaling exponents vary continuously in this phase. However, an extensive numerical study of the transition led to conclude that it shows algebraic, and not exponential, divergences of correlations, ruling out the BKT hypothesis. We computed the associated exponents, β/ν and γ/ν that take the BKT/Ising values $\frac{1}{8}$ and $\frac{7}{4}$, and $\nu = 2.4(1)$. The latter does not seem to correspond to any known class. To our knowledge, this model thus defines a new nonequilibrium critical point.

Finally, this result was strengthened by a study of the defects dynamics at both microscopic and hydrodynamic levels. Both approaches agree on the fact that, because of the coupling between density and order, defects cannot be considered as point-like objects, which deprives them from their usual role. This phenomenology should be generic in the context of dry active matter, and be present in the other classes.

Chapter 3

Robustness of kinetic theories for dry aligning active matter

3.1 Limits of the hydrodynamic description of active matter models

The different approaches for the derivation of hydrodynamic equations from simple models of active matter have been reviewed in Section 1.4. Most of them are based on a kinetic equation for the single particle distribution written in the dilute [80], mean field [123–125], or intermediate [133] regime, but always assuming molecular chaos. Well-behaved hydrodynamic equations, expressed in terms of the slow modes of the dynamics, can then be derived from a controlled truncation and closure procedure, as detailed in Section 1.4.1. Most of the time, they show almost all the terms allowed, and are formally the same as equations written heuristically on symmetry arguments. However, the main interest of such approaches is that they keep track of the microscopic details in the (typically many) coefficients of the equations, which are all expressed as functions of the (typically few) particle-level parameters and physical fields. The phase space of the problem is thus considerably reduced.

While it plays the role of an intermediate step in the computation, one would expect that more information is present at the kinetic than at the hydrodynamic levels, especially far from the transition. Indeed, although in the best cases they are able to reproduce the phase diagram of the microscopic models, hydrodynamic equations rely on a perturbative scheme, and are thus, in principle, a correct description only at the onset of order. Deep in the ordered phase, they can therefore show spurious instabilities [80, 89] (see Figures 1.4(a),1.5(b) and 2.3), or non monotonicity of the order (see Figure 1.5(a)). Moreover, we know that in the polar class the band solution selection is done at the hydrodynamic level only in presence of stochastic terms [67] (see Section 1.4.1), it is not obvious whether it should occur or not in the deterministic kinetic equations. Despite several works at the kinetic level [133, 156], this point is still unexplored.

This Chapter is thus dedicated to the study of the Boltzmann and Smoluchowski equations introduced in Section 1.4. We determine their phase diagram from the linear stability analysis of their homogeneous solutions, and show that it is *qualitatively different* from the one of the Vicsek model presented in Section 1.3.1. Indeed, the homogeneous ordered solution computed at the kinetic level is found to be unstable in the low noise/large density regime for Boltzmann, and for any parameter in the Smoluchowski case. The correct picture with the coexistence region confined close to the transition is recovered in the Boltzmann, but not Smoluchowski, case considering equations with additional spatial diffusion terms. We further discuss how such terms can be derived from a discrete time dynamics. Numerical simulations of the Boltzmann equation reveal that the instability of the order is at the origin of the coexistence phase close to the transition. However, deeper in the ordered phase it leads to a polar liquid in which small amplitude waves propagate. A detailed study of the propagating solutions of the Boltzmann equation leads to conclude that, as at the deterministic hydrodynamic level, there is no band selection. Finally, the Boltzmann equations for the other classes are presented and the corresponding linear phase diagrams are computed.

3.2 The Boltzmann equation

In this section we study the homogeneous solutions and the linear phase diagram of the Boltzmann equation introduced in Chapter 1. We recall its expression for the modes of the single-particle distribution expressed in angular Fourier space

$$\partial_t f_k + \frac{1}{2}\left(\nabla^* f_{k+1} + \nabla f_{k-1}\right) = \left(P_k - 1\right) f_k + \sum_{q=-\infty}^{\infty} J_{k,q} f_q f_{k-q}\,, \tag{3.1}$$

where we have considered its nondimensional form. We recall the notations that will be used throughout this Chapter: the P_k are the modes of the noise distribution whose variance is η^2 (we choose it Gaussian for numerical evaluations: $P_k = \exp(-k^2\eta^2/2)$), the complex gradient $\nabla = \partial_x + \imath\partial_y$ and the collisional integral coefficients are defined by $J_{k,q} = \rho_0\left(P_k I_{k,q} - I_{0,q}\right)$ with ρ_0 the nondimensional density and

$$I_{k,q} = \left\{ \begin{array}{cc} \frac{4}{\pi}\frac{1-(k-2q)(-1)^q \sin\left(\frac{k\pi}{2}\right)}{1-(k-2q)^2} & \text{if } |k-2q| \neq 1 \\ \frac{2}{\pi} & \text{otherwise} \end{array} \right. . \tag{3.2}$$

The problem therefore has two independent control parameters: ρ_0 and η.

Homogeneous solutions

For any density and noise values, the Hierarchy (3.1) admits a space-independent fixed point $\mathcal{F} = \left\{\bar{f}_k\right\}_{k\geq 0}$, satisfying

$$\left(P_k - 1\right)\bar{f}_k + \sum_{q=-\infty}^{\infty} J_{k,q}\bar{f}_q\bar{f}_{k-q} = 0 \quad \forall k > 0 \tag{3.3}$$

and $\bar{f}_0 = \bar{\rho} = 1$ from the density conservation. Because of the rotational invariance of the problem, we choose the global polar order $\bar{f}_1$ to be real, thus and since there is no explicit chirality[1], the modes of the corresponding solution are all real.

The nature of $\mathcal{F}$ is determined by the sign of the linear coefficient of the polar field equation: $\mu_1 = P_1 - 1 + \frac{4}{\pi}\left(P_1 - \frac{2}{3}\right)\rho_0$. When $\mu_1 < 0$, the only solution is disordered: $\bar{f}_k = 0\ \forall k > 0$. On the contrary, if μ_1 is positive $\bar{f}_1$ starts to grow as well as the other fields thanks to the nonlinear couplings, finally all saturate to reach the homogeneous ordered solution $\bar{f}_k \neq 0\ \forall k > 0$. $\mathcal{F}$ can be numerically approximated truncating (3.1) at a given order K, *i.e.* setting all the modes with index $k > K$ to 0. Hydrodynamic equations derived from the Boltzmann-Ginzburg-Landau approach (1.13) (see Section 1.4.1) are thus obtained with $K = 1$, but using a more sophisticated closure scheme that consists in enslaving the second mode to

---

[1] Otherwise the $J_{k,q}$ coefficients could be complex.

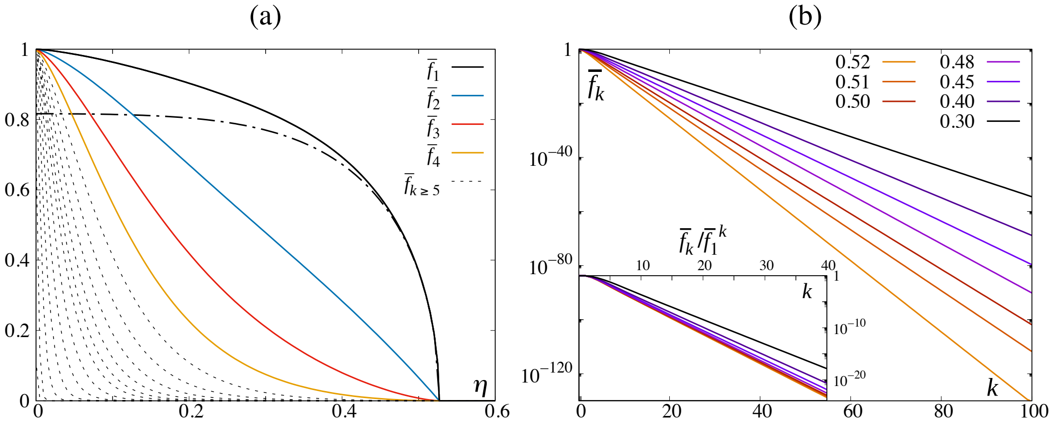

FIGURE 3.1 – Homogeneous solution of the Boltzmann equation (3.1) at fixed $\rho_0 = 0.5$ varying the noise η at $K = 100$. (a): The modes as function of η. The dashed lines correspond, from right to left, to $k = 5$, 6, 7, 8, 9, 10, 12, 15, 20, 30, 60, 100. The dashed-dotted black line shows the homogeneous solution of the hydrodynamic equations (1.13) at same parameters. (b): The modes as function of k for several noise values (transition at $\eta_c \approx 0.527$) showing an exponential decay. Inset: Zoom at smaller k for the same curves divided by f_1^k. Their collapse in the vicinity of the mean field transition indicates the scaling behavior (3.4).

the first one. In the following we will refer to truncations of the Hierarchy (3.1) with $K > 1$ without closure[2] as *kinetic level* .

The homogeneous solution of (3.3) is shown in Figure 3.1(a) for $K = 100$ at fixed density $\rho_0 = 0.5$, for which the transition occurs at $\eta_c \simeq 0.527$. We find a good agreement with the polar field solution of the hydrodynamic equations (1.13) for $0.48 \lesssim \eta \leq \eta_c$, indicating that the scaling of the modes used for their derivation

$$\bar{f}_k \approx \varepsilon^k \,, \tag{3.4}$$

should be valid in this region. Conversely, while the large k modes are negligible close to the ordering transition, they are all $\mathcal{O}(1)$ when η becomes small, leading to large deviations between hydrodynamic and kinetic levels.

Figure 3.1(b) shows that the modes at fixed noise scale exponentially with k large enough. The scaling hypothesis(3.4) implies that the modes $\bar{f}_k = \alpha_k \bar{f}_1^k$ where α_k is independent of η. Plotting $\bar{f}_k/\bar{f}_1^k$ for various noise values we indeed find that the curves collapse for low k and $0.48 \lesssim \eta \leq \eta_c$, in agreement with our preceding evaluation of the region where the scaling holds.

Linear stability analysis

In order to compute the stability of the numerical solution $\mathcal{F}$, we linearize the modes as $f_k = \bar{f}_k + \delta f_k$. The corresponding hierarchy for the perturbations reads

$$\partial_t \delta f_k + \frac{1}{2}\left(\nabla^* \delta f_{k+1} + \nabla \delta f_{k-1}\right) = \left(P_k - 1\right)\delta f_k + \sum_{\substack{q=-K \\ |k-q|\leq K}}^{K} \left(J_{k,q} + J_{k,k-q}\right) \bar{f}_{k-q} \delta f_q \,, \tag{3.5}$$

---

[2] We checked that for K large enough closure has no qualitative effect.

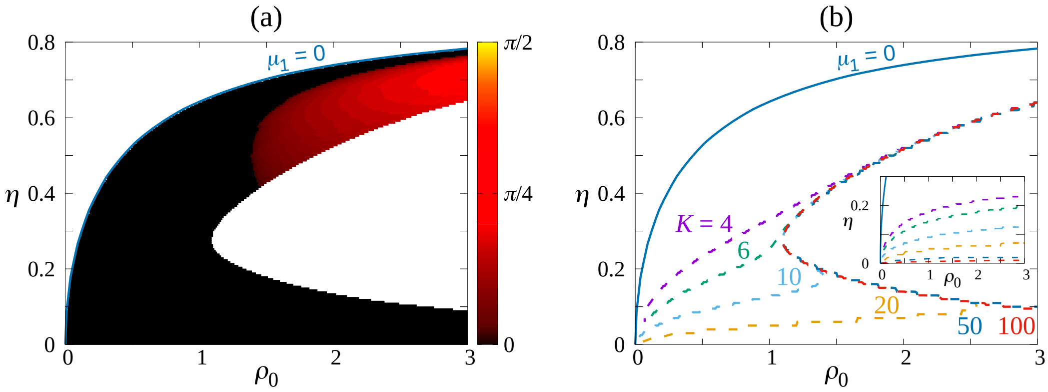

FIGURE 3.2 – (a): Asymptotic phase diagram of the Boltzmann equation (3.1) in the (ρ_0, η) plane. The colored surface marks points where the homogeneous ordered solution is unstable, the color code indicates the direction of the most unstable wave vector w.r.t. the order. (b): Evolution of the line marking the existence of the instability of the homogeneous ordered solution with the truncation order K. The inset shows the corresponding contours marking the upper limit of existence of the spurious instability. In both (a) and (b) the continuous blue line labels the mean field transition.

which can be written, defining the $(K+1)$-dimensional vector $\vec{\delta f} = (\delta\rho, \delta f_1, \ldots, \delta f_K)$, as

$$\partial_t \vec{\delta f} = \mathbf{\Gamma} \vec{\delta f}\,. \tag{3.6}$$

The complex matrix is given by

$$\begin{aligned}\Gamma_{kq} \;=\;& (P_k - 1)\,\delta_{kq} - \frac{1}{2}\nabla^*\delta_{k+1\,q} - \frac{1}{2}\nabla\left(\delta_{k0}\delta_{q1}\vartheta + \mathcal{I}_{1-k}\delta_{k-1\,q}\right) \\ &+ \left(J_{k,q} + J_{k,k-q}\right)\bar{f}_{k-q} + \sum_{p=1}^{K-k}\left(J_{k,-p} + J_{k,k+p}\right)\bar{f}_{k+p}\delta_{pq}\vartheta\,,\end{aligned} \tag{3.7}$$

where δ_{ij} is the Kronecker delta, the indicator function $\mathcal{I}_i$ returns 1 if $i \leq 0$ and 0 otherwise, and $\vartheta f_k = f_k^*$ is the complex conjugate operator. $\mathcal{F}$ is stable if and only if all the real parts of the eigenvalues of this matrix are negative or zero[3]. We computed them numerically in the spatial Fourier space, *i.e.* for $\vec{\delta g}(\vec{q}, t) = \int d\vec{r}\; \vec{\delta f}(\vec{r}, t)\exp(-2\imath\pi\vec{q}\cdot\vec{r})$, and the resulting phase diagram is shown in Figure 3.2.

As expected, the disordered solution for $\mu_1 < 0$ is always stable. Considering $\mu_1 > 0$, for truncation orders $K \lesssim 10$ the behavior of the hydrodynamic equations is recovered: the homogeneous ordered solution is unstable to longitudinal perturbations close to the line $\mu_1 = 0$ and the low noise phase exhibits another region of instability, already mentioned in Section 1.4.1. Increasing K this second instability becomes confined to lower noises so that it almost disappears at $K = 100$ (see inset of Figure 3.2(b)). We therefore conclude that it is an artifact of the truncation procedure.

However, for $K \geq 10$ the longitudinal instability domain, initially next to the transition, invades the whole low noise region, leaving asymptotically a pocket of stability limited to intermediate η and $\rho_0 \gtrsim 1$ (see Figure 3.2(a)). Consequently, the

---

[3] Because of the symmetries of the problem, we expect a Goldstone mode associated to zero eigenvalue, which corresponds to global rotations of the solution. Therefore its stability, in the sense considered here, does not require that all eigenvalues of $\mathbf{\Gamma}$ are strictly negative.

Boltzmann equation (3.1) does not show any homogeneous ordered solution stable at low densities, similarly to what was observed in Vicsek-style models with fore-aft asymmetry [105]. This result in particular contradicts the numerical study of the Boltmann equation carried out by Thüroff *et al.* [156] where a more "classic" phase diagram, with an instability restricted to the vicinity of the transition, was found. As we will show in Section 3.4, this discrepancy is related to their numerical scheme that is shown to suppress the low noise instability.

3.3 The Smoluchowski equation

We now study the mean field Smoluchowski equation introduced in Section 1.4.2, whose expression for the angular Fourier modes reads

$$\partial_t f_k + \frac{1}{2}\left(\nabla^* f_{k+1} + \nabla f_{k-1}\right) = -k^2 f_k + \rho_c k \left(f_1 f_{k-1} - f_1^* f_{k+1}\right) . \qquad (3.8)$$

In this case the linear coefficient of the polar field is given by $\rho_c - 1$ and the transition to order occurs at $\rho_c = 1$. Contrary to the Boltzmann case, for $\rho_c > 1$ perturbations of the disordered solution $\bar\rho = 1$, $\bar f_k = 0 \ \forall k > 0$ are not bounded so that the hierarchy (3.8) truncated at any order K does not admit a homogeneous ordered fixed point. We thus need to close it, to do so let us write the equation for the $K+1$ mode

$$\partial_t f_{K+1} + \frac{1}{2}\nabla^* f_{K+2} + \rho_c(K+1) f_1^* f_{K+2} = -(K+1)^2 f_{K+1} - \frac{1}{2}\nabla f_K + \rho_c(K+1) f_1 f_K \, , \qquad (3.9)$$

where, considering the scaling ansatz introduced in Section 1.4.1, terms on the r.h.s. scale like ε^{K+1} while the ones on the l.h.s. are of order greater than $K+2$ and can be discarded. f_{K+1} can then be slaved to f_1 and f_K. Moreover, it appears only in the equation of f_K, which yields

$$\begin{aligned}\partial_t f_K \ &= \ -K\left(K + \frac{\rho_c^2}{K+1}|f_1|^2\right) f_K + \rho_c K f_1 f_{K-1} - \frac{1}{2}\nabla f_{K-1} \\ &\quad + \frac{1}{4(K+1)^2}\Delta f_K + \frac{\rho_c}{2(K+1)}\left[\frac{K}{K+1} f_1^* \nabla f_K - \nabla^*\left(f_1 f_K\right)\right] \, , \end{aligned} \qquad (3.10)$$

where we note that setting $K = 1$, we recover the deterministic hydrodynamic equation (1.17) for the polar field f_1.

Homogeneous Equations (3.8) for $k < K$ and (3.10) together are well behaved and admit an ordered solution $\mathcal{F} = \left\{\bar f_k\right\}_{0 \le k \le K}$. Figure 3.3(a) shows that for $\rho_c \gtrsim 1$ kinetic and hydrodynamic level solutions are in good agreement. On the contrary, for larger ρ_c, $\bar f_1$ is monotonous at the kinetic level while its hydrodynamic counterpart is not, leading to large deviations. We deduce that the scaling (3.4) is verified only in the immediate vicinity of the transition, which is confirmed by the collapse of the curves $\bar f_k / \bar f_1^k$ occurring only for $\rho_c \lesssim 1.1$.

Using the procedure presented in the previous section, we study the linear stability of the solution $\mathcal{F}$. It is found to converge with K is faster than for the Boltzmann equation, probably because of the few nonlinearities at play, and we can safely consider $K = 10$. As at the hydrodynamic level, $\mathcal{F}$ is unstable for any $\rho_c > 1$, but for K large enough to longitudinal perturbations only, as shown in Figure 3.3(b). Contrary to the Boltzmann case, we therefore conclude that the large ρ_c instability seen at the hydrodynamic level is *not* spurious.

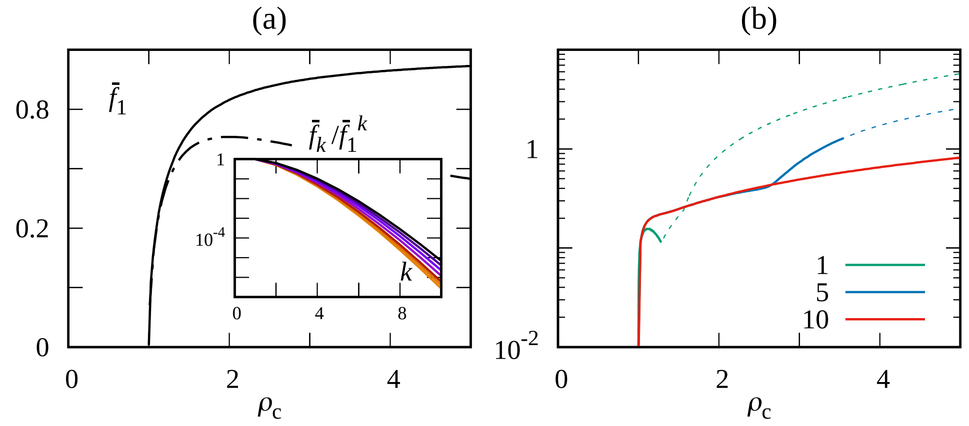

FIGURE 3.3 – (a): Polar order given by the homogeneous solution of the Smoluchowski equation (3.8) for $K = 10$. The dashed-dotted black line shows the homogeneous solution of the deterministic hydrodynamic equations (1.17). Inset: The modes as function of k divided by f_1^k for $\rho_c = 1$, 1.05, 1.1, 1.2, 1.3, 1.4, 1.5 showing the scaling close to the transition. (b): Growth rate of the instability of the homogeneous solution of Equation (3.8) for various K ($K = 1$ corresponding to the hydrodynamic equations). When continuous, the lines indicate that the most unstable wave vector is longitudinal to the order.

3.4 Introduction of spatial diffusion

3.4.1 Phase diagram with spatial diffusion

The phase diagram of Figure 3.2(a) is qualitatively different than the one determined in [156] from numerical simulations of the Boltzmann equation. The algorithm used in this work is based on first order in time finite volume methods. Such schemes are popular in the hydrodynamic community because they support steep solutions, such as the Vicsek polar waves present close to the ordering transition, and allow to consider irregular meshes and various types of boundary conditions [157]. However, these methods are known to introduce numerical diffusion, whose amplitude scales like $\frac{dx^2}{\tau}$, where dx and τ are respectively space and time resolutions. Correction terms of next order in τ can balance this effect, but were not considered in [156]. Moreover, the values used there are $dx = 5$ and $\tau \ll 1$, we thus expect that the corresponding simulations were subject to *strong numerical diffusion.*

In order to study the effect of spatial diffusion on the phase diagram of the Boltzmann equation (3.1), we compute its linear stability in the presence of an additional Laplacian term: $D_0 \Delta f_k$. Figure 3.4(a) shows that the instability on the low noise region disappears progressively increasing D_0. Finally, for $D_0 = 0.5$ the phase diagram corresponds to the one of the microscopic model with an instability confined close to the transition line, as observed by Thüroff *et al.*. The same analysis carried out for the Smoluchowski equation (3.8) reveals that the large ρ_c instability persists, even for large D_0, but becomes transversal (see Figure 3.4(b)).

To summarize at this point, the Boltzmann equation proposed by Bertin *et al.* exhibits an intriguing low noise instability of its homogeneous ordered solution. We have furthermore shown that adding positional diffusion, the “usual” phase diagram of the Vicsek model is recovered. Moreover, since spatial diffusion is nominally present at the hydrodynamic level because of the truncation and closure procedure (see Section 1.4.1, Equations (1.13)), the latter cannot capture the low noise instability of the

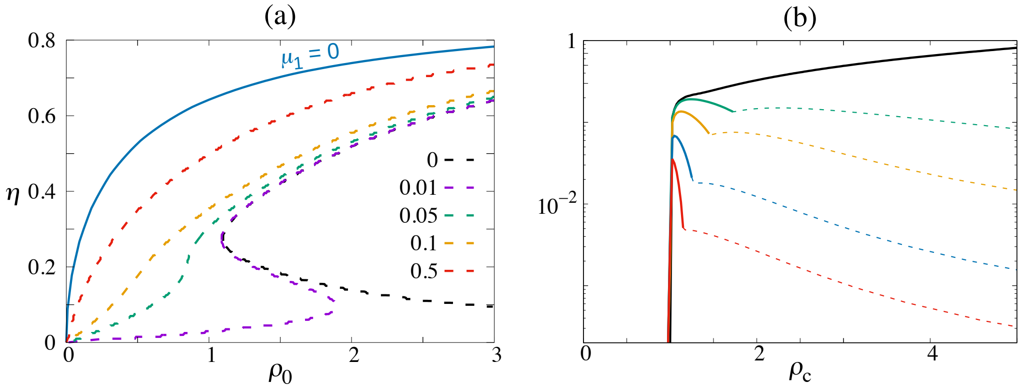

FIGURE 3.4 – Linear stability of the Boltzmann (3.1) and Smoluchowski (3.8) equations in presence of additional spatial diffusion (of the form $D_0\Delta f_k$). (a): The dashed lines delimit the instability region of the homogeneous ordered solution of the Boltzmann equation for several values of D_0 and $K = 50$. The mean field transition is given by the continuous blue line. (b): Growth rate of the instability of the homogeneous ordered solution of the Smoluchowski equation as function of ρ_c for, from top to bottom, $D_0 = 0$, 0.01, 0.1, 1, 5 and $K = 10$. The instability is directed along the order when lines are continuous.

order. On the contrary, the Smoluchowski equation does not have a stable homogeneous ordered solution for any parameter and additional diffusion. The Boltzmann description is thus found to be more faithful to the microscopic models it aims to describe, in the following we will therefore focus on this case.

The Vicsek model was first expressed in a discrete time form [68] ($\tau = 1$) and most of numerical studies are done in this framework. However, continuous descriptions are usually derived in the limit $\tau \to 0$ limit[4]. Because of this approximation, the resulting continuous equations lack of spatial diffusion. In the next section, we show how positional diffusion terms naturally arise in the finite τ limit.

3.4.2 Derivation of spatial diffusion terms: the discrete time limit

We thus consider Vicsek-style point-like particles that, at every timestep τ, jump with length $v_0\tau$ in the direction given by their polarity. In a Boltzmann spirit, collisions are treated separately from the free motion dynamics. We show that the resulting equations, written at second order in τ, have new spatial diffusion terms that modify substantially the phase diagram of the system at the kinetic level.

Free motion

Let us first write the evolution of the single-particle distribution function considering a collisionless dynamics. The discrete time Vicsek algorithm (1.2) is divided into two steps: agents first update their direction of motion, so with only noise kicks here, and then their position with the new velocity. The master equation for the distribution $f^t(\vec{r},\theta)$ thus reads

$$f^{t+\tau}(\vec{r},\theta) = \int_0^{2\pi} d\theta' \, P_\tau(\theta-\theta') f^t(\vec{r}-\delta\vec{r}(\theta),\theta') \,, \tag{3.11}$$

---

[4] Except for Ihle's approach from [133], where the kinetic equation is derived for finite timesteps, but no discussion of the low noise regime is provided.

where $\delta\vec{r}(\theta) = v_0\tau\hat{e}(\theta)$, P_τ is the τ-dependent noise distribution and we have adopted the superscript notation in order to emphasize that time is discrete. Naturally P_τ converges to a Dirac distribution when $\tau \to 0$. Since Equation (3.11) describes a dynamics where angles are updated before positions, the careful reader will remark that the two angles in the arguments of f^t inside the integral are different. The other scheme, which gives essentially the same results, is addressed in Section 3.4.3.

We note that in the discrete time implementations of the Vicsek rules, $v_0\tau$ is not small but of order $\lesssim 1$. In the following we thus Taylor expand of the r.h.s. of this equation keeping terms up to order $v_0^2\tau^2$

$$f^{t+\tau}(\vec{r},\theta) = \left[1 - v_0\tau e_\alpha(\theta)\partial_\alpha + \frac{v_0^2\tau^2}{2} e_\alpha(\theta)e_\beta(\theta)\partial_\alpha\partial_\beta\right]\left(P_\tau * f^t\right) , \tag{3.12}$$

where summation over repeated indices is assumed and the angular convolution is defined as $(P_\tau * f^t) = \int_0^{2\pi} d\theta'\, P_\tau(\theta-\theta')f^t(\vec{r},\theta')$. Denoting by $\Delta_\tau f^t = \frac{1}{\tau}\left(f^{t+\tau}(\vec{r},\theta) - f^t(\vec{r},\theta)\right)$ the time differential operator, we get the following evolution equation

$$\Delta_\tau f^t = \frac{1}{\tau}\left[\left(P_\tau * f^t\right) - f^t(\vec{r},\theta)\right] + \left[-v_0 e_\alpha(\theta)\partial_\alpha + \frac{v_0^2\tau}{2} e_\alpha(\theta)e_\beta(\theta)\partial_\alpha\partial_\beta\right]\left(P_\tau * f^t\right) . \tag{3.13}$$

Continuous time limit

In the limit $\tau \to 0$, P_τ converges to a Dirac distribution. Thus we can write for τ small

$$P_\tau(\theta) = \delta(\theta) + \tau\mathcal{A}(\theta) , \tag{3.14}$$

where, from the conservation of P_τ, $\mathcal{A}$ must satisfy $\int_{-\infty}^{\infty} d\theta\, \mathcal{A}(\theta) = 0$. We therefore get

$$\lim_{\tau\to 0} \Delta_\tau f^t = \partial_t f = (\mathcal{A} * f) - v_0 e_\alpha(\theta)\partial_\alpha f , \tag{3.15}$$

which corresponds to the collisionless part of the Boltzmann equation (1.6) that uses $\mathcal{A}(\theta) = P_\eta(\theta) - \delta(\theta)$ with η^2 the variance of the noise distribution P_η[5]. In the following we will thus use P_η to the detriment of P_τ.

Inserting this expression of P_τ in Equation (3.11), it formally describes a dynamics where tumblings occur at a probability τ. (Inversely the particles do not change their direction of motion with a probability $1 - \tau$.) This model therefore interpolates between discrete ($\tau = 1$) and continuous ($\tau \to 0$) time versions of the Vicsek rules.

The Boltzmann equation

To write the complete Boltzmann equation, we treat interactions separately from the free motion dynamics. Assuming binary collisions and molecular chaos, the collisional integral remains the one defined in the $\tau \to 0$ limit

$$\begin{aligned} I_{\text{coll}}\left[f^t\right] &= -f^t(\vec{r},\theta)\int_0^{2\pi} d\theta' K(\theta'-\theta)f^t(\vec{r},\theta') \qquad (3.16)\\ &+ \int_0^{2\pi} d\theta_1 \int_0^{2\pi} d\theta_2 f^t(\vec{r},\theta_1)f^t(\vec{r},\theta_2)K(\theta_2-\theta_1)P_\eta(\theta-\theta_1-H(\theta_2-\theta_1)) , \end{aligned}$$

---

[5] The tumbling rate λ in Equation (1.6) is given in units of τ and is by definition 1 here.

with $K(\theta) = 4r_0v_0 \left|\sin\left(\frac{\theta}{2}\right)\right|$ and $H(\theta) = \frac{\theta}{2}$ as defined in Section 1.4.1. The complete equation reads

$$\begin{aligned}\Delta_\tau f^t &= -v_0 e_\alpha(\theta)\partial_\alpha f^t + \left(P_\eta * f^t\right) - f^t + I_{\text{coll}}\left[f^t\right] \\ &\quad + v_0\tau\left[-e_\alpha(\theta)\partial_\alpha\left(\left(P_\eta * f^t\right) - f\right) + \frac{v_0}{4}\Delta f^t + \frac{v_0}{2}q_{\alpha\beta}(\theta)\partial_\alpha\partial_\beta f^t\right], \quad (3.17)\end{aligned}$$

where we have decomposed the spatial diffusion into an isotropic (Laplacian) and anisotropic ($\sim q_{\alpha\beta}(\theta) = e_\alpha(\theta)e_\beta(\theta) - \delta_{\alpha\beta}/2$) parts. Equation (3.17) describes the evolution of a discrete time aligning active matter model belonging to the Vicsek universality class. It simply takes the form of the continuous time Boltzmann equation to which are added advection and positional diffusion terms that vanish in the limit $\tau \to 0$. After rescaling space, K, f^t and denoting $D_0 = \frac{1}{4}$ and $D_1 = 2D_0$ we get a nondimensional equation, whose expression in angular Fourier space reads

$$\begin{aligned}\Delta_\tau f_k^t &= -\frac{1-\tau(1-P_{k+1})}{2}\nabla^* f_{k+1}^t - \frac{1-\tau(1-P_{k-1})}{2}\nabla f_{k-1}^t + (P_k - 1)f_k^t \\ &\quad + \sum_{q=-\infty}^{\infty} J_{k,q} f_q^t f_{k-q}^t + \tau\left[D_0\Delta f_k^t + \frac{D_1}{4}\left(\nabla^{*^2} f_{k+2}^t + \nabla^2 f_{k-2}^t\right)\right], \quad (3.18)\end{aligned}$$

where we kept the same notations as in Section 3.2. We choose $P_k = \exp(-k^2\eta^2/2)$ for numerical evaluations in the following.

Truncation and closure, hydrodynamic equations

As in the continuous time case, hydrodynamic equations can be derived from the Hierarchy (3.18). Since the new advection terms do not influence the stability of the disordered solution, we use the truncation and closure techniques presented in Section 1.4.1, which yield

$$\begin{aligned}\Delta_\tau \rho^t &= \tau D_0 \Delta\rho^t - [1-\tau(1-P_1)]\,\Re\left(\nabla^* f_1^t\right), \quad (3.19a)\\ \Delta_\tau f_1^t &= -\frac{1}{2}\nabla\rho^t + \left(\mu_1\left[\rho^t\right] - \xi|f_1^t|^2\right) f_1^t + \nu^\tau \Delta f_1^t + \chi^\tau \nabla^2 f_1^{t^*} \\ &\quad + \kappa_1^\tau f_1^t \nabla^* f_1^t + \kappa_2^\tau f_1^{t^*}\nabla f_1^t, \quad (3.19b)\end{aligned}$$

where the coefficients are listed in Table 3.1 and their dependences in ρ and τ have been made explicit. We note that Equations (3.19) have been derived assuming that the time evolution operator $\Delta_\tau \approx |f_1^t| \approx \varepsilon \ll 1$ in the vicinity of the the ordering transition. Therefore, these hydrodynamic equations are valid in the limit of τ “small”. We nevertheless checked that the coefficient of the Laplacian, ν^τ, remains positive for $\tau \leq 1$ in the range of parameters we consider.

Linear stability analysis of the homogeneous ordered solution

We now compute the linear stability of the homogeneous ordered solution of the kinetic (3.18) and hydrodynamic (3.19) equations. Because these equations are derived in the discrete time limit, the stability condition at finite τ is expressed slightly differently. In the following we detail the procedure for the kinetic case, which is easily generalizable to the hydrodynamic equation.

$\mu_1[\rho]$	$P_1 - 1 + \frac{4}{\pi}\left(P_1 - \frac{2}{3}\right)\rho_0\rho$
ξ	$\frac{16}{\pi}\frac{(5P_1-2)(3P_2+1)\rho_0^2}{15\pi(1-P_2)+8(7+5P_2)\rho_0}\ (>0)$
ν^τ	$\tau D_0 + \frac{15\pi(1-\tau(2-P_1-P_2))}{4(15\pi(1-P_2)+8(7+5P_2)\rho_0)}\ (>0)$
χ^τ	$\frac{\tau D_1}{4}$
κ_1^τ	$\frac{20(1+3P_2)(1-\tau(1-P_2))\rho_0}{15\pi(1-P_2)+8(7+5P_2)\rho_0}$
κ_2^τ	$\frac{6(2-5P_1)(1-\tau(1-P_1))\rho_0}{15\pi(1-P_2)+8(7+5P_2)\rho_0}$

Table 3.1 – Coefficients of the hydrodynamic equations (3.19).

We note $\left\{\bar{f}_k\right\}_{0\leq k\leq K}$ the homogeneous fixed point of the truncated Hierarchy (3.18). Small perturbations δf_k^t around this solution evolve according to

$$\begin{aligned} \delta f_k^{t+\tau} &= \delta f_k^t + \tau\Bigg\{-\frac{1-\tau(1-P_{k+1})}{2}\nabla^*\delta f_{k+1}^t - \frac{1-\tau(1-P_{k-1})}{2}\nabla\delta f_{k-1}^t + (P_k-1)\delta f_k^t \\ &+ \sum_{\substack{q=-K \\ |k-q|\leq K}}^{K} \left(J_{k,q}+J_{k,k-q}\right)\bar{f}_{k-q}\delta f_q^t + \tau\left[D_0\Delta\delta f_k^t + \frac{D_1}{4}\left({\nabla^*}^2\delta f_{k+2}^t + \nabla^2\delta f_{k-2}^t\right)\right]\Bigg\} \end{aligned} \quad (3.20)$$

Therefore, the vector $\vec{\delta f}^{\,t} = \left(\delta f_0^t, \delta f_1^t, \ldots, \delta f_K^t\right)$ satisfies

$$\vec{\delta f}^{\,t+\tau} = \left[\mathbf{I} + \tau\mathbf{\Gamma}\right]\vec{\delta f}^{\,t}, \quad (3.21)$$

where $\mathbf{I}$ is the identity matrix and $\mathbf{\Gamma}$ is computed from Equation (3.20). The fixed point $\left\{\bar{f}_k\right\}$ is stable if and only if $|\vec{\delta f}^{\,t+\tau}| \leq |\vec{\delta f}^{\,t}|$, *i.e.* if the eigenvalues of the matrix $\mathbf{\Gamma}$ are all negative or zero[6].

The linear stability of the homogeneous ordered solution of the kinetic equation (3.18) is shown in Figure 3.5(a) for $K = 50$. A value of τ larger than 10^{-2} is sufficient to suppress any instability far from the transition. In the scope of the preceding section, we relate this result to the additional diffusion terms appearing at this order in τ. The phase diagram of the Vicsek model is thus recovered in the finite τ regime.

At the hydrodynamic level, the region of spurious instability of the order is substantially reduced to low densities increasing τ, although not suppressed (see Figure 3.5(b)). At the same time, the instability close to the threshold is barely affected by the values of τ. As mentioned in Section 1.4.1, is it known that adding positional diffusion to the hydrodynamic equations derived from the Boltzmann-Ginzburg-Landau approach has a similar effect on the spurious instability [80]. We conclude that these hydrodynamic equations, as before, remain a good description at the onset of order.

---

[6] As in the continuous time case, the Goldstone mode satisfies $|\vec{\delta f}^{\,t+\tau}| = |\vec{\delta f}^{\,t}|$. Therefore the stability of the homogeneous solution, in the sense considered here, does not require a strictly contracting operator.

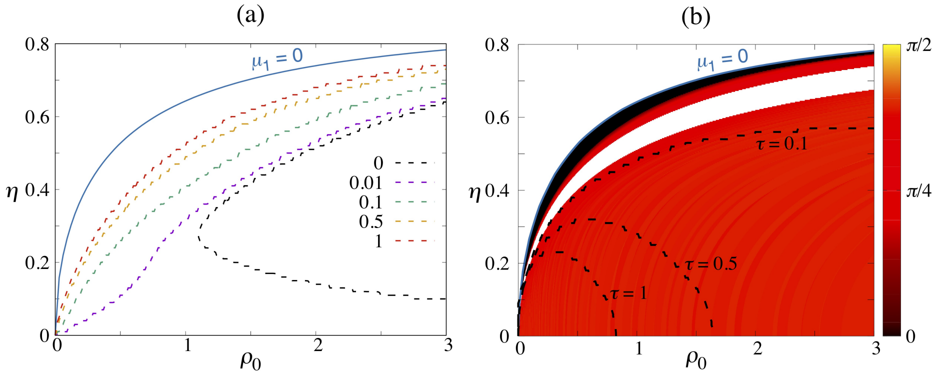

FIGURE 3.5 – Linear stability of the discrete time Boltzmann (3.17) (a) and hydrodynamic (3.19) (b) equations in the density-noise plane. (a): Limit of the instability region of the homogeneous ordered solution for different values of the timestep τ at $K = 50$. (b): Direction of the most unstable wave vector w.r.t. the order (white meaning that the solution is found stable) at $\tau = 0$. The dashed lines show the shape of the spurious instability region at finite τ. In both (a) and (b) the continuous blue line marks the mean field transition.

3.4.3 Forward vs. backward update rules

The formalism presented above allows to treat the "backward" case, *i.e.* when positions are updated before orientations. The corresponding Master equation reads

$$f^{t+\tau}(\vec{r},\theta) = \int_0^{2\pi} d\theta' \left[\tau P_\eta(\theta-\theta') + (1-\tau)\delta(\theta-\theta')\right] f^t(\vec{r}-\delta\vec{r}(\theta'),\theta')\,, \tag{3.22}$$

and differs from (3.11) only in the angular dependence of the position increment $\delta\vec{r}$. The procedure to derive the discrete time kinetic equation is essentially the same as presented before, after some algebra we find the following hierarchy for the modes

$$\begin{aligned}\Delta_\tau f_k^t \;&=\; -\frac{1-\tau(1-P_k)}{2}\nabla^* f_{k+1}^t - \frac{1-\tau(1-P_k)}{2}\nabla f_{k-1}^t + (P_k-1)f_k^t \\ &\quad + \sum_{q=-\infty}^{\infty} J_{k,q} f_q^t f_{k-q}^t + \tau\left[D_0\Delta f_k^t + \frac{D_1}{4}\left(\nabla^{*^2} f_{k+2}^t + \nabla^2 f_{k-2}^t\right)\right].\end{aligned} \tag{3.23}$$

We note that the difference between these equations and (3.18) lies in the coefficients of the advection terms that now depend on k instead of $k \pm 1$. It is then easy to check that, as in the other case, taking the limit $\tau \to 0$ we recover the continuous time Boltzmann equation (3.1).

The homogeneous ordered solution between the two cases is therefore the same. We computed its stability numerically and it is compared to the forward rule in Figure 3.6. The two schemes are shown to be qualitatively the same except that the wavelength of the most unstable mode is found to be larger in the backward than in the forward case, contrary to the growth rate of the instability that is smaller. We conclude that the backward scheme should be more subject to finite size effects. This result is in agreement with microscopic simulations of the Vicsek model for which it is known that the band regime typically appears for larger sizes and longer times using the backward update rule [158].

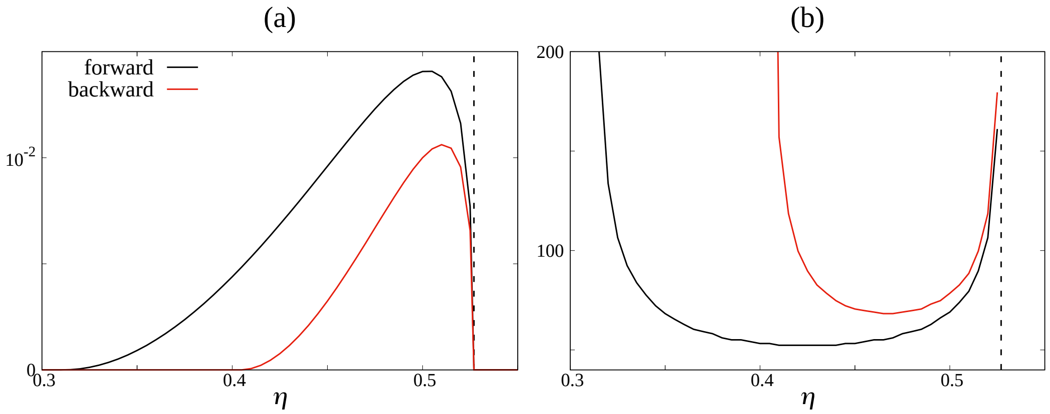

FIGURE 3.6 – Linear stability of the homogeneous ordered solution of the kinetic equations (3.18) and (3.23) for the forward and backward updating rules at $\rho_0 = 0.5$, $\tau = 1$ and $K = 100$. (a) and (b) represent respectively the growth rate of the instability and the wavelength of its most unstable mode. In both panels the vertical dashed line indicates the mean field transition at $\eta_c \simeq 0.527$.

3.5 Numerical integration of the Boltzmann equation

In order to go beyond the linear level, we simulated the hierarchy (3.1) with a pseudo-spectral scheme iterated in time by means of an explicit fourth-order Runge-Kutta method. In order to avoid confusion, we point out that simulations are done in angular Fourier space, pseudo-spectral referring only to space derivatives. The linear terms (advection, spatial and angular diffusions) were thus evaluated from the Fourier transform of the modes $g_k(\vec{q},t) = \int d\vec{r} f_k(\vec{r},t) \exp(-2\imath\pi\vec{q}\cdot\vec{r})$, while nonlinearities (collisions) were computed from the modes in real space. We considered rectangular domains of size $N_x dx \times N_y dy$ with periodic boundary conditions. In order to avoid aliasing effects due to the square nonlinearities, we applied the the 2/3 Rule, *i.e.* zero-padding $g_k(\vec{q},t)$ for $|q_x| > 2\pi/(3dx)$ or $|q_y| > 2\pi/(3dy)$. A large spatial resolution was needed because of the steep wave fronts that take place in regions where the order is unstable, in most cases we considered $dx = dy = \frac{1}{8}$ and $\tau \gtrsim 10^{-3}$. The simulations were all run until they reach a fixed point (or a limit cycle) of the equation, *i.e.* until all the space-averaged values of the modes $\langle f_k \rangle_{xy}$ converge to numerical precision. The code was parallelized in order to run large systems over long times.

The Smoluchowski equation (3.8) was simulated with the same code. Starting from an ordered initial condition close to the transition with 10 modes, we could observe its linear instability. However, the resulting band-like structures show sharp fronts and their amplitude is not bounded, we were not able to stabilize them increasing the spatial resolution. The full equations thus seem ill-behaved. Adding isotropic spatial diffusion regularizes the solutions and we were able to see the formation of polar bands. This case is still under investigation during the redaction of this manuscript, this section being entirely devoted to the Boltzmann approach.

3.5.1 Inhomogeneous solutions of the Boltzmann equation

Propagating band solutions

The Boltzmann equation was first integrated close to the transition starting from the homogeneous ordered solution, that was determined numerically, and on top of which some noise was added. Because of the instability highlighted previously, we observed

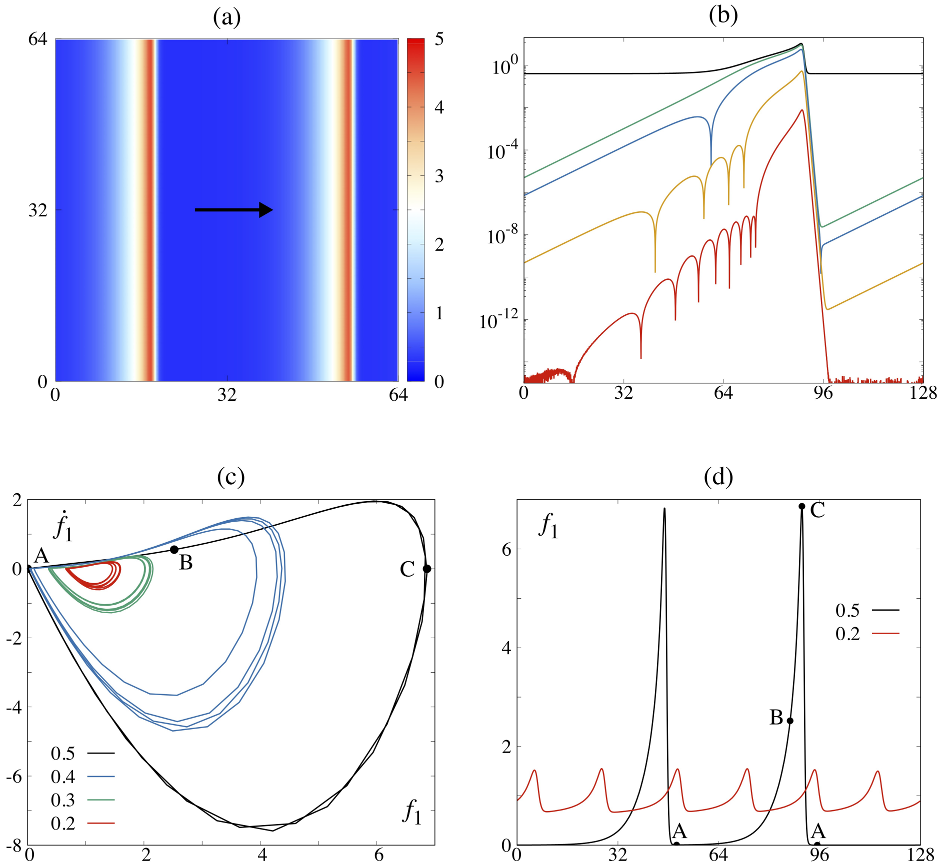

FIGURE 3.7 – Traveling solutions of the Boltzmann equation (3.1). (a): Snapshot of the density field at $\rho_0 = 1$, $\eta = 0.55$, $K = 30$ ($\lambda_u \lesssim 20$), $dx = dy = \frac{1}{4}$. (b): Profile of the modes along the x axis in a quasi-one dimensional geometry. The curves show, from top to bottom, ρ, f_1, f_2, f_5 and f_{10} at $\rho_0 = 0.5$, $\eta = 0.5$, $K = 10$, system size 128×1, $dx = \frac{1}{32}$, and $dy = \frac{1}{8}$. (c): Trajectories of the band solutions in the $(f_1, \dot{f}_1)$ plane for different noise values showing smaller cycles as η decreases. (d): The polar field profiles corresponding to (c) for $\eta = 0.5$ ($\lambda_u \lesssim 45$) and 0.2 ($\lambda_u \lesssim 20$). In (c-d) $\rho = 0.5$, $K = 20$, system size is 128×1, and $dx = dy = \frac{1}{8}$. The black arrow in (a) indicates the direction of propagation of the solutions. Simulations in (a,c-d) and (b) have been done starting respectively from homogeneous ordered and disordered initial conditions.

the formation of a train of one dimensional propagating structures (see Figure 3.7(a)) that constitutes a stable limit cycle of the equations. These bands can have large amplitudes, and in general exhibit abrupt fronts as shown in Figure 3.7(b). Because of this, numerical instabilities for low values of the fields can be avoided only with high resolution, thus in this part most of our simulations have been done in quasi-one dimensional geometries.

The number of bands is roughly given by the wavelength associated to the most unstable mode of the homogeneous ordered solution λ_u (see Figures 3.7(a,d)). However, starting from a disordered initial condition as in Figure 3.7(b), or moving them in the (ρ_0, η) plane, we notice that solutions with different number of bands are accessible. We checked that all of them remain stable when truncating the hierarchy for larger K.

The density and polar order decay exponentially to ρ_g, the mean field transitional density at fixed η, and 0 both at the front and the tail of the bands (see Figure 3.7(b)), as observed in micro simulations of the Vicsek model [70]. The associated lengthscales are generally much larger at the back than at the front, both remain constant when varying the number of bands. The other modes show a similar behavior but oscillate around $f_k = 0$, the number of oscillations being given by $k-1$. Except for the density, all the modes decrease quickly by several orders of magnitude when going away from the bands' maximum, we thus expect weak interactions between these objects.

It was shown in Section 3.2 that the homogeneous ordered solution of the Boltzmann equation is unstable in the whole low noise region and for all $\rho_0 \lesssim 1$ (see Figure 3.2(a)). Fixing the density to $\rho_0 = 0.5$, we ran simulations for various values of η from 0.5 to 0.2 starting from homogeneous ordered initial condition. We observed that when η decreases the "gas" level, *i.e.* the density far from the band, rises and become much larger than ρ_g, so that their amplitude decreases and the final state of the system consists is a spatially modulated ordered liquid with propagating waves shown in Figure 3.7(d). Bringing the bands initially close to the transition deeper in the ordered phase, their gas level also increases and they end up in a similar state. We thus conclude that band solutions corresponding to coexistence between disordered gas and polar liquid cannot be found in the low noise, large density regime.

In [121, 122], Caussin, Solon *et al.* have characterized the solutions propagating along x at constant speed c of the one dimensional hydrodynamic equations for the Vicsek class from a mapping to a dynamical system. In their approach, the band profiles correspond to the dynamics of a particle in a potential in presence of nonlinear energy sink and sources, where space and time coordinates are given respectively by the polar field f_1 and $z = x - ct$. Because of periodic boundary conditions, these solutions require closed trajectories in the $(f_1, \dot{f}_1)$ plane (see Figure 3.7(c,d)), where the dot denotes derivative w.r.t. z. Three of them have been identified:

- Smectic arrangement of polar bands, that corresponds to periodic orbits.
- Solitary localized wave, characterized by a homoclinic orbit that includes one saddle point of the potential: $(f_1 = 0, \dot{f}_1 = 0)$. Its width is then given by the time it takes for the particle to visit this point. These two types of solutions are the ones observed in our simulations of the Boltzmann equation and are shown in Figure 3.7.
- Polar liquid droplet, *i.e.* a macroscopic ordered domain traveling in a disordered gas, corresponding to a heteroclinic cycle in the dynamical system representation. This case thus requires that the particle visits two saddle points, the size of the object being given by the ratio of the waiting times there. Note that the second saddle point, which corresponds to a maxima of the potential, can be computed analytically from the hydrodynamic equations, but is *a priori* unknown at the kinetic level. These solutions are further discussed in Section 3.5.2.

These three families of solutions coexist at the hydrodynamic level. However only periodic orbits with a large enough amplitude are found to be stable, such that their cycle all visit the vicinity of the $(f_1 = 0, \dot{f}_1 = 0)$ saddle point. They thus correspond to phase separation between ordered liquid and disordered gas and are similar to the homoclinic trajectories. Trains of bands corresponding to the small cycles of Figure 3.7(c) can therefore be observed at the kinetic level only. Since they mainly consists of (weak) perturbations of the homogeneous ordered state, these solutions are probably destroyed by fluctuations. Indeed, the main effect of a noise term in the Boltzmann equation would be to introduce additional spatial diffusion, and we know from the linear stability analysis that the latter suppresses the low noise band phase. We looked for them in a continuous time version of the Vicsek model[7], but could not identify any deterministic structure for low values of the noise.

Cluster lane solutions

In [156], Thüroff *et al.* found out solutions made of polar clusters shifted transversally to their propagating axis and traveling in opposite directions, as shown in Figure 3.8(a). They identified the mechanism responsible for the stability of these configuration that is the following: While clusters tend to spread transversally when they travel alone, they exchange particles during their interactions and thus reinforce each other. This way, the system manages to balance density fluxes and this solution is stable. In this arrangement and if the bands have the same transversal size, the system has therefore a global nematic symmetry and the average polar order converges to zero. Thüroff and collaborators finally argued that these solutions appear more frequently when increasing system size.

In order to investigate whether cluster lanes are stable solutions of the Boltzmann equation without additional spatial diffusion, we considered initial conditions built from a numerically stabilized band propagating along the x axis and replicated it along y direction. We then applied the parity transformation along x: $f_k(x,y) \to (-1)^k f_k(N_x - x, y)$ to the copy so that the bands face each other. Running the dynamics, the system converges to the cluster lanes solutions observed in [156] if its extension in the y direction is large enough (see Figure 3.8(a)). These solutions seem to remain stable extending system size in the y direction. However, expanding them in the other direction, copying a stabilized configuration along x for instance, we observe that the global polar order grows slowly with time, suggesting that the solution is unstable and the system favors another configuration. It is nevertheless not easy to give a definitive conclusion at this stage because the kinetic level does not give us access to large systems and long timescales.

Applying the same initial condition to the hydrodynamic equations (3.19) (in the limit $\tau \to 0$), we get the same behavior and we conclude that cluster lanes are also present at the hydrodynamic level. Therefore, this observation gives us access to larger systems and longer simulation times for the study the stability of these solutions. As at the kinetic level, we note that cluster lanes are stable duplicating a stabilized configuration in the y direction (Figure 3.8(c)). They are moreover robust considering an initial configuration made from two unequal bands, in that case the system either equilibrates the sizes of the clusters or remains in a tilted configuration where the lanes are drifting along the y direction as in Figure 3.8(b). In order to observe them in microscopic simulations, these solutions need to tolerate the addition of stochastic terms in the equations. Following the derivation of Section 1.4.2, we considered a multiplicative noise of the form $\zeta\sqrt{\rho(\vec{r},t)}\Xi(\vec{r},t)$ in the polar field equation. Here Ξ is complex, has zero mean, $\langle \Xi(\vec{r},t)\Xi^*(\vec{r}',t')\rangle = 2\delta(\vec{r}-\vec{r}')\delta(t-t')$, and $\langle \Xi(\vec{r},t)\Xi(\vec{r}',t')\rangle = 0$. As shown in Figure 3.8(d), building cluster lanes from bands stabilized at the stochastic hydrodynamic level, we could see them survive on physical timescales of the order of 10^5-10^6 depending on system sizes, even for fairly large ζ. These solutions are thus expected to be robust to fluctuations.

Despite all these observations, duplicating a cluster lane configuration in the x direction we notice that after a time of the order of 10^4 the polar order grows exponentially, thus the system converges to another solution. Indeed, letting the dynamics evolve on large times we observe that, while the lanes still still exists at $t = 10^5$ they

---

[7] See Section 1.14 for a definition.

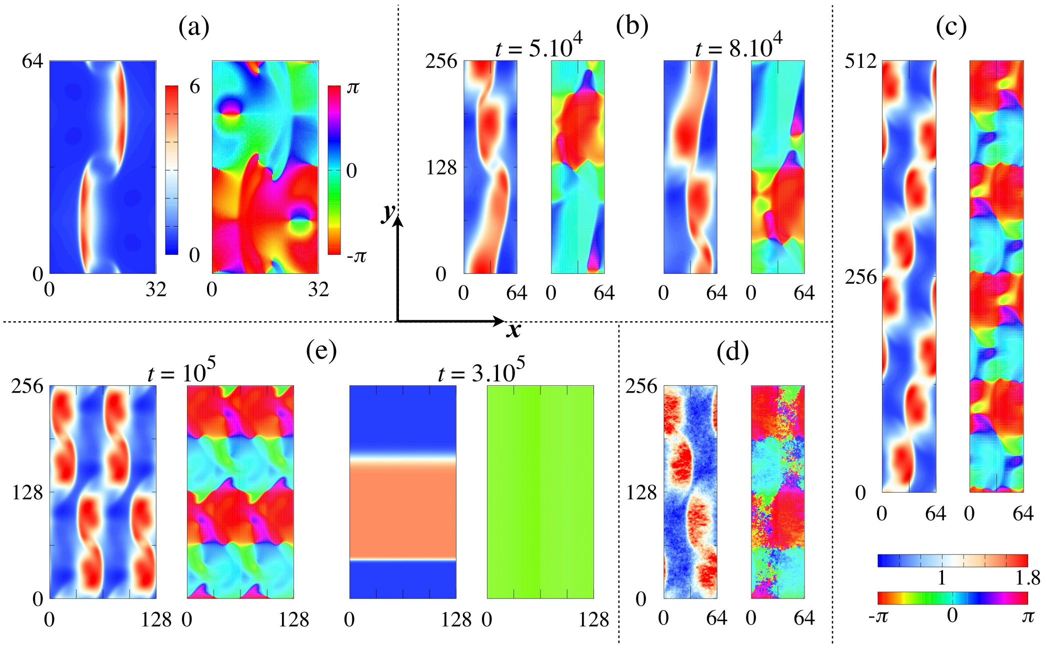

FIGURE 3.8 – Cluster lane solutions at the kinetic (a) and hydrodynamic (b-e) levels. All panels show snapshots of the density an polar orientation fields, the color code is common to (b-e). (a): $\rho_0 = 1$, $\eta = 0.6$, $K = 30$, $dx = dy = \frac{1}{4}$. (b-e): $\rho_0 = 0.5$, $\eta = 0.5$, $dx = dy = \frac{1}{2}$. In (d) the amplitude of the stochastic noise is $\zeta = 0.1$.

are replaced by a single band at $t = 3 \cdot 10^5$ as shown in Figure 3.8(e). We therefore conclude that asymptotically, *i.e.* on large time and length scales, cluster lanes are not a stable limit cycle of the hydrodynamic equations. This instability appears on timescales much larger than those considered by Thüroff and collaborators, and that are in general difficult to access at the kinetic level. However, since we have shown that hydrodynamic equations are a faithful approximation of the Boltzmann equation close to the transition, there is no evidence that the latter would exhibit a different behavior.

3.5.2 Band selection at the kinetic level

In [121, 122], Caussin, Solon *et al.* have shown that the three families of inhomogeneous propagating solutions of the hydrodynamic equations presented in the previous section coexist. On the contrary, at the microscopic level the Vicsek waves have a well defined size [70], macroscopic liquid drops corresponding to heteroclinic cycles are thus unstable and split into a smectic arrangement of bands. The hydrodynamic equations are therefore said to not select the correct solution. A faithful qualitative description of the coexisting phase can be recovered at the fluctuating level [67]. Indeed, large polar liquid domains that are solution of the deterministic equations are found to be unstable adding a noise term in the equations (see Section 1.4.1 and Figure 1.4).

In the following we investigate whether selection occurs at the deterministic kinetic level. Bands in simulations of the Boltzmann equation (3.1) with additional spatial diffusion $D_0\Delta f_k$ are typically smoother and less subject to small wavelength numerical instabilities. Since introduction of positional diffusion gives a global phase diagram in qualitative agreement with microscopic simulations and should not bring any major change in the region close to the mean field transition, from now one we thus set

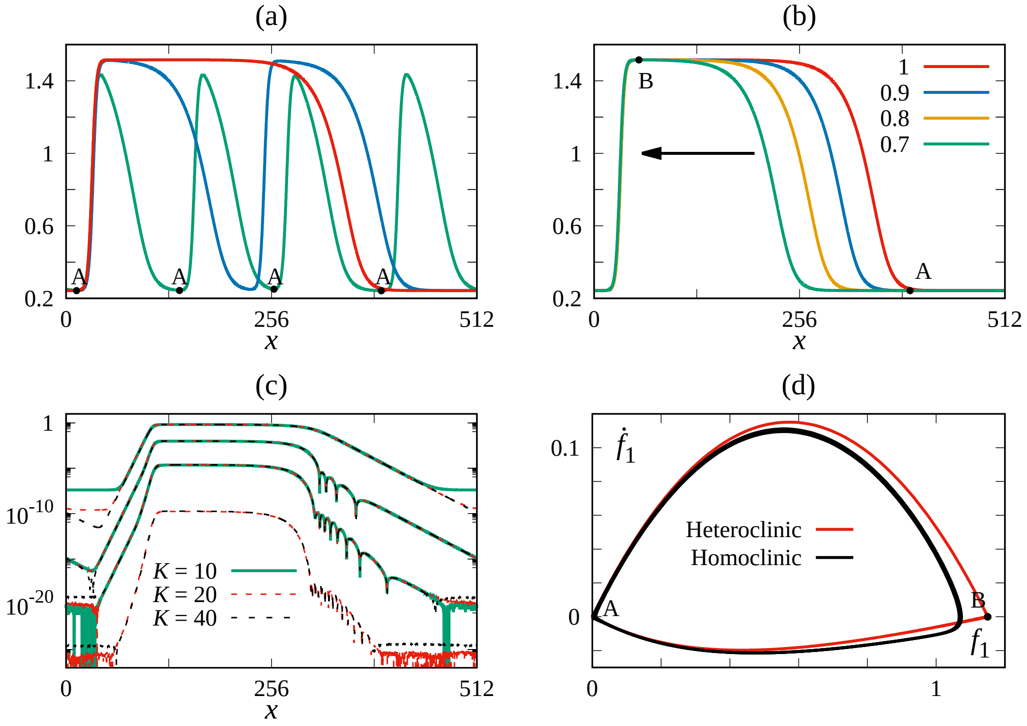

FIGURE 3.9 – Coexistence of traveling solutions at the kinetic level. (a): Stabilized density profiles of the bands increasing ρ_0 gradually from 0.7 to 1. (b): Same as (a) but decreasing the density from 1 to 0.7. (c): Stability of the one band solution increasing the number of modes K at density $\rho_0 = 0.7$. From top to bottom the curves represent f_1, f_5, f_{10} and f_{20}. (d) Trajectories corresponding to the single and four band(s) solutions in the $(f_1, \dot{f}_1)$, plane showing respectively heteroclinic and homoclinic cycles at $\rho_0 = 0.7$. The black arrow in (b) indicates the direction of motion of the bands. Parameters: $\eta = 0.5$, $D_0 = 0.5$, system size 512×1, $dx = dy = \frac{1}{8}$. In (a), (b) and (d) $K = 10$.

$D_0 = 0.5$. Because of the symmetries of this problem we also consider quasi-one dimensional systems.

At the hydrodynamic level, the saddle points associated to the three families of solutions can be computed from the dynamical system mapping, which is no more true here. In order to find out if macroscopic and quantized traveling structures coexist, we thus consider an arrangement of four bands obtained close to the transition ($\rho_0 = 0.7$, $\eta = 0.5$ and $K = 10$) from a polar initial condition and that is a limit cycle of the Boltzmann equation. We then increase the global density of a few percent at fixed noise and wait that the system relaxes to its new state. Repeating this procedure multiple times, Figure 3.9(a) shows that while the gas density remains constant, its fraction decreases. Moreover, we see that bands start to merge for large enough densities such that at $\rho_0 = 1$ only one remains. Since solutions for large values of ρ_0 could have intrinsic width comparable to our system size, at this point we cannot draw any conclusion. However, decreasing the density gradually from the single band configuration, we found the large droplet to be stable also at $\rho_0 = 0.7$ (see Figure 3.9(b)). Figure 3.9(d) shows that the cycle corresponding to this solution exhibits two saddle points at A $= (f_1 = 0, \dot{f}_1 = 0)$ and B $= (f_1 \simeq 1.15, \dot{f}_1 = 0)$. On the contrary, the orbit associated to the four bands configuration is clearly influenced by point B, but does not reach it. Hence, we have shown that solutions corresponding to two types of cycle coexist at the same parameter space point.

We checked that these two solutions remain stable increasing the number of modes K. The procedure used to add modes to an existing configuration is detailed in the following. Neglecting all the terms of order higher than ε^{K+1}, the Boltzmann equation (3.1) for the mode $K+1$ can be written as

$$\left(1 - P_{K+1} - J_{K+1,0} - J_{K+1,K+1}\right) f_{K+1} = -\frac{1}{2}\nabla f_K + \sum_{q=1}^{K} J_{K+1,q} f_q f_{K+1-q} \,, \qquad (3.24)$$

such that f_{K+1} depends only on the $k = 1, \ldots, K$ modes. Using Equation (3.24) we were thus able to add modes progressively without perturbing too much the system. Their dynamics was then updated with the full Boltzmann equation (3.1). Figure 3.9(c) shows the single large band profiles for various truncation order K. We find that they globally coincide with only minor deviations for low values of the modes. Similar results have been obtained for the four bands solution, giving strong evidences that both are stable in the $K \to \infty$ limit.

3.6 Results for the other classes of dry aligning active matter

In this section, we briefly present results on Boltzmann equations describing the models of dry active matter with nematic alignment introduced in Section 2.1.1, *i.e.* active nematics and self-propelled rods classes.

3.6.1 Active nematics

We first consider particles with velocity reversals, so called active nematics. The Boltzmann equation for this case is similar to the one presented in Section 2.3.2 for the Vicsek-shake model in the infinite reversal limit,

$$\partial_t f = D_0 \Delta f + D_1 q_{\alpha\beta} \partial_\alpha \partial_\beta f + \lambda \left[(P_\eta * f) - f \right] + I_{\text{coll}}[f] \,, \qquad (3.25)$$

where $D_1 = 2D_0$ and $I_{\text{coll}}[f]$ defined in (3.16), although with different kernel of interaction and alignment rules, that take into account the π-symmetry of motion and interaction. We thus have [90]

$$K_{\text{nem}}(\theta) = 2\left(\left| \sin\left(\frac{\theta}{2}\right) \right| + \left| \cos\left(\frac{\theta}{2}\right) \right| \right) , \qquad (3.26\text{a})$$

$$H_{\text{nem}}(\theta) = \frac{\theta}{2} + \begin{cases} 0 & \text{if} \quad 0 \leq |\theta| \leq \frac{\pi}{2} \\ \frac{\pi}{2} & \text{if} \quad \frac{\pi}{2} < |\theta| < \pi \end{cases} . \qquad (3.26\text{b})$$

We note that, because active nematics exhibit apolar motion, diffusion has replaced advection in the Boltzmann equation. From the results of Section 3.4, we therefore expect the kinetic level to be better behaved than in the polar case. Since the problem has the full nematic symmetry, all the odd angular Fourier modes of the distribution f can be set to zero. After de-dimentionalization of (3.25), the corresponding hierarchy reads

$$\partial_t f_{2k} = \frac{1}{2}\Delta f_{2k} + \frac{1}{4}\left(\nabla^{*^2} f_{2(k+1)} + \nabla^2 f_{2(k-1)} \right) + \left(P_{2k} - 1\right) f_{2k} + \sum_{q=-\infty}^{\infty} J^{\text{an}}_{k,q} f_{2q} f_{2(k-q)} \,, \qquad (3.27\text{a})$$

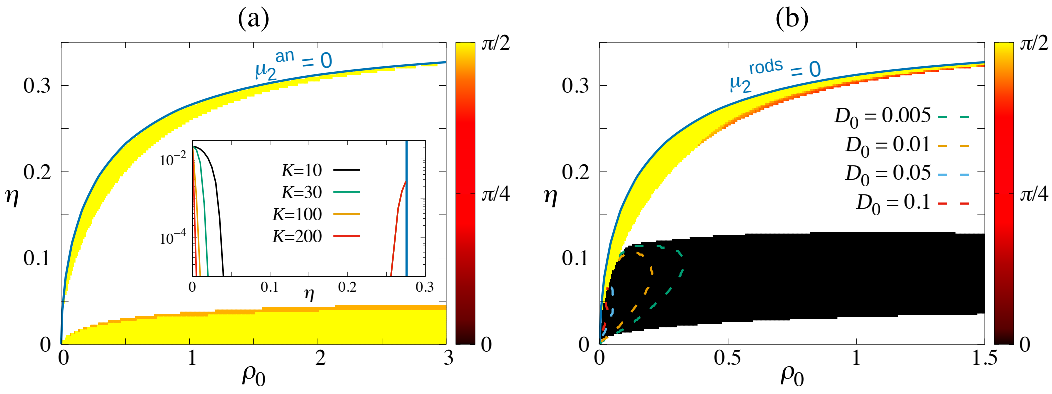

FIGURE 3.10 – Linear stability analysis of the homogeneous ordered solution of Equations (3.25) and (3.28) for classes with nematic alignment in the (ρ_0, η) plane. In both cases the color code indicates the direction of the most unstable wave vector w.r.t. the order (white meaning that the solution is stable), and the continuous blue line marks the mean field transition. (a): The active nematics class with $K = 10$. Inset: growth rate of the instability at fixed $\rho_0 = 1$ (transition at $\eta_c \simeq 0.280$, marked with vertical blue line) for several values of the truncation, showing how the spurious instability is suppressed when K increases. (b): The rods class with $K = 60$. The dashed lines show the limit of the low noise instability when spatial diffusion is added to the kinetic equation.

with $J^{\rm an}_{k,q} = \rho_0 \left(P_{2k} I^{\rm an}_{k,q} - I^{\rm an}_{0,q}\right)$ and

$$I^{\rm an}_{k,q} = \frac{4}{\pi}\frac{1-2\sqrt{2}(k-2q)(-1)^q \sin\left(\frac{k\pi}{2}\right)}{1-4(k-2q)^2}\,. \tag{3.27b}$$

The ordering field triggering the transition to order is now the *second* mode of the distribution. Hydrodynamic equations, derived from (3.27), are thus expressed in terms of the density ρ and f_2 [91]. For $\mu_2^{\rm an} = P_2 - 1 + \frac{8}{15\pi}\left(5(2\sqrt{2}-1)P_2 - 7\right)\rho_0 > 0$, they show a transition to homogeneous nematic order. This solution is unstable to transversal perturbations in the vicinity of the $\mu_2^{\rm an} = 0$ line, leading to a spatiotemporal chaos of nematic bands (see Figure 2.1), as observed in molecular dynamics simulations of the microscopic model (2.1). These equations are well behaved and do not exhibit any spurious instabilities, they thus provide a phase diagram in qualitative agreement with the microscopic level.

Using the formalism presented in the previous sections we computed the linear stability of the homogeneous ordered solution of Equations (3.27) for various truncation orders K. As shown in Figure 3.10(a), the order is unstable to transversal perturbations in the vicinity of the transition. Moreover a second instability, located at low noises, appears for finite K. Increasing the truncation order, this one is restricted to lower and lower values of η, we conclude thus that it is spurious. Asymptotically, a phase diagram qualitatively similar to the ones of the hydrodynamic and microscopic levels is observed.

3.6.2 Self propelled rods

We now turn to the mixed symmetry case, which consists of polar particle interacting nematically. At the Boltzmann level, it is thus defined by the kernel $K_{\rm pol}(\theta) = 2\left|\sin\left(\frac{\theta}{2}\right)\right|$ and the alignment rule $H_{\rm nem}(\theta)$ given in (3.26b). Like in the polar case, since particles are self propelled no diffusion appears on timescales resolved by the kinetic equation. Its nondimensional expression in angular Fourier space thus reads

$$\partial_t f_k + \frac{1}{2}\left(\nabla^* f_{k+1} + \nabla f_{k-1}\right) = \left(P_k - 1\right) f_k + \sum_{q=-\infty}^{\infty} J_{k,q}^{\text{rods}} f_q f_{k-q}\,, \tag{3.28a}$$

with $J_{k,q}^{\text{rods}} = \rho_0 \left(P_k I_{k,q}^{\text{rods}} - I_{0,q}^{\text{rods}}\right)$ and

$$I_{k,q}^{\text{rods}} = \begin{cases} \frac{4}{\pi}\frac{2+\sqrt{2}\left[\cos\left(\frac{\pi(k-2q)}{4}\right)+(k-2q)\sin\left(\frac{\pi(k-2q)}{4}\right)\right]\left[\cos\left(\frac{k\pi}{2}\right)-1\right]}{1-(k-2q)^2} & \text{if} \quad |k-2q| \neq 1 \\ \frac{2}{\pi} \quad \text{otherwise} & \end{cases}. \tag{3.28b}$$

From the nature of the alignment, the order parameter in this case is still given by f_2. However, because of the symmetry of the motion, hydrodynamic theory for this class is written in terms of the fields ρ, f_1 and f_2 [89]. These equations show a phase diagram with a transition to a homogeneous nematic ordered phase when the coefficient $\mu_2^{\text{rods}} = P_2 - 1 + \frac{16}{15\pi}\left(5(2\sqrt{2}-1)P_2 - 7\right)\rho_0$ becomes positive. As for the active nematics, the corresponding solution is unstable to transversal perturbations close to the transition, at the origin of a similar chaotic phase pictured in Figure 2.1, and also observed in microscopic simulations [87]. Another instability of the homogeneous ordered solution, at zero wavenumber and triggered by the polar field f_1, is observed deeper in the ordered phase. This one leads to unbounded solutions and is likely spurious. The hydrodynamic equations for this class thus constitutes a right qualitative description of the microscopic model close to the ordering transition.

We expect the Boltzmann equation (3.28) to be a better description far from the transition. This equation admits an homogeneous nematic solution for $\mu_2^{\text{rods}} > 0$. As at the hydrodynamic level, it is found to be unstable to transversal perturbations close to the mean field transition line. No zero wavenumber instability was observed, we therefore conclude that its presence at the hydrodynamic level is due to the truncation. However, at large K a longitudinal instability of the homogeneous ordered solution develops for $\eta \lesssim 0.13$ (Figure 3.10(b)). As in the polar case, it disappears when adding enough spatial diffusion to the Boltzmann equation.

3.7 Conclusion

In this Chapter, we have studied and compared kinetic, namely Boltzmann and Smoluchowski, equations for the polar class of dry aligning active matter. Their phase diagrams have been computed from a linear stability analysis of their homogeneous ordered solutions, and have been found to be qualitatively different from the microscopic model phenomenology. Indeed, while the Boltzmann equation shows an instability of the order close to the transition and in the low noise phase, such that a Toner Tu liquid is expected for intermediate η only, the Smoluchowski case is even worse since the homogeneous order is always unstable there. In the Boltzmann framework, the correct phase diagram is recovered with the addition of positional diffusion, which has been shown to naturally appear in the discrete time limit of the models considered in most studies of dry aligning active matter. For Smoluchowski on the contrary, spatial diffusion globally decreases the growth rate of the instability but does not suppress it. These two approaches rely on two different approximations, the dilute limit with binary collisions for Boltzmann, and large densities modeled by mean field interactions for Smoluchowski. The mean field description thus does not seem relevant for the Vicsek microscopic model, although better results could be obtained considering other interaction potentials. This is the topic of future work.

At the nonlinear level, numerical simulations of the Boltzmann equation reveal that propagative solutions close to the mean field transition are similar to the ones of the hydrodynamic equations, whereas the low noise instability gives rise to limit cycles that unstable at the hydrodynamic level. They indeed do not correspond to the usual coexistence between liquid and gas, but to a globally ordered phase in which small amplitude waves propagate. Like at the hydrodynamic level, the deterministic Boltzmann equation does not provide any band selection, emphasizing again the importance of fluctuations. Moreover, the cluster lane solutions identified by Thüroff and collaborators are also discovered to be solutions of the hydrodynamic equations, which gave us more freedom to characterize their stability. We found that they are robust in confined geometries. However, considering systems with a large extension longitudinal to their propagation axis, they may survive for long times but seem to be asymptotically unstable.

A linear analysis of the Boltzmann equation applied to classes with nematic alignment leads to the similar conclusions. Indeed, while the kinetic level for active nematics that nominally shows spatial diffusion terms accounts faithfully for the microscopic phase diagram, the one describing self propelled rods exhibits additional instabilities. As in the polar case, all dissimilarities are cured introducing positional diffusion in the Boltzmann equation for the rods.

Following these observations, we conclude that kinetic equations coarse graining *discrete time* dry aligning active matter models must possess spatial diffusion terms. Introduced by the truncation and closure procedure, such terms are present by default in hydrodynamic theories derived from the microscopic dynamics. We have moreover gathered evidence that at the onset of order the kinetic level does not seem to contain more information than the simpler hydrodynamic equations. However, and because their derivation rely on a perturbative approach, the latter may break down far from the transition, showing spurious instabilities for instance. On the contrary, if endowed with additional spatial diffusion terms, the Boltzmann equation constitutes a correct deterministic description of the simple active matter models, even deep in the ordered phase.

Chapter 4

Quantitative assessment of the Toner Tu theory

4.1 Characterization of fluctuations in the flocking phase: the Toner Tu theory

The theory proposed by Toner and Tu in [72, 73] describes the large-scale and long-time universal properties of ordered flocks, such as the fluctuating rotational symmetry broken phase of the Vicsek model. It is based on continuous equations for the evolution of the coarse-grained density ρ and velocity $\vec{v}$ fields, originally written from symmetry arguments as

$$\partial_t \rho + \vec{\nabla} \cdot (\rho \vec{v}) = 0\,, \tag{4.1a}$$

$$\begin{aligned} \partial_t \vec{v} + \lambda_1 \left(\vec{v} \cdot \vec{\nabla}\right) \vec{v} + \lambda_2 \left(\vec{\nabla} \cdot \vec{v}\right) \vec{v} + \lambda_3 \vec{\nabla} \left(|\vec{v}|^2\right) &= \left(\alpha - \beta\, |\vec{v}|^2\right) \vec{v} - \vec{\nabla} P \\ &+ D_{\mathrm{T}} \Delta \vec{v} + D_{\mathrm{B}} \vec{\nabla} \left(\vec{\nabla} \cdot \vec{v}\right) + D_2 \left(\vec{v} \cdot \vec{\nabla}\right)^2 \vec{v} + \vec{f}\,, \end{aligned} \tag{4.1b}$$

$$P = \sum_{n=1}^{\infty} \sigma_n \left(\rho - \rho_0\right)^n\,. \tag{4.1c}$$

These equations have been introduced in Chapter 1, see Section 1.3.2 for a detailed discussion of their terms[1], and can be derived from kinetic descriptions as discussed in Section 1.4. The most striking conclusion from Toner and Tu theory is that flocks must exhibit true long-range order, even in two dimensions, whereas in the equilibrium world this feature is forbidden by the Mermin-Wagner theorem [71]. This new nonequilibrium physics is in fact due to the nonlinear terms in Equations (4.1) that are shown to be relevant in any dimension below 4, implying a breakdown of the linearized hydrodynamics. Physically, presence of long-range order in two dimensions is related to the transmission of information that is convective and not diffusive, which because of interactions between agents, suppresses velocity fluctuations over large scales.

4.1.1 Anisotropic scaling in $d < 4$

Considering α and β positive, noiseless Equations (4.1) have an homogeneous ordered solution $\rho = \rho_0$ and $\langle v \rangle \hat{e}_{\parallel} = \sqrt{\alpha/\beta}\, \hat{e}_{\parallel}$, where $\hat{e}_{\parallel}$ is an arbitrary unit vector defining the orientation of the average global order. In the following $\parallel$ and $\perp$ subscript will be used for quantities respectively related to longitudinal and transverse directions w.r.t. the mean motion of particles. Considering the noise term $\vec{f}$, coarse grained density

---

[1] Because it is of higher order in fields and gradients, the D_2 nonlinear diffusion term is usually not considered.

and velocity can be written in terms of small perturbations,

$$\begin{aligned}\rho(\vec{r},t) &= \rho_0 + \delta\rho(\vec{r},t)\,, &(4.2a)\\ \vec{v}(\vec{r},t) &= \big(\langle v\rangle + \delta v_{\|}(\vec{r},t)\big)\,\hat{e}_{\|} + \delta\vec{v}_{\perp}(\vec{r},t)\,. &(4.2b)\end{aligned}$$

Since the equation describing the evolution of $\delta v_{\|}$ possesses a damping term $-2\alpha\delta v_{\|}$ coming from the Ginzburg-Landau potential, perturbations parallel to the mean orientation are nonhydrodynamic and can be enslaved to the other fields.

Therefore, Toner and Tu theory concerns only $\delta\rho$ and $\delta\vec{v}_{\perp}$. The two points equal time correlation functions of these fields are predicted to be scale-free, as observed experimentally in starling flocks [27], and as a consequence of long range order, to exhibit an anisotropic scaling. They are thus defined by two exponents. The velocity correlation function, $C_v\left(\vec{R}\right) = \left\langle \delta\vec{v}_{\perp}\left(\vec{r}+\vec{R},t\right)\cdot\delta\vec{v}_{\perp}\left(\vec{r},t\right)\right\rangle$ with brackets denoting an ensemble average, thus obeys

$$C_v\left(\vec{R}\right) = \left|\vec{R}_{\perp}\right|^{2\chi} f_v\left(\frac{|R_{\|}/\ell_0|}{|\vec{R}_{\perp}/\ell_0|^{\xi}}\right)\,, \tag{4.3}$$

where ℓ_0 is a microscopic length, the radius of interaction between particles for example, and f_v is a universal scaling function. The authors were unable to compute f_v, however the scaling form of (4.3) imposes that $f_v(x) \underset{x\to 0}{\sim} \mathcal{O}(1)$ and $f_v(x) \underset{x\to\infty}{\sim} x^{2\chi/\xi}$, such that

$$\begin{aligned}C_v\left(R_{\|}\right) &\sim |R_{\|}|^{\frac{2\chi}{\xi}} \quad \text{if} \quad |R_{\|}/\ell_0| \gg |\vec{R}_{\perp}/\ell_0|^{\xi}\,, &(4.4a)\\ C_v\left(\vec{R}_{\perp}\right) &\sim |\vec{R}_{\perp}|^{2\chi} \quad \text{if} \quad |R_{\|}/\ell_0| \ll |\vec{R}_{\perp}/\ell_0|^{\xi}\,. &(4.4b)\end{aligned}$$

The roughness exponent χ measures the damping of fluctuations in direction transverse to the global order, and the anisotropy is controlled by ξ. The linear theory predicts $\chi = 1 - d/2$ and $\xi = 1$, meaning that for $d = 2$ the velocity fluctuations should diverge logarithmically with system size. Yet, advective nonlinearities in (4.1) have been shown to be relevant perturbations for $d < 4$, leading to the breakdown of linearized hydrodynamics. Using the dynamical renormalization group approach Toner and Tu could calculate, within approximations that are discussed in Section 4.1.3, the exponents χ and ξ. Their computation gives $\chi = \frac{3-2d}{5}$ and $\xi = \frac{d+1}{5}$, and was initially claimed to be *exact* in two dimensions.

We will see in Section 4.3 that real space correlations are subject to strong finite size effects, which prevents us from computing the exponents from (4.4). On the contrary, their Fourier transform exhibit rather "clean" scalings and are thus more convenient to look at. The Fourier transform of (4.3) reads

$$\hat{C}_v(\vec{q}) = \left\langle\left|\delta\hat{\vec{v}}_{\perp}(\vec{q},t)\right|^2\right\rangle = |\vec{q}_{\perp}|^{1-d-2\chi-\xi}\,\hat{f}_v\left(\frac{|q_{\|}\ell_0|}{|\vec{q}_{\perp}\ell_0|^{\xi}}\right)\,, \tag{4.5}$$

where $\hat{f}_v$ is an unknown scaling function that nevertheless satisfies $\hat{f}_v(x) \underset{x\to 0}{\sim} \mathcal{O}(1)$ and $\hat{f}_v(x) \underset{x\to\infty}{\sim} x^{(1-d-2\chi-\xi)/\xi}$, hence

$$\begin{aligned}\hat{C}_v(q_{\|}) &\sim |q_{\|}|^{\frac{1-d-2\chi-\xi}{\xi}} \quad \text{if} \quad |q_{\|}\ell_0| \gg |\vec{q}_{\perp}\ell_0|^{\xi}\,, &(4.6a)\\ \hat{C}_v(\vec{q}_{\perp}) &\sim |\vec{q}_{\perp}|^{1-d-2\chi-\xi} \quad \text{if} \quad |q_{\|}\ell_0| \ll |\vec{q}_{\perp}\ell_0|^{\xi}\,. &(4.6b)\end{aligned}$$

The equal time density autocorrelation function was also derived by Toner and Tu in the Fourier space,

$$\hat{C}_\rho(\vec{q}) = \left\langle |\delta\hat{\rho}(\vec{q},t)|^2 \right\rangle = \frac{|q_\perp|^{3-d-2\chi-\xi}}{q^2} \hat{f}_\rho\left(\frac{|q_\parallel \ell_0|}{|\vec{q}_\perp \ell_0|^\xi}\right) Y\left(\theta_{\vec{q}}\right) , \tag{4.7}$$

where $q^2 = |\vec{q}|^2$, and $\hat{f}_\rho$ is unknown but has the same asymptotic properties as $\hat{f}_v$. Y is a finite $\mathcal{O}(1)$ unknown function that depends only on the direction $\theta_{\vec{q}}$ between the wave vector and the global order. Because of the $1/q^2$ pre-factor, $\hat{C}_\rho(\vec{q})$ exhibits three different regimes in the small q limit,

$$\hat{C}_\rho(\vec{q}) \sim |q_\parallel|^{-2+\frac{1-d-2\chi-\xi}{\xi}} |\vec{q}_\perp|^2 \quad \text{if} \quad |q_\parallel \ell_0| \gg |\vec{q}_\perp \ell_0|^\xi , \tag{4.8a}$$

$$\hat{C}_\rho(\vec{q}) \sim |q_\parallel|^{-2} |\vec{q}_\perp|^{3-d-2\chi-\xi} \quad \text{if} \quad |\vec{q}_\perp \ell_0|^\xi \gg |q_\parallel \ell_0| \gg |\vec{q}_\perp \ell_0| , \tag{4.8b}$$

$$\hat{C}_\rho(\vec{q}_\perp) \sim |\vec{q}_\perp|^{1-d-2\chi-\xi} \quad \text{if} \quad |\vec{q}_\perp \ell_0| \gg |q_\parallel \ell_0| . \tag{4.8c}$$

Contrary to velocity correlations, because of the Y factor the functional form of (4.7) does not allow for computation of density correlations in real space.

From Equations (4.6) and (4.8), we note that examining the velocity and density correlations both in the longitudinal and transverse directions will give access to the two exponents χ and ξ. In particular, for $d = 2$ where Toner and Tu predict $\chi = -\frac{1}{5}$ and $\xi = \frac{3}{5}$, we should see

$$\begin{aligned}
\hat{C}_v(q_\parallel) &\sim |q_\parallel|^{-2} \quad \text{if} \quad |q_\parallel \ell_0| \gg |\vec{q}_\perp \ell_0|^{\frac{3}{5}} , \\
\hat{C}_v(\vec{q}_\perp) &\sim |\vec{q}_\perp|^{-\frac{6}{5}} \quad \text{if} \quad |q_\parallel \ell_0| \ll |\vec{q}_\perp \ell_0|^{\frac{3}{5}} , \\
\hat{C}_\rho(\vec{q}) &\sim |q_\parallel|^{-4} |\vec{q}_\perp|^2 \quad \text{if} \quad |q_\parallel \ell_0| \gg |\vec{q}_\perp \ell_0|^{\frac{3}{5}} , \\
\hat{C}_\rho(\vec{q}) &\sim |q_\parallel|^{-2} |\vec{q}_\perp|^{\frac{4}{5}} \quad \text{if} \quad |\vec{q}_\perp \ell_0|^{\frac{3}{5}} \gg |q_\parallel \ell_0| \gg |\vec{q}_\perp \ell_0| , \\
\hat{C}_\rho(\vec{q}) &\sim |\vec{q}_\perp|^{-\frac{6}{5}} \quad \text{if} \quad |\vec{q}_\perp \ell_0| \gg |q_\parallel \ell_0| .
\end{aligned}$$

Giant number fluctuations

χ and ξ exponents can also be computed indirectly, for instance the scaling form (4.7) implies that flocks show giant density fluctuations in $d < 4$. Indeed, since $\xi < 1$ the structure factor $S(q) = \langle C_\rho(\vec{q}) \rangle_{\mathcal{S}^{d-1}}$, where $\mathcal{S}^{d-1}$ is the unit sphere in d dimensions, is dominated at small q by contributions from the transverse direction and essentially diverges as $q^{1-d-2\chi-\xi}$ when $q \to 0$. Moreover, in the same limit this quantity corresponds to the ratio between the variance and average of the number of particles in a volume $\ell^d \sim 1/q^d$ [159]. Thus,

$$S(q) \underset{q\to 0}{\sim} \frac{\langle \Delta N^2 \rangle}{\langle N \rangle} \sim \ell^{\,d-1+2\chi+\xi} . \tag{4.9}$$

Noticing that $\langle N \rangle \sim \ell^d$, we finally get

$$\left\langle \Delta N^2 \right\rangle \sim \langle N \rangle^\sigma \quad \text{with} \quad \sigma = 2 + \frac{2\chi + \xi - 1}{d} . \tag{4.10}$$

Because of long-range correlations, the variance of the number of particles in a box containing on average $\langle N \rangle$ particles does not satisfy the central limit theorem and scales faster than $\langle N\rangle$. In $d=2$ and 3 Toner and Tu therefore predict respectively $\left\langle\Delta N^2\right\rangle\sim\langle N\rangle^{\frac{8}{5}}$ and $\left\langle\Delta N^2\right\rangle\sim\langle N\rangle^{\frac{23}{15}}$.

Transverse superdiffusion

Another consequence of the scaling (4.5) is the presence of super-diffusion in the direction transverse to the order for $d=2$. Computing the mean square orthogonal displacement of a particle positioned in $\vec{r}_i$,

$$w^2(t)=\left\langle\left|\vec{r}_{i_\perp}(t)-\vec{r}_{i_\perp}(0)\right|^2\right\rangle\,, \tag{4.11}$$

Toner and Tu indeed found out that for $2\chi/\xi>-1$ it is given by

$$w^2(t)\sim t^{2(1+\chi/\xi)}\sim t^{\frac{4}{3}}\quad\text{in}\quad d=2\,. \tag{4.12}$$

In the case where $2\chi/\xi<-1$, which is supposedly true in three dimensions, diffusion should on the contrary be normal.

4.1.2 Propagative sound modes

Studying the time-dependent two point correlations, Toner and Tu could characterize the propagation of waves in ordered flocks. They indeed discovered that, for a given wave vector $\vec{q}$, the Fourier transform of the density autocorrelation function $\hat{C}_\rho(\vec{q},\omega)=\left\langle|\delta\hat{\rho}(\vec{q},\omega)|^2\right\rangle$ as function of the frequency ω shows two peaks whose dispersion relations obey

$$\omega_\pm(\vec{q})=c_\pm\left(\theta_{\vec{q}}\right)q-\imath|\vec{q}_\perp|^z\hat{f}_\pm\left(\frac{|q_\parallel\ell_0|}{|\vec{q}_\perp\ell_0|^\xi}\right)\,. \tag{4.13}$$

The physical interpretation of this result is that the system exhibits density waves, or sound modes, that propagate with a wavelength $2\pi/q$ proportional to their period $2\pi/\omega$, the constant of proportionality $c_\pm$ being therefore the speed of sound. Note that the latter depends on the direction (w.r.t. the order) in which the wave propagates, and reads

$$c_\pm\left(\theta_{\vec{q}}\right)=\frac{\gamma+\langle v\rangle}{2}\cos\left(\theta_{\vec{q}}\right)\pm\frac{1}{2}\sqrt{(\langle v\rangle-\gamma)^2\cos^2\left(\theta_{\vec{q}}\right)+4c_0^2\sin^2\left(\theta_{\vec{q}}\right)}\,, \tag{4.14}$$

where $\langle v\rangle=\sqrt{\alpha/\beta}$, $\gamma=\lambda_1\langle v\rangle$, and $c_0=\sqrt{\sigma_1\rho_0}$. From this expression, we immediately remark that as a consequence of Galilean invariance ($\lambda_1\neq 1$), two modes with different speeds should propagate in the direction longitudinal w.r.t. the order ($\theta_{\vec{q}}=0$). On the contrary, considering $\theta_{\vec{q}}=\frac{\pi}{2}$ the two modes have the same speed but travel in opposite directions.

The lifetime of such modes, or the inverse of the peaks width, is given by the imaginary part of $\omega_\pm(\vec{q})$ in (4.13). In the transverse direction it scales as $1/|\vec{q}_\perp|^z$, where the dynamical exponent z is universal. This damping is also anisotropic as suggested by the functions $\hat{f}_\pm$ that satisfies $\hat{f}_\pm(x)\underset{x\to 0}{\sim}\mathcal{O}(1)$ and $\hat{f}_\pm(x)\underset{x\to\infty}{\sim}x^{z/\xi}$. The linear theory predicts that z takes the equilibrium value 2, corresponding to viscous or diffusive damping. Toner and Tu, on the contrary, have shown that taking into account nonlinearities in (4.1) for $d<4$ modifies this value. Their analysis led to $z=\frac{2(d+1)}{5}=2\xi$ such that damping should be *conventional* (with an exponent equal to 2) longitudinally to the order and *unconventional* in all the other directions. In particular, for $d = 2$ the peaks' widths are supposed to scale as

$$\begin{aligned} \Im\omega(q_{\|}) &\sim |q_{\|}|^{-2} \quad \text{if} \quad |q_{\|}\ell_0| \gg |\vec{q}_{\perp}\ell_0|^{\frac{3}{5}} \,, \\ \Im\omega(\vec{q}_{\perp}) &\sim |\vec{q}_{\perp}|^{-\frac{6}{5}} \quad \text{if} \quad |q_{\|}\ell_0| \ll |\vec{q}_{\perp}\ell_0|^{\frac{3}{5}} \,. \end{aligned}$$

The peaks heights should finally follow

$$\mathcal{H}(\vec{q}) = |\vec{q}_{\perp}|^{-(2\chi+z+3\xi+d-3)} \hat{f}_{\mathcal{H}}\left(\frac{|q_{\|}\ell_0|}{|\vec{q}_{\perp}\ell_0|^{\xi}}\right) , \tag{4.15}$$

where $\hat{f}_{\mathcal{H}}(x) \underset{x\to 0}{\sim} \mathcal{O}(1)$ and $\hat{f}_{\mathcal{H}}(x) \underset{x\to\infty}{\sim} x^{-(2\chi+z+3\xi+d-3)/\xi}$. Exponents z and ξ can thus in principle be computed from an analysis of the scalings of the peaks widths and heights with the wave vector $\vec{q}$.

4.1.3 Discussion of Toner and Tu predictions

The set of universal exponents proposed by Toner and Tu fully characterizes dry active matter fluctuating polar ordered phases invariant under global rotations. Their derivation,

$$\chi = \frac{3-2d}{5} \quad ; \quad \xi = \frac{d+1}{5} \quad ; \quad z = \frac{2(d+1)}{5} \,, \tag{4.16}$$

was first claimed to be exact in two dimensions. However, in a more recent publication [112], it was shown that nonlinear terms essentially coming from the enslaving of $\delta v_{\|}$ were missed in the original study. Simple power counting shows that these new nonlinearities are all relevant in the renormalization group sense for any $d < 4$. The main consequence of this is that they will *a priori* affect the values of the exponents and thus invalidate the exactness of the $d = 2$ computation, although the presence of long-range order in two dimensions remains valid. Indeed, relevant nonlinearities tend to reduce velocity fluctuations, thus if χ is different than the original prediction, it is expected to be lower than $-\frac{1}{5}$ in $d = 2$ and lower than $-\frac{3}{5}$ in $d = 3$. All the terms omitted in the first works of Toner and Tu are related to density fluctuations $\delta\rho$. Thus the authors claimed that exact computations, leading possibly to different scaling forms and values of the exponents, can be carried out if those are suppressed. For example, dynamics with birth and death processes [139], and 'incompressible flocks" [140, 141] were considered.

Numerical tests of the Toner Tu theory thus far mainly rely on indirect measures of the exponents, and a *qualitative* agreement with the theory. The giant number fluctuations exponent has been estimated in both two and three dimensions from molecular dynamics simulations of the Vicsek model [70, 76]. In $d = 2$ this one seems slightly larger than the prediction $\frac{8}{5}$, while in $d = 3$ more limited simulations led to results compatible with $\frac{23}{15}$.

The transverse super-diffusion exponent has been measured in $d = 2$ [70, 160] and is found to be compatible with $\frac{4}{3}$, although not considering so large systems and time scales. In three dimensions super-diffusion with an exponent $\simeq 1.7$ has been reported in a Vicsek-style model with cohesion [85], thus contradicting Toner and Tu theory. Such measures are however very sensitive to global rotations of the order, which could easily have introduced some ballistic contribution to the "transverse" motion of particles, they should thus be considered with caution.

Another contribution to the evaluation of the theory was based on the response of flocks to external perturbations in $d = 2$ and 3 [161]. Indeed, the authors showed that the shift of global order parameter in presence of an external field h follows the scaling form

$$\delta\Phi = h^{1-\nu} f_\Phi\left(hL^z\right) \sim \left\{ \begin{array}{ll} h^{1-\nu} & h \gg L^{-z} \\ hL^\gamma & h \ll L^{-z} \end{array} \right. , \tag{4.17}$$

where γ and ν are related to the zero field exponents by

$$\nu = 1 + \frac{2\chi}{z} \quad ; \quad \gamma = \nu z \, . \tag{4.18}$$

Toner and Tu therefore predict $\nu = \frac{2}{3}$ and $\gamma = \frac{4}{5}$ for $d = 2$ and $\nu = \frac{1}{4}$ and $\gamma = \frac{2}{5}$ for $d = 3$. The results from numerical simulations presented in [161] are compatible with these values, although the scaling of $\delta\phi$ with h in the nonlinear regime should be a transient before its saturation, which makes it difficult to indentify. Moreover the data, as well as precision, are as usual limited for large system sizes.

The two-point autocorrelations of density and velocity have been measured in [160] in a system with reflective boundary conditions in one direction (see Figure 4.1(e)). In this work the authors could thus identify the sound modes and their anisotropic speed predicted by the linear theory. In addition, scale free equal time density correlation functions were observed, but the computation of the corresponding exponents strongly suffered from finite size effects. Moreover, we will show in the next section that the authors did not take into account inhomogeneities created by the walls that could introduce spurious correlations.

In fine, no precise numerical evaluation of the exponents predicted by Toner and Tu has been performed yet. In this Chapter, we thus present measures of the density and velocity aucorrelation functions obtained from large scale simulations of the Vicsek model. Our data provide a *quantitative* evaluation of the Toner and Tu theory in 2 dimensions and thus allow us to compute all the exponents characterizing the polar phase up to two digits. Although combinations of the exponents associated to giant density fluctuations and super-diffusion are close their predicted values, we find that the latter are individually in clear departure from their numerical estimates. In 3 dimensions, where our measures are strongly limited by system sizes, our partial results and a reasoning based on the two dimensional case suggest a similar picture with deviations from the theory.

4.2 Methodology

4.2.1 Model

We have simulated the discrete time Vicsek model using both scalar and vectorial noises, considering N particles in a box of size L^d with $d = 2$ or 3. Denoting by $\hat{e}_i(t)$ the polarity of the i^{th} particle at time t, it evolves according to

$$\hat{e}_i^{\,\text{scal}}(t+1) = \left(\mathcal{R}_{\eta^{\text{scal}}} \circ \Pi\right) \left[\sum_{j \in \partial_i} \hat{e}_j^{\,\text{scal}}(t) \right] , \tag{4.19a}$$

$$\hat{e}_i^{\,\text{vect}}(t+1) = \Pi \left[\frac{1}{\mathcal{N}_i(t)} \sum_{j \in \partial_i} \hat{e}_j^{\,\text{vect}}(t) + \eta^{\,\text{vect}} \hat{\xi}(t) \right] , \tag{4.19b}$$

and its position naturally obeys $\vec{r}_i(t+1) = \vec{r}_i(t) + v_0 \hat{e}_i(t+1)$. Here Π is an operator that normalizes vectors to unity, ∂_i is the neighborhood of i defined as the disk (sphere) of radius r_0, and $\mathcal{N}_i(t)$ is the number of particles in ∂_i at time t (including i). In the scalar noise case, $\mathcal{R}_\eta$ rotates vector uniformly in the interval $) - \pi\eta; \pi\eta]$

if the dynamics is 2 dimensional, or in the cap of surface $2\pi(1-\cos(\eta))$ for $d=3$. Considering vectorial noise, $\hat{\xi}(t)$ is a random vector uniformly distributed on the unit circle (sphere). η^{scal} and η^{vect} thus play the same role in the two variations of the model, thus in the following we will use η in both cases. Finally, v_0 denotes the speed of particles. Expressing distances in units of r_0, the problem depends on the three usual parameters: the average density ρ_0, the noise η and v_0.

Although the models have been written in a general form encompassing the $d=2$ and 3 cases, in the following we will mainly consider systems in two dimensions, which have already required a substantial numerical effort. The three dimensional case will be addressed in Section 4.5 only. We work at constant density $\rho_0 = 2$. The choice of the other parameters requires some care, indeed we do not want to sit too deep in the ordered phase, where fluctuations will be small so that the expected time and length scales at which scaling appears will be larger. We moreover need to remain sufficiently far from the coexistence phase such that the system is homogeneous on average. Since the nonlinear effects that lead to the Toner Tu phenomenology scale in v_0^2, we want it to be as large as possible, however v_0 also corresponds to the distance travelled by particles at each timestep that should not be large compared to the radius of interaction. For the study of the phase separation scenario mediating the ordering transition of the Vicsek model, asymptotic regimes typically appear at lower sizes considering vectorial noise [69, 70]. We thus expect to see scaling behavior in smaller systems for this case. We chose two sets of parameters that lead to similar values of the global order parameter $\left|\frac{1}{N}\sum_i \hat{e}_i(t)\right| \simeq 0.87$: the first uses scalar noise with $\eta = 0.2$ and $v_0 = 0.5$ (transition around $\eta \simeq 0.3$), and the second involves vectorial noise with $\eta = 0.5$ and $v_0 = 1$ (transition around $\eta \simeq 0.6$). We checked that for moderate system sizes, values of these parameter does not dramatically influence the scaling. Using a parallelized molecular dynamics code based on the Message Passing Interface language [153], we simulated systems with N ranging from a few millions to hundreds of millions of particles for the largest runs.

4.2.2 Measurement protocols

We tackle the Toner Tu theory by measuring the two points equal time density and velocity correlation functions resolved in the L^2 plane. These functions are obtained by coarse graining the density and polarity fields on boxes of size 1×1, we checked that this size does not influence our results, which is moreover natural since we are looking at the large-scale behavior of the system. We then subtract from the fields their space-averaged value, and compute the Fourier transforms of the fluctuations, $\delta\rho(\vec{q},t)$ and $\delta v_\perp(\vec{q},t)$, using a fast Fourier transform algorithm. Finally, the correlation functions in Fourier space are given by

$$C_\rho(\vec{q}) = \left\langle |\delta\rho(\vec{q},t)|^2 \right\rangle_t , \tag{4.20a}$$

$$C_v(\vec{q}) = \left\langle |\delta v_\perp(\vec{q},t)|^2 \right\rangle_t , \tag{4.20b}$$

and their real space counterparts are obtained from a backward Fourier transform. Since these correlations are supposed to be anisotropic, their evaluation requires to define a reference direction that is steady in time. Simulating the Vicsek dynamics in a periodic box, the global polar order is however free to rotate as shown in Figure 4.1(a). Therefore, averaging the correlation functions on large timescales, a naive computation will lead to their isotropic expression, from which we would not be able to deduce the two exponents χ and ξ. Three strategies have been explored to fix this problem, this

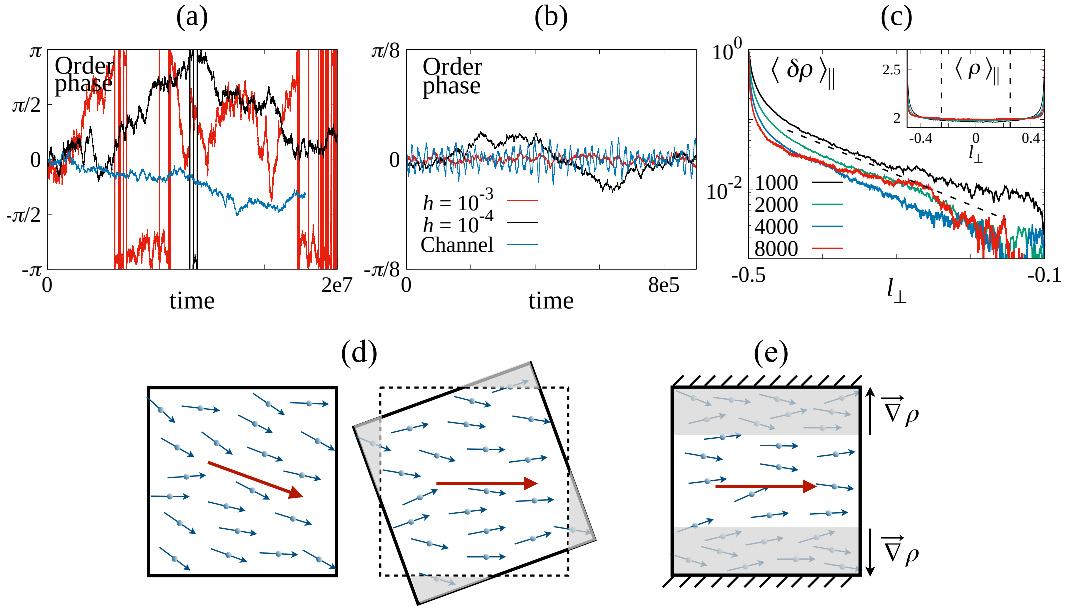

FIGURE 4.1 – (a): Direction of global polar order as function of time in periodic boxes of linear sizes $L = 250$ (red), 500 (black) and 1000 (blue). (b): Same as (a) but introducing an external field h or doing simulations in a channel configuration, at linear system size $L = 2000$. (In that case the global order is computed only in the region far from the reflective boundaries, see (e).) (c): Density field averaged over the direction longitudinal to the order as function of $l_\perp = (x_\perp/L_\perp - \frac{1}{2})$ for different system sizes, showing accumulation of particles near the walls in the channel configuration. In order to observe the exponential decay of the density with a characteristic length $\sim 0.1 \times L_\perp$ (dashed line), we have subtracted to it its average value computed in the central region delimited by the two vertical dashed lines in the inset. (d) Illustration of the procedure (i) consisting in rotating a copy of the system for the measurement of correlation functions. That way the global polar order (red arrow) is always oriented along the same direction (horizontal here), the grey shaded regions are not considered in the computation of the fields . (e): The channel configuration, where reflective boundaries in the vertical direction constrain the global order to be horizontal on average. As shown in (c) this creates density inhomogeneities, correlation functions are thus computed in the half-system excluding the shaded regions.

section is devoted to their presentation as well as the discussion of their advantages and drawbacks.

(i) Rotating the system

The first solution we examined was to keep periodic boundary conditions, but rotating a copy of the system at each measure such that the direction of the global polar order is kept fixed (see Figure 4.1(d) for an illustration). The main interest of this method is that it does not affect the dynamics, thus avoiding spurious effects. However, as pictured in Figure 4.1(a) rotations of the order in time become slower and slower increasing system size. Time necessary to collect suitable statistics then follows the same trend, making our access to large sizes limited. For example, $L = 1000$ requires typical averaging over of the order of $10^7 - 10^8$ timesteps.

(ii) Applying an external field

The second method consists in adding an external field $h\hat{e}_\parallel$ to the interaction in (4.19), such that the direction of the order is maintained around $\hat{e}_\parallel$ (see Figure 4.1(b)). That way, satisfactory statistics can be obtained on timescales that are roughly two orders of magnitude lower than with (i), which opens the way for large scale simulations. However, the main issue with applying an external field is that it introduces a global perturbation to the system. The limit of small h therefore needs to be considered. Indeed, the latter is expected to attenuate fluctuations on scales $q^{-1} > h^{-\frac{1}{z}}$ [161], implying to consider lower and lower values when system size is increased. To evaluate the influence of the field on our measures, we must also do our simulations for several values of h and check that the results converge in the limit $h \to 0$.

(iii) Simulations in a channel

The third and last protocol we considered is to impose reflective boundary conditions on one direction, the other one remaining periodic. With this local constraint, the global order naturally fixes its orientation along the axis parallel to the walls (see Figure 4.1(b)). As for (ii), this method considerably reduces averaging times, which enables to simulate large systems. However, active particles tend to stay close to the reflective border, creating and inhomogeneous density profile in the direction transversal to the order. As shown in Figure 4.1(c), averaging the density along the $\parallel$ axis, we find that it decays exponentially with the distance from the walls. The associated characteristic length scales roughly as $0.1 \times L_\perp$. We conclude that perturbations introduced by the boundaries are local. Therefore, in this case the fields are evaluated from half of the system only, excluding regions near the reflective walls (see Figure 4.1(e)). We note that this precaution has not been taken in [160], probably leading to spurious correlations.

Because of the walls, the fields are no more periodic in the direction transversal to the order. To avoid apparition of spurious effects in the transversal direction, the regions near the walls that are not involved in the computation of the fields are zero padded. Let $F[x_\parallel, x_\perp]$ be a two dimensional field computed this way, the Fast Fourier transform algorithm assumes that F is periodic and formally computes

$$G[n_\parallel, n_\perp] = \sum_{x_\parallel=0}^{L_\parallel-1} \sum_{x_\perp=L_\perp/4}^{3L_\perp/4-1} F[x_\parallel, x_\perp] \exp\left(-2\imath\pi \left[\frac{n_\parallel x_\parallel}{L_\parallel} + \frac{n_\perp x_\perp}{L_\perp}\right]\right) , \tag{4.21}$$

where we have used that $F[x_\parallel, x_\perp] = 0$ for all $x_\perp < L_\perp/4$ or $x_\perp \geq 3L_\perp/4$. From this expression, we note that for $n_\perp = 2k_\perp$ even, the Fourier transform of the (non periodic) original field is recovered

$$G[n_\parallel, k_\perp] = \sum_{x_\parallel=0}^{L_\parallel-1} \sum_{x_\perp=L_\perp/4}^{3L_\perp/4-1} F[x_\parallel, x_\perp] \exp\left(-2\imath\pi \left[\frac{n_\parallel x_\parallel}{L_\parallel} + \frac{k_\perp x_\perp}{L_\perp/2}\right]\right) , \tag{4.22}$$

whereas for $n_\perp$ odd the resulting function is shifted in the transverse direction. The correlation functions of the fields are thus obtained from the zero padded fast transforms considering only even indices.

We have evaluated the velocity and density correlation functions using the procedures (i), (ii) and (iii) with scalar noise and linear sizes ranging from 500 to 2000. Figure 4.2 shows the scaling of the velocity correlation functions along the longitudinal and transverse directions as function of $q_\parallel$ and $q_\perp$. As expected, applying a

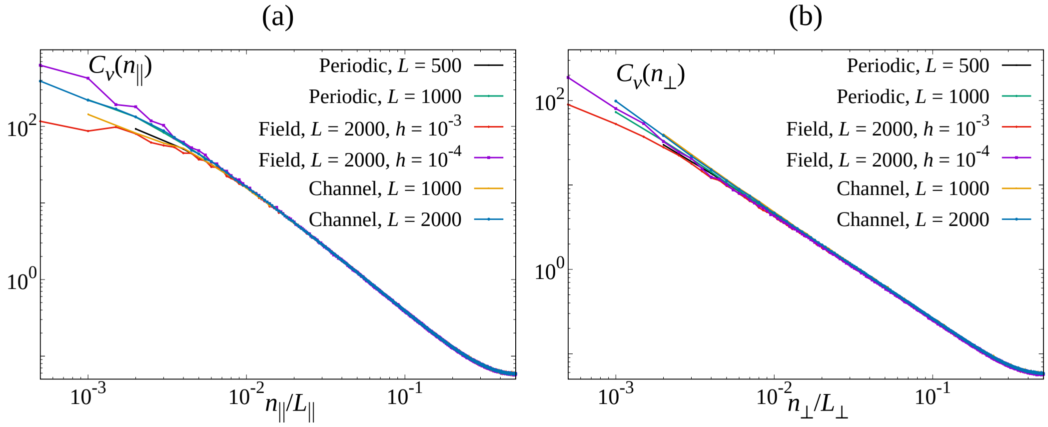

FIGURE 4.2 – Equal time velocity autocorrelation functions computed from the methods (i) (periodic systems with rotation), (ii) (applying an external field), and (iii) (in the channel configuration). (a) and (b) respectively represent the functions in the longitudinal ($n_\perp = 0$) and transverse ($n_\parallel = 0$) directions, that are rescaled in order to make them collapse.

too large external field damps the correlations in the small q limit. Apart from that, functions computed from simulations with comparable sizes collapse well if we rescale them properly. We thus conclude that, hopefully, if carried out precautiously the measure protocol does not influence much of the results. In the following section we will therefore focus on the channel configuration (iii).

4.3 Equal-time correlation functions, exponents χ and ξ

Correlations in Fourier space

We first present results related to the equal-time density and velocity correlation functions, plotted in the $(n_\parallel/L_\parallel = q_\parallel/2\pi, n_\perp/L_\perp = q_\perp/2\pi)$ plane in Figure 4.3. Both are clearly anisotropic with a $q \to 0$ divergence that appears slower transversally to the order. Following Toner and Tu theory, from (4.6) and (4.8) the roughness and anisotropy exponents χ and ξ can be computed from the scaling of these correlations in the longitudinal ($n_\perp = 0$) and transverse ($n_\parallel = 0$) directions.

Our cleanest and most convincing data concern the transverse velocity correlation function $C_v(n_\parallel = 0, n_\perp)$, shown in Figure 4.4(b). In this direction, the curves corresponding to vectorial noise exhibit a power law behavior at small $n_\perp$ at all sizes. They moreover collapse well, even in the small $q_\perp$ limit, suggesting weak finite size effects and minor influence from the reflective boundaries. The corresponding exponent is $1 + 2\chi + \xi = 1.33(2)$, a value relatively close to the theoretical prediction $\frac{6}{5}$. With scalar noise, the scaling is less clear, especially multiplying the curves by $q_\perp^{1.33}$. However, it is not excluded that a power law behavior with an exponent -1.33 would be reached for smaller $q_\perp$, *i.e.* considering larger systems. This is in agreement with the fact that asymptotic regimes typically appear at larger sizes using scalar noise [69, 70, 158].

According to Toner and Tu, the density correlation function in the transverse direction should exhibit the same low $q_\perp$ divergence. Figure 4.4(d) shows that this is indeed the case with vectorial noise, although the scaling is only visible on larger sizes than for velocity correlations. Using scalar noise, as for C_v, the power law behavior is not that convincing and may occur at larger sizes.

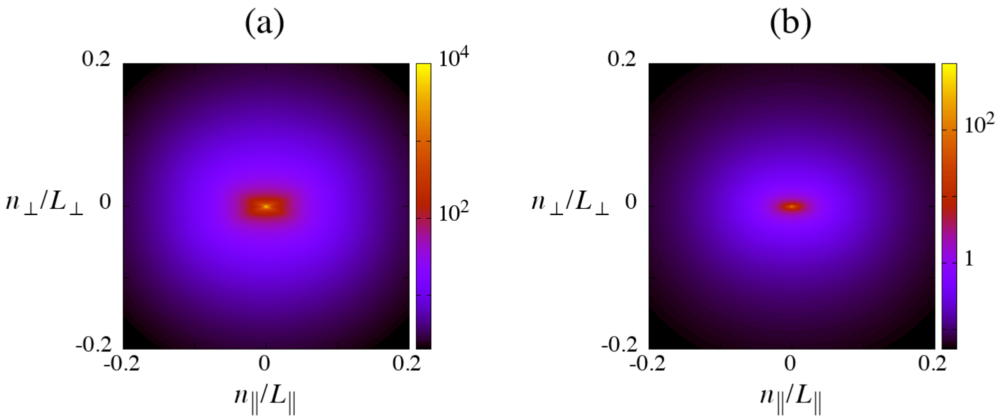

FIGURE 4.3 – The two dimensional density (a) and velocity (b) equal time correlation functions in Fourier space for scalar noise and $L = 2000$.

In the longitudinal direction, for $n_\parallel$ large enough the velocity correlation function curves seem to scale with an exponent close to -1.65 (see Figure 4.4(a)). Decreasing $n_\parallel/L_\parallel$ below $\simeq 10^{-2}$, we see the apparition of a crossover to $(1+2\chi+\xi)/\xi = 1.41(2)$, that is thus visible only considering very large systems. Contrary to the transverse direction, this value is in clear departure from the prediction 2. The crossover is moreover independent of system size, suggesting that it is present asymptotically. Here too, the scaling behavior occurs at smaller sizes considering vectorial noise, although it is qualitatively the same for both datasets. This direction also seems to be more subject to finite size effects, as pointed out by the absence of collapse of correlations and their saturation for small $n_\parallel$.

Longitudinal density correlations, shown in Figure 4.4(c), are more tricky to interpret. Indeed, like the velocity they exhibit a crossover at small $n_\parallel$ but to an exponent $\simeq -0.67 \simeq -1.33/2$, far from its predicted values that would be -2 or -4 from Equation (4.8). This exponent does not have any connection with Toner and Tu theory, their prediction for the scaling behavior of the density (4.6) could thus be incorrect. In fact, the new terms initially missed could modify the scaling form of the density correlation function derived in [73]. Another possibility is that the true asymptotic scaling could appear for larger systems, as stressed by the large $n_\parallel$ range on which the curves do not collapse.

From the measurement of the decay exponents of the density and velocity correlation functions in the two directions, we deduce $\chi = -0.30(2)$ and $\xi = 0.94(2)$. Comparing these values to the ones proposed by Toner and Tu, $-\frac{1}{5}$ and $\frac{3}{5}$, we find that, counterintuitively, flocks are much less anisotropic than expected since ξ is close to 1. Moreover, as mentioned in Section 4.1.3, χ is smaller than its prediction, meaning that the new nonlinearities spotted in [112] *are* relevant and tend to suppress fluctuations on large scales. It is nevertheless worth noticing that, even if both χ and ξ are different from their predicted values, the quantity $1+2\chi+\xi = 1.33(2)$ remains close to $\frac{6}{5}$. Averaging the correlation functions over all orientations of $\vec{q}$, since $\xi < 1$ the transversal contributions should dominate in the $q \to 0$ limit. Figures 4.4(c,d) show that both density and velocity decay with a value in excellent agreement with -1.33, leading to a giant density fluctuations exponent equal to 1.67(3) instead of $\frac{8}{5}$. We can thus explain why most studies measuring this quantity are compatible with Toner and Tu theory.

Since our measures cover the correlation functions in the whole space, we can also test the validity of the scaling forms (4.5) and(4.7) in the $(q_\parallel, q_\perp)$ plane. In order to

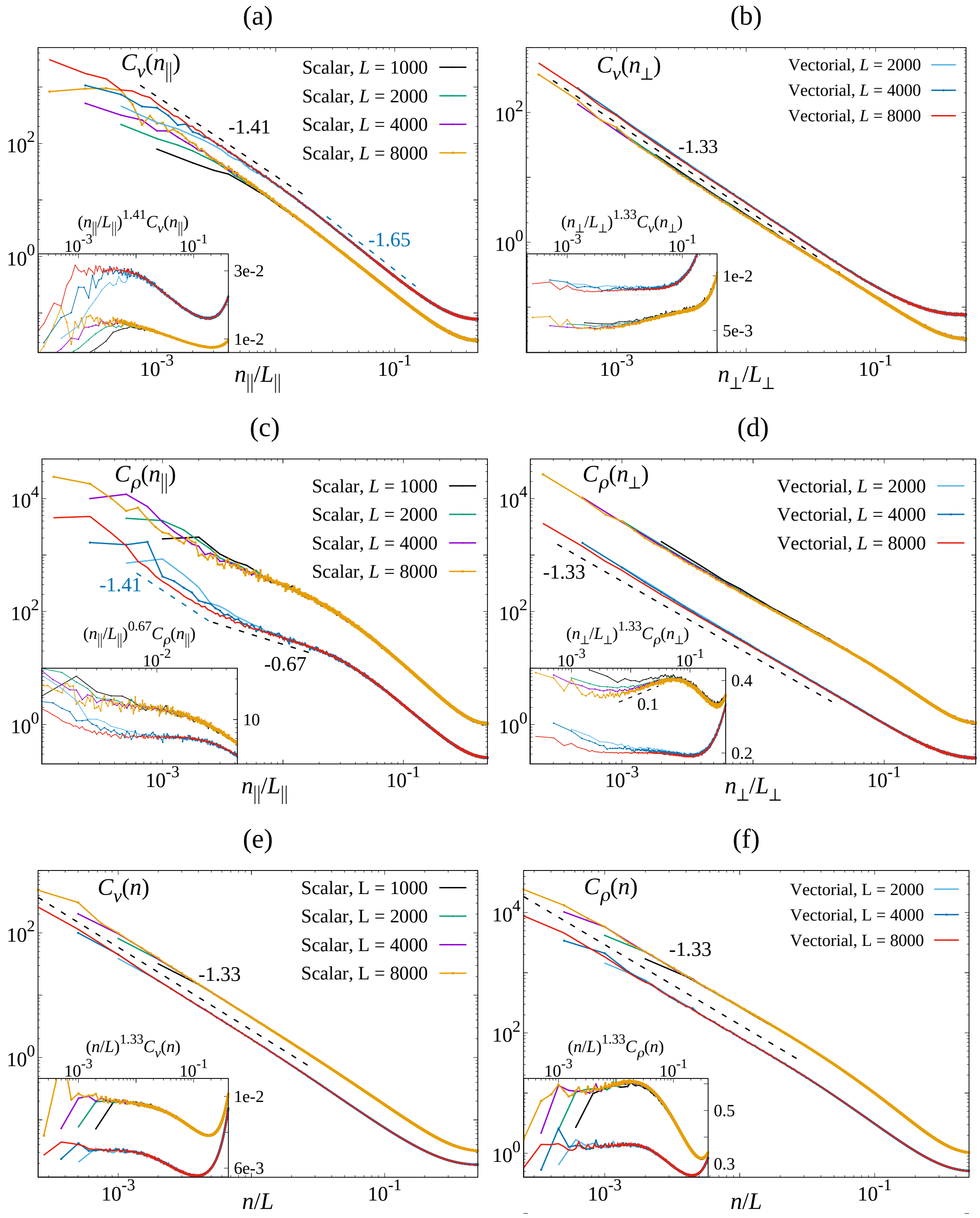

FIGURE 4.4 – Equal-time velocity and density correlation functions in Fourier space for both scalar and vectorial noises and several system sizes. The functions exhibit different scaling exponents in the longitudinal ($n_\perp = 0$) and transverse ($n_\parallel = 0$) directions. Averaging them over all orientations of the wave vector, their $q \to 0$ divergence is dominated by contributions from the $\perp$ direction. (a): Scaling of $\hat{C}_v(n_\parallel, n_\perp = 0)$ showing a crossover between two power laws with exponents -1.65 and -1.41. (b): $\hat{C}_v(n_\parallel = 0, n_\perp)$ showing an algebraic decay with an exponent -1.33. (c): $\hat{C}_\rho(n_\parallel, n_\perp = 0)$ showing a power law decay with an exponent -0.67 for intermediate longitudinal wave vector. (d): $\hat{C}_\rho(n_\parallel = 0, n_\perp)$ showing a power law decay with the same exponent -1.33 as the transverse velocity correlations. (e): Isotropic velocity correlation function showing an algebraic decay with an exponent -1.33. (f): Isotropic density correlation function showing an algebraic decay with an exponent in good agreement with -1.33. In all the panels vectorial noise curves have been shifted vertically for clarity.

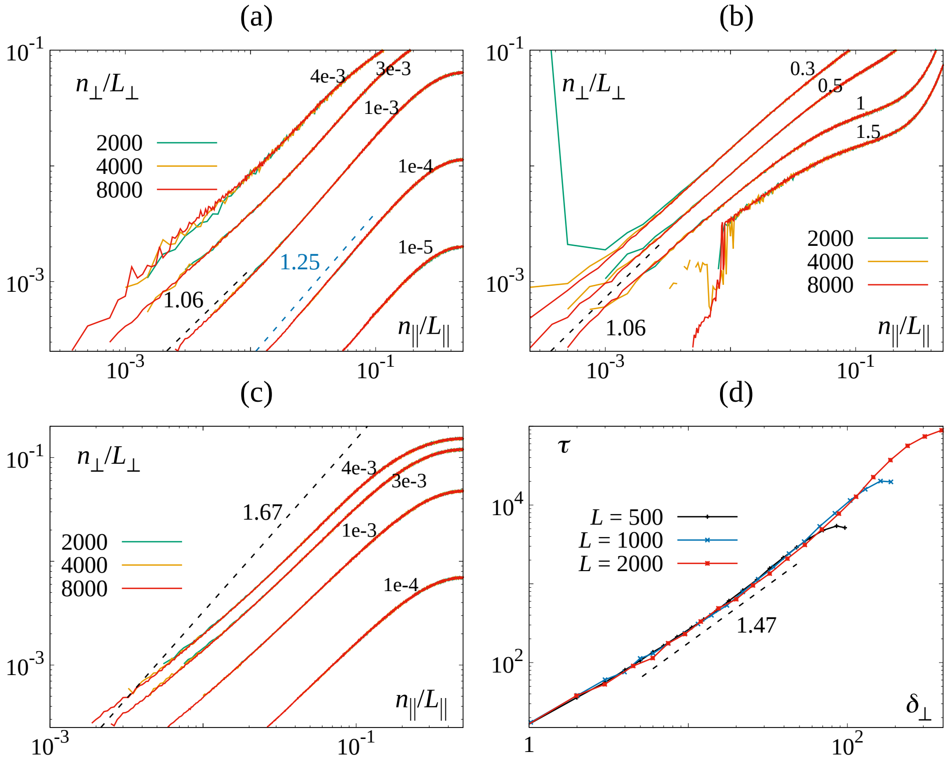

FIGURE 4.5 – (a): Isolines of the function (4.23a) for different system sizes. (b): Same as (a) but considering the function (4.23b). In (a) and (b) the black and blue dashed lines respectively mark the curves $q_\parallel \sim q_\perp^{0.94}$ and $q_\parallel \sim q_\perp^{0.8}$. (c): Same as (a) but using the Toner and Tu predicted exponents. The dashed line indicates the line $q_\parallel \sim q_\perp^{3/5}$. (d): Transverse super diffusion in the ordered phase of the 2 dimensional Vicsek model. The curves correspond to the mean time τ a pair of particles takes to double the initial transverse distance $\delta_\perp$ between them. The slope 1.47 predicted by our computation of the exponents is marked by the dashed line. Data in (a-d) correspond to vectorial noise.

do so, let us consider isolines of the functions

$$q_\perp^{1.33}\hat{C}_v(\vec{q}) = \hat{f}_v\left(\frac{q_\parallel \ell_0}{(q_\perp \ell_0)^{\xi}}\right), \tag{4.23a}$$

$$\frac{q_\perp^{1.33}q^2}{q_\perp^2}\hat{C}_\rho(\vec{q}) = \hat{f}_\rho\left(\frac{q_\parallel \ell_0}{(q_\perp \ell_0)^{\xi}}\right) Y\left(\theta_{\vec{q}}\right), \tag{4.23b}$$

plotted in Figures 4.5(a,b) for our best data corresponding to vectorial noise[2]. For the velocity correlations, these lines should in principle correspond to the curves defined by $q_\perp \sim q_\parallel^{1/\xi}$, at least in the $q \to 0$ limit. In this regime, we indeed observe a power law behavior with an exponent compatible with $1/\xi = 1/0.94 = 1.06$. At $n_\parallel/L_\parallel \gtrsim 10^{-2}$ the curves then exhibit a size-independent crossover leading to an exponent $\xi \simeq 1/1.25 = 0.8$. The latter is in agreement with the decay exponent of the longitudinal velocity correlation function, $\simeq -1.65$, observed at the same values of $n_\parallel/L_\parallel$. On the contrary, contour lines corresponding to the density correlation function do not show any small $n_\parallel/L_\parallel$ crossover, but a power law behavior with an exponent that stays close to 1. We note that the expected behavior of this function is not so obvious because of the presence of the $Y\left(\theta_{\vec{q}}\right)$ factor, which could have an

---

[2] Scalar noise leads to similar results.

influence in the small q region. Figure 4.5(c) finally shows that using Toner and Tu prediction, *i.e.* rescaling $\hat{C}_v(\vec{q})$ by $q_\perp^{6/5}$, our data are clearly incompatible with $1/\xi = \frac{5}{3} \simeq 1.67$.

The two exponents χ and ξ also lead to transverse super-diffusion in the symmetry broken phase of the Vicsek model. We have measured it in the the channel configuration with vectorial noise for L ranging from 500 to 2000. This computation requires some care given that small rotations of the global order can easily introduce a ballistic component to the transverse motion of particles. This is why we adopted the strategy put forward in [70], which consists in computing the average time τ two particles need to double their transverse distance $\delta_\perp$. From (4.12) we should thus have

$$\tau \sim \delta_\perp^{\frac{1}{1+\chi/\xi}} , \tag{4.24}$$

that is $\tau \sim \delta_\perp^{1.47}$, corresponding to a super-diffusion exponent equal to 1.36(6). Once again we note the proximity of this value with the Toner and Tu prediction $\frac{4}{3}$. Figure 4.4(d) shows that our data are roughly compatible with $\delta_\perp^{1.47}$, although from the crossover identified previously, this exponent should appear on scales $\simeq 100$, which correspond to the upper limit of our measurements. In fact, considering the set of exponents given by the $n_\parallel^{-1.65}$ decay of the longitudinal velocity correlations leads to super-diffusion with an exponent 1.38 (corresponding to $\tau \sim \delta_\perp^{1.45}$) indistinguishable from 1.36 with our current data. We thus expect that the super-diffusion exponent should be almost independent of system size, despite the apparent crossover of the velocity correlation functions.

Correlations in real space

Transforming back the two dimensional correlations, we obtain their expression in real space. As in Fourier space, Toner and Tu predict an anisotropic algebraic scaling at large distances $r = |\vec{r}|$ with exponents $2\chi/\xi$ and 2χ respectively in the longitudinal and transverse directions for the velocity. However, Figure 4.6 shows that for both velocity and density correlations with vectorial noise, the scaling behaviors are barely, if not, observed because of finite size effects. We therefore need to implement a finite size scaling procedure in order to check whether the exponents determined earlier are compatible with these data.

Let us consider $C(r, L)$, that can be any of the one dimensional correlation function, which for r large scales like

$$C(r, L) = r^\gamma f\left(\frac{r}{\zeta(L)}\right) , \tag{4.25}$$

where $\zeta(L)$ is the correlation length of the system. Because correlations are asymptotically scale free, we expect $\zeta_l \sim L$. Hence, denoting $r' = r/L$, we have

$$C(r', L) = (r'L)^\gamma f\left(r'\right) , \tag{4.26}$$

such that representing $L^{-\gamma}C(r', L)$ as function of r', our data should collapse on a universal curve.

Insets of Figures 4.6(a,b) show that applying this procedure to the longitudinal and transverse velocity correlations with the exponents $2\chi/\xi = -0.64(3)$ and $2\chi = -0.60(2)$ computed previously, we indeed observe a collapse of the curves at intermediate r on a small decade, in agreement with (4.4). We do not have any prediction for the density correlation function in real space, we nevertheless remark that

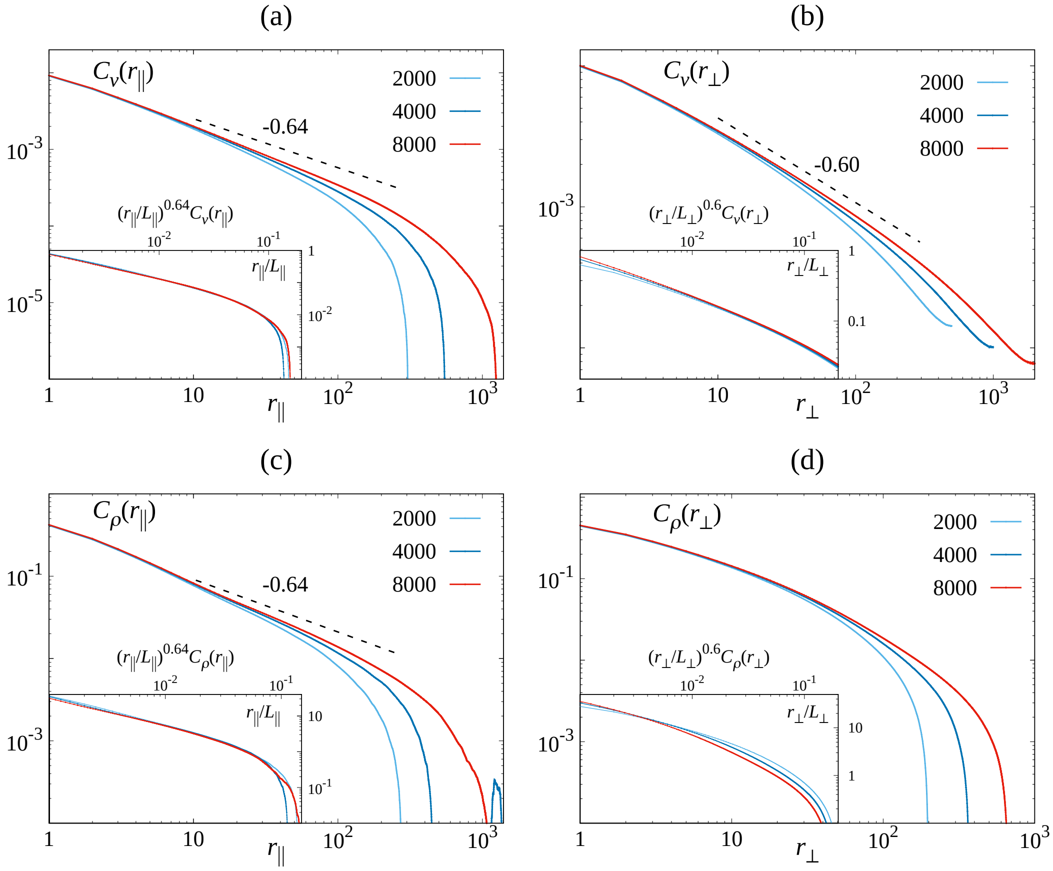

FIGURE 4.6 – Equal-time velocity (top) and density (bottom) correlation functions in real space for several system sizes. The functions do not exhibit obvious scaling behaviors neither in longitiuinal ($r_\perp = 0$) (a,c) nor transverse ($r_\| = 0$) (b,d) directions. The insets represent rescalings of the curves according to (4.26) with the exponents $2\chi/\xi = -0.64(1)$ and $2\chi = -0.60(2)$ computed previously.

longitudinal density correlations seem to scale as $r_\|^{2\chi/\xi}$, as shown in Figure 4.6(c). Figure 4.6(d) on the contrary reveals that the transverse density correlation do not scale as $r_\perp^{2\chi}$. Moreover, we could not find any exponent for which the curves collapse, suggesting a more complicated behavior. Although the collapses are not precise and cannot give accurate values of the exponents, we conclude that the above analysis is compatible with the values $\chi = 0.30(2)$ and $\xi = 0.94(2)$.

4.4 Sound modes, dynamical exponent z

In the preceding section, we have determined the exponents χ and ξ. To complete our assessment of the Toner Tu theory, we now need to evaluate the dynamical exponent z. From our previous results, we restrict ourselves to the the channel configuration and vectorial noise that have provided the cleanest data. The computation of z can be done through the study of the time-resolved density correlation function. The latter is calculated from the two dimensional field $\delta\rho(\vec{r}, t)$ measured at each time step for $0 \leq t < T = 1024$, and Fourier transformed in space and time[3]. The correlation

---

[3] Since the field iso also not periodic in the "time direction", we added a $L^2 \times T$ zero padding to it in order to avoid spurious correlations.

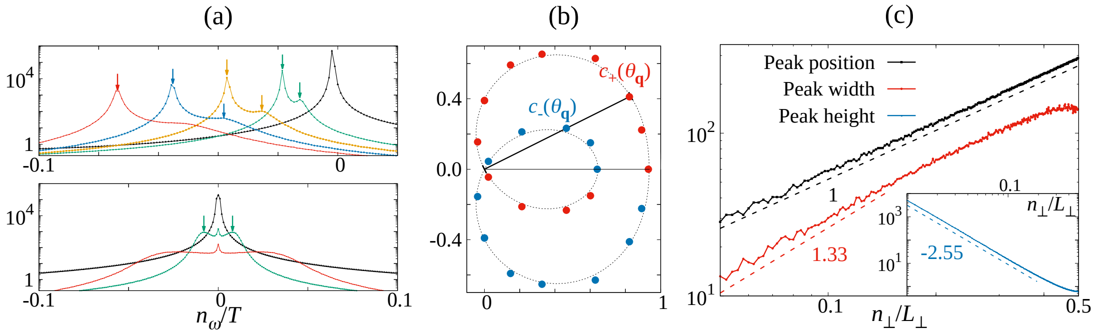

FIGURE 4.7 – (a): Top: $\hat{C}_\rho(n_\parallel, n_\perp = 0, n_\omega)$ as function of n_ω/T for, from right to left, $n_\parallel = 1$, 10, 20, 30, 40. Bottom: Same function, but in the transverse direction ($n_\parallel = 0$), for $n_\perp = 1$(black), 10(green) and 30(red). The small peak present at $n_\omega = 0$ does not spread increasing $n_\perp$ and is thus interpreted as spurious. The vertical arrows indicate the positions of the peaks if visible. (b): Direction dependent sound waves velocities represented in polar coordinates ($\theta_{\vec{q}} = 0$ on the horizontal line). The dashed line indicates the prediction (4.14) fitted from the longitudinal and transversal values of $c_\pm$. (c): Statistics of the right transversal peak represented in the bottom panel of (a). Its position increases linearly with $n_\perp$, its width scales with an exponent compatible with 1.33 for small $n_\perp$, and its height decays as $n_\perp^{-2.55}$.

function is then simply given by $\hat{C}_\rho(\vec{q}, \omega) = \left\langle |\delta\hat{\rho}(\vec{q}, \omega)|^2 \right\rangle$ and the average is taken over repetitions of this procedure.

The Toner and Tu theory presented in Section 4.1.2 predicts that at fixed $\vec{q}$, $\hat{C}_\rho(\vec{q}, \omega)$ exhibits two peaks situated in $\omega_\pm(\vec{q})$, which follows Equation (4.13). Figure 4.7(a) shows the behavior of this function in the directions longitudinal ($n_\perp = 0$) and transverse ($n_\parallel = 0$) to the average order parameter. In each case there are indeed two peaks whose positions satisfiy $\Re\omega_\pm = c_\pm|\vec{q}|$ (see the linear behavior in Figure 4.7(c) for the transverse direction), which defines their speed. In the longitudinal direction, we find $c_+(0) \simeq 0.93$ and $c_-(0) \simeq 0.64$. Toner and Tu relate these quantities to the average order parameter $c_+(0) = \langle v \rangle = \sqrt{\alpha/\beta}$ and $c_-(0) = \gamma = \lambda_1 \langle v \rangle$, these values thus lead to $\lambda_1 \simeq 0.69 \neq 1$ confirming that the system is not Galilean invariant. We also note that $\langle v \rangle \simeq 0.93$ is larger but not too far from the measure of the order parameter computed in the regions far from reflective boundaries ($\simeq 0.87$). The transverse speeds of sound can be computed setting $n_\parallel = 0$, we find $c_\pm\left(\frac{\pi}{2}\right) \simeq \pm 0.40 = \sqrt{\sigma_1 \rho_0}$. This leads to the first moment of the pressure σ_1 equal to $\simeq 0.08$, in clear departure from the value $\frac{1}{2}$ computed from the coarse graining approaches (see Section 1.4). According to (4.14), these three values completely determine the speeds of sound for all directions of $\vec{q}$. We have measured them for different orientations $0 \leq \theta_{\vec{q}} \leq \frac{\pi}{2}$[4] and find that, even if the measure can be complicated because some peaks are barely visible (see Figure 4.7(a) for example), all of our points nicely fall on the predicted curve shown in Figure 4.7(b) with no additional adjustable parameters.

The exponent z can be computed independently from the scalings of the widths (4.13) and the heights (4.15) of the peaks in the longitudinal and transverse directions. However, Figure 4.7(a) shows that our resolution is too low to characterize the sharp peak in the longitudinal direction for low $q_\parallel$. On the contrary, in the transverse direction peaks are rather smooth, even for the smallest $q_\perp$ values. The easiest measure is the height of the peaks that should scale as $q_\perp^{-(2\chi+z+3\xi-1)}$. For small $q_\perp$ we indeed find a power law decay of the height with an exponent $-2.55(2)$ (see inset of Figure 4.7(c)).

---

[4] The opposite orientations are then obtained from the invariance of the system under $q_\perp \to -q_\perp$.

Using the exponents computed in the previous section, $\chi = -0.30(2)$ and $\xi = 0.94(2)$, we thus find $z = 1.33(12)$[5]. The uncertainty on z, computed summing the ones on χ, ξ and the height scaling, is probably overestimated. This value of z satisfies the hyperscaling relation proposed by Toner and Tu, $z = d - 1 + 2\chi + \xi$, that was used for their exact derivation in $d = 2$. In fact, although the exponents are different this relation seems to remain valid. To explain it, we note that the equal time density correlation function can be computed from

$$\hat{C}_\rho(\vec{q}) = \int \frac{d\omega}{2\pi}\, \hat{C}_\rho(\vec{q}, \omega)\,, \tag{4.27}$$

leading to $\hat{C}_\rho(q_\perp) \sim q_\perp^{-z}$ if $q_\parallel \ll q_\perp^{\xi}$ [160]. Identifying this relation with (4.8c), we indeed get $z = d - 1 + 2\chi + \xi = 1.33(2)$ in $d = 2$.

We also computed the width of one of the transversal peaks. This measure is in fact more difficult than the maximum, because peaks become sharper as $q_\perp \to 0$, which requires a large resolution in frequencies. When $q_\perp$ is large enough, on the contrary, the two peaks are so large that they cover each other near the origin. We thus define the width as the distance $\Delta\omega$ between the maximum position ω_+ and the point where $C_\rho(q_\perp, \omega)$ reaches half of the total height when going in the opposite direction from the other peak. Restricting ourselves to the wave numbers for which the peak width is well defined, Figure 4.7(c) shows that it is compatible with 1.33 in the small $q_\perp$ limit, although our data lack precision.

4.5 Preliminary results in three dimensions

In this section we present partial results obtained in three dimensions. For these simulations, we have considered scalar noise with $\rho_0 = 1$, $\eta = 0.2$, $v_0 = 0.5$ (order parameter $\simeq 0.88$), and linear system sizes ranging from 100 to 500. These parameters allow to be safely out of the phase coexistence region, which takes the form of 2 dimensional polar "sheets" pictured in Figure 4.8(a). We imposed reflective boundary conditions in two directions such that particles are constrained to move globally along the third one. Figure 4.8(b) shows density profiles averaged over the longitudinal direction and orientations of $\vec{r}_\perp$. As in two dimensions, particles accumulate near the walls, moreover their density decreases exponentially when reaching the center of the channel with a characteristic length $\simeq 0.1 \times L_\perp$. Following the 2 dimensional case, we thus use only the central region of the channel, that represents one fourth of the total system, for the measure of correlations.

The computation of equal time density and velocity autocorrelation functions is similar to the one presented in Section 4.2.2 for $d = 2$. Moreover, because the problem is axisymmetric, correlations only depend on $q_\perp = |\vec{q}_\perp|$, the norm of the wave vector orthogonal to the global order. Therefore, we averaged them over all orientations of $\vec{q}_\perp$. Although the systems we considered are comparable to the two dimensional case in terms of number of particles, the linear sizes are one order of magnitude smaller. Figure 4.9 thus shows that scalings of velocity and density correlations are less clean than the ones presented in Section 4.3.

As for $d = 2$, the scaling is better in the transverse than in the longitudinal directions. The exponent predicted by Toner and Tu, with which both density and velocity correlation functions should diverge in the $q_\perp \to 0$ limit (with $q_\parallel \ll q_\perp^{\xi}$), is $-(2 + 2\chi + \xi) = -\frac{8}{5}$. Our data shown in Figures 4.9(b,d) are compatible with this

---

[5] Note that the set of exponents given by the $q_\parallel^{-1.65}$ decay of the longitudinal correlation function, $\chi \simeq -0.24$ and $\xi \simeq 0.81$, gives $z \simeq 1.6$ that does not satisfy the hyperscaling relation $z = d - 1 + 2\chi + \xi$.

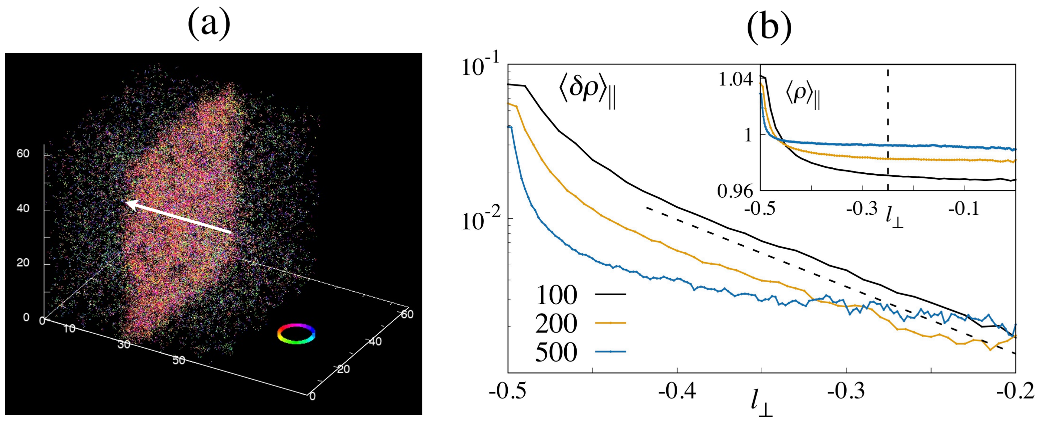

Figure 4.8 – (a): Snapshot of the phase coexistence in the 3 dimensional Vicsek model. Particles are colored according to the norm and direction of the projection of their orientation on the horizontal plane, those moving vertically being white. The white arrow indicates the direction of the global order. Parameters: $\rho_0 = 1$, $\eta = 0.52$, $L = 64$. (b): Density field averaged over the direction longitudinal to the order and orientations of $\vec{r}_\perp$ as function of $l_\perp = (|\vec{r}_\perp|/L_\perp - \frac{1}{2})$ for different system sizes, showing accumulation of particles near the walls in the channel configuration. In order to observe the exponential decay of the density with a characteristic length $\simeq 0.1 \times L_\perp$ (dashed line), we have subtracted to it its average value computed in the central region delimited by the vertical dashed line in the inset.

value, although the isotropic correlations, represented in Figures 4.9(e,f) suggest a slightly different estimation $\simeq -1.65$. Our precision is below the difference between these two values, insets of Figures 4.9(b,d) indeed show that a slope -1.65 or larger could eventually be reached in bigger systems.

At moderate $q_{||}$, the longitudinal velocity correlation function scales with an exponent $\simeq -1.9$ larger in absolute value, and saturates when $q_{||} \to 0$. The two exponents would give $\xi \simeq 1.65/1.9 \simeq 0.87$ lower than its estimated value in $d = 2$ (0.94(2)). However, since $\xi = 1$ for $d \geq 4$, we would expect it to interpolate between 0.94 and 1 in $d = 3$. Assuming $\xi \simeq 1$, we postulate the apparition of a crossover for $q_{||} \to 0$ to a decay exponent $\simeq -1.65$, thus accessible at larger sizes only. The longitudinal density correlation function, as in two dimensions, does not fit Toner and Tu predictions. For intermediate $q_{||}$ it scales with an exponent $\simeq -2.4$ then saturates when $q_{||} \to 0$. A crossover to a smaller slope seems to emerge at the largest size we considered, although our current data are not compete enough to draw any definitive conclusion.

Giant density fluctuations, measured for same parameters but in a fully periodic configuration, are shown in Figure 4.10(a). We find an exponent $\simeq 1.56$ fully compatible with both the Toner and Tu prediction $\frac{23}{15} \simeq 1.53$, as well as our estimation from the correlation functions $\simeq 1.55$. Assuming $\xi \simeq 1$, $2 + 2\chi + \xi \simeq 1.65$ thus gives $2\chi \simeq -1.35$. With these values $2\chi/\xi < -1$, therefore the polar phase of the Vicsek model should exhibit normal diffusion in three dimensions. We tried to evaluate it with the same procedure that was employed in Section 4.3, but Figure 4.10(b) shows that our data are related to too small systems to be able to conclude whether there is any super-diffusion in the transverse direction.

We did not carry out the analysis of the space-time correlations giving access to the dynamical exponent z. However, as shown in the preceding section, the hyperscaling relation $z = d - 1 + 2\chi + \xi$ is satisfied for $d = 2$, and should still be valid in 3 dimensions. Although we do not have a direct estimate of z for $d = 3$, we can nonetheless postulate $z \simeq 1.65$, which is compatible with the Toner Tu prediction $\frac{8}{5}$.

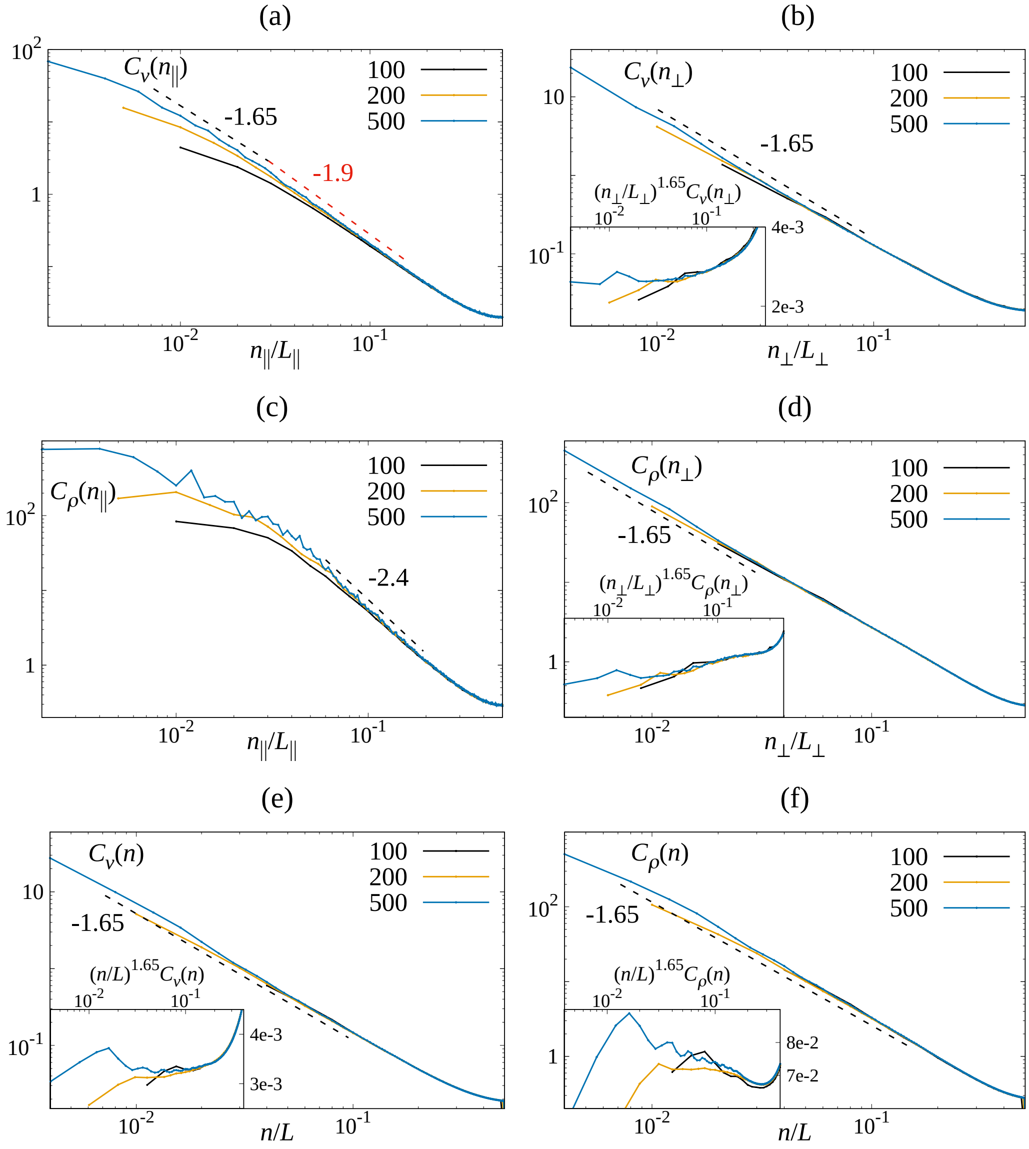

FIGURE 4.9 – Equal-time velocity and density correlation functions in Fourier space for several system sizes and $d = 3$. The functions exhibit different scaling exponents in the longitudinal ($n_\perp = 0$) and transverse ($n_\parallel = 0$) directions. Averaging them over all orientations of the wave vector, their $q \to 0$ divergence is dominated by contributions from the $\perp$ direction. (a): Scaling of $\hat{C}_v(n_\parallel, n_\perp = 0)$ showing a power law decay with an exponent $\simeq -1.9$. (b): $\hat{C}_v(n_\parallel = 0, n_\perp)$ showing an algebraic decay with an exponent $\simeq -1.65$. (c): $\hat{C}_\rho(n_\parallel, n_\perp = 0)$ showing a power law decay with an exponent $\simeq -2.4$ for intermediate longitudinal wave vectors. (d): $\hat{C}_\rho(n_\parallel = 0, n_\perp)$ showing a power law decay with the same exponent $\simeq -1.65$, as the transverse velocity correlations. (e): Isotropic velocity correlation function showing an algebraic decay with an exponent $\simeq -1.65$. (f): Isotropic density correlation function showing an algebraic decay with an exponent $\simeq -1.65$.

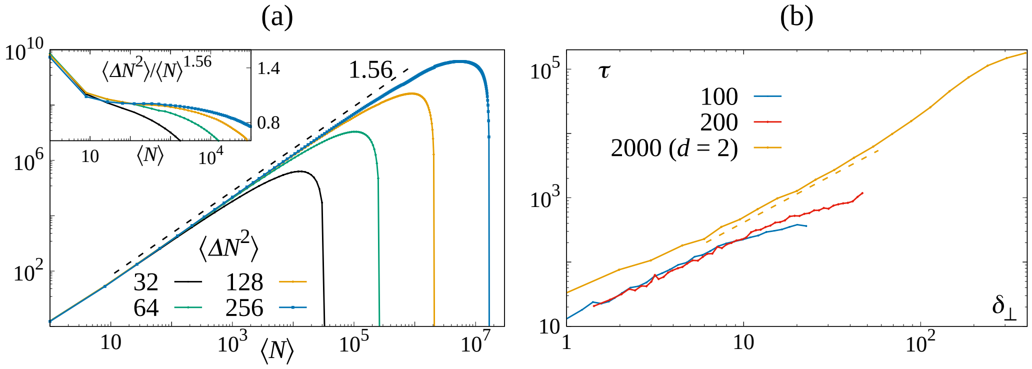

Figure 4.10 – (a): Variance vs. mean of the number of particles in sub-systems for several linear sizes showing giant density fluctuations with an exponent $\simeq 1.56$ (dashed line) in 3 dimensions. In the inset, the same curves have been rescaled by $\langle N\rangle^{-1.56}$. (b): Mean time τ a pair of particles takes to double the initial transverse distance $\delta_\perp$ between them for several system sizes. The curves are compared to the 2 dimensional case (orange) to show that our data in 3 dimensions are still rudimentary.

4.6 Conclusion

In this Chapter, we have numerically examined the Toner and Tu theory in two and three dimensions from large scale simulations of the Vicsek model. For $d = 2$, while the propagation of sound waves in flocks is in agreement with the analytical predictions from Toner and Tu and reveals the absence of Galiean invariance, the values of the exponents are *incompatible* with their theory. The latter are summarized in Table 4.1. Indeed, although the dynamical exponent $z = d - 1 + 2\chi + \xi = 1.33(2)$ is close to its predicted value $\frac{6}{5}$, giving a similar exponent of the giant density fluctuations, we find for the roughness and anisotropy exponents $\chi = -0.30(2)$ and $\xi = 0.94(2)$ instead of respectively $-\frac{1}{5}$ and $\frac{3}{5}$. Flocks are thus much less anisotropic on large scales than predicted by Toner and Tu. Moreover, since χ is lower than its predicted value, we conclude that the new nonlinearities identified in [112] are relevant and suppress velocity fluctuations on large distance, confirming the presence of long range order in $d = 2$.

Confronting our estimation of the exponents with the ones extracted from the response of flocks to external perturbations (see Section 4.1.3), we should get $\nu =$

	$d = 2$		$d = 3$	
	TT95	Simulations	TT95	Simulations
χ	$-\frac{1}{5}$	$-0.30(2)$	$-\frac{3}{5}$	$\simeq -0.68$
ξ	$\frac{3}{5}$	$0.94(2)$	$\frac{4}{5}$	$\simeq 1$
$z = d - 1 + 2\chi + \xi$	$\frac{6}{5}$	$1.33(2)$	$\frac{8}{5}$	$\simeq 1.65$

Table 4.1 – Comparison between the exponents originally computed by Toner Tu in [72, 73] and the results of our numerical simulations in two and three dimensions.

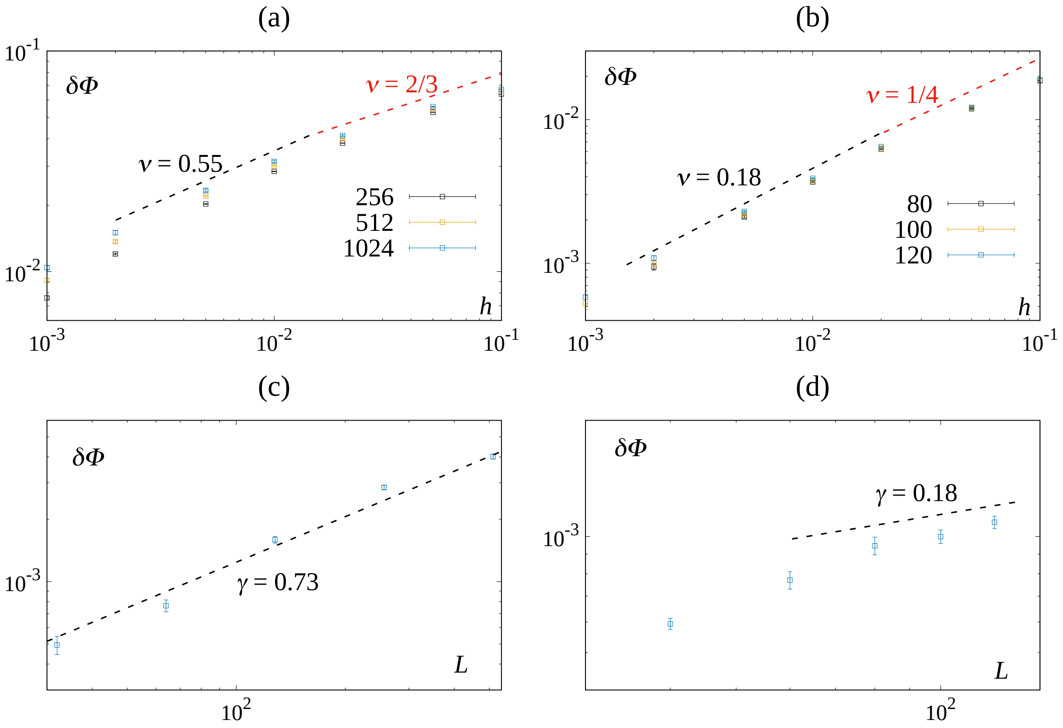

Figure 4.11 – Comparison of our estimation of the Toner Tu exponents with the data presented in [161], based on the scaling of the increment of global order parameter $\delta\Phi$ when the system is subject to an external field h (see Equation (4.17)). (a) and (b): Respectively $d = 2$ and 3 data points, for which $\delta\Phi$ should scale as $h^{1-\nu}$ in between the linear and saturating regimes, for different system sizes L. The data are compatible with our estimation of ν provided that the scaling appears for lower h values than if ν was the one predicted by the theory. (c) and (d): 2 and 3 dimensional estimation of the susceptibility: at fixed $h = 3 \cdot 10^{-4}\,(d = 2)$ and $2 \cdot 10^{-3}\,(d = 3)$ in the linear regime, $\delta\Phi$ should scale as L^{γ}. The data for system sizes large enough are compatible with our values.

0.55(3) and $\gamma = 0.73(5)$ instead of $\frac{2}{3}$ and $\frac{4}{5}$. Figures 4.11(a,c) show that our results are compatible with the data presented in [161][6]. Moreover, our exponents are compatible with the independent measures of giant density fluctuations and transverse superdiffusion in the ordered phase of the Vicsek model.

While the scaling of velocity correlations satisfies the form proposed by Toner and Tu, the last pending issue for $d = 2$ concerns the scaling of the equal time density autocorrelation in the longitudinal direction, which does not follow the predicted behavior. We expect that a further computation of this function, taking into account the new linear and nonlinear terms related to density fluctuations identified in [112], would clarify this point.

For $d = 3$, our results are much more limited by finite size effects. We could yet safely estimate $z = d - 1 + 2\chi + \xi \simeq 1.65$ compatible with Toner and Tu prediction $\frac{8}{5}$ within our accuracy. This value is also compatible with our measure of giant density fluctuations in the ordered phase of the 3 dimensional Vicsek model. We were unable to compute directly the exponent related to the decay of correlations in the longitudinal direction. However, from our data in two dimensions, ξ should in principle belong to the interval $[0.94, 1]$ and thus be $\simeq 1$. That way, we can postulate that $\chi \simeq -0.68$ (see Table 4.1 for a summary). From these values we do not expect the presence of

---

[6] We thank Francesco Ginelli for sharing these data points with us.

transverse super-diffusion in 3 dimensions, which still needs to be confirmed by direct measurements. Comparing with the results of [161], for $d = 3$ we should have $\nu \simeq 0.18$ and $\gamma \simeq 0.29$ instead of $\frac{1}{4}$ and $\frac{2}{5}$. Figures 4.11(b,d) show again that our values are compatible with the data. Improvement of the data in 3 dimensions is nonetheless needed in order to get more accurate estimations of the Toner Tu exponents. This work is still ongoing during the redaction of this manuscript.

For the first time, we have thus tested the Toner Tu predictions quantitatively. Our main conclusion is that the universal exponents characterizing the ordered phase of the Vicsek model, summarized in Table 4.1, are incompatible with the ones computed from the theory. We interpret this from the fact that the new nonlinearities identified by Toner in a later publication constitute relevant perturbations of the order. Moreover, we find that their main effect is to damp velocity fluctuations and make the system less anisotropic on large scales. We hope that this work will pave the way for new theoretical studies of the universal properties of ordered flocks, which are crucial for our understanding of dry aligning active matter.

Chapter 5

Deriving hydrodynamic equations for dry active matter models in three dimensions

5.1 Introduction

This Chapter has been adapted from an article now submitted to *Journal of Statistical Mechanics: Theory and Experiment*. In this work, we build a formalism based on the Boltzmann-Ginzburg-Landau (BGL) approach presented in Section 1.4.1 for the derivation of hydrodynamic equations describing Vicsek-style models in 3 dimensions (3D). Indeed, among the several approaches proposed for similar computations in 2D, the BGL framework has been shown to allow for a controlled derivation of well-behaved nonlinear hydrodynamic equations. Is is in particular able to reproduce qualitatively the microscopic phase diagrams of Vicsek-style models, and provides a simple theoretical understanding of the common phase-separation scenario [67, 89, 91, 121, 122]. The above successes were all obtained in 2D and not much is known in 3D. In particular, the connection between the microscopic and hydrodynamic levels remains essentially unexplored. We thus treat the three universality classes that have been introduced in 2 dimensions in Section 2.1.1. We study the linear stability of the spatially-homogeneous solutions of the corresponding equations. All results are compared to the 2D case.

The organization of the chapter is as follows, in Section 5.2 we define the microscopic models that we use as a starting point. Section 5.3 introduces the general framework for the BGL approach in three dimensions. In 5.3.1 we build the Boltzmann equation for the single particle distribution starting from the microscopic dynamics. The decomposition of this distribution in terms of spherical harmonics and the connections to physical fields is presented in 5.3.2. The expression of the Boltzmann equation in terms of spherical harmonics modes is given in 5.3.4. Sections 5.4 and 5.5 are dedicated to the derivation of the hydrodynamic equations and the linear stability analysis of their homogeneous solutions for, respectively, systems with ferromagnetic and nematic alignment. A brief discussion of our results and an outlook of future work can be found in Section 5.6.

5.2 Microscopic models

Vicsek-style models consist of N pointlike particles moving at a constant speed v_0 in a periodic domain of volume $\mathcal{V}$. The only interaction, competing with noise, is the local alignment of particle velocities. Here velocity and position of particle i are updated

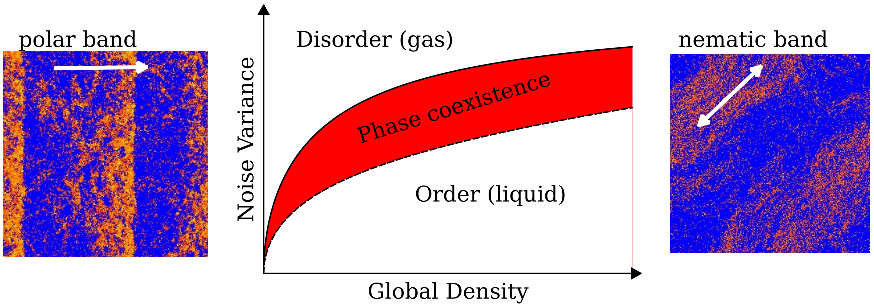

Figure 5.1 – The central panel shows the schematic phase diagram of Vicsek-style models in two dimensions. All classes (polar, active nematics, rods) show a disordered gas phase at low densities and large noise, a (quasi)-ordered liquid phase for large densities and low noise, and a coexistence phase in between them. Left panel: snapshot of the coarse-grained density field in the coexistence phase of the polar class. Here two parallel high-density ordered bands travel from left to right amidst a disordered gas. Right panel: same as left panel but in the active nematics class. Here the nematic order is along the band. Such nematic bands do not travel ballistically as in the polar class, but they are known to be linearly unstable, so that the coexistence phase consists in a spatiotemporal chaos of bands.

at discrete time steps following:

$$\vec{v}_i(t+1) = (\mathcal{R}_\eta \circ \vartheta)\,\langle \vec{v}(t)\rangle_i \tag{5.1}$$

$$\vec{r}_i(t+1) = \vec{r}_i(t) + \varepsilon(t)\vec{v}_i(t+1)\ , \tag{5.2}$$

where ϑ is an operator returning unit vectors ($\vartheta(\vec{u}) = \vec{u}/\|\vec{u}\|$), and $\mathcal{R}_\eta\vec{v}$ rotates the vector $\vec{v}$ by a random angle drawn from a uniform distribution inside the cap of surface $2\pi(1-\cos(\eta))$ (an arc of length $2\pi\eta$ in 2D) centered on $\vec{v}$. In the polar and rods cases, $\varepsilon = 1$, while in the active nematics case where velocity reversals occur, $\varepsilon = \pm 1$ and changes sign with probability α. Finally, $\langle\cdot\rangle_i$ stands for the (equal-weight) average of the polarities of all particles present in the local neighborhood of particle i (including i itself), ∂_i, defined in 3D (2D) by the sphere (disk) of radius r_0 centered on $\vec{r}_i$. Particles interacting ferromagnetically align their polarities while nematic symmetry involves anti-alignment of polarities that initially point in opposite directions:

$$\langle \vec{v}(t)\rangle_i^{\mathrm{f}} = \sum_{j\in\partial_i} \vec{v}_j(t) \quad ; \quad \langle \vec{v}(t)\rangle_i^{\mathrm{n}} = \sum_{j\in\partial_i} \mathrm{sign}[\vec{v}_i(t)\cdot\vec{v}_j(t)]\vec{v}_j(t)\ . \tag{5.3}$$

It is now well-known that the main parameters of these models are the global number density $\rho_0 = N/\mathcal{V}$ and the noise strength η, while the speed of particles v_0 and the reversal rate α play only minor roles. As already shown in Section 1.4.1, r_0 and v_0 can be set to unity at the kinetic level, and thus also at hydrodynamic level. Anticipating our results, we will confirm that in 3D also, the reversal rate α has no qualitative influence (at least at the deterministic, linear level considered below), leaving us with the usual two main parameters ρ_0 and η. In this parameter plane, the phase diagrams of these models for the 2D case all take the form depicted in Figure 5.1. In the polar case (ferromagnetic alignment and no velocity reversals), the liquid phase has true long-range polar order, and the coexistence phase is a smectic arrangement of dense, ordered, traveling bands moving in a disordered gas (left panel of Figure 5.1). With nematic alignment, the liquid shows global nematic order (quasi-long-range for active nematics and possibly truly long-range for rods), and a spatiotemporal chaos of dense, ordered, nematic bands is observed in the coexistence phase (right panel of

Figure 5.1) [67, 69, 87, 89, 91].

5.3 Boltzmann-Ginzburg-Landau approach in 3 dimensions

In this section we describe the implementation of the Boltzmann-Ginburg-Landau (BGL) approach in three dimensions. The path followed is the same as in two dimensions, and was described in detail in Section 1.4.1. The aim is to derive hydrodynamic equations from microscopic models of dry aligning active matter, keeping track of the particle-level parameters in the transport coefficients. The starting point is a Boltzmann equation, considered a good approximation in the dilute regime, although the results obtained in two dimensions have proven to remain qualitatively good even at high densities as long as steric interactions do not become dominant. The Boltzmann equation governs a one-body density. Expanding it in term of spherical harmonics modes of the orientations, a hierarchy of field equations is obtained. A scaling ansatz valid near the onset of orientational order is then used to truncate and close this hierarchy, keeping only the slow modes.

5.3.1 Building blocks of the Boltzmann equation

The easiest way to transform the microscopic model in a time-continuous model is to consider that the tumbling events, given by the angular noise, become probabilistic with a time rate $\lambda \sim \frac{1}{\Delta t} = 1$. This preserves the statistical properties of the angular noise of the microscopic model. Therefore, a particle experiences a random variation of its direction of motion, drawn from a distribution of width σ that plays the role of the microscopic angular noise strength η.

In the dilute limit and assuming the molecular chaos hypothesis [117], the evolution of the system can be reduced to the study of the evolution of the coarse-grained single particle distribution function $f(\vec{r},\vec{v},t)$, which measures the density of particles in a phase space domain of mesoscopic dimensions centered on $(\vec{r},\vec{v})$ where $\vec{r}$ is the spatial location of the particles and $\vec{v} = v_0\hat{e}$ is their velocity, with $\hat{e}$ a unit vector. The dynamics of $f(\vec{r},\vec{v},t)$ is governed by the generic Boltzmann equation [80]

$$\begin{aligned} \partial_t f(\vec{r},\vec{v},t) + \bar{v}\,\hat{e}\cdot\vec{\nabla} f(\vec{r},\vec{v},t) &= D_0\Delta f(\vec{r},\vec{v},t) + D_1 q_{\alpha\beta}\partial_\alpha\partial_\beta f(\vec{r},\vec{v},t) \\ &\quad - a\left[f(\vec{r},\vec{v},t) - f(\vec{r},-\vec{v},t)\right] + I_{\mathrm{sd}}[f] + I_{\mathrm{col}}[f]\ , \end{aligned} \tag{5.4}$$

where $\vec{\nabla} = (\partial_x, \partial_y, \partial_z)$.

The first line of equation (5.4) is the general form of the free motion contribution, which we derive in detail now [80]. In the case of polar particles, or when velocity reversals occur on timescales larger than the ones resolved by the Boltzmann equation, we trivially have $\bar{v} = v_0$ and $D_0 = D_1 = 0$. On the other hand if the reversal rate of velocities is sent to infinity the free motion of particles is apolar at the kinetic level. In that case particles update their positions with a random displacement $\vec{v}\,'\Delta t$ drawn from the distribution

$$\Phi(\vec{v}\,' - v_0\hat{e}) = \frac{1}{2}\left[\delta^{(3)}(\vec{v}\,' - v_0\hat{e}) + \delta^{(3)}(\vec{v}\,' + v_0\hat{e})\right]\ . \tag{5.5}$$

The corresponding evolution of f can then be computed from Itô calculus to second order and reads

$$\partial_t f(\vec{r},\vec{v},t) = \frac{v_0^2\Delta t}{6}\left(\Delta f(\vec{r},\vec{v},t) + 3q_{\alpha\beta}\partial_\alpha\partial_\beta f(\vec{r},\vec{v},t)\right)\ , \tag{5.6}$$

where $q_{\alpha\beta} = e_\alpha e_\beta - \delta_{\alpha\beta}/3$ and summation over repeated indices is assumed. We thus obtain the free transport terms in (5.4) with $\bar{v} = 0$, $D_0 = v_0^2 \Delta t/6$ and $D_1 = 3D_0$. We note that these relations only hold for simple Vicsek-style dynamics while in more complicated cases $\bar{v}$, D_0 and D_1 can be different. However, as we will see in the following $\bar{v}$ can be eliminated by nondimensionalizing the Boltzmann equation and the diffusion coefficients do not affect qualitatively the results, therefore and for simplicity we focus this work on simple Vicsek-like models.

The second line of equation (5.4) regroups terms that account for the dynamics of velocities. From left to right we find an exchange term that models reversal of $\vec{v}$ at a finite (small) rate a and the integrals describing angular self diffusion of velocities and collision events.

The integrals I_{sd} and I_{col} depend on the microscopic model as well. The microscopic dynamics can be described in terms of rotations of the direction of motion of the particles. Rotation transformations in three dimensions belong to the $SO(3)$ group, which can be parameterized by the three Euler's angles. Rotations of a generic vector $\vec{v}$ are thus obtained by

$$\vec{v}\,' = R(\alpha, \theta, \psi)\vec{v} = R_z(\psi)R_y(\theta)R_z(\alpha)\vec{v} \ , \tag{5.7}$$

where $R_i(\varphi)$ represents a rotation around the i axis of an angle φ and α, θ, ψ are the Euler's angles. Any velocity vector can be obtained from rotations of the north pole $\hat{e}_z$, which is the unit vector pointing along the z axis. Such a rotation is only given by the two zenith and azimuthal angles (θ, ψ) (position on the unit sphere, $0 \leq \theta \leq \pi$, $0 \leq \psi < 2\pi$) since the north pole is invariant under rotations around the z axis. In order to lighten the notations we define the two angles as $\Omega = (\theta, \psi)$, and a velocity vector is represented by

$$\vec{v}(\Omega) = v_0 \hat{e}(\Omega) = v_0 R(\Omega)\hat{e}_z \ . \tag{5.8}$$

In order to map the action of the microscopic angular noise in the self-diffusion integral $I_{\text{sd}}[f]$ we consider tumbling events that are rotations of the velocity of a particle. We define the angular noise operator as

$$\mathcal{P}_\Lambda \vec{v}(\Omega) = R(\Omega)R(\Lambda)R^{-1}(\Omega)\vec{v}(\Omega) = v_0 R(\Omega)R(\Lambda)\hat{e}_z \ , \tag{5.9}$$

where the couple of angles Λ is drawn from a probability distribution $P_{\text{sd}}(\Lambda)$. The noise operator first rotates the velocity direction to a reference direction $\hat{e}_z$, then it adds the noise in the form of a rotation and finally it rotates back the vector. This way of applying the noise was chosen so that P_{sd} does not depend on the current orientation Ω. The self-diffusion operator is then given by the sum of a loss and a gain terms

$$\begin{aligned} I_{\text{sd}}[f] &= -\lambda f(\Omega) + \lambda \int d\Omega' \int d\Lambda P_{\text{sd}}(\Lambda) f(\Omega')\delta^{(3)}\left(\vec{v}(\Omega) - \mathcal{P}_\Lambda \vec{v}(\Omega')\right) \\ &= -\lambda f(\Omega) + \lambda \int d\Omega' f(\Omega') P_{\text{sd}}(\mathrm{Arg}[\mathrm{R}^{-1}(\Omega')\mathrm{R}(\Omega)\hat{\mathrm{e}}_\mathrm{z}]) \\ &= -\lambda f(\Omega) + \lambda (f * P_{\text{sd}})(\Omega) \ , \end{aligned} \tag{5.10}$$

where $\int d\Omega$ stands for $\int_0^\pi \sin(\theta) d\theta \int_0^{2\pi} d\phi$. The short notation $f(\Omega)$ stands for $f(\vec{r}, \vec{v}(\Omega), t)$ where we have hidden the space and time dependencies in order to lighten the notations. The Arg function returns the couple of angles defining the direction of a vector on the unit sphere, thus $\mathrm{Arg}[\hat{\mathrm{e}}(\Omega)] = \Omega$. The gain term of the self-diffusion corresponds to a kind of angular convolution[1] [162, 163] between the distribution function f and the noise probability P_{sd}.

The collision integral is also the sum of a loss and a gain terms, considering the two processes by which the direction of motion of a reference particle can move away from or reach Ω during a two-body collision

$$I_{\mathrm{col}}[f] = -I_{\mathrm{col,loss}}[f] + I_{\mathrm{col,gain}}[f] \ . \tag{5.11}$$

The loss part of the integral counts all the collisions of a reference particle moving initially along the direction Ω with the other particles at distance r_0 and moving in a direction parameterized by Ω'

$$I_{\mathrm{col,loss}}[f] = f(\Omega) \int d\Omega' f(\Omega') K(\Omega, \Omega') \ , \tag{5.12}$$

where the function $K(\Omega, \Omega')$ is the *collision kernel* that measures the frequency of collisions. The gain part of the integral, on the contrary, counts all the collisions after which the reference particle aligns its motion along the direction Ω

$$\begin{aligned} I_{\mathrm{col,gain}}[f] \ &= \ \int d\Omega_1 \int d\Omega_2 \int d\Lambda P_{\mathrm{col}}(\Lambda) f(\Omega_1) f(\Omega_2) K(\Omega_1, \Omega_2) \ \times \\ &\quad\ \delta^{(3)}\left([R(\Omega) - \mathcal{P}_\Lambda R(\Psi(\Omega_1, \Omega_2))] \, \vec{e}_z \right) \ . \end{aligned} \tag{5.13}$$

The function $\Psi(\Omega_1, \Omega_2)$ returns the direction of the post collision state of the two aligned particles and P_{col} is the probability distribution of the collisional noise.

The collision integral varies with the symmetries of the microscopic dynamics that define the different classes. First of all, the kernel is proportional to the relative velocity between the two colliding particles, and depends on how the they approach each other in the microscopic free motion. In the propagative cases with polar particles not reversing their velocity, such as in the standard Vicsek and rods models, the kernel reads $K_{\mathrm{p}}(\Omega_1, \Omega_2) = \pi r_0^2 v_0 |(R(\Omega_1) - R(\Omega_2))\hat{e}_z|$. Thanks to its invariance under global rotations, it depends only on the relative zenith angle between the particles

$$\begin{aligned} K_{\mathrm{p}}(\Omega_1, \Omega_2) \ &= \ \pi r_0^2 v_0 \left| (Id - R(\bar{\Omega}))\hat{e}_z \right| \\ &= \ \widetilde{K}_{\mathrm{p}}(\bar{\Omega}) = 2\pi r_0^2 v_0 \left| \sin\left(\frac{\bar{\theta}}{2}\right) \right| \ , \end{aligned} \tag{5.14}$$

where $R(\bar{\Omega}) = R^{-1}(\Omega_1) R(\Omega_2)$. Conversely, when particles reverse their velocity at some finite rate (*e.g.* in active nematics), they locally diffuse and the same collision cannot discriminate if the colliding particle comes from the front or from the back. In this case the collisional kernel reads

$$K_{\mathrm{a}}(\Omega_1, \Omega_2) \sim |\vec{e}_1 - \vec{e}_2| + |\vec{e}_1 + \vec{e}_2| \ , \tag{5.15}$$

since the particles move forward or backward to their velocity director with equal probability. In the reference frame of the particle 1, the kernel for apolar particles

---

[1] In our notation using both rotations and angles, the convolution operation between two functions $A(\Omega), B(\Omega)$ corresponds to $(A * B)(\Omega) = \int d\Omega_1 A(\Omega_1) B(\mathrm{Arg}[\mathrm{R}^{-1}(\Omega_1)\mathrm{R}(\Omega)\hat{\mathrm{e}}_\mathrm{z}])$ where $\hat{e}_z$ is the north pole. In 2 dimensions it correspond to the usual convolution operator because $\mathrm{Arg}[\mathrm{R}^{-1}(\Omega_1)\mathrm{R}(\Omega)\hat{\mathrm{e}}_\mathrm{z}] = \theta - \theta_1$.

reads

$$\widetilde{K}_{\mathrm{a}}(\bar{\Omega}) = \pi r_0^2 v_0 \left(\left| \sin\left(\frac{\bar{\theta}}{2}\right) \right| + \left| \cos\left(\frac{\bar{\theta}}{2}\right) \right| \right) \ , \tag{5.16}$$

where $\bar{\theta}$ is the relative zenith angle defining the orientation of the particle 2 with respect to 1.

The post collisional state of the particles is encoded in the function Ψ that depends on the alignment rules. In the case of polar (ferromagnetic) alignment the function $\Psi(\Omega_1, \Omega_2)$ returns the mean direction between $R(\Omega_1)\vec{e}_z$ and $R(\Omega_2)\vec{e}_z$. Using the rotation properties of Ψ, the alignment rule is

$$R\left(\Psi(\Omega_1, \Omega_2)\right) = R(\Omega_1) R\left(\widetilde{\Psi}(\bar{\Omega})\right) \ , \tag{5.17}$$

where the aligned angle for ferromagnetic alignment is

$$\widetilde{\Psi}_{\mathrm{f}}(\Omega) = \left(\frac{\theta}{2}, \psi\right) \ . \tag{5.18}$$

It corresponds to the mean direction of the colliding particles in the reference frame of the vector $\vec{v}(\Omega_1)$. In the case of nematic alignment the post collisional direction is

$$\widetilde{\Psi}_{\mathrm{n}}(\Omega) = \left(\frac{\theta}{2} + h(\theta), \psi\right) \ \text{with} \left\{ \begin{array}{lll} h(\theta) = 0 & \text{if} & 0 \leq \theta \leq \frac{\pi}{2} \\ h(\theta) = \frac{\pi}{2} & \text{if} & \frac{\pi}{2} < \theta \leq \pi \end{array} \right. \ , \tag{5.19}$$

which is polar alignment at small relative angles and anti-alignment when the relative angle between the particles is larger than $\frac{\pi}{2}$.

In order to simplify the derivation of the hydrodynamic equations, we consider that the distributions of the angular noise in the self-diffusion and collision processes are identical and that they are isotropic with respect to the azimuthal angle

$$P_{\mathrm{sd}}(\Omega) = P_{\mathrm{col}}(\Omega) = P(\Omega) = P(\theta) \ . \tag{5.20}$$

The same symmetry is also present in the collision kernel $\widetilde{K}$. Finally, we nondimensionalize the Boltzmann equation by rescaling space, time and the homogeneous density. This is equivalent to set the speed $\bar{v} = v_0$ and the rate of angular self-diffusion λ to unity without loss of generality (equivalently for apolar particles $\bar{v} = 0$ and we set D_0 to $\frac{1}{3}$). The interaction radius r_0 is eliminated defining the nondimensional homogeneous density $\tilde{\rho}_0 = \frac{2\pi r_0^2 v_0}{\lambda} \rho_0$ (we remove the tilde in the following). We are left with only three free parameters: the (nondimensional) density ρ_0, the noise strength σ and the nondimensional velocity reversal rate a.

5.3.2 Generalities on spherical harmonics

In the following, we manipulate functions (distributions) that depend on the two angles parameterizing the velocity (while the speed is kept constant). This motivates us to decompose the distribution using Laplace's spherical harmonics (SH) [164]

$$f(\theta, \psi) = \sum_{l=0}^{\infty} \sum_{m=-l}^{l} \hat{f}_m^l Y_l^m(\theta, \psi) = \sum_{l=0}^{\infty} \sum_{m=-l}^{l} \hat{f}_m^l Y_l^m(\Omega) \ , \tag{5.21a}$$

$$\hat{f}_m^l = \int_0^{\pi} \sin(\theta) d\theta \int_0^{2\pi} d\psi Y_l^{m^*}(\theta, \psi) f(\theta, \psi) = \int d\Omega Y_l^{m^*}(\Omega) f(\Omega) \ , \tag{5.21b}$$

where $\hat{f}^l_m$ are called hereafter the modes of the SH decomposition of the function $f(\Omega)$, or shortly the *modes*. The functions Y^m_l are the spherical harmonics. They are defined by

$$Y^m_l(\theta,\psi) = A^m_l \mathcal{L}^m_l(\cos(\theta)) e^{\imath m\psi} \,, \tag{5.22}$$

where $A^m_l = \sqrt{\frac{(2l+1)(l-m)!}{4\pi(l+m)!}}$ is a normalization constant and $\mathcal{L}^m_l$ is the associated Legendre polynomial of degree l and order m defined by:

$$\mathcal{L}^m_l(x) = \frac{(-1)^m}{2^l l!}(1-x^2)^{\frac{m}{2}} \frac{d^{l+m}}{dx^{l+m}}(x^2-1)^l \,. \tag{5.23}$$

From this definition and after lengthy but straightforward algebra we obtain the following useful recurrence relations

$$\begin{aligned}
x\mathcal{L}^m_l(x) &= \frac{1}{2l+1}\big((l-m+1)\mathcal{L}^m_{l+1}(x) + (l+m)\mathcal{L}^m_{l-1}(x)\big) && (5.24a)\\
\sqrt{1-x^2}\mathcal{L}^m_l(x) &= \frac{1}{2l+1}\big((l-m+1)(l-m+2)\mathcal{L}^{m-1}_{l+1}(x) \\
&\qquad -(l+m-1)(l+m)\mathcal{L}^{m-1}_{l-1}(x)\big) && (5.24b)\\
\sqrt{1-x^2}\mathcal{L}^m_l(x) &= \frac{1}{2l+1}\big(\mathcal{L}^{m+1}_{l-1}(x) - \mathcal{L}^{m+1}_{l+1}(x)\big) \,, && (5.24c)
\end{aligned}$$

for all $l \geq 0, -l \leq m \leq l$ and $x \in [-1;1]$.

As a natural basis of $L^2(\mathcal{S}^2)$, the spherical harmonics are an orthogonal and normalized set:

$$\int d\Omega\, Y^{m_1}_{l_1}(\Omega) Y^{m_2^*}_{l_2}(\Omega) = \delta_{l_1 l_2}\delta_{m_1 m_2} \,. \tag{5.25}$$

The SH decomposition of distributions (real, positive and normalizable functions) induces relations between the modes. The *reality* of the distribution implies that

$$\hat{f}^l_{-m} = (-1)^m \hat{f}^{l*}_m \,. \tag{5.26}$$

The *positivity* of the distribution implies a bound on the modes

$$\left|\hat{f}^l_m\right| \leq \int d\Omega |Y^{m*}_l(\Omega)||f(\Omega)| = \int d\Omega |Y^{m*}_l(\Omega)| f(\Omega) \leq \frac{A^m_l}{A^0_0}\hat{f}^0_0 \,, \tag{5.27}$$

since the associated Legendre polynomials are functions of $\cos(\theta)$ and bounded to 1 in the window $[-1:1]$. This relation allows us to separate physical and unphysical solutions, since all the modes must be smaller or equal to the zero mode times a constant. [2]

The rotation of a spherical harmonic of degree l is simply given by a linear combination in terms of spherical harmonics of same degree. Denoting $R(\Omega')\vec{e}_z = R^{-1}(\alpha,\theta,\psi)R(\Omega)\vec{e}_z$, with $R(\alpha,\theta,\psi)$ defined in Eq. (5.7), we have

$$Y^m_l(\Omega') = \sum_{m'=-l}^{l} D^l_{m',m}(\alpha,\theta,\psi) Y^{m'}_l(\Omega) \,, \tag{5.28}$$

---

[2] The *normalization* condition means that the distribution $f(\vec{r},\theta,\phi,t)$ is $L^1(\mathbb{R}^3 \times \mathcal{S}^2)$ and the SH decomposition requires the modes to be $L^2(\mathbb{R}^3)$ integrable.

where $D^l_{m',m}(\alpha,\theta,\psi) = d^l_{m',m}(\theta)\exp(-\imath m\alpha - \imath m'\psi)$ are the Wigner D-matrices, with

$$\begin{aligned} d^l_{m',m}(\theta) &= \left[(l+m')!(l-m')!(l+m)!(l-m)!\right]^{\frac{1}{2}} \times \\ & \sum_k \frac{(-1)^k \left[\cos\left(\frac{\theta}{2}\right)\right]^{2l+m-m'-2k} \left[\sin\left(\frac{\theta}{2}\right)\right]^{m'-m+2k}}{(l+m-k)!k!(m'-m+k)!(l-m'-k)!} \end{aligned} \tag{5.29}$$

and the sum over k is taken such that the factorials are non negative. Note that in the following we will consider only the case corresponding to $\alpha = 0$ since we deal with rotations of vectors on the sphere. We therefore introduce the notation $D^l_{m',m}(\Omega)$ for $D^l_{m',m}(0,\theta,\psi)$, which are related to the spherical harmonics from

$$D^l_{m,0}(\Omega) = \sqrt{\frac{4\pi}{2l+1}} Y_l^{m^*}(\Omega) \;, \tag{5.30}$$

and follow the condition

$$\begin{aligned} \int d\Omega\, D^{l_1}_{m'_1,m_1}(\Omega) D^{l_2}_{m'_2,m_2}(\Omega) D^{l_3^*}_{m'_3,m_1+m_2}(\Omega) &= \frac{4\pi}{2l_3+1} \langle l_1\, l_2\, m'_1\, m'_2 | l_3\, m'_3\rangle \times \\ & \langle l_1\, l_2\, m_1\, m_2 | l_3\, m_1+m_2\rangle \;, \end{aligned} \tag{5.31}$$

with $\langle l_1\, l_2\, m_1\, m_2 | l_3\, m_3\rangle$ denoting the Clebsch-Gordan coefficient [165] which is non zero only if $|l_1 - l_2| \leq l_3 \leq l_1 + l_2$ and $m_1 + m_2 = m_3$.

5.3.3 Relations between the spherical harmonics modes and the physical fields

We first define the decomposition of the useful observable fields we are interested in. In order to accomplish this, we simplify the notations considering the functions

$$\hat{g}^l_m(\vec{r},t) \equiv \frac{\hat{f}^l_m(\vec{r},t)}{A_l^m} \;. \tag{5.32}$$

The density field is the zero mode

$$\rho(\vec{r},t) = \frac{\hat{f}^0_0(\vec{r},t)}{\sqrt{4\pi}} = \hat{g}^0_0(\vec{r},t) \;. \tag{5.33}$$

The polar field as function of $\{\hat{g}^1_m\}$ reads

$$\vec{w}(\vec{r},t) = \int d\vec{v} f(\vec{r},\vec{v},t)\vec{v} = \begin{pmatrix} 2\Re(\hat{g}^1_{-1}) \\ 2\Im(\hat{g}^1_{-1}) \\ \hat{g}^1_0 \end{pmatrix} (\vec{r},t) \;. \tag{5.34}$$

Therefore, when the global polar order points in the z direction, the scalar order parameter is simply given by $|\hat{g}^1_0|$.

The nematic tensor $\mathbf{q}$ in terms of the director $\hat{e}$ is defined by

$$\mathbf{q}(\theta,\phi) = \hat{e}(\theta,\psi) \otimes \hat{e}(\theta,\psi) - \frac{1}{3}\mathbf{I} \;, \tag{5.35}$$

with $\mathbf{I}$ the identity matrix and $\otimes$ the tensorial product between the two vectors. Note that this tensor is traceless and symmetric. Like the polar field, $\mathbf{q}$ can be expressed in term of the spherical harmonics of order $l = 2$. Thus the nematic order parameter is related to the $\{\hat{g}^2_m\}$ modes by

$$\mathbf{Q} = \int d\Omega\, \mathbf{q}(\Omega) f(\Omega) = 2 \begin{pmatrix} 2\Re(\hat{g}^2_{-2}) - \frac{1}{6}\hat{g}^2_0 & 2\Im(\hat{g}^2_{-2}) & \Re(\hat{g}^2_{-1}) \\ 2\Im(\hat{g}^2_{-2}) & -2\Re(\hat{g}^2_{-2}) - \frac{1}{6}\hat{g}^2_0 & \Im(\hat{g}^2_{-1}) \\ \Re(\hat{g}^2_{-1}) & \Im(\hat{g}^2_{-1}) & \frac{1}{3}\hat{g}^2_0 \end{pmatrix} . \tag{5.36}$$

The scalar nematic order parameter is usually defined as the largest eigenvalue (in absolute value) of the tensor $\mathbf{Q}$ [138]. In the reference frame where the nematic order lies along the z direction, $\mathbf{Q}$ is diagonal and the scalar nematic order parameter is given by $\hat{g}^2_0$.

5.3.4 Spherical harmonics decomposition of the Boltzmann equation

Using the SH decomposition (5.21), the advection part of the free transport operator, $-\vec{e}(\Omega)\cdot\vec{\nabla}$, can be recast into the following form

$$-\vec{e}(\Omega)\cdot\vec{\nabla} = \sqrt{\frac{2\pi}{3}}\left[Y_1^1(\Omega)\nabla^* - Y_1^{-1}(\Omega)\nabla - \sqrt{2}Y_1^0(\Omega)\partial_z\right] , \tag{5.37}$$

where $\nabla = \partial_x + \imath\partial_y$ and $\nabla^* = \partial_x - \imath\partial_y$. The decomposition of the corresponding term in the Boltzmann equation reads

$$\begin{aligned} \mathcal{T}^l_m\left[\left\{\hat{g}^l_m\right\}\right] &\equiv -\frac{1}{A^m_l}\int d\Omega\, Y_l^{m^*}(\Omega)\vec{e}(\Omega)\cdot\vec{\nabla}f(\Omega) = \frac{1}{2(2l+1)}\nabla\left[\hat{g}^{l+1}_{m+1} - \hat{g}^{l-1}_{m+1}\right] \\ &+\frac{1}{2(2l+1)}\nabla^*\left[(l+m-1)(l+m)\hat{g}^{l-1}_{m-1} - (l-m+1)(l-m+2)\hat{g}^{l+1}_{m-1}\right] \\ &-\frac{1}{2l+1}\partial_z\left[(l-m+1)\hat{g}^{l+1}_m + (l+m)\hat{g}^{l-1}_m\right] , \end{aligned} \tag{5.38}$$

which follows from the recurrence relations (5.24) between associated Legendre polynomials.

The Laplacian operator is isotropic and thus commutes with the SH decomposition. On the contrary, the term associated to the anisotropic spatial diffusion operator, $q_{\alpha\beta}\partial_\alpha\partial_\beta$, is transformed into

$$\begin{aligned} \mathcal{D}^l_m\left[\left\{\hat{g}^l_m\right\}\right] &\equiv \frac{1}{A^m_l}\int d\Omega\, Y_l^{m^*}(\Omega) q_{\alpha\beta}(\Omega)\partial_\alpha\partial_\beta f(\Omega) = \left[\frac{1}{(2l+1)(2l+3)}\times\right. \\ &\left(\frac{(l-m+4)!}{4(l-m)!}\nabla^{*^2}\hat{g}^{l+2}_{m-2} + \frac{(l-m+3)!}{(l-m)!}\partial_z\nabla^*\hat{g}^{l+2}_{m-1} + \frac{(l-m+2)!}{2(l-m)!}\Box\hat{g}^{l+2}_m\right. \\ &\left.-(l-m+1)\partial_z\nabla\hat{g}^{l+2}_{m+1} + \frac{1}{4}\nabla^2\hat{g}^{l+2}_{m+2}\right) \\ &-\frac{1}{(2l-1)(2l+3)}\left(\frac{(l-m+2)!(l+m)!}{2(l-m)!(l+m-2)!}\nabla^{*^2}\hat{g}^l_{m-2} - \frac{l^2+l-3m^2}{3}\Box\hat{g}^l_m\right. \\ &\left.+(2m-1)(l-m+1)(l+m)\partial_z\nabla^*\hat{g}^l_{m-1} + (2m+1)\partial_z\nabla\hat{g}^l_{m+1} + \frac{1}{2}\nabla^2\hat{g}^l_{m+2}\right) \\ &+\frac{1}{(2l+1)(2l-1)}\left(\frac{(l+m)!}{4(l+m-4)!}\nabla^{*^2}\hat{g}^{l-2}_{m-2} - \frac{(l+m)!}{(l+m-3)!}\partial_z\nabla^*\hat{g}^{l-2}_{m-1}\right. \\ &\left.\left.+\frac{(l+m)!}{2(l+m-2)!}\Box\hat{g}^{l-2}_m + (l+m)\partial_z\nabla\hat{g}^{l-2}_{m+1} + \frac{1}{4}\nabla^2\hat{g}^{l-2}_{m+2}\right)\right] , \end{aligned} \tag{5.39}$$

where $\Box = 2\partial^2_{zz} - \partial^2_{xx} - \partial^2_{yy}$.

Considering $l = 0$ we get the continuity equation

$$\begin{aligned}\partial_t \rho &= -\left[2\Re(\nabla^* \hat{g}^1_{-1}) + \partial_z \hat{g}^1_0\right] \\ &\quad + D_0 \Delta \rho + D_1 \left[4\Re\left(\nabla^{*^2} \hat{g}^2_{-2}\right) + 4\Re\left(\partial_z \nabla^* \hat{g}^2_{-1}\right) + \frac{1}{3}\Box \hat{g}^2_0\right] \ , \end{aligned} \tag{5.40}$$

which exhibits similar terms as in 2D: if the dynamics of particles is propagative the density will be advected by the polar field as pointed out on the first line. On the other hand the terms in the second line reflect a diffusive dynamics with isotropic spatial diffusion of the density and advection by the curvature induced current generated by the nematic field.

The SH decomposition of the velocity reversal term is straightforward knowing how spherical harmonics transform under parity: $Y_l^m(\Omega) \to Y_l^m(\Pi\Omega) = (-1)^l Y_l^m(\Omega)$ with $\Pi\Omega = (\pi - \theta, \psi + \pi)$. This relation yields

$$-\frac{a}{A_l^m}\int d\Omega \, Y_l^{m^*}(\Omega)\left(f(\Omega) - f(\Pi\Omega)\right) = -a\left(1 - (-1)^l\right)\hat{g}^l_m \ . \tag{5.41}$$

The angular self-diffusion operator, defined in (5.10), can be seen as a convolution between the distribution and the noise probability. Therefore, as in the 2 dimensional case, the SH decomposition of the self-diffusion term of the Boltzmann equation is simply given by the multiplication of the two modes of the convoluted functions.

$$\frac{1}{A_l^m}\int d\Omega Y_l^{m^*}(\Omega) I_{\rm sd}[f] = -\hat{g}^l_m + \sqrt{\frac{4\pi}{2l+1}}\hat{P}^l_0 \hat{g}^l_m = -\hat{g}^l_m + \widetilde{P}^l_0 \hat{g}^l_m \ , \tag{5.42}$$

where $\widetilde{P}^l_0 = \hat{P}^l_0 / A^0_l$ and $\hat{P}^l_0$ is the SH mode of degree l of the noise distribution (5.20). Note that from the symmetry of P its modes are different from 0 only for $m = 0$.

We now turn to the spherical harmonics decomposition of the collision gain term (5.13). In the following and for simplicity we will use a slight abuse of notations and denote by $R(\Omega_1)\Omega_2$ the orientation of the vector given by $R(\Omega_1)R(\Omega_2)\hat{e}_z$. Using the rotational symmetry properties of the kernel and alignment rule (5.14) and (5.17), with $\bar{\Omega} = R^{-1}(\Omega_1)\Omega_2$, the collision integral reads

$$I_{\rm col,gain}[f] = \int d\Omega_1 \int d\bar{\Omega}\, P\left(R^{-1}\left(\widetilde{\Psi}(\bar{\Omega})\right) R^{-1}(\Omega_1)\Omega\right) f(\Omega_1) f(R(\Omega_1)\bar{\Omega}) \widetilde{K}(\bar{\Omega}) \ . \tag{5.43}$$

Expanding the distributions in spherical harmonics modes, together with the rotation identity (5.28) and the axial symmetry of P (5.20), give

$$\begin{aligned}\frac{1}{A_l^m}\int d\Omega\, Y_l^{m^*}(\Omega) I_{\rm col,gain}[f] &= \frac{1}{A_l^m}\sum_{l_1,m_1} A^{m_1}_{l_1}\hat{g}^{l_1}_{m_1}\sum_{l_2,m_2} A^{m_2}_{l_2}\hat{g}^{l_2}_{m_2}\sum_{l_3}\hat{P}^{l_3}_0 \times \\ &\quad \sum_{m'_2,m'_3,m''_3}\int d\Omega\, Y_l^{m^*}(\Omega) Y^{m''_3}_{l_3}(\Omega) \times \\ &\quad \int d\Omega_1 Y^{m_1}_{l_1}(\Omega_1) D^{l_2^*}_{m_2,m'_2}(\Omega_1) D^{l_3}_{m''_3,m'_3}(\Omega_1) \times \\ &\quad \int d\bar{\Omega}\, Y^{m'_2}_{l_2}(\bar{\Omega}) D^{l_3}_{m'_3,0}\left(\widetilde{\Psi}(\bar{\Omega})\right)\widetilde{K}(\bar{\Omega}) \ , \end{aligned} \tag{5.44}$$

where $\sum_{l,m}$ is the shortened form of $\sum_{l=0}^{\infty}\sum_{m=-l}^{l}$ and the sum over integers m with index i are taken between $-l_i$ and l_i. We now make use of the orthogonality relation

(5.25) and the identity (5.31) together with the correspondence between spherical harmonics and Wigner D-matrices (5.30), this yields

$$\begin{aligned}\frac{1}{A_l^m}\int d\Omega\, Y_l^{m^*}(\Omega) I_{\mathrm{col,gain}}[f] &= \frac{\hat{P}_0^l}{A_l^0}\sum_{l_1,m_1}\sum_{l_2,m_2}\frac{A_{l_1}^{m_1}A_{l_2}^{m_2}}{A_l^m}\sqrt{\frac{2l_1+1}{2l+1}}\langle l_1\, l_2\, m_1\, m_2|l\, m\rangle \times \\ &\left[\sum_{m_2'=-\mathrm{Min}(l,l_2)}^{\mathrm{Min}(l,l_2)} \widetilde{K}_{m_2'}^{l_2,l}\langle l_1\, l_2\, 0\, m_2'|l\, m_2'\rangle\right]\hat{g}_{m_1}^{l_1}\hat{g}_{m_2}^{l_2}\ , \qquad (5.45)\end{aligned}$$

where, from the properties of the Clebsch-Gordan coefficients, the sum over l_2 is now taken between $|l-l_1|$ and $l+l_1$, and

$$\widetilde{K}_{m_2}^{l_1,l_2} = \sqrt{\frac{4\pi}{2l_2+1}}\int d\bar{\Omega}\, Y_{l_1}^{m_2}(\bar{\Omega})Y_{l_2}^{m_2^*}\left(\widetilde{\Psi}(\bar{\Omega})\right)\ . \qquad (5.46)$$

Note that the decomposition of the angular self diffusion integral (5.42) can be obtained using the same properties of spherical harmonics as the ones that have been employed for this calculation. After computation of the SH decomposition of the loss part of the collision integral, which follows straightforwardly from this derivation and is thus not detailed here, the decomposition of the full collision term reads

$$\frac{1}{A_l^m}\int d\Omega\, Y_l^{m^*}(\Omega) I_{\mathrm{col}}[f] = \sum_{l_1,m_1}\sum_{l_2=|l-l_1|,m_2}^{l+l_1} J_{m,m_1,m_2}^{l,l_1,l_2}\hat{g}_{m_1}^{l_1}\hat{g}_{m_2}^{l_2}\ , \qquad (5.47)$$

where

$$J_{m,m_1,m_2}^{l,l_1,l_2} = \widetilde{P}_0^l \widetilde{J}_{m,m_1,m_2}^{l,l_1,l_2} - \widetilde{I}_{m,m_1,m_2}^{l,l_1,l_2}\ , \qquad (5.48)$$

and

$$\begin{aligned}\widetilde{J}_{m,m_1,m_2}^{l,l_1,l_2} &= \frac{A_{l_1}^{m_1}A_{l_2}^{m_2}}{A_l^m}\sqrt{\frac{2l_1+1}{2l+1}}\langle l_1\, l_2\, m_1\, m_2|l\, m\rangle\delta_{m,m_1+m_2}\times \\ &\left[\sum_{m_2'=-\mathrm{Min}(l_2,l)}^{\mathrm{Min}(l_2,l)}\widetilde{K}_{m_2'}^{l_2,l}\langle l_1\, l_2\, 0\, m_2'|l\, m_2'\rangle\right]\ , \\ \widetilde{I}_{m,m_1,m_2}^{l,l_1,l_2} &= \frac{A_{l_1}^{m_1}A_{l_2}^{m_2}}{A_l^m}\sqrt{\frac{2l_1+1}{2l+1}}\hat{K}_0^{l_2}\langle l_1\, l_2\, m_1\, m_2|l\, m\rangle\langle l_1\, l_2\, 0\, 0|l\, 0\rangle\ .\end{aligned}$$

The function $\hat{K}_m^l$ is the SH decomposition of the collision kernel and it is zero $\forall\, m \neq 0$ thanks to the global rotation invariance of the system.

Collecting all the SH transformed terms of the kinetic equation we obtain the mode decomposition of the 3 dimensional Boltzmann equation (5.4)

$$\begin{aligned}\partial_t g_m^l &= \mathcal{T}_m^l\left[\left\{g_m^l\right\}\right] + D_0\Delta g_m^l + D_1\mathcal{D}_m^l\left[\left\{g_m^l\right\}\right] - a\left(1+(-1)^l\right)g_m^l \\ &+ \left[P_0^l - 1\right]g_m^l + \sum_{l_1,m_1}\sum_{l_2=|l-l_1|,\, m_2}^{l+l_1} J_{m,m_1,m_2}^{l,l_1,l_2}g_{m_1}^{l_1}g_{m_2}^{l_2}\ , \qquad (5.49)\end{aligned}$$

where we have removed the hats and tildes in order to simplify the notations.

Although this computation holds for any axisymmetric noise distribution, numerical evaluations of the coefficients of the hydrodynamic equations derived in the following have been done using Gaussian weights $P_0^l = \exp(-l^2\sigma^2/2)$. We have checked that results that are presented are not qualitatively influenced by the precise form of the distribution.

5.4 Hydrodynamic equations for ferromagnetic alignment

In this section, we derive hydrodynamic equations for particles which align their velocities in a ferromagnetic way. In the restricted Vicsek framework, this symmetry of the interaction requires the particles to exhibit polar free motion in order to be able to generate spontaneous order. Therefore, we only consider Vicsek-like particles moving at constant speed with no velocity reversal.

5.4.1 Derivation of the hydrodynamic equations

As argued in Section 5.3.1, the Boltzmann equation does not show any spatial diffusion nor velocity reversal term:

$$\partial_t g^l_m = \mathcal{T}^l_m\left[\left\{g^l_m\right\}\right] + \left[P^l_0 - 1\right] g^l_m + \sum_{l_1,m_1} \sum_{l_2=|l-l_1|,\, m_2}^{l+l_1} J^{l,l_1,l_2}_{m,m_1,m_2} g^{l_1}_{m_1} g^{l_2}_{m_2} \;. \tag{5.50}$$

The system of equations (5.50) exhibits a trivial solution: the homogeneous disordered (HD) solution, existing for any value of the microscopic parameters (ρ_0, σ). For this solution the zero mode is equal to the homogeneous density: $g^0_0 = \rho_0$, and all the other modes vanish: $g^l_m = 0$ for all $l > 0$ and m. Linearizing the Boltzmann hierarchy (5.50) around the HD state with respect to homogeneous perturbations (space independent), the modes evolve as

$$\begin{aligned} g^0_0 &= \rho = \rho_0 + \delta\rho, \qquad g^l_m = \delta g^l_m \quad \forall l > 0, & \text{(5.51a)}\\ \partial_t \delta g^l_m &= \left[\left(P^l_0 - 1\right) + \left(J^{l,0,l}_{m,0,m} + J^{l,l,0}_{m,m,0}\right)\rho_0\right]\delta g^l_m, & \text{(5.51b)}\\ &\equiv \mu^l_m[\rho_0]\delta g^l_m, & \text{(5.51c)}\end{aligned}$$

where the linear coefficients μ^l_m are given by

$$\mu^l_m[\rho_0] = P^l_0 - 1 + \frac{\rho_0}{\sqrt{4\pi}}\left[P^l_0\left(\frac{1}{\sqrt{2l+1}}\sum_{m'=-l}^{l} \tilde{K}^{l,l}_{m'} + \tilde{K}^{0,l}_0\right) - \frac{\hat{K}^l_0}{\sqrt{2l+1}} - \hat{K}^0_0\right] \;. \tag{5.52}$$

Note that, as a consequence of global rotational invariance, they do not depend on the index m, which we omit in the following. The HD state is linearly stable when all the linear coefficients μ^l are negative, while the physical field associated to g^l grows when μ^l becomes positive. For $l = 0, 1, 2$ the coefficients are

$$\begin{aligned} \mu^0 &= 0\;, & \text{(5.53a)}\\ \mu^1 &= (P^1_0 - 1) + \left(\frac{\pi}{4}P^1_0 - \frac{8}{15}\right)\rho_0\;, & \text{(5.53b)}\\ \mu^2 &= (P^2_0 - 1) + \left(\frac{2}{15}P^2_0 - \frac{68}{105}\right)\rho_0 \quad (\le 0)\;. & \text{(5.53c)}\end{aligned}$$

The linear coefficient μ^1 associated to the polar field becomes positive at large densities ρ_0 and small angular noise strength σ. Figure 5.2 shows the line $\sigma_t(\rho_0)$ along which the coefficient $\mu^1 = 0$ in the (ρ_0, σ) plane, comparing the 2 dimensional [79] and the 3 dimensional results. The HD state is stable above this line. Below, the Boltzmann

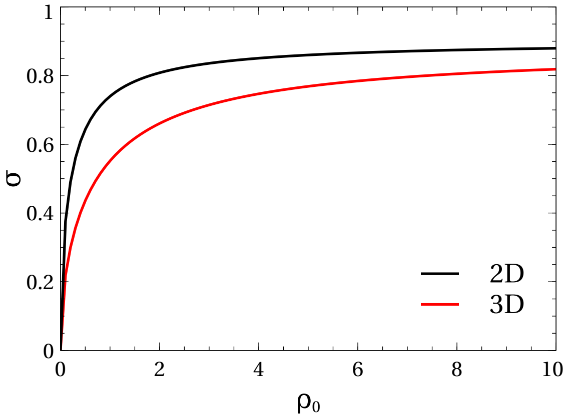

FIGURE 5.2 – Linear stability limit of the homogeneous disordered solution in the density-noise plane for the polar class. The transition line given by $\mu^1 = 0$, the stable region is above. The black and red lines, below which the disordered solution is unstable to homogeneous perturbations, correspond respectively to the 2D and 3D cases.

equation possesses another homogeneous solution with polar order that we call the homogeneous ordered (HO) state. We checked until $l = 10$ that the linear coefficients μ^l are more and more negative with l. We assume that for larger values of l they do the same.

From the global rotational invariance of the system we can choose the reference frame such that the global polar order is along the z axis. In Section 5.3.3 we have shown that this comes down to set the g^1_m fields to 0 for any $m \neq 0$. Then from the property of the nonlinear coefficients in the Boltzmann equation, $J^{l,l_1,l_2}_{m,m_1,m_2} = J^{l,l_1,l_2}_{m,m_1,m_2}\delta_{m,\,m_1+m_2}$, the numerical evaluation of its HO solution can be done considering only real g^l_0 fields for all l.

Figure 5.3 shows the result for the Boltzmann equation (5.49) truncated at the 10th mode with homogeneous density $\rho_0 = 1$, varying the noise strength σ. (We checked that results are stable considering up to 20 modes.) As expected, $|g^1_0|$ grows below the critical noise $\sigma_c \simeq 0.551$ like $\sqrt{\sigma_c - \sigma}$, and all the others modes grow consequently due to nonlinear couplings in the Boltzmann equation. The inset of Figure 5.3 shows that the first three modes exhibit a scaling behavior in the vicinity of the transition: comparing $|g^2_0|$ with $|g^1_0|^2$ and $|g^3_0|^{\frac{2}{3}}$ we show that they fall on the same curve. (This is also true for the next modes, but they are not shown for clarity.) Defining the scaling parameter ε by the amplitude of the polar field ($|g^1| \approx \varepsilon \ll 1$), we thus find that

$$g^l_m \approx \varepsilon^l, \qquad \forall l > 0, \quad \forall m\ , \tag{5.54}$$

which we assume to be true in all generality.

Moreover, it is assumed that the spatial and the temporal variations of the modes are small and comparable in magnitude to the parameter introduced above. For systems such as the 3 dimensional polar class considered here, one uses the *propagative ansatz* where the temporal variations are of the same order as the spatial variations:

$$\nabla \approx \nabla^* \approx \partial_x \approx \partial_z \approx \partial_t \approx \varepsilon\ , \tag{5.55}$$

implying that the density variations scale as $\delta\rho \approx \varepsilon$ in order to balance the first equation of the hierarchy.

Using this scaling ansatz, we expand the Boltzmann hierarchy in series of ε and

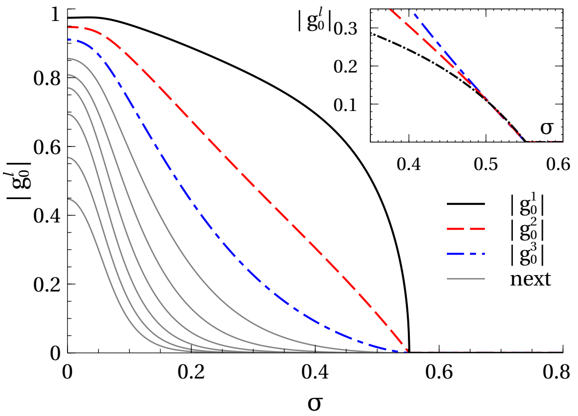

FIGURE 5.3 – Numerical evaluation of the homogeneous ordered solution of the Boltzmann equation for the polar class truncating the hierarchy at the 10th mode (density $\rho_0 = 1$). The solid black line indicates the first mode $|g_0^1|$, saturating at a finite value. The dashed red and dashed-dotted blue lines correspond respectively to the second and third modes. The next modes from $l = 4$ to $l = 9$ are shown with grey lines. The inset shows the scaling between $\sim |g_0^1|^2$, $|g_0^2|$ and $\sim |g_0^3|^{\frac{2}{3}}$ close to the transition point.

truncate it at the first non-trivial order, ε^3. This leads to equations for the density, polar and nematic fields. The density and polar fields are governed by

$$\partial_t \rho = -\nabla^* g_{-1}^1 + \frac{1}{2}\nabla g_1^1 - \partial_z g_0^1 \tag{5.56a}$$

$$\begin{aligned}\partial_t g_{-1}^1 = {} & -2\nabla^* g_{-2}^2 + \frac{1}{6}(\nabla g_0^2 - \nabla\rho) - \partial_z g_{-1}^2 + \mu^1[\rho] g_{-1}^1 + X_{-1\,-1\,0}^{1\,1\,1}\; g_0^1 g_{-1}^1 \\ & + X_{-1\,-1\,0}^{1\,1\,2}\; g_0^2 g_{-1}^1 + X_{-1\,0\,-1}^{1\,1\,2}\; g_0^1 g_{-1}^2 + X_{-1\,1\,-2}^{1\,1\,2}\; g_1^1 g_{-2}^2\end{aligned} \tag{5.56b}$$

$$\begin{aligned}\partial_t g_0^1 = {} & -\nabla^* g_{-1}^2 + \frac{1}{6}\nabla g_1^2 - \frac{2}{3}\partial_z g_0^2 - \frac{1}{3}\partial_z \rho + \mu^1[\rho] g_0^1 + X_{0\,-1\,1}^{1\,1\,1}\; g_{-1}^1 g_1^1 \\ & + X_{0\,-1\,1}^{1\,1\,2}\; g_{-1}^1 g_1^2 + J_{0\,0\,0}^{1\,1\,1}\; g_0^1 g_0^1 + X_{0\,0\,0}^{1\,1\,2}\; g_0^1 g_0^2 + X_{0\,1\,-1}^{1\,1\,2}\; g_1^1 g_{-1}^2\end{aligned} \tag{5.56c}$$

with $X_{m\,m_1\,m_2}^{l\,l_1\,l_2} = J_{m\,m_1\,m_2}^{l\,l_1\,l_2} + J_{m\,m_2\,m_1}^{l\,l_2\,l_1}$. The nematic field g^2, at this order, is slaved to the density and the polar fields, as in the 2 dimensional case [79]:

$$\begin{aligned} g_{-2}^2 &= \frac{1}{10\mu^2}\nabla g_{-1}^1 - \frac{J_{-2\,-1\,-1}^{2\,1\,1}}{\mu^2}\; g_{-1}^1 g_{-1}^1 \,, \\ g_{-1}^2 &= \frac{1}{10\mu^2}\nabla g_0^1 + \frac{1}{5\mu^2}\partial_z g_{-1}^1 - \frac{X_{-1\,-1\,0}^{2\,1\,1}}{\mu^2}\; g_{-1}^1 g_0^1 \,, \\ g_0^2 &= -\frac{2}{5\mu^2}\Re(\nabla^* g_{-1}^1) + \frac{2}{5\mu^2}\partial_z g_0^1 + 2\frac{X_{0\,-1\,1}^{2\,1\,1}}{\mu^2}\; |g_{-1}^1|^2 - \frac{J_{0\,0\,0}^{2\,1\,1}}{\mu^2}\; g_0^1 g_0^1 \,. \end{aligned}$$

Injecting these relations into Eq. (5.56) we obtain a closed set of equations for the density and the polar fields. After some algebra and going back to the representation in the real space (5.34), the hydrodynamic equations for the 3 dimensional polar class are

$$\partial_t \rho = -\vec{\nabla}\cdot\vec{w} \,, \tag{5.57a}$$

$$\begin{aligned}\partial_t \vec{w} = {} & \left(\mu^1[\rho] - \frac{\xi}{4}|\vec{w}|^2\right)\vec{w} - \frac{1}{3}\vec{\nabla}\rho + D_{\mathrm{B}}\vec{\nabla}\left(\vec{\nabla}\cdot\vec{w}\right) + D_{\mathrm{T}}\Delta\vec{w} \\ & -\lambda_1\left(\vec{w}\cdot\vec{\nabla}\right)\vec{w} - \lambda_2\left(\vec{\nabla}\cdot\vec{w}\right)\vec{w} - \lambda_3\vec{\nabla}\left(|\vec{w}|^2\right) \,.\end{aligned} \tag{5.57b}$$

	3D	2D
$\mu^1[\rho]$	$P_0^1 - 1 + \left(\frac{\pi}{4}P_0^1 - \frac{8}{15}\right)\rho$	$P_1 - 1 + \frac{8}{\pi}\left(P_1 - \frac{2}{3}\right)\rho$
$\xi\,(>0)$	$\frac{2(128-105\pi P_0^1)(2+7P_0^2)}{25(-105-68\rho_0+7(15+2\rho_0)P_0^2)}$	$\frac{16}{\pi}\frac{(5P_1-2)(3P_2+1)}{15\pi(1-P_2)+8(7+5P_2)\rho_0}$
$D_T\,(>0)$	$\frac{42}{2(105+68\rho_0-7(15+2\rho_0)P_0^2)}$	$\frac{15\pi}{4(15\pi(1-P_2)+8(7+5P_2)\rho_0)}$
D_B	$\frac{D_T}{3}$	0
λ_1	$-\frac{3(352-105\pi P_0^1+784P_0^2)}{40(-105-68\rho_0+7(15+2\rho_0)P_0^2)}$	$\frac{2(16+30P_2-15P_1)}{15\pi(1-P_2)+8(7+5P_2)\rho_0}$
λ_2	$-\frac{208+105\pi P_0^1+1176P_0^2}{20(-105-68\rho_0+7(15+2\rho_0)P_0^2)}$	$\frac{2(4+30P_2+15P_1)}{15\pi(1-P_2)+8(7+5P_2)\rho_0}$
λ_3	$\frac{224(2+7P_0^2)+(384-315\pi P_0^1)}{80(105+68\rho_0-7(15+2\rho_0)P_0^2)}$	$-\frac{\lambda_2}{2}$

TABLE 5.1 – Comparison of the hydrodynamic parameters of the polar class between the 3 dimensional case and the 2 dimensional case [79]. The main difference between the two cases lies in the fact that there is an anisotropic diffusion term and $\lambda_2 \neq -2\lambda_3$ in three dimensions. In the right column, the P_i parameters are the moments of the angular noise distribution in 2D, analogous to the P_0^i in 3D.

These equations are nothing but the Toner-Tu equations presented in Section 1.3.2. They are formally the same as those derived in 2D using the same method. The definition of all the hydrodynamic parameters are given in Table 5.1 and their dependency on the local fields is made explicit with the use of the square brackets.

The non conservation of the momentum in the microscopic model forces the hydrodynamic equations to reflect the absence of Galilean invariance which would have required $\lambda_1 = \lambda_2 = \frac{1}{\rho}$ and $\lambda_3 = 0$. Moreover, although breakdown of Galilean invariance is also allowed at equilibrium, derivation of Equations (5.57) from a free energy implies that $\lambda_3 = -2\lambda_2$ [21]. This relation holds in the 2 dimensional equations for the Vicsek model without steric interactions, derived from the BGL approach, but remarkably it is no more the case in 3 dimensions as shown in Table 5.1. Another difference is the presence of the anisotropic diffusion term $\vec{\nabla}\left(\vec{\nabla}\cdot\vec{w}\right)$ which is allowed in 2D although it has a zero coefficient [79]. Finally, similarly to the 2 dimensional result, the isotropic pressure term is not modified by activity and remains linear in ρ.

5.4.2 Homogeneous solutions

The homogeneous solutions of (5.57) satisfy $\rho = \rho_0$ and evolve according to the Ginzburg-Landau equation

$$\partial_t w_0 = \left(\mu^1[\rho_0] - \frac{\xi}{4}w_0^2\right) w_0 \, , \tag{5.58}$$

where $w_0 = |\vec{w}|$.

The homogeneous disordered solution $w_0 = 0$ becomes unstable whenever μ^1 becomes positive. Below the transition line in the (ρ_0, σ) parameter plane, the polar field grows until the cubic nonlinearity is saturated, and the homogeneous ordered

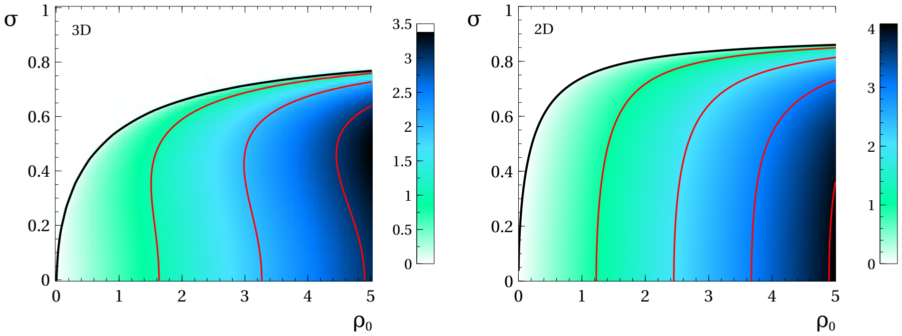

FIGURE 5.4 – Phase diagram in the density-noise plane of the hydrodynamic equations for the polar class. The color codes for w_0, the strength of the polar order of the homogeneous ordered solution. Solid black line: $\mu^1[\rho] = 0$, limit of linear stability of the homogeneous disordered solution. Red lines: contours $w_0 = 1, 2, 3$. Left panel: 3D case for which w_0 is not monotonously varying with σ. Right panel: 2D case, with monotonous variation of w_0.

solution is found:

$$\rho = \rho_0 \quad ; \quad w_0 = 2\sqrt{\frac{\mu^1[\rho_0]}{\xi}} \ . \tag{5.59}$$

When it exists, the HO solution is always physical, being smaller than the homogeneous density ρ_0 in all the parameter space. This is shown in Figure 5.4 where the red isolines correspond to the values $w_0 = 1, 2, 3$. Remarkably, the global order w_0 is not monotonous and shows a maximum at finite noise at any fixed density, in contrast with the 2 dimensional case. This effect depends on the distribution of the noise considered. For instance, if one uses the Von Mises distribution, $P(\theta) \propto \exp\left(\cos(\theta)/\sigma^2\right)$, this non-monotonicity is reduced although it is not removed.

5.4.3 Linear stability analysis

We now compute the linear stability of the homogeneous solutions assuming small fluctuations of the fields around $\rho = \rho_0 + \delta\rho$ and $\vec{w} = \vec{w}_0 + \delta\vec{w}$. The linearized hydrodynamic equations are

$$\begin{aligned}
\partial_t \delta\rho &= -\vec{\nabla}\cdot\delta\vec{w} \ , && (5.60\text{a})\\
\partial_t \delta\vec{w} &= \partial\mu^1 \vec{w}_0 \delta\rho - \frac{\xi}{2}\vec{w}_0(\vec{w}_0\cdot\delta\vec{w}) + D_B \vec{\nabla}(\vec{\nabla}\cdot\delta\vec{w}) + D_T \triangle\delta\vec{w} && \\
&\quad -\lambda_1(\vec{w}_0\cdot\vec{\nabla})\delta\vec{w} - \lambda_2\vec{w}_0(\vec{\nabla}\cdot\delta\vec{w}) - 2\lambda_3\vec{\nabla}(\vec{w}_0\cdot\delta\vec{w}) && (5.60\text{b})\\
&\quad +(\mu^1[\rho_0] - \frac{\xi}{4}|\vec{w}_0|^2)\delta\vec{w} - \frac{1}{3}\vec{\nabla}\delta\rho \ , &&
\end{aligned}$$

with $\partial\mu^1 = \partial\mu^1/\partial\rho$. Using Fourier transform in space ($\vec{q}$ is the wave vector) these linear equations become

$$\begin{aligned}
\partial_t \delta\rho &= -\imath\vec{q}\cdot\delta\vec{w} \ , && (5.61\text{a})\\
\partial_t \delta\vec{w} &= \partial\mu^1 \vec{w}_0 \delta\rho - \frac{\xi}{2}\vec{w}_0(\vec{w}_0\cdot\delta\vec{w}) - D_B \vec{q}(\vec{q}\cdot\delta\vec{w}) - D_T q^2\delta\vec{w} && \\
&\quad -\lambda_1\imath(\vec{w}_0\cdot\vec{q})\delta\vec{w} - \lambda_2\imath\vec{w}_0(\vec{q}\cdot\delta\vec{w}) - 2\lambda_3\imath\vec{q}(\vec{w}_0\cdot\delta\vec{w}) && (5.61\text{b})\\
&\quad +(\mu^1[\rho_0] - \frac{\xi}{4}|\vec{w}_0|^2)\delta\vec{w} - \frac{\imath}{3}\vec{q}\delta\rho \ . &&
\end{aligned}$$

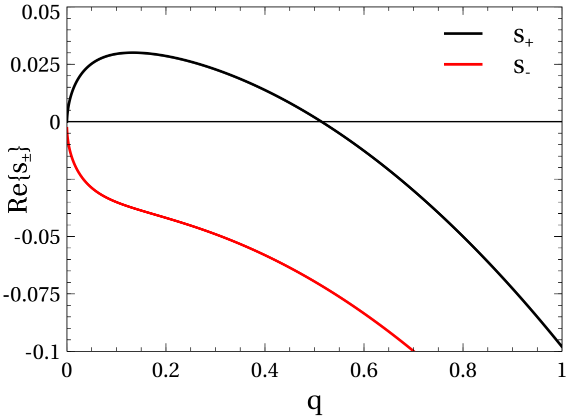

FIGURE 5.5 – Behavior of the real part of the eigenvalue governing the long wavelength linear stability of the homogeneous ordered solution of the polar hydrodynamic equations, given by Eq. (5.68). Parameters: $\rho_0 = 1$ and $\sigma = 0.55$. Solid black line: real part of s_+. Solid red line: real part of s_-.

Solving this eigenvalue problem yields four solutions $s_i = s_i(\vec{q}, \vec{w}_0)$, with $i = 1, \ldots, 4$. The system is linearly unstable whenever any real part of these solutions is positive.

In the disordered case $\left(\vec{w}_0 = \vec{0}\right)$ the global rotational invariance implies that only wave-vectors parallel to the perturbation $\delta\vec{w} \parallel \vec{q}$ evolve and can destabilize the system. Inserting the solution of (5.61a) in (5.61b) we obtain the following relations between the wave vectors and the eigenvalues

$$\left(s + D_T q^2 - \mu^1\right)^2 = 0 \; , \tag{5.62}$$

$$s^2 + s\left((D_T + D_B)q^2 - \mu^1\right) + \tfrac{1}{3}q^2 = 0, \qquad q = |\vec{q}| \; . \tag{5.63}$$

Defining $D = D_T + D_B$ to lighten notations, the independent solutions are

$$s_r \;=\; \mu^1 - D_T q^2 \; , \tag{5.64}$$

$$s_\pm \;=\; \frac{\mu^1 - Dq^2}{2} \pm \frac{1}{2}\sqrt{\mu^2 - 2\mu^1 D q^2 - \frac{1}{3}q^2 + D^2 q^4} \; . \tag{5.65}$$

They are negative for all $D_T > 0$, $D_T + D_B > 0$ and $\mu^1 < 0$. Consequently, the disordered state is stable in all the region where $\mu^1 < 0$, as in the 2 dimensional case.

Considering only longitudinal perturbations of the ordered state $\vec{w}_0 = w_0\hat{e} \neq \vec{0}$, we have $\vec{q} = q\hat{e}$ and $\delta\vec{w} = \delta w\hat{e}$. The equations for this family of perturbations are

$$\partial_t \delta\rho \;=\; -\imath q \delta w \; , \tag{5.66a}$$

$$\partial_t \delta w \;=\; w_0 \partial\mu^1 \delta\rho - 2\mu^1 \delta w - \frac{\imath}{3} q \delta\rho - D q^2 \delta w - \lambda w_0 \imath q \delta w \; , \tag{5.66b}$$

where $\lambda = \lambda_1 + \lambda_2 + 2\lambda_3$. After some algebra, the corresponding equation for the eigenvalues [3] reads

$$s^2 + s\left(2\mu^1 + Dq^2 + \imath\lambda w_0 q\right) + \left(\frac{1}{3}q^2 + \imath\partial\mu^1 w_0 q\right) = 0 \; . \tag{5.67}$$

---

[3] The other two relations come from the transverse perturbations.

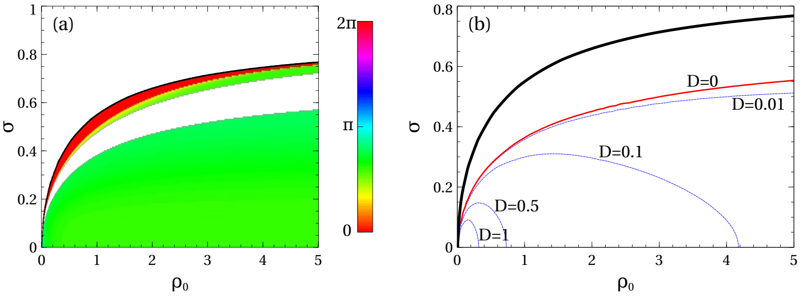

FIGURE 5.6 – (a): phase diagram of the hydrodynamic equations for the polar class. Solid black line: $\mu^1[\rho] = 0$. Below this line the homogeneous ordered solution exists. It is linearly unstable in the colored regions, where the color represents the direction of the most unstable mode. In the red region close to the transition the instability is parallel to the global order $\vec{w}_0$. The green region of transversal modes deep in the ordered phase corresponds to the spurious instability described in the text. (b): variation of the upper limit of spurious instability with the spatial diffusion constant D. Solid red line: $D = 0$. Dashed blue lines: $D = 0.01, 0.1, 0.5, 1$.

Defining $B(q) = 2\mu^1 + Dq^2 + \imath\lambda w_0 q$ and $C(q) = \frac{1}{3}q^2 + \imath\partial\mu^1 w_0 q$, the two solutions of this equation are

$$s^l_\pm = -\frac{B(q)}{2} \pm \frac{1}{2}\sqrt{B^2(q) - 4C(q)}\ . \tag{5.68}$$

The real part of the $(-)$ solution is negative, while the real part of the $(+)$ solution has a range of wave-vectors for which it is positive as shown in Figure 5.5. Hence, the ordered phase is longitudinally unstable in the region close to the transition line. At small wave vectors the solutions behave as

$$\begin{aligned} s^l_- &= -2\mu^1 + \imath w_0\left(\frac{\partial\mu^1}{2\mu^1} - \lambda\right)q - \left(D + \frac{(\partial\mu^1)^2}{2(\mu^1)^2\xi} - \frac{\lambda\partial\mu^1}{\mu^1\xi} - \frac{1}{6\mu^1}\right)q^2 + \mathcal{O}\left(q^3\right)\ , \\ s^l_+ &= -\imath w_0\frac{\partial\mu^1}{2\mu^1}q + \left(\frac{(\partial\mu^1)^2}{2\mu^1\xi} - \frac{\lambda\partial\mu^1}{\xi} - \frac{1}{6}\right)\frac{q^2}{\mu^1} + \mathcal{O}\left(q^3\right)\ . \end{aligned} \tag{5.69}$$

The real part of the $(+)$ solution is driven by a q^2 term that grows at small wave-vectors on a scale $\sim \frac{1}{\mu^1}$ which is diverging at the transition. The resulting instability is thus due to the $\partial\mu^1$ term, which comes from the density dependence of the linear coefficient $\mu^1[\rho]$ in the polar field equation.

The full linear stability analysis of the homogeneous solutions was also computed numerically (Figure 5.6(a)). Close to the order/disorder threshold (black line), the ordered solution is linearly unstable with respect to longitudinal perturbations at a finite wavelength. Deeper in the ordered phase the ordered solution becomes linearly stable. At even lower noise, a second instability appears. From the analysis of the 2 dimensional Boltzmann equation presented in Chapter 3, this instability is likely to be an artifact of the truncation procedure. Moreover, like in 2D [80], its impact strongly depends on the presence of spatial diffusion: adding spatial diffusion directly at the kinetic level, its domain in parameter space shrinks rapidly (Figure 5.6(b)). We hereafter call it the *spurious* instability.

5.5 Hydrodynamic equations for nematic alignment

In this section, we derive the hydrodynamic equations for 3D Vicsek-style systems with nematic alignment, represented by the active nematics and the rods classes.

5.5.1 Boltzmann equations for classes with nematic alignment

Kinetic equations for active nematics and rods

In the active nematics class, particles reverse their velocity on short time scales, the computation sketched in Section 5.3.1 shows that the resulting Boltzmann equation has no drift term but only spatial diffusion with coefficients $D_0 = \frac{1}{3}$ and $D_1 = 3D_0$. Moreover, as this problem possesses a full nematic symmetry, only even modes (with respect to l index) need to be considered. Hence, for active nematics the Boltzmann equation becomes

$$\begin{aligned} \partial_t g^{2l}_m &= D_0 \Delta g^{2l}_m + D_1 \mathcal{D}^{2l}_m \left[\left\{ g^{2l}_m \right\}\right] \,, \\ &\quad + \left[P^{2l}_0 - 1\right] g^{2l}_m + \sum_{l_1, m_1} \sum_{l_2 = |l - l_1|, \, m_2}^{l + l_1} J^{\mathrm{A}}{}^{2l, 2l_1, 2l_2}_{m, m_1, m_2} \, g^{2l_1}_{m_1} g^{2l_2}_{m_2} \,, \end{aligned} \tag{5.70}$$

where the coefficients $J^{\mathrm{A}}{}^{2l,2l_1,2l_2}_{m,m_1,m_2}$ are the ones computed in Section 5.3.4 using the apolar kernel (5.16) and the nematic alignement rule (5.19).

On the contrary, in the rods class particles reverse their directions of motion on a finite timescale a such that no spatial diffusion is attained at the kinetic level. Their dynamics is therefore propagative and the resulting Boltzmann equation reads

$$\begin{aligned} \partial_t g^l_m &= \mathcal{T}^l_m \left[\left\{ g^l_m \right\}\right] - a \left(1 + (-1)^l\right) g^l_m + \left[P^l_0 - 1\right] g^l_m \\ &\quad + \sum_{l_1, m_1} \sum_{l_2 = |l - l_1|, \, m_2}^{l + l_1} J^{\mathrm{R}}{}^{l, l_1, l_2}_{m, m_1, m_2} g^{l_1}_{m_1} g^{l_2}_{m_2} \,, \end{aligned} \tag{5.71}$$

with $J^{\mathrm{R}}{}^{l,l_1,l_2}_{m,m_1,m_2}$ evaluated considering the polar kernel (5.14) and nematic alignment rule (5.19). Here, as the motion possesses polar symmetry, we can not set the odd modes to zero.

The large reversal rate diffusive limit (5.70) can be retrieved from the propagative hierarchy (5.71) with finite reversal. To do this we need to temporarily reintroduce v_0, the microscopic velocity of particles, which was set to 1 in Section 5.3.1 when the Boltzmann equation was de-dimentionalized. Indeed, in the infinite reversal rate limit the odd field equations (with respect to l index) possess a diverging damping term $\sim -2a$ and can thus be enslaved to the even fields. The latter then acquire an effective diffusion coefficient that scales like $\frac{v_0^2}{a}$. In order to keep it finite, we assume that $v_0^2 \underset{a \to \infty}{\sim} a$. After enslaving the odd modes, the hierarchy (5.71) at $\mathcal{O}\left(\frac{v_0^2}{a}\right)$ is formally the same as (5.70), with $D_0 = \frac{v_0^2}{6a}$ and $D_1 = 3D_0$. Therefore, in the following, when we refer to the large reversal rate limit for the rods we will implicitly consider a nondimensionalization where $v_0^2 \sim a$ instead of $v_0 = 1$ as previously set for the polar class. For numerical evaluations, we have considered the scaling form $v_0 = \sqrt{1 + a}$ such that $v_0 = 1$ when $a = 0$ and $v_0^2 \sim a$ when a becomes large.

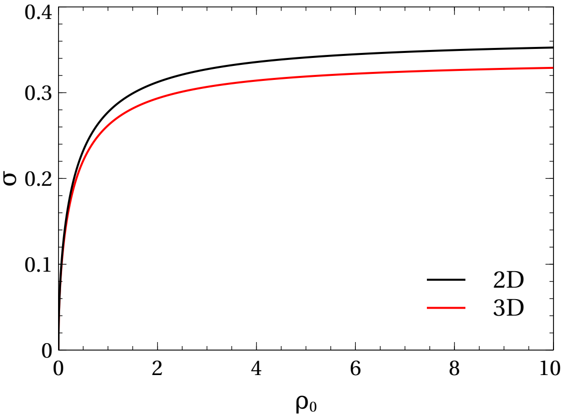

FIGURE 5.7 – The transition line ($\mu^2 = 0$) delimiting the stability region of the homogeneous disordered solution in the density-noise plane for the active nematics class. The solution is unstable to homogeneous perturbations below the black line in 2D, and below the red line in 3D.

Homogeneous solutions of the Boltzmann equation

In this section, we compute the homogeneous solutions of the Boltzmann equation considering nematic alignment (both active nematics and rods classes). Since the rods hierarchy (5.71) does not show any homogeneous solution with non-zero odd modes, the two classes are formally the same at this stage. Therefore, we will focus on the active nematics class, the results of this section being easily generalized to the rods.

The Boltzmann hierarchy (5.70) has the trivial homogeneous disordered solution: $g_0^0 = \rho_0$, $g_m^{2l} = 0$ $\forall l > 0$ $\forall m$. Homogeneous perturbations of this solution are

$$g_0^0 = \rho = \rho_0 + \delta\rho, \quad g_m^{2l} = \delta g_m^{2l} \quad \forall l > 0\ ,\ \forall m \tag{5.72}$$

and linearizing the Boltzmann hierarchy around this particular solution gives the linear coefficients

$$\partial_t \delta g_m^{2l}(\vec{r},t) = \left[\left(P_0^{2l} - 1\right) + \left(J_{m,0,m}^{2l,0,2l} + J_{m,m,0}^{2l,2l,0}\right)\rho_0\right]\delta g_m^{2l} \equiv \mu_m^{2l}[\rho_0]\delta g_m^{2l}\ . \tag{5.73}$$

As in the polar case, the coefficients μ_m^{2l} do not depend on the index m, and we thus omit it thereafter. The first three coefficients are

$$\mu^2 = (P_0^2 - 1) + \frac{2}{15}\left((8+3\sqrt{2})P_0^2 - \frac{68}{7}\right)\rho_0\ , \tag{5.74a}$$

$$\mu^4 = (P_0^4 - 1) + \frac{1}{3}\left(\frac{1}{\sqrt{2}}P_0^4 - \frac{920}{131}\right)\rho_0\ (\leq 0)\ , \tag{5.74b}$$

$$\mu^6 = (P_0^6 - 1) - \frac{1}{5}\left(\frac{59}{24\sqrt{2}}P_0^6 + \frac{952}{143}\right)\rho_0\ (\leq 0)\ . \tag{5.74c}$$

Only the μ^2 coefficient, corresponding to the nematic field, can change sign while the others are negative. The disordered solution is stable at large noise and small densities and it becomes unstable to homogeneous perturbations below the line $\sigma_t(\rho_0)$ defined by $\mu^2 = 0$, as shown in Fig 5.7. Like for the polar case studied in the previous section, the transition line in 3D is at lower noises than in the 2 dimensional case.

As in the polar case, assuming that the nematic order is along the z direction we can set all the $m \neq 0$ modes to zero for the numerical evaluation of the HO solution of

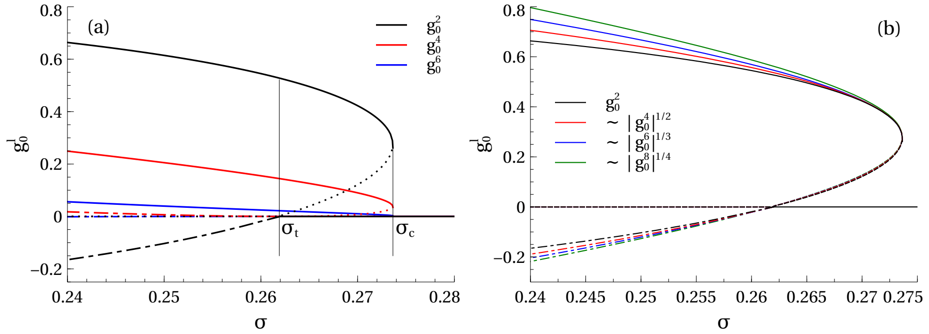

FIGURE 5.8 – Numerical evaluation of the homogeneous ordered solution of the Boltzmann equation for the active nematics class, truncating the hierarchy at the 10th mode. (a) shows the discontinuous character of the transition with the bistability region between σ_t and σ_c. The full lines are the values of the modes following the uniaxial solution, while the dotted lines are the values of the modes along the biaxial solution at the transition. The biaxial solution below σ_t are shown with a dot-dashed line. (b) shows the rescaled modes following the scaling ansatz (5.76), giving a good collapse close to the transition, although the first non zero mode g_0^2 is not small. For convenience the positive values of the modes $g_0^4, g_0^6, \ldots$, following the biaxial solution (negative g_0^2) are shown with a minus sign in order to highlight the validity of the scaling.

the Boltzmann equation (see Section 5.3.3 for details). Figure 5.8(a) shows the result for the first 10 even modes of the Boltzmann hierarchy (5.70) for $\rho_0 = 1$ as function of the noise. This computation was done using the Newton method in order to capture both stable and unstable solutions. Decreasing the noise, the disordered solution becomes unstable for $\sigma \leq \sigma_t$ and the $l > 0$ modes jump discontinuously to a positive value. Then a hysteresis loop can be built increasing the noise up to $\sigma_c > \sigma_t$ defining an upper bound for the existence of the ordered solution. Therefore, active nematics in three dimensions exhibit a discontinuous transition with coexistence of disordered and homogeneous ordered solutions at the mean field level. As for equilibrium liquid crystals, we will show that this can be understood at the hydrodynamic level from symmetry reasons [138]. We also see that equations (5.70) admit solutions with a negative order parameter which will be discussed in the following and are always unstable to homogeneous perturbations[4].

5.5.2 Derivation of the hydrodynamic equations

The following sections are dedicated to the derivation of the hydrodynamic equations for classes with nematic alignment. As in Section 5.4.1, they are obtained using a scaling parameter ε that allows to truncate and close the Boltzmann hierarchy with an ansatz compatible with the symmetries of the problem.

Hydrodynamic equations for the active nematics class

The scaling ansatz necessary to truncate and close the infinite Boltzmann hierarchy (5.70) for active nematics relates space and time *diffusively*:

$$\nabla^2 \approx \nabla^{*^2} \approx \partial_{ij}^2 \approx \partial_t \approx \varepsilon^2 \, , \tag{5.75}$$

---

[4] These solutions are stable considering only the $m = 0$ modes as we do for the computation of the HO solution. This is because below σ_t the instability is located on the other components of the nematic field (those for which $m \neq 0$), as shown in Section 5.5.3.

with $i, j = x, y, z$. Close to and below the transition line $\sigma_t(\rho_0)$, we assume that the nematic field saturates to a small value ε, therefore, balancing the hierarchy terms we can obtain the self-consistent scaling

$$g_m^{2l} \approx \varepsilon^l, \qquad \forall l > 0, \quad \forall m \,. \tag{5.76}$$

As usual, the first non trivial order is then ε^3, leaving the density field ρ, the nematic field g_m^2 and g_m^4. The dynamics of the g_m^4's is completely slaved to the lower order modes.

After lengthy algebraic calculations, similar to those shown Section 5.4.1 for ferromagnetic alignment, the continuity equation in real space takes the simple form

$$\partial_t \rho = D_0 \Delta \rho + D_1 \left(\mathbf{\Gamma} : \mathbf{Q} \right) \,, \tag{5.77}$$

where the traceless symmetric matrix $\mathbf{\Gamma}$ is

$$\mathbf{\Gamma} = \frac{1}{3} \begin{pmatrix} 2\partial_{xx}^2 - \partial_{yy}^2 - \partial_{zz}^2 & 3\partial_{xy}^2 & 3\partial_{xz}^2 \\ 3\partial_{xy}^2 & 2\partial_{yy}^2 - \partial_{xx}^2 - \partial_{zz}^2 & 3\partial_{yz}^2 \\ 3\partial_{xz}^2 & 3\partial_{yz}^2 & 2\partial_{zz}^2 - \partial_{xx}^2 - \partial_{yy}^2 \end{pmatrix} , \tag{5.78}$$

and the Frobenius inner product between rank 2 tensors is defined by $\mathbf{A} : \mathbf{B} = \sum_{\alpha,\beta} A_{\alpha\beta} B_{\alpha\beta}$.

Knowing the relation between the second angular mode of the single-particle distribution f and the nematic order parameter, explicited in Eq. (5.36), we can write the hydrodynamic equations in real space in the following compact form:

$$\partial_t \mathbf{Q} = \frac{2D_1}{15} \mathbf{\Gamma} \rho + \left[\mu^2[\rho] - \xi(\mathbf{Q} : \mathbf{Q}) \right] \mathbf{Q} + \alpha \left[\mathbf{Q}\mathbf{Q} \right]_{\text{ST}} + D_0 \Delta \mathbf{Q} + \frac{4D_1}{7} \left[\mathbf{\Gamma}\mathbf{Q} \right]_{\text{ST}} \,, \tag{5.79}$$

where $[\mathbf{A}]_{\text{ST}} = \frac{1}{2}(\mathbf{A} + \mathbf{A}^t) - \frac{1}{3}\mathbf{I}\text{Tr}\mathbf{A})$ is the symmetric traceless part of the tensor $\mathbf{A}$ and $\mathbf{I}$ is the identity matrix. The dependencies of the coefficients in terms of the microscopic parameters ρ_0 and σ are listed in Table 5.2. Once more Eq. (5.79) has the familiar Ginzburg-Landau structure and a linear coupling to the density field. Note,

	3D	2D
$\mu^2[\rho]$	$P_0^2 - 1 + \frac{2}{15}\left((8+3\sqrt{2})P_0^2 - \frac{68}{7}\right)\rho$	$P_2 - 1 + \frac{8}{3\pi}\left((2\sqrt{2}-1)P_2 - \frac{7}{5}\right)\rho$
$\xi\,(>0)$	$\frac{393\sqrt{2}(304-11(-32+203\sqrt{2})P_0^2)(16+(384+35\sqrt{2})P_0^4)}{528220\left((393\sqrt{2}+131\rho_0)P_0^4-393\sqrt{2}-920\sqrt{2}\rho_0\right)}$	$\frac{4}{45\pi}\frac{(1+15P_2)(9(1+6\sqrt{2})P_4-13)}{315\pi(1-P_4)+8(21P_4+155)\rho_0}$
α	$\frac{2}{49}\left(4+(-16+21\sqrt{2})P_0^2\right)\ (>0)$	0
D_0	$\frac{1}{3}$	$\frac{1}{2}$
D_1	$3D_0$	$2D_0$

Table 5.2 – Comparison of the hydrodynamic coefficients of active nematics equations between the 3 and 2 dimensional cases [90]. The functional form of the linear (μ^2) and the cubic (ξ) parameters is comparable between the two cases. The quadratic term (α) is absent in 2D because of rotational invariance while it gets a non zero (positive for rod shaped particles) value in 3D. In the right column, the P_i parameters are the moments of the angular noise distribution in 2D, analogous to the P_0^i in 3D.

however, the presence of the quadratic term in the field tensor $\mathbf{Q}$ with coefficient α in addition to anisotropic spatial diffusion, allowed by the symmetries of the system [5]. Unlike in 2D and because of the presence of anisotropic spatial diffusion, the structure of Eq. (5.79) cannot be derived from a free energy in the single Frank constant approximation [90] [6]. Moreover, as in 2D, the active current in Eq. (5.77) cannot be derived from a free energy, therefore Eqs. (5.77) and (5.79) cannot be obtained together at equilibrium.

We note that the discontinuous nature of the transition, in principle, prevents us from using a perturbative analysis to truncate the hierarchy around σ_t. Indeed when the disordered solution starts to be unstable, the global nematic order, and thus ε, does not go continuously to zero. However, Figure 5.8(b) shows that the Ginzburg-Landau ansatz is a good approximation around σ_c, supporting the enslaving of the higher order modes to the nematic field in this region. Moreover, as shown in the following, the hydrodynamic equations obtained at the usual third order are well-behaved, with bounded solutions. We expect them to continue providing the right qualitative picture.

Hydrodynamic equations for the rods class

Even though only nematic order arises in the rods class, we retain the polar field in our description because its dynamics depends non-linearly on the density and the nematic fields. In this case the reversal rate of velocities is sufficiently small so that no diffusive dynamics is attained on the kinetic timescales. Therefore, we consider the propagative ansatz from Eq. (5.55) for space and time. Since only nematic order grows in such system, we consider its saturated value as a small parameter $\varepsilon \approx |g^2|$. Balancing the modes in the Boltzmann hierarchy, we obtain the following ansatz for the relative strength of the fields

$$\delta\rho \approx \varepsilon, \quad g_m^{2l} \approx g_m^{2l-1} \approx \varepsilon^l, \qquad \forall l > 1, \quad \forall m \; . \tag{5.80}$$

The computation of the terms in the hydrodynamic equations follows the procedure described in the previous sections, truncating the Boltzmann hierarchy at order ε^3. We thus retain equations for the fields up to $l = 4$, but the $l = 3, 4$ fields can be enslaved to the $l = 0, 1, 2$ fields. After tedious calculations, we obtain the lengthy equations:

$$\begin{aligned} \partial_t \rho &= -\partial_i w_i \; , && (5.81\text{a}) \\ \partial_t w_i &= -\partial_k Q_{ik} - \frac{1}{3}\partial_i \rho + \gamma \left(2 Q_{kl} \partial_k Q_{il} + Q_{kl} \partial_i Q_{kl} - \frac{4}{5} Q_{ik} \partial_l Q_{kl} \right) \\ &\quad + \left(\mu^1[\rho] - \beta Q_{kl} Q_{lk} \right) w_i + \zeta Q_{ik} w_k - \frac{6}{5} \beta Q_{ik} Q_{kl} w_l \; , && (5.81\text{b}) \end{aligned}$$

---

[5] In 2 dimensions both these terms are not allowed by rotational symmetry. Although using the tensorial notation of Eq.(5.79) the reason why these terms are not allowed in 2D is not evident, it is easy to show that $[\mathbf{QQ}]_{\mathrm{ST}} = 0 = [\mathbf{\Gamma Q}]_{\mathrm{ST}}$ in 2D.

[6] The structure of Eq. (5.79) can be obtained from a free energy density $\mathcal{F} = a Q_{ij} \partial_{ij}^2 \rho + \frac{b}{2} \left(\partial_i Q_{kl} \right)^2 + \frac{c}{2} \left(\partial_k Q_{ik} \right)^2 + ...$, then denoting by Γ_{Q} the coupling constant with the nematic order parameter we have $D_0 = \Gamma_{\mathrm{Q}} \left(b - \frac{c}{3} \right)$ and $D_1 = \frac{7}{4} \Gamma_{\mathrm{Q}} c = -\frac{15}{2} \Gamma_{\mathrm{Q}} a$. In the single Frank constant approximation $c = 0$ [166].

$$
\begin{aligned}
\partial_t Q_{ij} \quad = \quad & -\frac{2}{5}\left[\partial_i w_j\right]_{\mathrm{ST}} + D_{\mathrm{I}}\Delta Q_{ij} + D_{\mathrm{A}}\left[\Gamma_{ik}Q_{kj}\right]_{\mathrm{ST}} \\
& -\kappa\left(w_k\partial_k Q_{ij} + 2\left[w_k\partial_i Q_{kj} - \frac{2}{5}w_i\partial_k Q_{kj}\right]_{\mathrm{ST}}\right) \\
& -\chi\left(\partial_k\left(w_k Q_{ij}\right) + 2\left[\partial_k\left(w_i Q_{kj}\right) - \frac{2}{5}\partial_i\left(w_k Q_{kj}\right)\right]_{\mathrm{ST}}\right) \\
& + \left(\mu^2[\rho] - \xi Q_{kl}Q_{lk}\right)Q_{ij} + \alpha\left[Q_{ik}Q_{kj}\right]_{\mathrm{ST}} \\
& +\omega\left[w_i w_j\right]_{\mathrm{ST}} + \tau\left(|\vec{w}|^2 Q_{ij} + \frac{6}{5}\left[Q_{ik}w_k w_j\right]_{\mathrm{ST}}\right)\,, \qquad (5.81c)
\end{aligned}
$$

where implicit summation over repeated indices is assumed. Although this representation differs from the compact form (5.79) for active nematics, we kept explicit notations for tensorial and inner products in order to avoid possible confusions between similar terms. As before, square brackets take the symmetric traceless part of a tensor: $[A]_{ST} = \frac{1}{2}(A + A^t) - \frac{1}{3}\mathbf{I}(\mathrm{Tr}A)$, and the operator $\mathbf{\Gamma}$, defined in (5.78), is $\Gamma_{ij} = \left[\partial^2_{ij}\right]_{\mathrm{ST}}$.

The coefficients in the equation for the polar field are listed in Table 5.3. The number of parameters does not change between the 2 and the 3 dimensional cases, although terms coupling the polar field with its gradients are still allowed by rotational symmetry.

The coefficients in the equation for the nematic field are listed in Table 5.4. Like in the case of active nematics, the nematic field equation has a Ginzburg-Landau term with a quadratic contribution with coefficient α and shows anisotropic spatial diffusion. Both are not allowed for symmetry reasons in 2 dimensions. The coefficient in front of the anisotropic diffusion term is smaller in modulus than the isotropic diffusion one $|D_A| < |D_I|$, this prevents a trivial short wavelength instability to occur and we thus expect these equations to be well behaved.

	3D	2D
$\mu^1[\rho]\,(< 0)$	$P_0^1 - 1 + \left(\frac{\pi}{8}P_0^1 - \frac{8}{15}\right)\rho - 2a$	$P_1 - 1 + \frac{4}{\pi}\left(P_1 - \frac{4}{3}\right)\rho - 2a$
$\mu^3\,(< 0)$	$P_0^3 - 1 + \left(\frac{20-3\pi}{96}P_0^3 - \frac{208}{315}\right)\rho_0 - 2a$	$P_3 - 1 - \frac{272}{35\pi}\rho_0 - 2a$
$\beta\,(> 0)$	$\frac{\left((-3360+315\pi)P_0^1+512\right)\left(35(4+9\pi)P_0^3+512\right)}{21073920\mu^3}$	$-\frac{32(5P_3+4)(7P_1-2)}{105\pi^2\mu^3}$
$\zeta\,(> 0)$	$\frac{16}{35} + \frac{3(4-\pi)}{16}P_0^1$	$\frac{16}{5\pi}$
$\gamma\,(> 0)$	$\frac{1}{\mu^3}\left[\frac{4}{147} - \frac{5(32-3\pi)}{896}P_0^1\right]$	$-\frac{4(7P_1-2)}{21\pi\mu^3}$

TABLE 5.3 – Comparison of the hydrodynamic coefficients of the equation for the polar field in the rods class in 3 and 2 dimensions [89]. The form of the equation does not change with respect to the 2 dimensional case and thus no new parameter appears. In the right column, the P_i parameters are the moments of the angular noise distribution in 2D, analogous to the P_0^i in 3D.

	3D	2D
$\mu^2[\rho]$	$P_0^2 - 1 + \left(\frac{8+3\sqrt{2}}{15} P_0^2 - \frac{68}{105}\right)\rho$	$P_2 - 1 + \frac{16}{3\pi}\left(P_2(2\sqrt{2}-1) - \frac{7}{5}\right)\rho$
$\mu^4\,(<0)$	$P_0^4 - 1 + \left(\frac{1}{6\sqrt{2}} P_0^4 - \frac{460}{693}\right)\rho_0$	$P_4 - 1 + \frac{16}{15\pi}\left(P_4 + \frac{155}{21}\right)\rho_0$
$D_I\,(>0)$	$-\frac{1}{5\mu^3}$	$-\frac{1}{4\mu^3}$
$D_A\,(>0)$	$-\frac{6}{35\mu^3}$	0
κ	$-\frac{44+(24-45\sqrt{2})P_0^2}{735\mu^3}$	$\frac{8\left(19-P_2 7(1+\sqrt{2})\right)}{105\pi\mu^3}$
χ	$-\frac{512+35(4+9\pi)P_0^3}{7840\mu^3}$	$\frac{2(5P_3+4)}{5\pi\mu^3}$
α	$\frac{4+(21\sqrt{2}-16)P_0^2}{49}\,(>0)$	0
$\xi\,(>0)$	$\frac{\left(304+(352-2233\sqrt{2})P_0^2\right)\left(16+(384+35\sqrt{2})P_0^4\right)}{528220\mu^4}$	$-\frac{128(15P_4+1)\left(13-P_2 9(1+6\sqrt{2})\right)}{4725\pi^2\mu^4}$
ω	$\frac{8+(15\sqrt{2}-32)P_0^2}{50}$	$\frac{8\left(1-P_2 3(\sqrt{2}-1)\right)}{3\pi}$
τ	$-\frac{\left(44+(24-45\sqrt{2})P_0^2\right)\left(512+35(4+9\pi)P_0^3\right)}{823200\mu^3}$	$-\frac{64(5P_3+4)\left(19-P_2 7(1+\sqrt{2})\right)}{525\pi^2\mu^3}$

TABLE 5.4 – Comparison of the hydrodynamic coefficients of the equation for the nematic field in the rods class in 3 and 2 dimensions [89]. The functional form of the linear (μ^2) and the cubic (ξ) parameters is comparable between the two dimensions, whereas the quadratic term (α) is zero in 2 dimensions because of rotational invariance while it takes a positive value in 3 dimensions. Moreover, anisotropic diffusion appears in 3D, like for the polar class. In the right column, the P_i parameters are the moments of the angular noise distribution in 2D, analogous to the P_0^i in 3D.

5.5.3 Homogeneous and periodic solutions

Homogeneous solutions

Since no polar order can grow homogeneously in these cases, both the hydrodynamic equations for active nematics (5.79) and for rods (5.81) share the same Ginzburg-Landau functional form when setting spatial derivatives to zero

$$\partial_t \mathbf{Q} = \left[\mu[\rho] - \xi(\mathbf{Q}:\mathbf{Q})\right]\mathbf{Q} + \alpha\,[\mathbf{Q}\mathbf{Q}]_{\mathrm{ST}}\ , \tag{5.82}$$

with $\mu[\rho] = \mu^2[\rho]$. This equation admits both the homogeneous disordered ($\rho = \rho_0$, $Q_{ij} = 0\ \forall i,j$) and homogeneous ordered solutions. The case where all particles' orientations are aligned along a given direction is referred as *uniaxial.* Assuming without loss of generality that the direction of global order is along the z axis, the nematic tensor reads

$$\mathbf{Q} = \begin{pmatrix} -\bar{Q}/2 & 0 & 0 \\ 0 & -\bar{Q}/2 & 0 \\ 0 & 0 & \bar{Q} \end{pmatrix}\ , \tag{5.83}$$

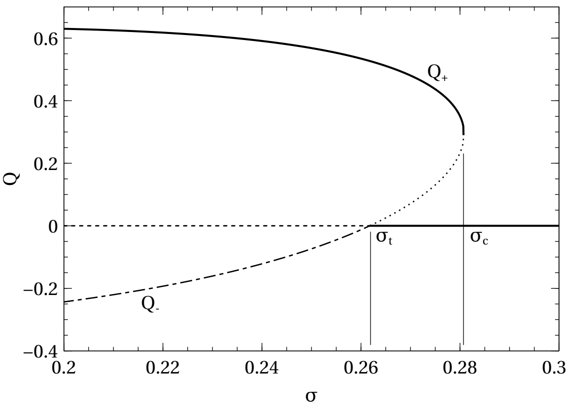

FIGURE 5.9 – The homogeneous solutions $\bar{Q}$ of the hydrodynamic equations for particles with nematic interactions using the active nematics parameters of Table 5.2 for $\rho_0 = 1$. Like at the kinetic level, there is a region in between σ_t and σ_c where the disordered and uniaxial solutions are both stable, showing a "true" discontinuous transition.

where the parameter $\bar{Q}$ solves

$$\mu + \frac{\alpha}{2}\bar{Q} - \frac{3}{2}\xi\bar{Q}^2 = 0 \; . \tag{5.84}$$

This quadratic equation has two solutions

$$\bar{Q}_{\pm} = \frac{\alpha}{6\xi} \pm \frac{1}{3\xi}\sqrt{\frac{\alpha^2}{4} + 6\mu\xi} \; , \tag{5.85}$$

that are both real only for $\alpha^2/4 + 6\mu\xi \geq 0$. Since α and ξ are strictly positive in the range of density and noise we consider (see Tables 5.2 and 5.4), we can define a critical linear coefficient

$$\mu_c = -\frac{\alpha^2}{24\xi} \quad (< 0) \; , \tag{5.86}$$

such that these solutions exist for $\mu \geq \mu_c$. Thus $\sigma_c(\rho_0)$ is defined at the hydrodynamic level by the line where $\mu = \mu_c$, two homogeneous solutions stable with respect to homogeneous perturbations coexist in the region $\sigma_t < \sigma < \sigma_c$: the disordered solution and $\bar{Q}_+$, as shown in Figure 5.9. Therefore, the transition from disorder to order is discontinuous, something already shown at kinetic level in Section 5.5.1. Remarkably, like in the polar case, the order is not a monotonous function of the noise, as shown in Figure 5.11, whereas it is in the 2D case (not shown).

Below the transition line σ_t the disordered solution becomes unstable and the solution $\bar{Q}_-$ is negative. To get a physical insight of this solution we remark that a unit vector $\hat{n}$ can represent both a direction or the Hodge dual of this direction, corresponding to any plane orthogonal to $\hat{n}$ in 3 dimensions. The dual space can be represented in tensorial notations by

$$M_{ij} = \varepsilon_{ijk} n_k \; ,$$

where $\{i, j, k\} \in \{1, 2, 3\}$ and ε is the Levi-Civita totally antisymmetric tensor. From the definition of the nematic order (5.35), multiplying $\mathbf{M}$ by its transpose, removing the trace, we obtain

$$\mathbf{M}^t\mathbf{M} - \frac{2}{3}\mathbf{I} = -\mathbf{Q} \; . \tag{5.87}$$

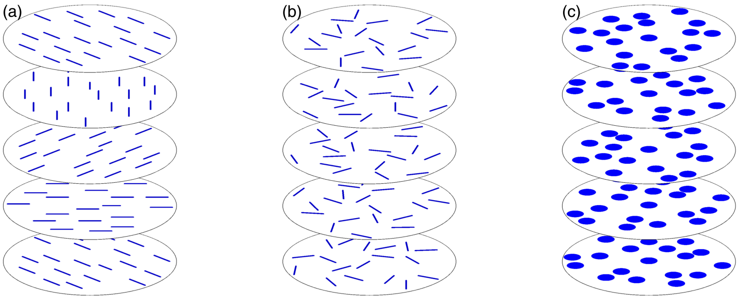

FIGURE 5.10 – Sketch of configurations of particles in parallel layers leading to a nematic order parameter $\bar{Q} < 0$. (a): cholesteric configuration where rod-like particles are aligned on parallel planes and order rotates along the third direction. In (b) the same particles are still arranged on parallel layers but with random orientations. (c): ordering of oblate particles on parallel layers.

Thus, a tensor $\mathbf{Q}$ whose largest eigenvalue (in absolute value) is negative states that the order is orthogonal to the direction given by $\hat{n}$, while if it is positive the order is parallel to the direction $\hat{n}$. [7]

Solutions with negative nematic order are physically possible and represent so-called *biaxial* phases [138], pictured in Figure 5.10. There are two typical homogeneous configurations: planes of uniaxial particles with random orientations (in the planes), and oblate particles moving along their axis, with their axes ordered. An elementary linear stability analysis with respect to homogeneous perturbations shows that $\bar{Q}_-$ is always unstable whenever the quadratic coefficient α is positive. For instance, in the case of active nematics, the homogeneous linear perturbations around this state evolve as

$$\begin{aligned}
\partial_t \delta Q_{zz} &= \mp \bar{Q}_\pm \sqrt{6\xi(\mu-\mu_c)}\,\delta Q_{zz} \ , \\
\partial_t \delta Q_{xx} &= -\frac{3\alpha}{2}\bar{Q}_\pm \delta Q_{xx} + \bar{Q}_\pm \left(\frac{3}{2}\xi\bar{Q}_\pm - \alpha\right)\delta Q_{zz} \ , \\
\partial_t \delta Q_{xy} &= -\frac{\alpha}{2}\bar{Q}_\pm \delta Q_{xy} \ , \\
\partial_t \delta Q_{xz} &= -\frac{\alpha}{2}\bar{Q}_\pm \delta Q_{xz} \ , \\
\partial_t \delta Q_{yz} &= -\frac{\alpha}{2}\bar{Q}_\pm \delta Q_{xy} \ .
\end{aligned}$$

In the region $\sigma_t < \sigma < \sigma_c$ the solution $\bar{Q}_-$ is positive and δQ_{zz} is unstable, while below the transition point σ_t it is negative and the instability is transferred to the other directions.

Physically, this instability relies on particle's shape. Having a homogeneous negative order along z for rod shaped agents, a small perturbation in the region where $\mu \leq 0$ brings the system to the disordered phase. On the contrary, if $\mu \geq 0$ a small perturbation of the order in the (x,y) plane is not damped, aligning the rods in the same direction favoring the $\bar{Q} > 0$ solution. From the previous linear stability analysis, a stable biaxial nematic state requires the coefficient α to be negative. This would be the case, for example, considering oblate agents with an alignment rule privileging biaxial phases, as shown in Figure 5.10(c). However, this is beyond the scope of this work that deals only with rod shaped particles.

---

[7] In 2 dimensions $-\mathbf{Q}$ corresponds to a rotation of the space of $\pi/2$ of the order because the geometric object perpendicular to a unit vector is a vector itself, instead of a plane.

Periodic solutions: Cholesterics

The hydrodynamic equations for active nematics and rods possess spatially-periodic solutions (with zero polar field), called cholesteric, that depend on only one direction, say x. Borrowing from liquid crystals theory, a cholesteric phase is the assembly of identical 2 dimensional homogeneously ordered “layers" into a helical structure (see Figure 5.10(a)). In such solutions, the density and the local norm of the nematic tensor are homogeneous $\rho(x) = \rho_0$, $\|\mathbf{Q}\|^2(x) = (\mathbf{Q} : \mathbf{Q})(x) = Q_0^2$. Moreover, as the nematic field is constrained in the plane formed by the y and z axis we impose $Q_{xy} = Q_{xz} = 0$ and $Q_{xx} = -\bar{Q}/2$ constant. With these constraints, and after some lengthy algebra, the hydrodynamic equations for the density and the nematic fields simplify to

$$\left(\mu - \alpha\frac{\bar{Q}}{2} - \xi Q_0^2\right)\frac{\bar{Q}}{2} + \alpha\frac{Q_0^2}{3} = 0\ , \tag{5.88a}$$

$$\left(\mu + \alpha Q_{zz} - \xi Q_0^2\right)Q_{zz} + \alpha\left(Q_{yz}^2 - \frac{Q_0^2}{3}\right) + D\partial_{xx}^2 Q_{zz} = 0\ , \tag{5.88b}$$

$$\left(\mu + \alpha\frac{\bar{Q}}{2} - \xi Q_0^2\right)Q_{yz} + D\partial_{xx}^2 Q_{yz} = 0\ , \tag{5.88c}$$

with $D = D_0 - 4D_1/21$ (or $D = D_I - D_A/3$ for rods) positive. Equation (5.88a) gives a relation between $\bar{Q}$ and Q_0 and Eq. (5.88c) describes a harmonic oscillator

$$\partial_{xx}^2 Q_{yz} + \omega^2 Q_{yz} = 0\ , \tag{5.89}$$

with a twist frequency related to the norm of the nematic field

$$D\omega^2 = \mu + \alpha\frac{\bar{Q}}{2} - \xi Q_0^2\ , \tag{5.90}$$

As we are looking for solutions periodic along x, we are interested in the case where ω^2 is positive. Assuming then that the order is along the z-axis at $x = 0$ a general solution of (5.89) can be written as

$$Q_{yz}(x) = B\sin(\omega x)\ . \tag{5.91}$$

Equations (5.88a) and (5.90) give the expressions of $\bar{Q}$ and Q_0^2 as a function of ω^2 and of the hydrodynamic parameters

$$\bar{Q} = \frac{\alpha}{6\xi} + \frac{D\omega^2}{2\alpha} + \sqrt{\frac{2}{3\xi}(\mu - \mu_c(\omega^2))}\ , \tag{5.92}$$

$$Q_0^2 = \frac{1}{\xi}\left(\mu - \frac{3D\omega^2}{4} + \frac{\alpha^2}{12\xi} + \frac{\alpha}{2}\sqrt{\frac{2}{3\xi}(\mu - \mu_c(\omega^2))}\right)\ , \tag{5.93}$$

$$\mu_c(\omega^2) = D\omega^2 - \frac{3\xi}{8\alpha^2}\left(D\omega^2 + \frac{\alpha^2}{3\xi}\right)^2\ . \tag{5.94}$$

Note that in the limit $\omega^2 \to 0$ the period of the oscillations goes to infinity, and one recovers the homogeneous uniaxial phase.

In order to find a solution to Eq. (5.88b) we assume the functional form

$$Q_{zz}(x) = \lambda\cos(\omega x) + \kappa\ , \tag{5.95}$$

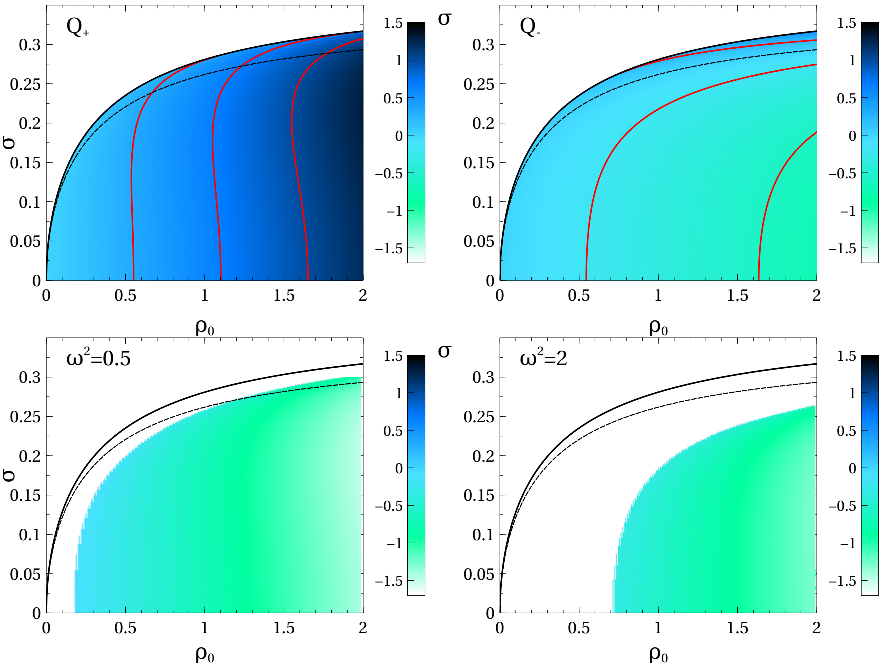

FIGURE 5.11 – Phase diagrams in the density-noise plane indicating the degree of nematic order (scalar order parameter) for various homogeneous ordered solutions of the hydrodynamic equations (5.79) for the active nematics class. In each panel, the solid and dashed black lines correspond to σ_c and σ_t, respectively. Top panels: uniaxial and biaxial solutions $\bar{Q}_+$ and $\bar{Q}_-$ where the red lines mark the contours $\bar{Q}_+ = 0.5, 0.75, 1$ and $\bar{Q}_- = 0, -0.25, -0.5$. Bottom panels: order Q_0 of the cholesteric solution for twists $\omega^2 = 0.5$ and 2.

and we obtain

$$\begin{aligned} 0 &= \left[(\mu - \xi Q_0^2)\kappa + \alpha\left(\kappa^2 + \lambda^2 - \frac{Q_0^2}{3}\right)\right] \\ &\quad + \lambda\left[\mu - \xi Q_0^2 + 2\alpha\kappa - D\omega^2\right]\cos(\omega x) + \alpha\left[B^2 - \lambda^2\right]\sin^2(\omega x)\,. \end{aligned} \tag{5.96}$$

For this equation to be satisfied, all three terms inside square brackets must vanish. The first two correspond to the same constraint, resulting in $\kappa = \bar{Q}/4$, while the third term gives $\lambda = B > 0$. Finally, knowing the form of the nematic tensor we obtain

$$Q_0^2 = \frac{3\bar{Q}^2}{8} + 2B^2\,, \tag{5.97}$$

where B^2 has to be positive. Figure 5.11 shows the regions of existence of the cholesteric states in the phase diagram (ρ_0, σ) plane for various twist frequencies ω. Larger the frequency of the solution is, the more it is confined at higher densities.

5.5.4 Linear stability analysis

Homogeneous uniaxial ordered solution

We computed the linear stability analysis of the active nematics hydrodynamic equations (5.77) and (5.79) around the uniaxial homogeneous ordered state $\bar{Q}$ semi-numerically (panel (*a*) of Figure 5.12). Close to and below the line σ_c limiting the existence of the ordered solution a transversal instability appears at finite wavelength, much like in the 2 dimensional case. Deeper in the ordered phase, the homogeneous order is

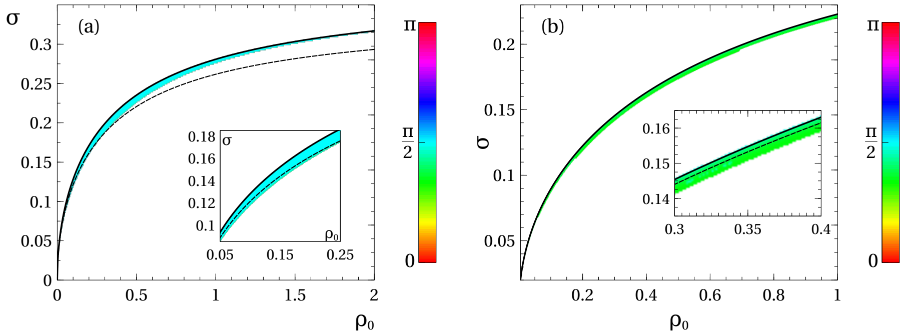

FIGURE 5.12 – Linear stability of the homogeneous uniaxial ordered solution of the hydrodynamic equations for the nematic classes in the density-noise plane. The solid and dashed black lines correspond to σ_c and σ_t, respectively. The solution exists below the black solid line. It is linearly unstable in the colored region, and stable below. The color represents the angle between the most unstable wave vector and the direction of order. (a): active nematics case (Eqs.(5.77) and (5.79)). The instability, confined close to the upper transition line, is transversal to the direction of the order of the unperturbed solution. Inset: zoom at low densities where the linear instability covers the mean field bistability region although it does not go deeper in the ordered phase. (b): rods case (Eqs.(5.57) at zero reversal rate ($a = 0$)). The instability, confined close to the upper transition line, is nearly transversal to the direction of the order of the unperturbed solution. Inset: zoom close to the transition line in order to show that the linear instability covers all the region between the transition line (dashed black line) and critical line (full black line).

stable and, again like in the 2D case, no "spurious instability" is found. The transversal instability region becomes thinner increasing the density while the region where both the ordered and the disordered phase exist becomes larger. Therefore, it is possible to find both the homogeneous phases linearly stable, resulting in a bistability of the system. Note, however, that nonlinear phenomena and strong fluctuations may invalidate this statement.

In the case of the rods equations the linear stability at finite wavelength of the nematic phase resembles that of the active nematics case, as shown in Figure 5.12(b). The ordered solution is unstable close to σ_c, but this instability is not purely transversal, and involves a component along the order, although not a dominant one. Increasing the reversal rate of velocities a, this instability becomes transversal to the global order. Moreover, for large values of a the homogeneous ordered solution is stable in the bistability region at large densities, and one retrieves the active nematics structure. There is, however, a strong difference between the 3D and 2D cases: in 3 dimensions one does not find an instability deep in the ordered phase where nematic order triggers polar order and no purely nematic solution is stable [89].

Transverse linear stability of cholesteric solutions

The linear stability analysis of the cholesteric solutions is not straightforward because of their spatial dependence, leading to non diagonal matrices in Fourier space. It can however be performed for a family of particular perturbations given by the symmetry of the solutions. The cholesteric steady solution can be written compactly in the form

$$\mathbf{Q_c} = \frac{\bar{Q}}{4}\mathbf{Q_0} + \frac{B}{2}\left(e^{\imath\omega x}\mathbf{Q_1} + e^{-\imath\omega x}\mathbf{Q_1}^*\right) \ , \tag{5.98}$$

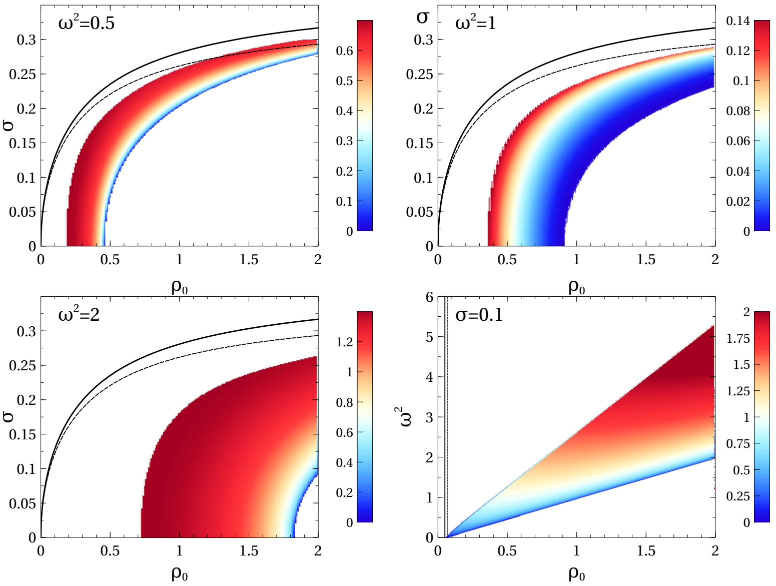

FIGURE 5.13 – Growth rate of the instability of the cholesteric solution of the active nematics equation for various twists ω^2. The dashed line represents the instability of the disordered solution and the full line above the existence of the homogeneous ordered solution. The first three panels show the linear stability of various fixed twist solutions in the density-noise plane. The fourth, bottom right panel shows the linear stability at fixed noise $\sigma = 0.1$ varying twist and density. The lower limit of the colored area corresponds to $\omega^2 = \omega_u^2$, the upper limit of linear stability of the solution.

with $\bar{Q}$ and B calculated in the previous section and

$$\mathbf{Q_0} = \begin{pmatrix} -2 & 0 & 0 \\ 0 & 1 & 0 \\ 0 & 0 & 1 \end{pmatrix} \qquad \mathbf{Q_1} = \begin{pmatrix} 0 & 0 & 0 \\ 0 & -1 & -\imath \\ 0 & -\imath & 1 \end{pmatrix} . \tag{5.99}$$

We consider perturbations of the form of spatially-varying amplitudes. The nematic field then becomes

$$\mathbf{Q} = A_0(x,t)\mathbf{Q_0} + A_1(x,t)e^{\imath\omega x}\mathbf{Q_1} + A_1^*(x,t)e^{-\imath\omega x}\mathbf{Q_1}^* , \tag{5.100}$$

where A_0 is real and A_1 is complex. For this family of perturbations the twist ω is kept constant such that they are transversal to the cholesteric axis. In the active nematics setting, the coupled equations for the density ρ and the amplitudes A_0 and A_1 are

$$\partial_t \rho = D_0 \partial_{xx}^2 \rho - 2D_1 \partial_{xx}^2 A_0 , \tag{5.101a}$$

$$\begin{aligned} \partial_t A_0 &= \left(\mu[\rho] - \alpha A_0 - 2\xi\left(3A_0^2 + 4|A_1|^2\right)\right) A_0 + \frac{4}{3}\alpha|A_1|^2 \\ &\quad + \left(D_0 + \frac{4D_1}{21}\right)\partial_{xx}^2 A_0 - \frac{2D_1}{45}\partial_{xx}^2 \rho , \end{aligned} \tag{5.101b}$$

$$\begin{aligned} \partial_t A_1 &= \left(\mu[\rho] + 2\alpha A_0 - 2\xi\left(3A_0^2 + 4|A_1|^2\right)\right) A_1 \\ &\quad + \left(D_0 - \frac{4D_1}{21}\right)\left(\partial_x + \imath\omega\right)^2 A_1 . \end{aligned} \tag{5.101c}$$

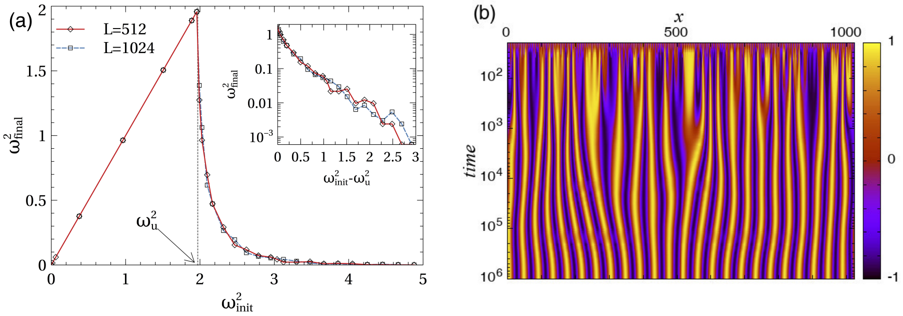

FIGURE 5.14 – (a): The final twist of the cholesteric state ω^2_{final} found in numerical simulations of the one dimensional version of the active nematics equations (5.77) and (5.79) (see text), as function of the twist of the initial cholesteric configuration ω^2_{init} for system sizes $L = 512$ and 1024. The cholesteric solutions are stable as long as ω^2_{init} is smaller than the linear stability threshold ω^2_{u}, while above it they are unstable and converge to a new cholesteric solution whose twist depends on $\omega^2_{\text{init}} - \omega^2_{\text{u}}$. The inset suggest a possible exponential decay of ω^2_{final} as function of $\omega^2_{\text{init}} - \omega^2_{\text{u}}$. ($b$): Space time variations of the Q_{yz} component of the nematic tensor ($\sim B\sin(\omega x)$ for a cholesteric solution) starting from a cholesteric configuration with $\omega^2_{\text{init}} - \omega^2_{\text{u}} \simeq 1.69$ and ending with $\omega^2_{\text{final}} \simeq 0.02$ at system size $L = 1024$. All the simulations are performed at $\rho_0 = 2$ and $\sigma = 0.1$ ($\omega^2_u \simeq 1.97$), using a pseudo-spectral Euler scheme with resolutions $dt = 0.01$ and $dx = \frac{1}{8}$.

Figure 5.13 shows the numerical evaluation of the linear stability of this set of equations around the fixed point

$$\rho = \rho_0 \quad ; \quad \bar{A}_0 = \frac{\bar{Q}}{4} \quad ; \quad \bar{A}_1 = \frac{B}{2}\ . \tag{5.102}$$

For $\omega = 0$, we of course recover the phase diagram shown in Figure 5.12. For finite ω we observe that the cholesteric solutions are linearly unstable close to their existence line, while they are stable deeper in the ordered phase. Note, however, that the instability region grows quickly with twist.

To get an idea of the respective stability of cholesteric solutions, we performed numerical simulations of the hydrodynamic equations (5.77) and (5.79) but in their reduced one-dimensional form, *i.e.* setting ∂_y and ∂_z to 0, and using a periodic domain in x. As expected, the cholesteric solutions with $\omega^2 < \omega^2_u$, where ω^2_u is the threshold given by the linear stability analysis performed above, are stable (Figure 5.14(a)). On the other hand in the linear instability region, we find that a cholesteric initial configuration of twist ω^2_{init} typically settles to a stable, lower-twist, cholesteric solution (see Figure 5.14(b)). We find that the final cholesteric solution possesses a well defined twist ω^2_{final} independent of system size (for large-enough domains). This final twist decreases quickly when ω^2_{init} increases, *i.e.* when the solution is more and more unstable, as shown in the last panel of Figure 5.13. Finally, as we can only simulate finite systems, the homogeneous ordered uniaxial solution is always reached for large-enough unstable initial twist.

For rods one also needs to consider perturbations of the polar field $\vec{w}$. Those compatible with (5.100) read

$$\mathbf{w} = F_0(x,t)\mathbf{w_0} + F_1(x,t)e^{\frac{\imath\omega x}{2}}\mathbf{w_0} + F_1^*(x,t)e^{-\frac{\imath\omega x}{2}}\mathbf{w_1}^* \tag{5.103}$$

where the complex vectors are

$$\mathbf{w_0} = \begin{pmatrix} 1 \\ 0 \\ 0 \end{pmatrix} \qquad \mathbf{w_1} = \begin{pmatrix} 0 \\ -\imath \\ 1 \end{pmatrix} \tag{5.104}$$

and the amplitudes F_0 and F_1 are equal to zero in the unperturbed state.

Inserting the perturbed cholesteric solution into the hydrodynamic equations for rods (5.81) we obtain coupled equations for the density and the amplitudes

$$\begin{aligned}
\partial_t \rho &= -\partial_x F_0 \,, && (5.105\text{a}) \\
\partial_t F_0 &= 2\partial_x A_0 - \frac{1}{3}\partial_x \rho + \gamma \partial_x \left(\frac{27}{5}A_0^2 + 4|A_1|^2\right) && \\
&\quad + \left[\mu^1[\rho] - 2\zeta A_0 - 2\beta\left(\frac{27}{5}A_0^2 + 4|A_1|^2\right)\right] F_0 \,, && (5.105\text{b}) \\
\partial_t F_1 &= \left[\mu^1[\rho] - \frac{4\beta}{5}\left(9A_0^2 + 16|A_1|^2\right)\right] F_1 - \frac{24}{5}\beta A_0 A_1 F_1^* + \zeta\left(A_0 F_1 + 2A_1 F_1^*\right) \,, && (5.105\text{c}) \\
\partial_t A_0 &= \frac{2}{15}\partial_x F_0 + \left(D_\text{I} + \frac{2}{3}D_\text{A}\right)\partial_{xx}^2 A_0 - \frac{9}{5}\left(\kappa F_0 \partial_x A_0 + \chi \partial_x (F_0 A_0)\right) && \\
&\quad + \left[\mu^2[\rho] - \alpha A_0 - 2\xi\left(3A_0^2 + 4|A_1|^2\right)\right] A_0 + \frac{4}{3}\alpha |A_1|^2 && \\
&\quad - \frac{\omega}{3}\left(F_0^2 - 2|F_1|^2\right) + \tau\left[\frac{9}{5}\left(F_0^2 + 4|F_1|^2\right) A_0 - 8\Re\left(A_1^* F_1^2\right)\right] \,, && (5.105\text{d}) \\
\partial_t A_1 &= \left(D_\text{I} - \frac{2}{3}D_\text{A}\right)(\partial_x + \imath\omega)^2 A_1 - \kappa A_0 (\partial_x + \imath\omega) A_1 - \chi(\partial_x + \imath\omega)(A_0 A_1) && \\
&\quad + \left[\mu^2[\rho] + 2\alpha A_0 - 2\xi\left(3A_0^2 + 4|A_1|^2\right)\right] A_1 && \\
&\quad + \left(\omega + \frac{12}{5}\tau A_0\right) F_1^2 + \tau\left(F_0^2 + \frac{44}{5}|F_1|^2\right) A_1 \,. && (5.105\text{e})
\end{aligned}$$

Linear stability analysis of these equations gives results similar to the active nematics case, shown in Figure 5.13, *i.e.* a region of instability close to the limit of existence of the solution whose extension grows with ω^2. This instability region also increases with the reversal rate, but its size saturates in the limit of large a such that the active nematics picture is recovered.

5.6 Conclusion

We have derived the hydrodynamic equations of the three main classes of dry, aligning, dilute active matter in three spatial dimensions, and compared them to their two-dimensional counterparts. We have used the Boltzmann-Ginzburg-Landau approach that, by construction, yields well-behaved partial differential equations governing the main physical fields. For convenience, we first treated the polar class with ferromagnetic alignment, then the cases with nematic alignment, *i.e.* the fast-velocity-reversal limit of active nematics, and the slow-reversal case, including the zero-reversal “rods” limit.

For the polar ferromagnetic class, we find the classic Toner-Tu equations, although here, starting from a Vicsek-style model, we obtain an anisotropic diffusion term not present in 2D using the same approach. We also find other differences between 2D and 3D, notably the non-monotonicity of order as a function of noise strength for the 3D homogeneous order solution. The linear stability of the spatially-homogeneous solutions of the 3D Toner-Tu equations is similar to that of the 2D case: the ordered solution shows a finite wavelength longitudinal instability near the continuous onset of order, and a residual, "spurious" instability deep in the ordered phase.

In the case of nematic alignment, the differences with the 2D case are much more pronounced: first of all, the general scenario departs from the ubiquitous liquid-gas phase separation found in 2D, as the transition to order is found discontinuous even at the mean-field level studied here. This situation is related to the presence of a quadratic term in the nematic field equation, a term ruled out by rotational symmetry in 2D. There is thus a genuine bistability region defining hysteresis loops at the level of homogeneous solutions. Nevertheless, we find that the homogeneous ordered solution still retains the generic transversal long-wavelength instability present in 2D, complicating further the mean-field phase diagram. In addition, we showed that the 3D hydrodynamic equations with nematic alignment support biaxial periodic solutions corresponding to cholesteric configurations. We show that these solutions too are generically unstable near their existence limit, and we discuss their relative stability. We note finally that, as in 2D, we find no qualitative difference between the active nematics and rods cases at the level considered here.

Naturally, this work now calls for further studies at the nonlinear and fluctuating levels.

At the nonlinear but still deterministic level, the inhomogeneous solutions of the hydrodynamic equations derived here must be found. As in the 2D case, we expect them to exist beyond the narrow band of linear instability of the homogeneous order solution where no homogeneous solutions exist. In the phase-separation framework described in the introduction, the lines delimiting this region are the spinodal lines. The binodal lines, which ultimately delimit the domain of existence of the coexistence phase sketched in Figure 5.1, are determined by the existence and stability limits of inhomogeneous solutions.

For the polar case, we expect these inhomogeneous solutions to take the form of travelling dense sheets as observed in microscopic models [70]. For the nematic alignment cases, as of now, not much is known: the only published account of the structures observed in 3D can be found in [85], where a dense ordered cylinder with its axis along the global nematic order is shown for the Vicsek-style active nematics model.

The fluctuating level of either microscopic models or our hydrodynamic equations complemented by stochastic terms remains, as of now, essentially virgin territory. Studies of the 3D Vicsek model and others in the same class have revealed the emergence of the dense traveling sheets mentioned above, but no work has studied in depth the microphase vs macrophase separation scenario found, in 2D, to distinguish the active Ising and the Vicsek models [67]. For nematic alignment, it is fair to say that almost everything remains to be done. An interesting study of a microscopic model of self propelled rods in 3D has shown the existence and stability of cholesteric solutions that coexist with the homogeneous ordered nematic phase, but it remains rather partial [167].

Our ongoing work is devoted to the above endeavours: careful study of 3D Vicsek-style models, search for inhomogeneous solutions to the hydrodynamic equations derived here, and the eventual complete understanding of 3D dry aligning active matter at the fluctuating hydrodynamic level.

Chapter 6

General conclusion and perspectives

Dry aligning active matter constitutes a simple framework that has been instrumental to reach a deeper understanding of emergent phenomena such as collective motion. Despite much progress in the past few years, some issues related to microscopic, kinetic, and hydrodynamic levels are still pending. A few of them have been addressed in this thesis, mainly through the study of Vicsek-style models. This global conclusion is meant to give an overview of the further problems raised by our work and possible perspectives it can offer.

In Chapter 2, we have shown that despite its apparent proximity with the equilibrium XY model, the Vicsek-shake class exhibits a novel type of critical point with a second order transition to a polar quasi-ordered phase with continuously varying exponents. This feature has been linked to the interplay between density and order that has a dramatic impact on the nonequilibrium dynamics of defects. We indeed found that $+1$ charged defects in particular nucleate dilute, orderless, domains in their core and can no longer be defined as a singular objects. Similar phenomenology is also present in the polar class, however in this case we find that the diameter of the disordered area created by a positive defect does not grow like $\sqrt{t}$ but linearly with time. More generally, we also expect interesting defects dynamics to show up in the classes with nematic alignment. Although recent experimental works have stressed the role of density in the behavior of defects [168, 169], many studies place themselves in the dense limit and/or neglect it [170–174]. Therefore, defects dynamics in dry dilute aligning active matter is mostly unexplored and seems promising.

The main conclusion of Chapter 3 is that deterministic kinetic equations are not necessarily more reliable than the simpler hydrodynamic level description of active matter models. We indeed found that they can exhibit remarkable qualitative differences with the microscopic models they are derived from. We have moreover shown evidence that the two-body collisions assumed in the Boltzmann approach is a better approximation than the mean field description of interactions provided by the Smoluchowski equation. In order to reach more quantitative agreement with microscopic models, going beyond these approximations and consider multi-particle interactions is presumably required. This program has been carried out by Ihle [133] although his resulting kinetic equation seems to be hardly tractable numerically if considering more than two body-body collisions. He moreover seems to achieve quantitative agreement only in the limit of large particles' speed, ensuring molecular chaos, that is usually not considered in the study of microscopic models. This point thus remains an open question.

We have shown in Chapter 4 that, while the Toner Tu theory is of precious help for the understanding of emergence of polar long-range-order in the two dimensional Vicsek model and thus qualitatively correct, scaling exponents are not those predicted.

Our numerical study thus calls for further theoretical analysis of the field theory. It is however probably hopeless to get accurate predictions of the exponents from perturbative renormalization group computation in $d = 2$. The solution to this problem could then lie in the application of nonperturbative techniques [175].

Our derivation of deterministic hydrodynamic equations for three dimensional dry aligning active matter models in Chapter 5 calls for the study of corresponding microscopic models and the characterization of their inhomogeneous solutions. Another important related problem concerns the derivation of stochastic terms and the study of fluctuating hydrodynamic equations. Indeed, we know from the band solutions selection in two dimensions that fluctuations play a major role in the correct description of simple Vicsek-style models. More generally, a pending issue concerns the precise form of the noise terms (additive or multiplicative, see Section 1.4) and the qualitative and quantitative effects it could have on the dynamics.

We are moreover now capable of simulating hundreds of millions of particles, which allows to address problems that were inaccessible before. There is indeed still a debate on the true nature of the nematic long-range-order of two dimensional self-propelled rods without reversals, that was identified both numerically [87] and experimentally [36]. As explained in Section 2.1.1, the theoretical analysis of Shankar *et al.* predicts the existence of a nonuniversal length scale below which order could seem long-ranged, although it would appear quasi-long-ranged above it [95]. In principle, self-propelled rods are thus expected to behave as active nematics asymptotically. In [87] Ginelli and collaborators identified another system size independent scale corresponding to the typical distance a particle travels in the nematic ordered phase before it reverses its velocity. This scale is comparable to the sizes that were simulated in this paper, it is thus still possible that larger systems would effectively behave as an active nematics, leading to a power law decay of the order with size. We now have the numerical power to go beyond those scales and finally answer this long-time pending question.

Finally, works on simple dry systems are important because they helped to uncover some of the basic universal features of active matter. However, they often sit far from reality, for example, when long-ranged hydrodynamic interactions are not negligible. This is usually the case in systems composed of bacteria [35, 38, 39], or microtubules propelled by molecular motors [42]. For these cases we can imagine to generalize the two and three dimensional approaches presented in Chapters 1 and 5 to the wet case. This could be done, for instance, coupling a simple model of rod like swimmers (and thus the corresponding Boltzmann equation) to a Stokes equation for the surrounding fluid as in [35, 176–178].

Annexe A

Résumé de la thèse en français

A.1 La matière active

Définition et exemples

La *matière active* est un champ de recherche de la physique statistique hors équilibre étudiant des collections de particules pouvant exploiter l'énergie présente dans leur environnement afin de s'auto-propulser. Les systèmes actifs sont donc maintenus hors d'équilibre au niveau microscopique (dans leur bulk), ce qui leur confère des propriétés spécifiques telles que celles observées dans les ensembles d'agents de déplaçant de façon cohérente, phénomènes connu sous le nom de *mouvements collectifs*.

Le monde du vivant fournit naturellement de nombreux exemples de systèmes actifs tels que les foules [24, 25] ou les groupes d'animaux [20, 27, 31, 32]. Aux échelles microscopiques les bactéries [35-37] et cellules [40] montrent aussi des comportements collectifs pouvant être décrits par des modèles simples de particules auto-propulsées en interaction. Au niveau intra-cellulaire, les assemblages de microtubules ou filaments d'actine avec des moteurs moléculaires peuvent aussi donner lieu à l'émergence de phénomène collectifs [41-43].

Les systèmes actifs artificiels, quant à eux, offrent souvent un meilleur contrôle expérimental. La plupart sont contraints à deux dimensions tels que les colloïdes actifs asymétriques [47-53], les « rollers » de [44, 56], ou les granulaires agités dans la troisième direction [45, 57-59].

Une illustration de certains des exemples présentés dans cette section est fournie en Figure 1.1.

Un modèle minimal pour la transition vers le mouvement collectif

Bien que les systèmes mentionnés précédemment puissent paraître dissemblables et couvrent une large gamme d'échelles, la plupart d'entre eux exhibent des propriétés collectives similaires provenant de leur caractère actif ainsi que de la nature des interactions entre particules. Leur description en terme de modèles minimaux, sans qu'elle recherche un accord quantitatif avec les expériences, est donc cruciale pour notre compréhension profonde des caractéristiques génériques des systèmes actifs. Ces modèles ont en outre l'avantage de ne dépendre que d'un ensemble restreint de paramètres de contrôle, et leur simplicité les rend efficaces à simuler numériquement. De plus, ils permettent souvent la dérivation de théories continues à partir de leur dynamique microscopique, faisant le lien entre ce niveau et les équations phénoménologiques.

Un des modèles les plus simple et populaire pour décrire les mouvements collectifs est sûrement celui introduit en 1995 par Vicsek et collaborateurs [68]. Celui-ci considère des particules se déplaçant à vitesse constante à deux dimensions et interagissant de façon à aligner leurs orientations localement en présence de bruit angulaire. Ce modèle ne dépend essentiellement que de deux paramètres de contrôle : la densité moyenne de particules ρ_0 et l'amplitude du bruit η, reflétant la compétition entre l'ordre (renforcé lorsque ρ_0 est large) et le désordre induit par le bruit. Afin de rester aussi simple que possible, le modèle de Vicsek ne prend pas en compte les interactions provenant du fluide entourant les particules, ceci est pertinent dans les situations où celles-ci sont en contact et échangent de l'impulsion avec un substrat, on parle alors de matière active *sèche*. La seule loi de conservation autorisée par la dynamique est donc celle du nombre total de particules, en particulier comme l'impulsion totale n'est pas conservée, le modèle ne satisfait pas l'invariance Galiléenne et doit être exprimé dans le référentiel dans lequel l'impulsion est dissipée.

Le diagramme des phases du modèle de Vicsek est représenté en Figure 1.3(c) et montre trois phases distinctes. A haut bruit (basse densité) le système est désordonné, comme en témoignent les corrélations décroissant exponentiellement et le paramètre d'ordre M, définit comme la norme de la somme des orientations de toutes les particules (normalisée), qui prend une valeur nulle. Diminuant η (ou augmentant ρ_0), le système subit une transition de phase hors équilibre caractérisée par une brisure spontanée de symétrie vers un état tel que $M > 0$ car toutes les particules de déplacent dans la même direction. Cette phase est dotée d'un vrai ordre polaire, une propriété impossible à l'équilibre à cause des ondes de spin [71], de fluctuations de densité géantes et de super-diffusion [70, 72-74]. La transition vers le mouvement collective était initialement décrite comme continue [68, 77], cependant plusieurs travaux aux niveaux microscopique [69, 70] et continu [78-80] ont montré que ceci était dû à la présence de forts effets de taille finie. En effet, elle est maintenant bien comprise en terme d'un scénario impliquant une *séparation de phase* avec coexistence entre des domaines de liquide denses et ordonnés, prenant la forme de *bandes* se propageant dans la direction perpendiculaire à leur axe (voir Figure 1.2(b)), et du gas dilué et désordonné. Cette phénoménologie, typique de la classe définie par le modèle de Vicsek, est provoquée par une boucle de rétroaction positive qui déstabilise l'ordre homogène près de la transition : les particules alignées ont tendance à rester ensemble et les régions denses sont plus ordonnées. Les bandes ainsi formées possèdent une taille caractéristique bien définie, et froment donc asymptotiquement un arrangement smectique comme représenté en Figure 1.2(b). On parle alors de *séparation microphase*, à opposer à la *séparation macrophase* pour laquelle les domaines de liquide ont une extension macroscopique (voir Figure 1.2(c)).

Descriptions hydrodynamiques du modèle de Vicsek

Les équations hydrodynamiques décrivant le modèle de Vicsek furent d'abord écrites par Toner et Tu en considérant tous les termes autorisés par les symétries du problème [72-74]. Les modes lents (ou hydrodynamiques) sont alors les champs de densité et polarité, qui satisfont les Equations (1.3). A partir de celles-ci et sur la base d'arguments provenant du Groupe de Renormalisation Dynamique, Toner et Tu proposèrent une « théorie quantitative » des movements collectifs et purent caractériser les propriétés universelles des fluctuations autour de la phase ordonné du modèle de Vicsek. Ils furent alors en mesure de montrer l'existence d'un vrai ordre polaire, même à deux dimensions, et prédirent les autres propriétés de cette phase. Cependant, leur théorie ne fournit aucune connexion avec les modèles microscopiques qu'elle cherche à décrire. En particulier, les nombreux coefficients présents dans les Equations (1.3) ne sont pas indépendants et sont en principe fonctions des quelques paramètres microscopiques du modèle, cette information pouvant s'avérer précieuse si l'on veut procéder à une analyse complète du diagramme des phases.

Plusieurs approches permettent d'établir la relation entre les niveaux microscopique et continu, l'une d'entre elles fut proposée par Bertin *et al.* [78, 79], dite *Boltzmann-Ginzburg-Landau* (BGL), et débute par l'écriture d'une équation de Boltzmann (1.6) décrivant l'évolution de la densité de probabilité $f(\vec{r}, \theta, t)$ qu'une particule a d'être en une position $\vec{r}$ avec une orientation θ à un instant t. Comme toutes les équations de Boltzmann, celle-ci suppose un régime dilué tel que les collisions sont essentiellement binaires ainsi que le chaos moléculaire nécessaire afin d'exprimer la distribution à deux corps comme le produit de deux distributions à un corps. f est ensuite décomposée en termes de modes de Fourier angulaires, conduisant à une hiérarchie infinie d'équations non linéaires couplées. Celle-ci est finalement tronquée et fermée à l'aide d'un ansatz de façon à ne garder que les modes lents, c.a.d. ceux qui ne sont pas amortis, et correspondent aux champs de densité et polarité. Les équations de Toner et Tu sont ainsi obtenues, à ceci près que leurs coefficients sont tous exprimés comme fonctions des champs et paramètres du modèle microscopique. L'analyse de leurs solutions homogènes, ainsi que leur stabilité, conduit au diagramme des phase présenté en Figure 1.4(a), qui montre un accord qualitatif avec celui obtenu via des simulations du modèle microscopique proche de l'émergence de l'ordre polaire [80].

A.2 Une classe de matière active avec une transition du second-ordre vers un quasi-ordre polaire

Les modèles de matière active sèche avec alignement local

Tous les systèmes actifs ne présentent pas les mêmes symétries que celles du modèle de Vicsek et appartiennent donc à différentes classes d'universalité. Celles-ci sont au nombre de trois, et chacune possède un représentant dans le cadre donné par Vicsek. Les particules polaires alignant leurs vitesses de façon ferromagnétiques correspondent au cas *polaire* qui est décrit par le modèle de Vicsek original, si à l'inverse l'alignement se fait de façon nématique, c.a.d. si les particules anti-alignent leurs directions lorsque celles-ci forment initialement un angle obtus, alors on parle des *rods* auto-propulsés. Si maintenant le mouvement des particules est apolaire, si elles renversent leur vitesse avec une certaine probabilité par exemple, et qu'elles s'alignent de façon nématique elles forment la classe des *nématiques actifs*.

De façon analogue au cas polaire présenté précédemment, ces classes supplémentaires ont été étudiées intensivement à la fois numériquement [82, 85, 87, 91, 94] et au niveau continu [80, 81, 84, 86, 88-90, 95, 123]. Elles exhibent toutes un diagramme des phases similaire à celui montré en Figure 1.3(c) avec trois régions distinctes. A bas bruit (haute densité) la phase ordonnée nématique est quasi-ordonnée dans le cas des nématiques actifs, alors que des résultats numériques et expérimentaux semblent pointer vers un vrai ordre nématique pour les rods. Les fluctuations de densité géantes sont aussi présentes dans les deux cas. Un autre point commun à toutes les classes est la phase de coexistence séparant les domaines ordonné et désordonné, et qui prend la forme de bandes dont l'axe est aligné avec l'ordre instables vis à vis des perturbations de grande longueur d'onde, conduisant donc à un chaos spatio-temporel représenté Figure 2.1(a). L'approche BGL a aussi été appliquée à ces autres classes, et conduit à un diagramme des phases au niveau hydrodynamique qualitativement correct.

Une nouvelle classe avec une transition continue

Une transition avec un point (ou une ligne) critique ne peut donc pas être observée dans ces modèles de matière active sèche avec alignement local. En réalité, cet objectif peut être atteint en définissant une nouvelle classe qui considère des particules apolaires et un alignement ferromagnetique, tout en s'affranchissant de la contrainte « Vicsek » qui fait correspondre polarité et vitesse. En effet, afin d'obtenir dans ce cas des résultats non triviaux nous considérons un modèle où les particules peuvent de déplacer dans le même sens que et en opposition avec leur polarité et renversent leurs vitesse avec une certaine probabilité au cours du temps.

A la fois les simulations numériques ainsi que les équations hydrodynamiques dérivées à l'aide de l'approche BGL confirment que la transition est continue dans ce cas là (Figures 2.2(a) and 2.3). De plus, la phase ordonnée montre un quasi-ordre polaire avec des exposants variant continument (voir Figures 2.2(c,d)), et présente donc des propriétés similaires au modèle XY à l'équilibre. Etonnamment, une caractérisation extensive de la transition à l'aide de simulations numériques porte à conclure que celle-ci n'appartient pas à la classe d'universalité Berezinskii-Kosterlitz-Thouless [146-148]. En revanche, elle tend fortement à montrer que la transition est mieux décrite comme un point critique standard avec une divergence algébrique des corrélations. Ce résultat est enfin rationalisé par une étude de la dynamique des défauts dans la phase quasi-ordonnée, qui présente des caractéristiques propres à la nature hors d'équilibre du modèle, et notamment à l'interaction entre densité et polarité. En effet, les défauts ne peuvent plus être décrits comme des objets ponctuels (voir Figure 2.7), ce qui les prive probablement d'exercer leur rôle habituel.

A.3 Robustesse des théories cinétiques pour la matière active sèche avec alignement

Les limites de la description hydrodynamique

Bien que le niveau cinétique soit généralement utilisé en tant qu'intermédiaire dans la dérivation d'équations hydrodynamiques, par exemple en employant l'approche BGL, on pourrait s'attendre à ce que plus d'information soit présente à ce stade qu'au niveau hydrodynamique. En effet, ces dernières proviennent d'une approche perturbative et ne sont donc en principe valides que proche de la transition. Plus profondément dans la phase ordonnée, des artefacts de la troncation peuvent en effet se manifester sous la forme d'instabilités additionnelles de la solution homogène ordonnée [80, 89]. De plus, il a été montré que les équations de Toner et Tu déterministes admettent à la fois les solutions de bandes correspondant aux séparations microphase et macrophase [121, 122], et que la sélection du bon profil ne se fait qu'au niveau fluctuant [67]. On peut alors s'interroger si celle-ci apparaît au niveau cinétique déterministe.

L'équation de Boltzmann, solutions et diagramme des phases

L'étude de l'équation de Boltzmann décrivant la classe polaire peut se faire par troncature de la hiérarchie de Fourier en ne gardant que les modes d'indice inférieur à K, où K est généralement pris supérieur à 10. La solution homogène ordonnée du système d'équation non linéaires correspondant peut ainsi être calculée numériquement et sa stabilité évaluée. La Figure 3.2(b) montre qu'alors que l'instabilité présente au coeur de la phase ordonnée tend à disparaître lorsque K augmente, celle confinée au voisinage de la transition au niveau hydrodynamique, et qui engendre les bandes polaires observées dans les simulations microscopiques, s'étend aux bruits faibles ne laissant qu'une poche de stabilité aux valeurs intermédiaires de η. Le diagramme des phases de l'équation de Boltzmann est donc *qualitativement différent* de celui attendu. Cependant, on peut voir en Figure 3.4(a) que le diagramme des phases correct peut être retrouvé en ajoutant de la diffusion positionnelle au niveau cinétique, celle ci apparaissant notamment lorsque l'équation est dérivée dans la limite des temps discrets (voir la Section 3.4.2). Des simulations numériques de l'équation de Boltzmann révèlent que ses solutions propagatives au voisinage de la transition champ moyen sont similaires à celles des équations hydrodynamiques. A l'inverse, l'instabilité présente à bas bruits donne lieu à des cycles limite instables au niveau hydrodynamique, correspondant à une phase liquide globalement ordonnée dans laquelle des ondes de faible amplitude se propagent (voir la Figure 3.7). De plus, comme au niveau hydrodynamique la Figure 3.9 montre que la sélection de la solution de bande correcte ne se fait pas au niveau cinétique déterministe, soulignant encore une fois le rôle important des fluctuations [67].

L'équation de Boltzmann décrivant un modèle de type Vicsek avec alignement *à temps discret* doit donc comporter des termes de diffusion spatiale, ceux-ci étant naturellement présents au niveau hydrodynamique car introduits par la procédure de troncature et fermeture. Les observations tendent par ailleurs à montrer qu'à l'émergence de l'ordre, le niveau cinétique ne contient pas plus d'information que les équations hydrodynamiques, pourtant bien plus simples. Néanmoins et parce que leur dérivation repose sur une approche perturbative, ces dernières peuvent échouer loin du seuil et montrer des instabilités supplémentaires n'ayant pas d'existence au niveau microscopique. Au contraire, si dotée de termes de diffusion spatiale additionnels, l'équation de Boltzmann constitue une description déterministe qualitativement correcte de la classe polaire, même profondément dans la phase ordonnée.

A.4 Une évaluation quantitative de la théorie de Toner et Tu

La théorie de Toner et Tu

La théorie proposée par Toner et Tu [72, 73] décrit les propriétés asymptotiques universelles du mouvement collectif tel qu'on le trouve dans la phase ordonnée fluctuante du modèle de Vicsek. Elle se base sur des équations hydrodynamiques gouvernant l'évolution des champs de densité et vitesse (voir (4.1)), et a pour but de caractériser les fluctuations autour de la solution homogène ordonnée. Toner et Tu prédirent d'abord une décroissance algébrique des corrélations spatiales à deux points. De plus, comme le modèle de Vicsek présente un vrai ordre polaire même à deux dimensions, quelque soit $d < 4$ les exposants correspondants sont différents selon que l'on regarde le scaling longitudinalement ou transversalement à l'ordre. Celui-ci est donc définit par deux exposants : χ mesure comment les fluctuations de vitesse décroissent avec la taille du système dans la(les) direction(s) transverse(s) à l'ordre (exp. de *rugosité*), alors que l'*anisotropie* du scaling est caractérisée par ξ. Un autre résultat important de Toner et Tu est la présence d'ondes sonores dont la vitesse dépend de la direction dans laquelle elles se propagent. Par ailleurs, pour une direction donnée il est prédit qu'à cause de la non conservation de l'impulsion deux modes avec des vitesses différentes coexistent. Finalement, l'exposant dynamique z caractérise l'amortissement de ces ondes.

Toner et Tu revendiquèrent d'abord un calcul *exact* des exposants χ, ξ et z à deux dimensions. Cependant, dans une publication plus récente [112], Toner affirme que certains termes, probablement importants, n'avaient pas été pris en compte dans les travaux initiaux, et que ceux-ci pourraient donc invalider cette revendication. Bien qu'il n'y ait aucune raison pour laquelle les valeurs des exposants soient celles calculées dans [72, 73], les prédictions qualitatives qui y sont faites, c.a.d. la présence d'un vrai ordre polaire pour $d = 2$, la présence d'ondes sonores propagatives, ainsi que les fluctuations géantes restent valides.

Simulations numériques, mesure des exposants

Jusqu'à présent, les tests numériques de la théorie de Toner et Tu reposent sur des mesures indirectes des exposants, et se limitent à un accord qualitatif [70, 76, 85, 160, 161]. Aucune mesure précise et directe n'a donc encore été réalisée.

Des simulations numériques du modèle de Vicsek à grande échelle à deux dimensions montrent que la propagation des ondes sonores dans la phase ordonnée est en accord avec la prédiction de Toner et Tu (voir Figure 4.7). A l'inverse les valeurs des exposants χ, ξ et z, répertoriées dans la Table 4.1, sont *incompatibles* avec la théorie. Il est donc naturel de conclure que les nouvelles non linéarités identifiées dans [112] constituent bien des perturbations de l'ordre pertinentes au sens du Groupe de Renormalisation. Comparant les valeurs des exposants avec celles prédites, les effets principaux de ces termes sont d'amortir les fluctuations de vitesses, confirmant la présence d'un vrai ordre à deux dimensions, et de rendre le système moins anisotrope aux grandes échelles.

A.5 Dérivation d'équation hydrodynamiques pour les modèles de matière active sèche en trois dimensions

A deux dimensions, l'approche BGL permet une dérivation contrôlée d'équations non linéaires hydrodynamiques à partir de dynamiques microscopiques de type Vicsek. Elle est de plus capable de reproduire qualitativement les diagrammes des phases de ces modèles et fournit un cadre théorique simple décrivant la transition comme une séparation de phases [67, 89, 91, 121, 122]. Malgré ces succès à deux dimensions (2D), peu est connu à 3D, en particulier la connexion entre les niveaux microscopique et hydrodynamique reste essentiellement inexplorée.

Un formalisme général pour l'approche BGL à 3D est donc proposé, et les trois classes d'universalité introduites à la Section A.2 sont traitées. De façon analogue au cas 2D, les équations hydrodynamiques sont obtenues à partir d'une théorie de Boltzmann exprimée sous la forme d'une expansion en harmoniques sphériques. Le cas polaire mène aux équations de Toner et Tu qui montrent peu de différences avec le cas 2D. A l'inverse, pour un alignement nématique les écarts avec les équations à 2D sont plus prononcés : Premièrement, la transition est trouvée discontinue au niveau champ moyen avec une région de bistabilité entre les solutions homogènes ordonnée et désordonnée, et son mécanisme diffère donc de la séparation de phase habituelle. Ceci est dû à un nouveau terme dans l'équation du champ nématique qui n'est pas présent à 2D pour des raisons de symétrie. De plus, la solution homogène ordonnée est aussi trouvée instable proche de la transition, compliquant un peu plus le diagramme des phases. Deuxièmement, les équations à 3D avec alignement nématique supportent des solutions périodiques avec un ordre global biaxial correspondant à des configurations cholestériques. Celles-ci sont instables au voisinage de leur limite d'existence, et leur stabilité relative est discutée à la Section 5.5.4.

Bibliography

[1]R. Kubo and H. Ichimura, *Statistical Mechanics: An Advanced Course with Problems and Solutions*, North-Holland personal library (North-Holland, 1990).

[2]J. Zinn-Justin, *Quantum Field Theory and Critical Phenomena*, International Series of Monographas on Physics (Clarendon Press, 2002).

[3]M. Le Bellac, F. Mortessagne, and G. G. Batrouni, *Equilibrium and Non-Equilibrium Statistical Thermodynamics* (Cambridge University Press, 2004).

[4]R. Kubo, M. Toda, and N. Hashitsume, *Statistical Physics II: Nonequilibrium Statistical Mechanics*, Vol. 31 (Springer Science & Business Media, 2012).

[5]L. Berthier and G. Biroli, “Theoretical perspective on the glass transition and amorphous materials”, Reviews of Modern Physics **83**, 587 (2011).

[6]B. Derrida, “Non-equilibrium steady states: fluctuations and large deviations of the density and of the current”, Journal of Statistical Mechanics: Theory and Experiment **2007**, P07023 (2007).

[7]J. Krug, “Boundary-induced phase transitions in driven diffusive systems”, Physical Review Letters **67**, 1882 (1991).

[8]M. Kardar, G. Parisi, and Y.-C. Zhang, “Dynamic scaling of growing interfaces”, Physical Review Letters **56**, 889 (1986).

[9]U. Frisch, *Turbulence: the Legacy of AN Kolmogorov* (Cambridge University Press, 1995).

[10]G. Schaller, *Open Quantum Systems far from Equilibrium*, Vol. 881 (Springer, 2014).

[11]H. Hinrichsen, “Non-equilibrium critical phenomena and phase transitions into absorbing states”, Advances in Physics **49**, 815–958 (2000).

[12]P. Krapivsky, S. Redner, and E. Ben-Naim, *A Kinetic View of Statistical Physics* (Cambridge University Press, 2010).

[13]U. Täuber, *Critical Dynamics: A Field Theory Approach to Equilibrium and Non-Equilibrium Scaling Behavior* (Cambridge University Press, 2014).

[14]I. Dornic, H. Chaté, J. Chave, and H. Hinrichsen, “Critical coarsening without surface tension: the universality class of the voter model”, Physical Review Letters **87**, 045701 (2001).

[15]G. Ódor, “Universality classes in nonequilibrium lattice systems”, Reviews of Modern Physics **76**, 663 (2004).

[16]L. Canet, B. Delamotte, O. Deloubrière, and N. Wschebor, “Nonperturbative renormalization-group study of reaction-diffusion processes”, Physical Review Letters **92**, 195703 (2004).

[17]I. Corwin, “The Kardar–Parisi–Zhang equation and universality class”, Random matrices: Theory and applications **1**, 1130001 (2012).

[18] S. Ramaswamy, “The Mechanics and Statistics of Active Matter”, Annual Review of Condensed Matter Physics **1**, 323–345 (2010).

[19] P. Romanczuk, M. Bär, W. Ebeling, B. Lindner, and L. Schimansky-Geier, “Active Brownian Particles”, The European Physical Journal Special Topics **202**, 1–162 (2012).

[20] T. Vicsek and A. Zafeiris, “Collective motion”, Physics Reports **517**, 71–140 (2012).

[21] M. C. Marchetti, J.-F. Joanny, S. Ramaswamy, T. B. Liverpool, J. Prost, M. Rao, and R. A. Simha, “Hydrodynamics of soft active matter”, Reviews of Modern Physics **85**, 1143 (2013).

[22] J. Elgeti, R. G. Winkler, and G. Gompper, “Physics of Microswimmers—Single Particle Motion and Collective Behavior”, Reports on Progress in Physics **78**, 056601 (2015).

[23] C. Bechinger, R. Di Leonardo, H. Löwen, C. Reichhardt, G. Volpe, and G. Volpe, “Active Particles in Complex and Crowded Environments”, Reviews of Modern Physics **88**, 045006 (2016).

[24] D. Helbing, “Traffic and related self-driven many-particle systems”, Reviews of Modern Physics **73**, 1067 (2001).

[25] C. Castellano, S. Fortunato, and V. Loreto, “Statistical physics of social dynamics”, Reviews of Modern Physics **81**, 591 (2009).

[26] M. Ballerini, N. Cabibbo, R. Candelier, A. Cavagna, E. Cisbani, I. Giardina, V. Lecomte, A. Orlandi, G. Parisi, A. Procaccini, et al., “Interaction ruling animal collective behavior depends on topological rather than metric distance: Evidence from a field study”, Proceedings of the National Academy of Sciences **105**, 1232–1237 (2008).

[27] A. Cavagna, A. Cimarelli, I. Giardina, G. Parisi, R. Santagati, F. Stefanini, and M. Viale, “Scale-free correlations in starling flocks”, Proceedings of the National Academy of Sciences **107**, 11865–11870 (2010).

[28] W. Bialek, A. Cavagna, I. Giardina, T. Mora, E. Silvestri, M. Viale, and A. M. Walczak, “Statistical mechanics for natural flocks of birds”, Proceedings of the National Academy of Sciences **109**, 4786–4791 (2012).

[29] J. E. Herbert-Read, A. Perna, R. P. Mann, T. M. Schaerf, D. J. Sumpter, and A. J. Ward, “Inferring the rules of interaction of shoaling fish”, Proceedings of the National Academy of Sciences **108**, 18726–18731 (2011).

[30] Y. Katz, K. Tunstrøm, C. C. Ioannou, C. Huepe, and I. D. Couzin, “Inferring the structure and dynamics of interactions in schooling fish”, Proceedings of the National Academy of Sciences **108**, 18720–18725 (2011).

[31] C. Becco, N. Vandewalle, J. Delcourt, and P. Poncin, “Experimental evidences of a structural and dynamical transition in fish school”, Physica A: Statistical Mechanics and its Applications **367**, 487–493 (2006).

[32] A. Attanasi, A. Cavagna, L. Del Castello, I. Giardina, S. Melillo, L. Parisi, O. Pohl, B. Rossaro, E. Shen, E. Silvestri, et al., “Collective behaviour without collective order in wild swarms of midges”, PLoS Computational Biology **10**, e1003697 (2014).

[33] A. Attanasi, A. Cavagna, L. Del Castello, I. Giardina, S. Melillo, L. Parisi, O. Pohl, B. Rossaro, E. Shen, E. Silvestri, et al., “Finite-size scaling as a way to probe near-criticality in natural swarms”, Physical Review Letters **113**, 238102 (2014).

[34] A. Cavagna, D. Conti, C. Creato, L. Del Castello, I. Giardina, T. S. Grigera, S. Melillo, L. Parisi, and M. Viale, “Dynamic scaling in natural swarms”, Nature Physics **13**, 914 (2017).

[35] C. Chen, S. Liu, X.-q. Shi, H. Chaté, and Y. Wu, “Weak synchronization and large-scale collective oscillation in dense bacterial suspensions”, Nature **542**, 210 (2017).

[36] D. Nishiguchi, K. H. Nagai, H. Chaté, and M. Sano, “Long-range nematic order and anomalous fluctuations in suspensions of swimming filamentous bacteria”, Physical Review E **95**, 020601 (2017).

[37] H.-P. Zhang, A. Be’er, E.-L. Florin, and H. L. Swinney, “Collective motion and density fluctuations in bacterial colonies”, Proceedings of the National Academy of Sciences **107**, 13626–13630 (2010).

[38] H. H. Wensink, J. Dunkel, S. Heidenreich, K. Drescher, R. E. Goldstein, H. Löwen, and J. M. Yeomans, “Meso-scale turbulence in living fluids”, Proceedings of the National Academy of Sciences **109**, 14308–14313 (2012).

[39] J. Dunkel, S. Heidenreich, K. Drescher, H. H. Wensink, M. Bär, and R. E. Goldstein, “Fluid dynamics of bacterial turbulence”, Physical Review Letters **110**, 228102 (2013).

[40] A. J. Ridley, M. A. Schwartz, K. Burridge, R. A. Firtel, M. H. Ginsberg, G. Borisy, J. T. Parsons, and A. R. Horwitz, “Cell migration: integrating signals from front to back”, Science **302**, 1704–1709 (2003).

[41] Y. Sumino, K. H. Nagai, Y. Shitaka, D. Tanaka, K. Yoshikawa, H. Chaté, and K. Oiwa, “Large-scale vortex lattice emerging from collectively moving microtubules”, Nature **483**, 448–452 (2012).

[42] S. J. DeCamp, G. S. Redner, A. Baskaran, M. F. Hagan, and Z. Dogic, “Orientational order of motile defects in active nematics”, Nature Materials **14**, 1110 (2015).

[43] V. Schaller, C. Weber, C. Semmrich, E. Frey, and A. R. Bausch, “Polar patterns of driven filaments”, Nature **467**, 73 (2010).

[44] A. Bricard, J.-B. Caussin, N. Desreumaux, O. Dauchot, and D. Bartolo, “Emergence of macroscopic directed motion in populations of motile colloids”, Nature **503**, 95 (2013).

[45] J. Deseigne, O. Dauchot, and H. Chaté, “Collective motion of vibrated polar disks”, Physical Review Letters **105**, 098001 (2010).

[46] R. Dreyfus, J. Baudry, M. L. Roper, M. Fermigier, H. A. Stone, and J. Bibette, “Microscopic artificial swimmers”, Nature **437**, 862 (2005).

[47] W. F. Paxton, K. C. Kistler, C. C. Olmeda, A. Sen, S. K. St. Angelo, Y. Cao, T. E. Mallouk, P. E. Lammert, and V. H. Crespi, “Catalytic nanomotors: autonomous movement of striped nanorods”, Journal of the American Chemical Society **126**, 13424–13431 (2004).

[48] J. Palacci, C. Cottin-Bizonne, C. Ybert, and L. Bocquet, “Sedimentation and effective temperature of active colloidal suspensions”, Physical Review Letters **105**, 088304 (2010).

[49] I. Buttinoni, J. Bialké, F. Kümmel, H. Löwen, C. Bechinger, and T. Speck, “Dynamical clustering and phase separation in suspensions of self-propelled colloidal particles”, Physical Review Letters **110**, 238301 (2013).

[50] J. Palacci, S. Sacanna, A. P. Steinberg, D. J. Pine, and P. M. Chaikin, "Living crystals of light-activated colloidal surfers", Science, 1230020 (2013).

[51] F. Ginot, I. Theurkauff, D. Levis, C. Ybert, L. Bocquet, L. Berthier, and C. Cottin-Bizonne, "Nonequilibrium equation of state in suspensions of active colloids", Physical Review X **5**, 011004 (2015).

[52] H.-R. Jiang, N. Yoshinaga, and M. Sano, "Active motion of a janus particle by self-thermophoresis in a defocused laser beam", Physical Review Letters **105**, 268302 (2010).

[53] D. Nishiguchi and M. Sano, "Mesoscopic turbulence and local order in Janus particles self-propelling under an ac electric field", Physical Review E **92**, 052309 (2015).

[54] S. Thutupalli, R. Seemann, and S. Herminghaus, "Swarming behavior of simple model squirmers", New Journal of Physics **13**, 073021 (2011).

[55] Z. Izri, M. N. Van Der Linden, S. Michelin, and O. Dauchot, "Self-propulsion of pure water droplets by spontaneous Marangoni-stress-driven motion", Physical Review Letters **113**, 248302 (2014).

[56] A. Bricard, J.-B. Caussin, D. Das, C. Savoie, V. Chikkadi, K. Shitara, O. Chepizhko, F. Peruani, D. Saintillan, and D. Bartolo, "Emergent vortices in populations of colloidal rollers", Nature Communications **6**, 7470 (2015).

[57] A. Kudrolli, G. Lumay, D. Volfson, and L. S. Tsimring, "Swarming and swirling in self-propelled polar granular rods", Physical Review Letters **100**, 058001 (2008).

[58] N Kumar, H Soni, S Ramaswamy, and A. Sood, "Flocking at a distance in active granular matter.", Nature Communications **5**, 4688–4688 (2013).

[59] V. Narayan, S. Ramaswamy, and N. Menon, "Long-lived giant number fluctuations in a swarming granular nematic", Science **317**, 105–108 (2007).

[60] J. Bialké, H. Löwen, and T. Speck, "Microscopic theory for the phase separation of self-propelled repulsive disks", EPL (Europhysics Letters) **103**, 30008 (2013).

[61] G. S. Redner, M. F. Hagan, and A. Baskaran, "Structure and dynamics of a phase-separating active colloidal fluid", Physical Review Letters **110**, 055701 (2013).

[62] J Tailleur and M. Cates, "Statistical mechanics of interacting run-and-tumble bacteria", Physical Review Letters **100**, 218103 (2008).

[63] M. E. Cates and J. Tailleur, "Motility-induced phase separation", Annu. Rev. Condens. Matter Phys. **6**, 219–244 (2015).

[64] M. B. Miller and B. L. Bassler, "Quorum sensing in bacteria", Annual Reviews in Microbiology **55**, 165–199 (2001).

[65] A. Solon and J. Tailleur, "Revisiting the flocking transition using active spins", Physical Review Letters **111**, 078101 (2013).

[66] A. P. Solon and J. Tailleur, "Flocking with discrete symmetry: The two-dimensional active Ising model", Physical Review E **92**, 042119 (2015).

[67] A. P. Solon, H. Chaté, and J. Tailleur, "From phase to microphase separation in flocking models: the essential role of nonequilibrium fluctuations", Physical Review Letters **114**, 068101 (2015).

[68] T. Vicsek, A. Czirók, E. Ben-Jacob, I. Cohen, and O. Shochet, "Novel type of phase transition in a system of self-driven particles", Physical Review Letters **75**, 1226 (1995).

[69] G. Grégoire and H. Chaté, "Onset of collective and cohesive motion", Physical Review Letters **92**, 025702 (2004).

[70] H. Chaté, F. Ginelli, G. Grégoire, and F. Raynaud, "Collective motion of self-propelled particles interacting without cohesion", Physical Review E **77**, 046113 (2008).

[71] N. D. Mermin and H. Wagner, "Absence of ferromagnetism or antiferromagnetism in one-or two-dimensional isotropic Heisenberg models", Physical Review Letters **17**, 1133 (1966).

[72] J. Toner and Y. Tu, "Long-range order in a two-dimensional dynamical XY model: how birds fly together", Physical Review Letters **75**, 4326 (1995).

[73] J. Toner and Y. Tu, "Flocks, herds, and schools: A quantitative theory of flocking", Physical Review E **58**, 4828 (1998).

[74] J. Toner, Y. Tu, and S. Ramaswamy, "Hydrodynamics and phases of flocks", Annals of Physics **318**, 170–244 (2005).

[75] C. A. Weber, T. Hanke, J Deseigne, S Léonard, O. Dauchot, E. Frey, and H. Chaté, "Long-range ordering of vibrated polar disks", Physical Review Letters **110**, 208001 (2013).

[76] S. Ngo, "Physique Statistique des Groupes en Mouvement", PhD thesis (Université Pierre et Marie Curie, 2013).

[77] A. Czirók, H. E. Stanley, and T. Vicsek, "Spontaneously ordered motion of self-propelled particles", Journal of Physics A: Mathematical and General **30**, 1375 (1997).

[78] E. Bertin, M. Droz, and G. Grégoire, "Boltzmann and hydrodynamic description for self-propelled particles", Physical Review E **74**, 022101 (2006).

[79] E. Bertin, M. Droz, and G. Grégoire, "Hydrodynamic equations for self-propelled particles: microscopic derivation and stability analysis", Journal of Physics A: Mathematical and Theoretical **42**, 445001 (2009).

[80] A Peshkov, E Bertin, F Ginelli, and H Chaté, "Boltzmann-Ginzburg-Landau approach for continuous descriptions of generic Vicsek-like models", The European Physical Journal. Special topics **223**, 1315–1344 (2014).

[81] S. Ramaswamy, R. A. Simha, and J. Toner, "Active nematics on a substrate: giant number fluctuations and long-time tails", EPL (Europhysics Letters) **62**, 196 (2003).

[82] H. Chaté, F. Ginelli, and R. Montagne, "Simple model for active nematics: quasi-long-range order and giant fluctuations", Physical Review Letters **96**, 180602 (2006).

[83] F. Peruani, A. Deutsch, and M. Bär, "Nonequilibrium clustering of self-propelled rods", Physical Review E **74**, 030904 (2006).

[84] A. Baskaran and M. C. Marchetti, "Enhanced diffusion and ordering of self-propelled rods", Physical Review Letters **101**, 268101 (2008).

[85] H. Chaté, F. Ginelli, G. Grégoire, F. Peruani, and F. Raynaud, "Modeling collective motion: variations on the Vicsek model", The European Physical Journal B-Condensed Matter and Complex Systems **64**, 451–456 (2008).

[86] A. Baskaran and M. C. Marchetti, "Nonequilibrium statistical mechanics of self-propelled hard rods", Journal of Statistical Mechanics: Theory and Experiment, P04019 (2010).

[87] F. Ginelli, F. Peruani, M. Bär, and H. Chaté, "Large-scale collective properties of self-propelled rods", Physical Review Letters **104**, 184502 (2010).

[88] S. Mishra, R. A. Simha, and S. Ramaswamy, “A dynamic renormalization group study of active nematics”, Journal of Statistical Mechanics: Theory and Experiment, P02003 (2010).

[89] A. Peshkov, I. S. Aranson, E. Bertin, H. Chaté, and F. Ginelli, “Nonlinear field equations for aligning self-propelled rods”, Physical Review Letters **109**, 268701 (2012).

[90] E. Bertin, H. Chaté, F. Ginelli, S. Mishra, A. Peshkov, and S. Ramaswamy, “Mesoscopic theory for fluctuating active nematics”, New Journal of Physics **15**, 085032 (2013).

[91] S. Ngo, A. Peshkov, I. S. Aranson, E. Bertin, F. Ginelli, and H. Chaté, “Large-scale chaos and fluctuations in active nematics”, Physical Review Letters **113**, 038302 (2014).

[92] E. Putzig and A. Baskaran, “Phase separation and emergent structures in an active nematic fluid”, Physical Review E **90**, 042304 (2014).

[93] E. Bertin, A. Baskaran, H. Chaté, and M. C. Marchetti, “Comparison between Smoluchowski and Boltzmann approaches for self-propelled rods”, Physical Review E **92**, 042141 (2015).

[94] R. Großmann, F. Peruani, and M. Bär, “Mesoscale pattern formation of self-propelled rods with velocity reversal”, Physical Review E **94**, 050602 (2016).

[95] S. Shankar, S. Ramaswamy, and M. C. Marchetti, “Low-noise phase of a two-dimensional active nematic system”, Physical Review E **97**, 012707 (2018).

[96] A Kaiser and H Löwen, “Vortex arrays as emergent collective phenomena for circle swimmers”, Physical Review E **87**, 032712 (2013).

[97] M. Mijalkov and G. Volpe, “Sorting of chiral microswimmers”, Soft Matter **9**, 6376–6381 (2013).

[98] J. Denk, L. Huber, E. Reithmann, and E. Frey, “Active curved polymers form vortex patterns on membranes”, Physical Review Letters **116**, 178301 (2016).

[99] B. Liebchen, M. E. Cates, and D. Marenduzzo, “Pattern formation in chemically interacting active rotors with self-propulsion”, Soft Matter **12**, 7259–7264 (2016).

[100] B. Liebchen and D. Levis, “Collective behavior of chiral active matter: pattern formation and enhanced flocking”, Physical Review Letters **119**, 058002 (2017).

[101] K. H. Nagai, Y. Sumino, R. Montagne, I. S. Aranson, and H. Chaté, “Collective motion of self-propelled particles with memory”, Physical Review Letters **114**, 168001 (2015).

[102] L. Barberis and F. Peruani, “Large-scale patterns in a minimal cognitive flocking model: incidental leaders, nematic patterns, and aggregates”, Physical Review Letters **117**, 248001 (2016).

[103] L. P. Dadhichi, R. Chajwa, A. Maitra, and S. Ramaswamy, “Asymmetric exchange in flocks”, arXiv preprint arXiv:1605.00981 (2016).

[104] M. Durve and A. Sayeed, “First-order phase transition in a model of self-propelled particles with variable angular range of interaction”, Physical Review E **93**, 052115 (2016).

[105] Q.-s. Chen, A. Patelli, H. Chaté, Y.-Q. Ma, and X.-Q. Shi, “Fore-aft asymmetric flocking”, Physical Review E **96**, 020601 (2017).

[106]A. Cavagna, L. Del Castello, I. Giardina, T. Grigera, A. Jelic, S. Melillo, T. Mora, L. Parisi, E. Silvestri, M. Viale, et al., “Flocking and turning: a new model for self-organized collective motion”, Journal of Statistical Physics **158**, 601–627 (2015).

[107]A. Cavagna, I. Giardina, T. S. Grigera, A. Jelic, D. Levine, S. Ramaswamy, and M. Viale, “Silent flocks: constraints on signal propagation across biological groups”, Physical Review Letters **114**, 218101 (2015).

[108]X. Yang and M. C. Marchetti, “Hydrodynamics of Turning Flocks”, Physical Review Letters **115**, 258101 (2015).

[109]O. Chepizhko, E. G. Altmann, and F. Peruani, “Optimal noise maximizes collective motion in heterogeneous media”, Physical Review Letters **110**, 238101 (2013).

[110]C. Sándor, A Libál, C Reichhardt, and C. O. Reichhardt, “Dynamic phases of active matter systems with quenched disorder”, Physical Review E **95**, 032606 (2017).

[111]R. Das, M. Kumar, and S. Mishra, “Polar flock in the presence of random quenched rotators”, arXiv preprint arXiv:1802.08861 (2018).

[112]J. Toner, “Reanalysis of the hydrodynamic theory of fluid, polar-ordered flocks”, Physical Review E **86**, 031918 (2012).

[113]O. Al Hammal, H. Chaté, I. Dornic, and M. A. Munoz, “Langevin description of critical phenomena with two symmetric absorbing states”, Physical Review Letters **94**, 230601 (2005).

[114]F. Benitez, C. Duclut, H. Chaté, B. Delamotte, I. Dornic, and M. A. Muñoz, “Langevin equations for reaction-diffusion processes”, Physical Review Letters **117**, 100601 (2016).

[115]M. A. Munoz, “Nature of different types of absorbing states”, Physical Review E **57**, 1377 (1998).

[116]S. Ramaswamy, “Active matter”, Journal of Statistical Mechanics: Theory and Experiment **2017**, 054002 (2017).

[117]C. Cercignani, *Mathematical Methods in Kinetic Theory* (Springer, 1969).

[118]T. Hanke, C. A. Weber, and E. Frey, “Understanding collective dynamics of soft active colloids by binary scattering”, Physical Review E **88**, 052309 (2013).

[119]T. Ihle, “Towards a quantitative kinetic theory of polar active matter”, The European Physical Journal Special Topics **223**, 1293–1314 (2014).

[120]M. Bixon and R. Zwanzig, “Boltzmann-Langevin equation and hydrodynamic fluctuations”, Physical Review **187**, 267 (1969).

[121]J.-B. Caussin, A. Solon, A. Peshkov, H. Chaté, T. Dauxois, J. Tailleur, V. Vitelli, and D. Bartolo, “Emergent spatial structures in flocking models: a dynamical system insight”, Physical Review Letters **112**, 148102 (2014).

[122]A. P. Solon, J.-B. Caussin, D. Bartolo, H. Chaté, and J. Tailleur, “Pattern formation in flocking models: A hydrodynamic description”, Physical Review E **92**, 062111 (2015).

[123]A. Baskaran and M. C. Marchetti, “Hydrodynamics of self-propelled hard rods”, Physical Review E **77**, 011920 (2008).

[124]P. Degond and S. Motsch, “Continuum limit of self-driven particles with orientation interaction”, Mathematical Models and Methods in Applied Sciences **18**, 1193–1215 (2008).

[125] P. Romanczuk and L. Schimansky-Geier, "Mean-field theory of collective motion due to velocity alignment", Ecological Complexity **10**, 83–92 (2012).

[126] R. Grossmann, L. Schimansky-Geier, and P. Romanczuk, "Active Brownian particles with velocity-alignment and active fluctuations", New Journal of Physics **14**, 073033 (2012).

[127] R. Grossmann, L. Schimansky-Geier, and P. Romanczuk, "Self-propelled particles with selective attraction–repulsion interaction: from microscopic dynamics to coarse-grained theories", New Journal of Physics **15**, 085014 (2013).

[128] A. B. Barbaro and P. Degond, "Phase transition and diffusion among socially interacting self-propelled agents", Discrete & Continuous Dynamical Systems-B **19**, 1249–1278 (2014).

[129] D. S. Dean, "Langevin equation for the density of a system of interacting Langevin processes", Journal of Physics A: Mathematical and General **29**, L613 (1996).

[130] F. Farrell, M. Marchetti, D Marenduzzo, and J Tailleur, "Pattern formation in self-propelled particles with density-dependent motility", Physical Review Letters **108**, 248101 (2012).

[131] G. Tucci, "Stochastic hydrodynamic equations for dry active matter", MA thesis (Polytechnic University of Turin, 2017).

[132] G. Pavliotis and A. Stuart, *Multiscale methods: averaging and homogenization* (Springer Science & Business Media, 2008).

[133] T. Ihle, "Kinetic theory of flocking: Derivation of hydrodynamic equations", Physical Review E **83**, 030901 (2011).

[134] T. Ihle, "Chapman–Enskog expansion for the Vicsek model of self-propelled particles", Journal of Statistical Mechanics: Theory and Experiment **2016**, 083205 (2016).

[135] T. Ihle, "Invasion-wave-induced first-order phase transition in systems of active particles", Physical Review E **88**, 040303 (2013).

[136] M. Kourbane-Houssene, C. Erignoux, T. Bodineau, and J. Tailleur, "Exact Hydrodynamic Description of Active Lattice Gases", arXiv preprint arXiv:1801.08952 (2018).

[137] B. Mahault, X.-c. Jiang, E. Bertin, Y.-q. Ma, A. Patelli, X.-q. Shi, and H. Chaté, "Self-Propelled Particles with Velocity Reversals and Ferromagnetic Alignment: Active Matter Class with Second-Order Transition to Quasi-Long-Range Polar Order", Physical Review Letters **120**, 258002 (2018).

[138] P.-G. de Gennes and J. Prost, "The Physics of Liquid Crystals", Oxford University Press, USA (1995).

[139] J. Toner, "Birth, death, and flight: A theory of Malthusian flocks", Physical Review Letters **108**, 088102 (2012).

[140] L. Chen, J. Toner, and C. F. Lee, "Critical phenomenon of the order–disorder transition in incompressible active fluids", New Journal of Physics **17**, 042002 (2015).

[141] L. Chen, C. F. Lee, and J. Toner, "Mapping two-dimensional polar active fluids to two-dimensional soap and one-dimensional sandblasting", Nature Communications **7**, 12215 (2016).

[142] F. Ginelli and H. Chaté, "Relevance of metric-free interactions in flocking phenomena", Physical Review Letters **105**, 168103 (2010).

[143] A. Peshkov, S. Ngo, E. Bertin, H. Chaté, and F. Ginelli, “Continuous theory of active matter systems with metric-free interactions”, Physical Review Letters **109**, 098101 (2012).

[144] M. Aldana and C. Huepe, “Phase transitions in self-driven many-particle systems and related non-equilibrium models: a network approach”, Journal of Statistical Physics **112**, 135–153 (2003).

[145] Y.-L. Chou, R. Wolfe, and T. Ihle, “Kinetic theory for systems of self-propelled particles with metric-free interactions”, Physical Review E **86**, 021120 (2012).

[146] V. Berezinskii, “Destruction of long-range order in one-dimensional and two-dimensional systems having a continuous symmetry group i. classical systems”, Sov. Phys. JETP **32**, 493–500 (1971).

[147] J. M. Kosterlitz and D. J. Thouless, “Ordering, metastability and phase transitions in two-dimensional systems”, Journal of Physics C: Solid State Physics **6**, 1181 (1973).

[148] J. Kosterlitz, “The critical properties of the two-dimensional xy model”, Journal of Physics C: Solid State Physics **7**, 1046 (1974).

[149] J. V. Jos, *40 years of Berezinskii-Kosterlitz-Thouless theory* (World Scientific, 2013).

[150] R. Gupta, J. DeLapp, G. G. Batrouni, G. C. Fox, C. F. Baillie, and J. Apostolakis, “Phase transition in the 2 d xy model”, Physical Review Letters **61**, 1996 (1988).

[151] W. Janke and K. Nather, “High-precision Monte Carlo study of the two-dimensional XY Villain model”, Physical Review B **48**, 7419 (1993).

[152] M. Hasenbusch, “The two-dimensional XY model at the transition temperature: a high-precision Monte Carlo study”, Journal of Physics A: Mathematical and General **38**, 5869 (2005).

[153] M. Snir, W. Gropp, S. Otto, S. Huss-Lederman, J. Dongarra, and D. Walker, *MPI–the Complete Reference: The MPI core*, MPI: The Complete Reference : The MPI Core (Mass, 1998).

[154] J. C. Neu, “Vortices in complex scalar fields”, Physica D: Nonlinear Phenomena **43**, 385–406 (1990).

[155] E Weinan, “Dynamics of vortices in Ginzburg-Landau theories with applications to superconductivity”, Physica D: Nonlinear Phenomena **77**, 383–404 (1994).

[156] F. Thüroff, C. A. Weber, and E. Frey, “Numerical treatment of the Boltzmann equation for self-propelled particle systems”, Physical Review X **4**, 041030 (2014).

[157] R. LeVeque, *Finite Volume Methods for Hyperbolic Problems*, Cambridge Texts in Applied Mathematics (Cambridge University Press, 2002).

[158] G. Baglietto and E. V. Albano, “Nature of the order-disorder transition in the vicsek model for the collective motion of self-propelled particles”, Physical Review E **80**, 050103 (2009).

[159] F. Ginelli, “The Physics of the Vicsek model”, The European Physical Journal Special Topics **225**, 2099–2117 (2016).

[160] Y. Tu, J. Toner, and M. Ulm, “Sound waves and the absence of galilean invariance in flocks”, Physical Review Letters **80**, 4819 (1998).

[161] N. Kyriakopoulos, F. Ginelli, and J. Toner, “Leading birds by their beaks: the response of flocks to external perturbations”, New Journal of Physics **18**, 073039 (2016).

[162] J. R. Driscoll and D. M. Healy, “Computing Fourier transforms and convolutions on the 2-Sphere”, Advances in Applied Mathematics **15**, 202–250 (1994).

[163] N. Baddour, “Operational and convolution properties of three-dimensional Fourier transforms in spherical polar coordinates”, JOSA A **27**, 2144–2155 (2010).

[164] E. T. Whittaker and G. N. Watson, *Modern Analysis*, 1927.

[165] C. Cohen-Tannoudji, B. Diu, and F. Laloë, *Quantum Mechanics*, Vol. 2, Quantum Mechanics (Wiley, 1977).

[166] F. C. Frank, “I. Liquid crystals. On the theory of liquid crystals”, Discussions of the Faraday Society **25**, 19–28 (1958).

[167] R. E. Breier, R. L. Selinger, G. Ciccotti, S. Herminghaus, and M. G. Mazza, “Spontaneous chiral symmetry breaking in collective active motion”, Physical Review E **93**, 022410 (2016).

[168] M. M. Genkin, A. Sokolov, O. D. Lavrentovich, and I. S. Aranson, “Topological defects in a living nematic ensnare swimming bacteria”, Physical Review X **7**, 011029 (2017).

[169] K. Kawaguchi, R. Kageyama, and M. Sano, “Topological defects control collective dynamics in neural progenitor cell cultures”, Nature **545**, 327–331 (2017).

[170] L. Giomi, M. J. Bowick, X. Ma, and M. C. Marchetti, “Defect annihilation and proliferation in active nematics”, Physical Review Letters **110**, 228101 (2013).

[171] S. P. Thampi, R. Golestanian, and J. M. Yeomans, “Velocity correlations in an active nematic”, Physical Review Letters **111**, 118101 (2013).

[172] S. P. Thampi, R. Golestanian, and J. M. Yeomans, “Instabilities and topological defects in active nematics”, EPL (Europhysics Letters) **105**, 18001 (2014).

[173] L. Giomi, “Geometry and topology of turbulence in active nematics”, Physical Review X **5**, 031003 (2015).

[174] S. Shankar, S. Ramaswamy, M. C. Marchetti, and M. J. Bowick, “Defect unbinding in active nematics”, arXiv preprint arXiv:1804.06350 (2018).

[175] B. Delamotte, “An introduction to the nonperturbative renormalization group”, in *Renormalization group and effective field theory approaches to many-body systems* (Springer, 2012), pp. 49–132.

[176] D. Saintillan and M. J. Shelley, “Orientational order and instabilities in suspensions of self-locomoting rods”, Physical Review Letters **99**, 058102 (2007).

[177] D. Saintillan and M. J. Shelley, “Instabilities and pattern formation in active particle suspensions: kinetic theory and continuum simulations”, Physical Review Letters **100**, 178103 (2008).

[178] A. Baskaran and M. C. Marchetti, “Statistical mechanics and hydrodynamics of bacterial suspensions”, Proceedings of the National Academy of Sciences **106**, 15567–15572 (2009).

universite
PARIS-SACLAY

ÉCOLE DOCTORALE
Physique
en île-de-France
(EDPIF)

Titre : Problèmes en Suspens dans la Physique Statistique de la Matière Active

Mots clés : Physique statistique hors équilibre, matière active, mouvements collectifs, phénomènes complexes

Résumé : La matière active, désignant les systèmes hors d'équilibre composés de particules étant capable d'utiliser l'énergie présente dans leur environnement afin de se déplacer de façon systématique, a suscité beaucoup d'attention auprès des communautés de mécanique statistique et matière molle ces dernières décennies. Les systèmes actifs couvrent en effet un large panel d'exemples allant de la biologie aux granulaires. Cette thèse se concentre sur l'étude de modèles minimaux de matière active sèche (ceux pour lesquels le fluide dans lequel les particules sont immergées est négligé), tel que le modèle de Vicsek qui considère des particules ponctuelles se déplaçant à vitesse constante tout en alignant leur direction de mouvement avec celles de leurs voisins localement en présence de bruit, et définit une classe d'universalité hors équilibre pour la transition vers le mouvement collectif. Quatre problèmes en suspens ont été abordés: La définition d'une classe d'universalité en matière active sèche qui décrit des systèmes de particules présentant un alignement polaire et un mouvement apolaire. Cette nouvelle classe exhibe une transition continue vers un quasi-ordre polaire doté d'exposants variant continument, et donc analogue au modèle XY à l'équilibre, mais n'appartenant pas à la classe d'universalité Kosterlitz-Thouless. Ensuite, l'étude de la validité des théories cinétiques décrivant les modèles de type Vicsek, qui sont confrontées aux résultats obtenus aux niveaux microscopique et hydrodynamique. Puis une évaluation quantitative de la théorie de Toner et Tu, permettant de mesurer les exposants caractérisant les fluctuations dans la phase ordonnée du modèle de Vicsek, à partir de simulations numériques à grande échelle du modèle microscopique. Enfin, la création d'un formalisme pour la dérivation d'équations hydrodynamiques à partir de modèles de matière active sèche à trois dimensions, ainsi que leur étude au niveau linéaire.

Title: Outstanding Problems in the Statistical Physics of Active Matter

Keywords: Nonequilibrium statistical physics, active matter, collective motion, complex phenomena

Abstract: Active matter, *i.e.* nonequilibrium systems composed of many particles capable of exploiting the energy present in their environment in order to produce systematic motion, has attracted much attention from the statistical mechanics and soft matter communities in the past decades. Active systems indeed cover a large variety of examples that range from biological to granular. This Ph.D. focusses on the study of minimal models of dry active matter (when the fluid surrounding particles is neglected), such as the Vicsek model: point-like particles moving at constant speed and aligning their velocities with those of their neighbors locally in presence of noise, that defines a nonequilibrium universalilty class for the transition to collective motion. Four current issues have been addressed: The definition of a new universality class of dry active matter with polar alignment and apolar motion, showing a continuous transition to quasi-long-range polar order with continuously varying exponents, analogous to the equilibrium XY model, but that does not belong to the Kosterlitz-Thouless universality class. Then, the study of the faithfulness of kinetic theories for simple Vicsek-style models and their comparison with results obtained at the microscopic and hydrodynamic levels. Follows a quantitative assessment of Toner and Tu theory, which has allowed to compute the exponents characterizing fluctuations in the flocking phase of the Vicsek model, from large scale numerical simulations of the microscopic dynamics. Finally, the establishment of a formalism allowing for the derivation of hydrodynamic field theories for dry active matter models in three dimensions, and their study at the linear level.

Université Paris-Saclay
Espace Technologique / Immeuble Discovery
Route de l'Orme aux Merisiers RD 128 / 91190 Saint-Aubin, France